Vapour Detection of Explosives, Chemical Agents and Drugs

A thesis submitted for the degree of Doctor of Philosophy



Benjamin Armitage

Wolfson College

Department of Materials, University of Oxford

Hilary Term 2021

Preface

The author carried out the work described herein, under the supervision of Professor M. R. Castell, at the Department of Materials at the University of Oxford, between October 2016 and March 2021. All the work is original and has not been submitted in support of an application for another degree or qualification, at either this university or any other institute of learning. Where the work of others has been drawn upon, it has been referenced and acknowledged. The author was funded by an EPSRC DSTL iCASE Award. Contract reference number DSTLX-1000110461.

Some of this work has been published in peer-reviewed journals or presented at international conferences as follows:

Papers & Conferences

Murugappan, K, Armitage, B. I., Lefferts, M. J., Castell, M.R. Electrochemical Bridging of Conducting Polymers at the Percolation Threshold for Chemiresistors. *Poster presented at Matrafured ICECS Conference,* **2017.**

Armitage, B. I., Murugappan, K., Lefferts, M. J. Castell, M. R. Chemiresistive Vapour Sensing with a Conducting Polymer Percolation Network. *Presented at the 12th International Symposium on the Analysis and Detection of Explosives.* **2017.**

Armitage, B. I., Lefferts, M. J., Murugappan, K., Castell, M. R. Scents & Sensibility: Chemiresistive Vapour Sensors Based on a Percolation Network. *Presented at STEM for Britain.* **2020.**

Armitage, B. I., Murugappan, K., Lefferts, M. J., Cowsik, A. Castell, M. R. Conducting Polymer Percolation Gas Sensor on a Flexible Substrate. *Journal of Materials Chemistry C,* **2020**, **8**, 12669.

Approx word count of thesis: 40,000

Abstract

The detection of ultra-low concentrations of clandestine material has many applications across many sectors, particularly in relation to the military and security. The detection of many of these types of materials, and especially in the case of explosives, is made challenging because of low vapour pressures and intentional attempts at concealment. The aim of this project is to create a new type of sensing system for portable, in the field detection, where the active components are chemiresistive layers operating in the specifically targeted region between being insulating and fully conducting, known as the percolation region. Applying percolation theory to chemiresistive conducting layers increases sensitivity, and exploring new methods of analysis, deposition and deployment has the potential to increase selectivity.

When considering how sensors may be deployed in the field, the first challenge to overcome is to assess how current lab-based analytical techniques are, in some cases, inhibited by the parameters imposed on them as a function of being carried out in a highly controlled environment, and how that may not always translate into real-world utility. Next, sensors are created based on a percolation network of conductive polymers on a glass substrate, and the effect of incorporating gold nano-islands onto the substrate to support percolation network formation is assessed. In order to increase potential applications, percolation sensors are then created on flexible substrates and compared against both those on glass substrates and against other polymer sensors created in other research groups using different methods. One drawback of conducting polymers is that humidity often has an adverse effect on sensing performance. Metal organic frameworks have shown improved stability under humid conditions, and so finally conductive 2D MOFs are synthesized and deposited in novel ways on a variety of substrates and assessed as sensing materials.

To my wife, Chloe and my Mum, Jan. Thank you for all of your love and support. I couldn't have done it without you.

To my children, Finn and Matilda. You both came along in the middle of this work. It wasn't always easy, but the best things in life rarely are.

Be good, be kind, always look out for each other, and work hard.

You never know where it might take you.

This is for you.

Daddy loves you.

Acknowledgements

Firstly, I would like to thank my supervisor, Martin Castell for his continued support, advice and understanding over the course of my project. He gave me the opportunity to come and experience Oxford and all that it offers, for which I am eternally grateful. I would like to extend that thanks to all members of the Surface Nanoscience group, past and present, who have made this experience rewarding and fun for the majority of my time in Oxford. Particular thanks go to Merel and Krish, who took me under their wing in the early days and helped me figure out where I needed to head to have a chance at success. Tabby, Fubiao and Sisheng, who collaborated and contributed hugely along the way, and Abi, who continues to work tirelessly to advance some of the ideas here.

I am grateful to DSTL for their financial and intellectual support. Particular thanks goes to Matt Brookes, Pete Hickey, Pete Glover and Kerry Alton. They were always available for me to seek advice and access to DSTL facilities.

I would like to thank all of those with whom I have collaborated. The research groups of Harish Bhaskaran and Hazel Assender have been amazing to work with in Oxford, as have Lisa Humphreys and Jeff Pons at Cranfield University. I would also like to thank Mark Heron and Chris Gabbutt at the University of Huddersfield, for all their advice on chemistry and academic life in general.

I would like to thank everyone in the Materials Department. I have made many great friends thanks to the department. To all the staff in the SEM suite, OMCS, Estates, Graduate Studies and Admin, thank you for all of your help over the years. You are the cogs that keep the machine running and you do a fantastic job.

Finally, I am grateful to Wolfson College and its community of graduate students, particularly Wolfson football team. I made many friends along the way, and enjoyed college life immensely.

Contents

Preface…….. 2

Abstract…….. 3

Dedication…… 4

Acknowledgements…… 5

Contents…… 6 - 10

Abbreviations……... 11 - 13

1. Introduction…….. 14 - 17

2. Methodology…… 18 - 31

2.1 General methods…… 19

2.2 Interdigitated electrodes…… 19

2.2.1 Platinum interdigitated electrodes on a glass substrate... 20

2.2.2 Gold interdigitated electrodes on a flexible PET substrate……. 20

2.3 Conductive sensing material preparation and deposition…… 21

2.3.1 Electrochemical conductive polymer deposition…… 21

2.3.2 Metal-organic framework preparation and deposition….. 23

2.3.3 Vapour adsorption analysis…….. 24

2.4 Custom sensing chamber setup……... 25

2.5 Ultra-high vacuum gold nanoparticle deposition…… 27

2.6 Sensing demonstrator…… 30

2.7 Summary…….. 31

3. Background (I): Vapour detection of clandestine material……. 32 – 54

3.1 Explosive materials…… 33

3.2 The gold standard: Animal olfaction…… 36

3.3 Challenges for explosives detection…… 39

3.4 Existing detection techniques…….. 42

3.4.1 Bulk detection…….. 43

3.4.2 Trace detection…… 43

3.4.3 Molecular separation…….. 44

3.4.4 Trace detection inspired by the natural world…… 45

3.4.5 Chemical sensors……... 47

3.5 Summary…….. 52

4. Background (II): Electrochemical vapour detection and percolation…… 55 - 85

4.1 Electrochemical transduction…… 56

4.2 Chemiresistive materials…… 58

4.3 Conductive polymers…….. 61

4.3.1 Analyte interaction with conductive polymers…… 62

4.3.2 Polymer deposition and electrochemistry……... 64

4.4 Conductive metal organic frameworks…… 69

4.4.1 MOF deposition……... 72

4.4.2 Silver nanowires…….. 75

4.5 Percolation……... 76

4.5.1 Percolation theory……... 77

4.5.2 Percolation applications……. 80

4.5.3 Percolation sensing…… 81

4.6 Sensor arrays: An electronic nose approach…… 82

4.7 Summary…….. 83

5. Chemiresistive sensing data analysis…….. 86 - 126

5.1 Situational analysis……. 87

5.1.1 Monitoring approach…….. 87

5.1.2 The detection environment: Lab & field..... 88

5.1.3 Step-change monitoring output…… 89

5.2 The $\Delta R/R_0$ method of analysis……. 93

5.3 Definition of terms……... 96

5.4 Rate change analysis for in the field sensing……. 98

5.5 Experimental case studies…… 106

5.5.1 Case 1: Analytical method comparison in a controlled environment…….. 106

5.5.2 Case 2: Analysis of data from conditions simulating field-based acquisition……. 115

5.6 Summary…….. 126

6. Conducting polymer percolation sensors……... 127 - 147

6.1 Materials and methods…….. 128

6.1.1 Platinum IDEs on a glass substrate……. 128

6.1.2 Gold nanoparticle scaffold……. 129

6.1.3 Conductive polymer deposition…… 130

6.2 Gold nanoparticle size and separation…… 131

6.3 Conducting polymer percolation networks…….. 133

6.3.1 Percolation theory applied to chemiresistors……. 134

6.3.2 Dynamic electrochemical polymer networks…….. 137

6.4 Percolation sensing…… 141

6.5 Summary…….. 146

7. Flexible substrates for increased utility……... 148 - 165

7.1 Materials and methods…….. 149

7.2 Conducting polymer percolation networks on flexible substrates…….. 150

7.2.1 Electrochemical polymer deposition…… 151

7.2.2 Percolation networks on flexible substrates…….. 154

7.3 Percolation sensing…… 157

7.4 Sensor comparisons…….. 160

7.4.1. Comparison of CP percolation sensors……. 161

7.4.2. Comparison to other chemiresistive ammonia sensors.. 162

7.5 Summary……. 165

8. Metal-organic frameworks…… 166 - 198

8.1 Materials and methods…….. 167

8.2 Organic linker synthesis…… 168

8.2.1. 2,3,6,7,10,11-Hexabromotriphenylene…….. 168

8.2.2. Triphenylene-2,3,6,7,10,11-hexaylhexakis(1,1-diphenylmethanimine)…….. 169

8.2.3. 2,3,6,7,10,11-Hexaminotriphenylene……. 171

8.3 MOF characterisation ……... 172

8.4 Sensor preparation……. 174

8.4.1. Solvent selection…… 174

8.4.2. MOF sensor preparation on glass electrodes…….. 179

8.4.3. MOF sensor preparation on paper substrates…….. 181

8.5 MOF sensing……... 183

8.5.1. Glass substrate MOF sensing……. 183

8.5.2 Paper substrate MOF sensing…….. 189

8.6 Silver nanowire incorporation…… 192

8.6.1 AgNW concentration…….. 192

8.6.2 AgNW/MOF sensing……. 196

8.7 Summary…….. 197

9. Summary……... 199 - 205

9.1 Explosives detection: Challenges and current solutions…….. 200

9.2 Chemiresistors and percolation…… 201

9.3 Chemiresistive sensing data analysis……. 201

9.4 Novel percolation sensors……. 203

10. Future work…… 206 - 207

References…… 208 - 233

Abbreviations

AFM	Atomic force microscopy
AgNW	Silver nanowires
ANFO	Ammonium nitrate/Fuel oil
CA	Chronoamperometry
CE	Counter electrode
CM	Continuous monitoring
CNT	Carbon nanotube
CP	Conducting polymer
Cu-CAT	$Cu_3(HHTP)_2$
CV	Cyclic voltammetry
CVD	Chemical vapour deposition
CWE	Coated wire electrode
DMMP	dimethyl methylphosphonate
EDOT	3.4-ethylenedioxythiophene
E-nose	Electronic nose
FET	Field effect transistor
FWHM	Full width at half maximum
GC-MS	Gas chromatography-Mass spectroscopy
HATP	2,3,6,7,10,11-Hexaaminotriphenylene
HHTP	2,3,6,7,10,11-Hexahydroxytriphenylene
HITP	2,3,6,7,10,11-Hexaiminotriphenylene
HME	Home-made explosive
HMTD	Hexamethylene triperoxide diamine
IDE	Interdigitated electrode
IED	Improvised explosive device
IPD	Inter-particle distance
ISE	Ion selective electrode
ISFET	Ion selective field effect transistor

K-cell	Knudsen cell
LOD	Limit of detection
MFC	Mass flow controller
MOF	Metal-organic framework
MW	Molecular weight
MWCNT	Multi-walled carbon nanotubes
MOS	Metal oxide semiconductor
NAC	Nitroaromatic compound
p	Probability
p_c	Critical probability
PANI	Polyaniline
PBN	Pyrolytic boron nitride
PEDOT	Polyethylenedioxythiophene
PET	Photon-induced electron transfer
PETN	Pentaerythritol tetranitrate
ppb	Parts per billion
ppm	Parts per million
ppt	Parts per trillion
PPy	Polypyrrole
PT	Polythiophene
PVD	Physical vapour deposition
Py	Pyrrole
p-XRD	Powder X-ray diffraction
RDX	Royal demolition explosive (1,3,5-trinitro-1,3,5-triazine)
RMM	Relative molecular mass
RE	Reference electrode
RH	Relative humidity
RT	Room temperature
SAW	Surface acoustic wave
sccm	Standard cubic centimetres per minute

SCM	Step-change monitoring
SEM	Scanning electron microscopy
SF	Sensitivity factor
SMM	Single measurement monitoring
STM	Scanning tunnelling microscopy
TATP	Triacetone triperoxide
TNT	Trinitrotoluene
TP	Triphenylene
WE	Working electrode
XRD	X-ray diffraction spectroscopy

Chapter 1

Introduction

Fast and accurate detection of vapour analytes is necessary in many environments, particularly those that may be hazardous to human health.[1] Devices that utilise optical absorption, chromatography or spectrometry currently accomplish environmental monitoring of vapour analytes of interest.[2] For example, the cheapest and thus a popular type of CO detector utilises colorimetric changes in a chemical layer, triggering an alarm if a colour change occurs.[3] The fact that this type of CO detector is relatively cheap is an anomaly compared to most commercially available, low concentration detection systems.

Generally, and particularly for the detection of clandestine material, increases in device selectivity and sensitivity are proportional to cost.[4] In the majority of cases these instruments are large and multifaceted. Portability is also problematic, because many of these instruments require highly specific conditions to operate efficiently, increasing complexity and size. For these reasons, the most successful and frequently used field based detectors are still working dogs.[5] However, canine deployment is not without drawbacks, where dogs require care, handling and large expense to train and work.[6]

The complications inherent in attempting to utilise either animals or the capabilities of large, static detectors in a portable gas sensing device has led to attempts to find novel ways of creating portable sensors that fit the criteria in a ‘bottom up’ approach. Much current research is focussed on designing sensors that meet the portable, cheap and easy to use remit from inception.[4] The most promising areas currently are focussed on utilising the intrinsic properties of nanomaterials, polymers and enzymes to mimic some of the capabilities of the animal olfactory system.[7]

The value of these methods and materials is that in nearly all cases an optical or an electrochemical response can be recorded from a chemical interaction. Generating a

physical, measurable response from a chemically produced transducer accesses simplified response recognition and allows rapid numerical interpretation. The resultant data can be either qualitative, quantitative or both, but must provide enough information for identification of target molecules. Current challenges include finding new materials to expand the scope of such sensors, which can operate in ambient conditions and detect target compounds at sufficiently low enough levels and with enough selectivity between analytes to be genuinely competitive and viable against more established techniques.

The aim of this thesis is to address some of these challenges by depositing conductive chemical layers which will act as chemiresistive vapour sensors, with particular focus on analytes associated with explosives, and detection in a field-based setting. Some of the materials used here have been investigated in other work, generally in the form of thin films. This work will show that careful selection of both material and deposition method can result in large improvements in sensitivity by exploiting percolation theory. Specifically targeting the percolation region will enable relatively small amounts of analyte to have a large impact on conductivity across the whole network, and as a result sensing response and sensitivity will improve. Selectivity is often challenging for chemiresistive layers, particularly when used in isolation. This work aims to explore percolation theory applied to different types of conductive sensing layers deposited in novel ways, and methods of analysis that allow different layers to be compared and assessed together at the same time, in real time. This will move towards being able to deploy multiple different types of sensors together in an array, resulting in a fingerprint response, and thus increased selectivity.

The thesis begins by introducing the methods used to carry out the work described here. An outline of the chemicals used is supplied, followed by a description of the interdigitated electrodes used and how they were prepared prior to being used. Then, the conductive layers employed throughout this work and the way in which they are deposited is discussed. For sensor interrogation, a custom-built sensing chamber was

constructed, and details of this are provided. Some of the work in this thesis involved UHV deposition of gold nanoparticles, and the setup used to achieve this is described. Finally, this project involved the design and creation of a sensor testing demonstrator device, and this is described.

Chapters 3 and 4 are background and literature review chapters. The first gives a broad background to the detection of clandestine material, with a particular focus on explosives. This chapter includes a description of some explosive materials, current methods of detection and challenges faced by those who wish to research new ways of detecting analyte vapours. It then details some examples of chemical sensors, and how chemiresistors in particular can be deployed together in an array. Chapter four is focussed on chemiresistive materials, electrochemical transduction and deposition methods of some well-known examples of conductive chemical layers capable of vapour detection. This chapter also provides a detailed introduction to percolation theory, and how it can be applied in this context to improve sensors constructed in this way.

Chapter 5 is the first experimental chapter of this thesis, and is concerned with analysis of the sensing output of chemiresistive sensors. Current methods of analysing sensor data may be inefficient and flawed in some unpredictable environments, and this chapter provides new analytical methods that are effective regardless of the setting in which they are used. The ultimate aim is to enable analyses that provide new insights into sensor behaviour and allow comparison and interpretation of multiple sensor outputs operating together during a detection event, rather than afterwards, that may have been created in different ways at different times.

Chapter six is focussed on the creation of percolation sensors on glass substrates using conducting polymers. The percolation region is identified, and then sensors operating both within and outside this region are compared. In addition, gold nanoparticles are

used to improve sensitivity further, by manipulating the architecture and amount of polymer required to access the percolation region.

Chapter 7 is an extension of the work carried out in the previous chapter, and aims to improve the scope and applicability of percolation sensors by exploring their use on flexible substrates. Flexible sensors are produced and tested.

Chapter 8 introduces a different type of material for use in percolation sensors, conductive MOFs. New materials provide new challenges for deposition, substrate choice and sensing capability. In this chapter, MOFs are suspended in an ‘ink’ type solution containing different solvent mixtures to aid with particulate distribution, and augmented with silver nanowires to stabilise conductivity. These mixtures are deposited onto both glass and paper substrates by drop-casting, with a view to being used in inkjet printing applications, and sensing performance is assessed.

Finally, chapters 9 and 10 provide a summary of the results achieved in this thesis, and provide some suggestions for future work to build on the results obtained here.

Chapter 2

Methods

In this chapter, the methods and instrumentation used to produce the work described in this thesis are described. The chapter begins with a general methods section describing chemicals and analytical instruments used, and how interdigitated electrodes were sourced and treated prior to use. The next section outlines the primary techniques used to deposit chemical sensing layers, namely conducting polymers (CPs) and metal-organic frameworks (MOFs). Next, the custom-built sensing chamber used to interrogate sensing layer performance is described. In some cases gold nanoparticle scaffolds were produced to enhance the behaviour of the percolation networks. This process is explained. Finally, in order to improve selectivity, sensors were deployed in an array using a device designed and made for the sensors produced in this work. This demonstrator device is defined.

2.1 General methods

Chemicals were used as received, purchased from either Sigma Aldrich or Fisher Scientific. Electrochemical polymer growth was facilitated using a PGSTAT204 Autolab potentiostat (Eco Chemie, Netherlands) interfaced to a PC with NOVA version 1.1 software. Powder X-ray diffraction (P-XRD) data was gathered using Bruker D8 Eco, employing a copper X-ray tube operating at 40 kV and 25 mA. Spectra are presented corrected for K-α and with background subtracted. Scanning electron microscopy (SEM) was carried out on a Zeiss Merlin 60-62 with accelerating voltages of between 1 – 3 kV. Samples were mounted on a custom-made stub with clips to secure samples in place (Agar Scientific), and all images were taken with no prior sample preparation.

2.2 Interdigitated electrodes

Interdigitated electrodes (IDEs) typically consist of two individually addressable electrodes deposited on an insulating substrate and arranged in a comb-like pattern. Since their development in the 1970s, they have proven to be a popular choice of electrode configuration in many applications including deposition of ceramic films,[8] component fabrication in tuneable devices[9] and as transducers in solid state sensing.[10,11] They are readily available, relatively cheap and the gap size between fingers from each electrode is variable dependent on requirements. Figure 2.1 shows a schematic of a typical IDE studied here. All IDEs used in this study were purchased and used either directly or treated as detailed below.

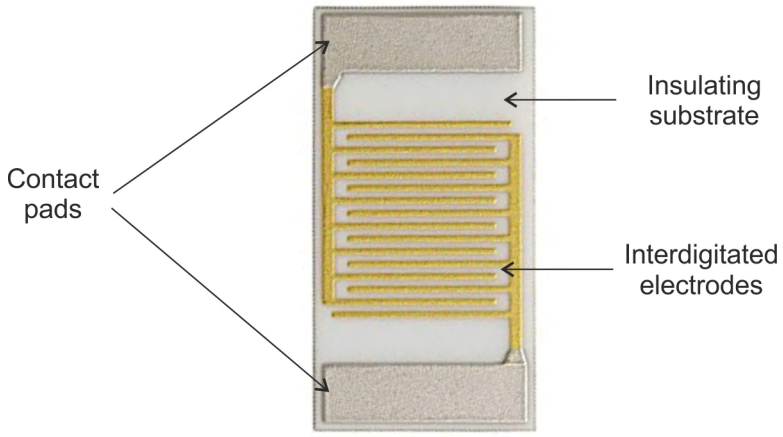


***Figure 2.1**. An interdigitated electrode. The area between electrode fingers is where conductive layers can be deposited to connect opposing electrodes.*

2.2.1 Platinum interdigitated electrodes on a glass substrate

The IDEs primarily studied in chapter 6 consist of a Pt IDE with a 5 μm gap size deposited on a glass substrate. A gap size of 5 μm is the smallest available commercially, and was chosen here as a smaller gap size has proven more conducive for percolation network formation.[12] These Pt/glass electrodes were purchased from Micrux (Spain). Prior to use, in all cases the IDEs were submerged in HNO_3 for 20 s, before being sonicated sequentially in MeOH, EtOH then d.H_20 for 20 s each. They were then left to air dry for a minimum of 10 minutes.

2.2.2 Gold interdigitated electrodes on a flexible PET substrate

The flexible electrodes discussed in chapter 7 are fabricated from gold IDEs deposited on a flexible PET substrate. The minimum available gap size in this case was 100 μm. Owing to the degradation of PET in some of the cleaning solvents used in chapter 2.1.1, these electrodes were used as purchased from DropSens (UK).

2.3 Conductive sensing material preparation and deposition

The sensors described in this work all rely on a conductive chemical layer in order to monitor changes in the local environment, normally as a function of a reversible reaction or interaction at the surface of the sensing layer. In order to satisfy the remit of the project, the layers should ideally be relatively simple in terms of both production and deposition. For that reason, the two primary types of sensing layer utilised in this work were CPs and MOFs. The techniques used to produce these sensing layers are described here.

2.3.1 Electrochemical conductive polymer deposition

All of the work described in chapter 6 and 7 of this thesis focuses on CPs, and in this project all CPs were deposited using two closely related electrochemical techniques, either cyclic voltammetry (CV) or chronoamperometry (CA).

In electrochemical polymerisation, a known concentration of monomer is dissolved in a salt solution, into which are placed three electrodes, forming a three-electrode chemical cell. In this work, typical salt solutions contain 0.1 M $LiClO_4$ and 0.1 M monomer in acetonitrile or d.H_2O. In cases where the salt solution is changed, this will be detailed in the relevant chapter. Now, the IDEs used for polymer deposition become the working electrode (WE), which is accompanied by an Ag/AgCl reference electrode (RE) and Pt counter electrode (CE). A potentiostat is then used to apply a predetermined potential or range of potentials and the current is monitored and recorded. Figure 2.2 shows a schematic representation of a typical three-electrode chemical cell.

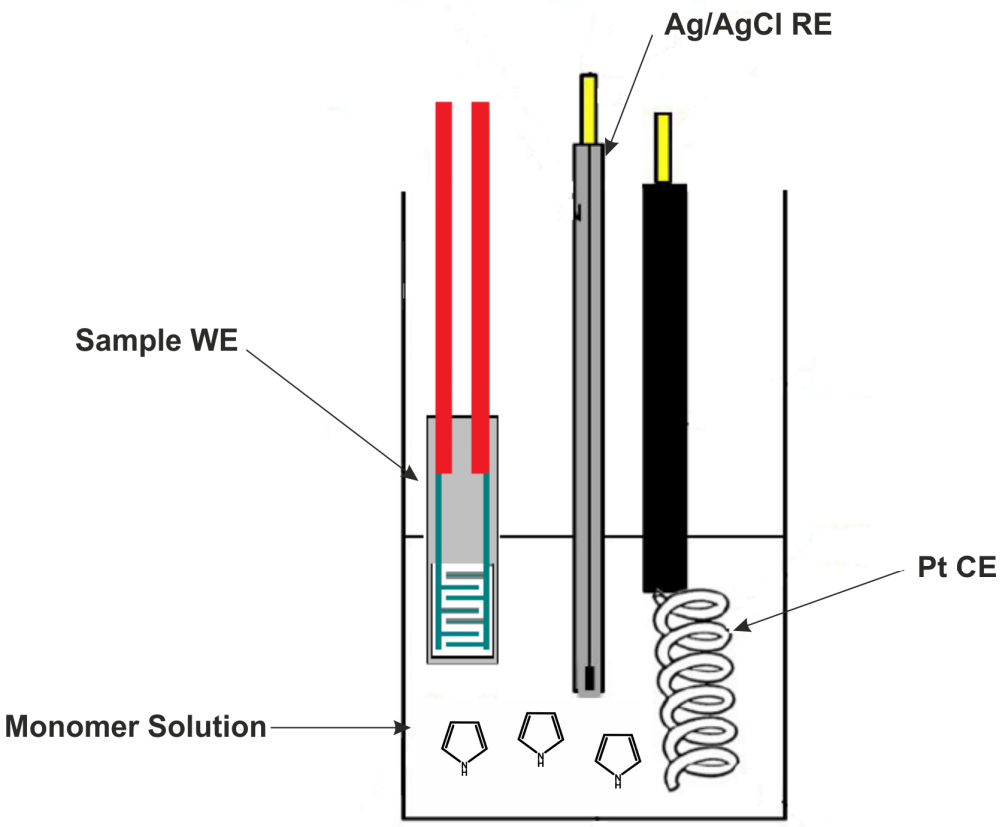


***Figure 2.2**. A schematic representation of a standard three-electrode electrochemical cell.*

Now, all three electrodes in the cell are connected to a potentiostat and the monomer is polymerised and deposited on the sample by either scanning across a range of potentials (CV) or holding the potential at a predetermined polymerisation potential (CA) and monitoring the change in current as a function of either applied potential (CV) or time (CA). Owing to the nature of the IDEs, polymer growth always starts on the metallic electrodes and grows across the insulating gap after the electrodes are covered with polymer. For CV, typical scans range from -1 to 2 V, and for CA typical oxidation potentials fall between 1 – 1.5 V for deposition times of between 1 and 120 seconds.

Doping is a common way to stabilise or modify the polymer network,[13] maximise conductivity and ensure uniformity in the deposited layer. The purpose of p- or n-doping

is to incorporate anions or cations from the salt solution into the polymer matrix. In some cases, dopants can serve to modify the behaviour of polymer networks by incorporating additional molecular architecture into the polymer backbone. Post-polymer deposition, all samples in this work were p- or n-doped prior to use. To p- or n-dope a sample for increased sensitivity and stability, first the samples were allowed to dry in air. Then, the same process described for CA was repeated, in a salt solution devoid of monomer, with an applied potential of 1 – 1.4 V, and for a fixed time of 60 s in each case. In the cases where dopants were employed to modify selectivity, dopants were incorporated into the monomer deposition solution.

2.3.2 Metal-organic framework preparation and deposition.

The work described in chapter 8 is based on the electrical behaviour of conductive MOFs. In the majority of the work herein, MOFs were produced using 'wet-chemistry' methods. Some of the collaborative work described in chapter 8 also involved attempting to deposit MOF monolayers in a UHV system.

Generally, conductive MOFs form from a metal salt and an organic ligand in solution via self-assembly. In this case the two-dimensional (2D) π-conjugated MOFs in this study consist of a layered network of stoichiometry $M_3(Ligand)_2$.

MOFs were prepared by preparing an aqueous solution containing a 1:2 molar ratio of 2,3,6,4,10,11-hexahydroxytriphenylene or 2,3,6,7,10,11-Hexaaminotriphenylene (HATP) & (HHTP) and metal (II) acetate respectively. The mixture was then heated at between 85 °C and 95 °C for 24 h to give a precipitate of needle shaped crystals. These were gravity filtered and rinsed with two aliquots (20 mL) of d.H_2O and one aliquot (20 mL) of acetone to yield $M_3(HHTP)_2$ or $M_3(HITP)_2$ respectively.

In order to increase and stabilise conductivity, in some cases MOFs were mixed in solution with silver nanowires (AgNW, 60 nm x 10 μm in IPA). Most commonly in this work, MOFs and MOF mixtures were drop cast onto the substrate. Drop casting is a

simple method of deposition where a suspension of MOF is prepared in a solvent or mixture of solvents, before a droplet of known volume is applied to the substrate. The solvent evaporates either at room temperature (RT) or after heat is applied depending on the solvent, leaving the solid sample behind. One issue with this method is that fine control over the thickness of the deposited layer is difficult to achieve. Furthermore, drop cast layers can display patterns or so-called 'coffee rings' as a result of the Marangoni effect. This can be countered to some extent by solvent choice, and is discussed in detail in chapter 8.

Where MOFs were deposited on a paper substrate, the paper used was standard A4 80 gsm printer paper, and electrodes were hand drawn after MOF deposition using a Circuit Scribe conductive ink pen. After deposition, some MOF mixtures were pressed under a force of 10 kN for 10 seconds using a Clarke CSE10BB 10 tonne hydraulic bench press.

2.3.3 Vapour adsorption Analysis

Adsorption of vapour analytes onto a solid surface or thin film was studied by Langmuir who developed an empirical model based on the surface coverage, θ.[14] The Langmuir adsorption isotherm assumes that (1) the surface on which the gas adsorbs is homogeneous, (2) a specific number of sites are available for gas adsorption, and once all these sites are occupied, further adsorption is not possible. This is called monolayer adsorption, and (3) all sites on which gas is adsorbed are equivalent in terms of heat of adsorption (Q). Assuming that the relationship between surface coverage at time t (θ_t), and change in conductance at time t (G_t) are linearly related, then a sensor that adheres to the Langmuir model can be expressed as:

$$G_t^{response} = G_0 + G_1 \left[1 - e^{\frac{-t}{\tau_{res}}}\right]$$

(Eq. 2.1)

Where G_0 is the baseline conductance at t = 0, G_1 is a fitting parameter and τ_{res} is the response time. This equation is only valid if all three of Langmuir's assumed criteria are satisfied. Now, since

$$G_1 = \frac{P}{P+b}$$

When P is the gas pressure and b is related to heat of adsorption. At low concentration, it can be assumed that P ≈ analyte concentration (C), and we can write

$$\frac{G_1}{1- G_1} = \frac{C}{b}$$

(Eq. 2.2)

Now, changes in $G_1/1-G_1$ against C should give a linear plot, the gradient of which gives an estimate of b. b is related to Q, and from that a value can be obtained for the analyte and concentration dependent activation energy, E_a. Attempts were made in this work to apply the Langmuir isotherm to the sensing results shown in chapters 6 and 7. However, the fitting parameters never gave the expected linear response required to obtain b (Eq. 2.2) and so in this work the Langmuir isotherm was not applicable. This is likely to be a result of the fact that the percolative sensing layers in this work didn't fully satisfy criteria (1) and (3) of the Langmuir model. Attempts to redesign aspects of the Langmuir model have been attempted and continue to be explored by the Castell research group. Access to values for analyte specific E_a would be highly valuable when attempting to improve device selectivity, and it is hoped that a new model designed specifically for percolative regimes will be achieved in the future.

2.4 Custom sensing chamber setup

In order to test any sensors produced in a controlled way, a custom designed sensing chamber was used. The setup consists of a small central sealed chamber, serviced by ten feedthroughs. Analyte gas flow rates are controlled by mass flow controllers (MFCs,

Alicat, USA), which flow into a T-joint (Swagelock) for mixing before entering the chamber. All MFCs are interfaced to a PC equipped with Alicat FlowVisionSC software. Figure 2.3 shows a schematic diagram of the sensing set up.

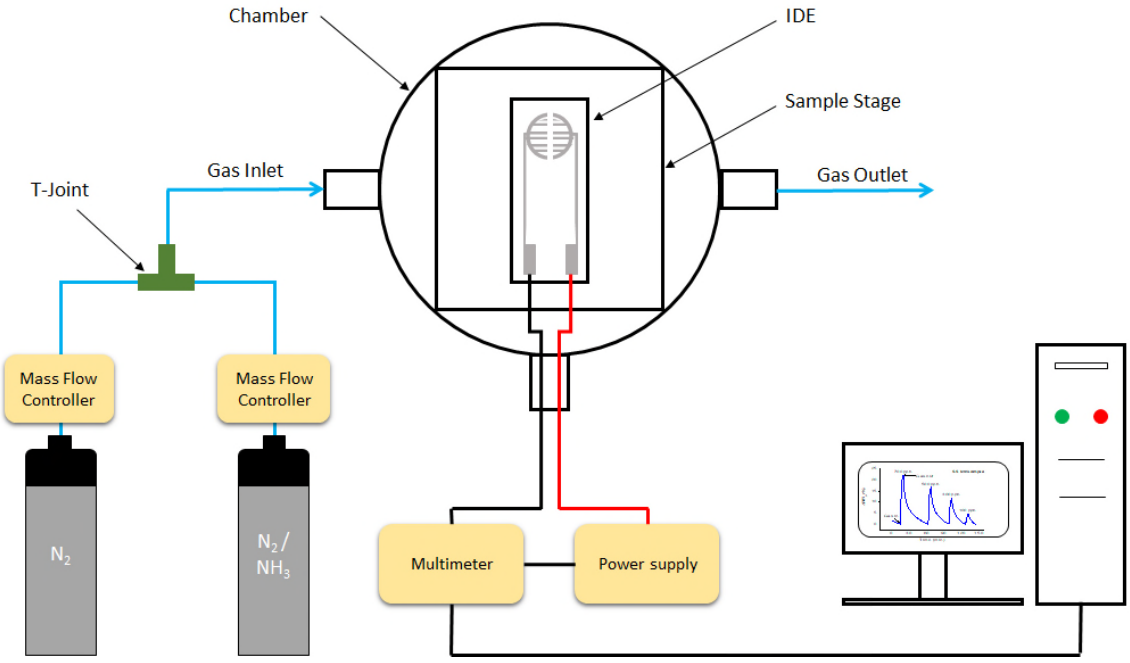


***Figure 2.3**. Schematic layout of the gas sensing chamber.*

Sensors are placed on a central stage, capable of heating samples if required. Electrical connections run via a feedthrough from an external power supply and multimeter, or a source meter. These instruments are controlled with a PC equipped with BenchVue software and connect either directly to the contact pads of the sample (Figure 2.1) or in the case of commercially sourced IDEs, to a sample holder. An exhaust outlet allows vapour egress. Optional feedthroughs offer the capability to operate the system under vacuum, test humidity capability and solid-state analyte samples in a custom made glass vessel. An image of the chamber is shown in Figure 2.4.

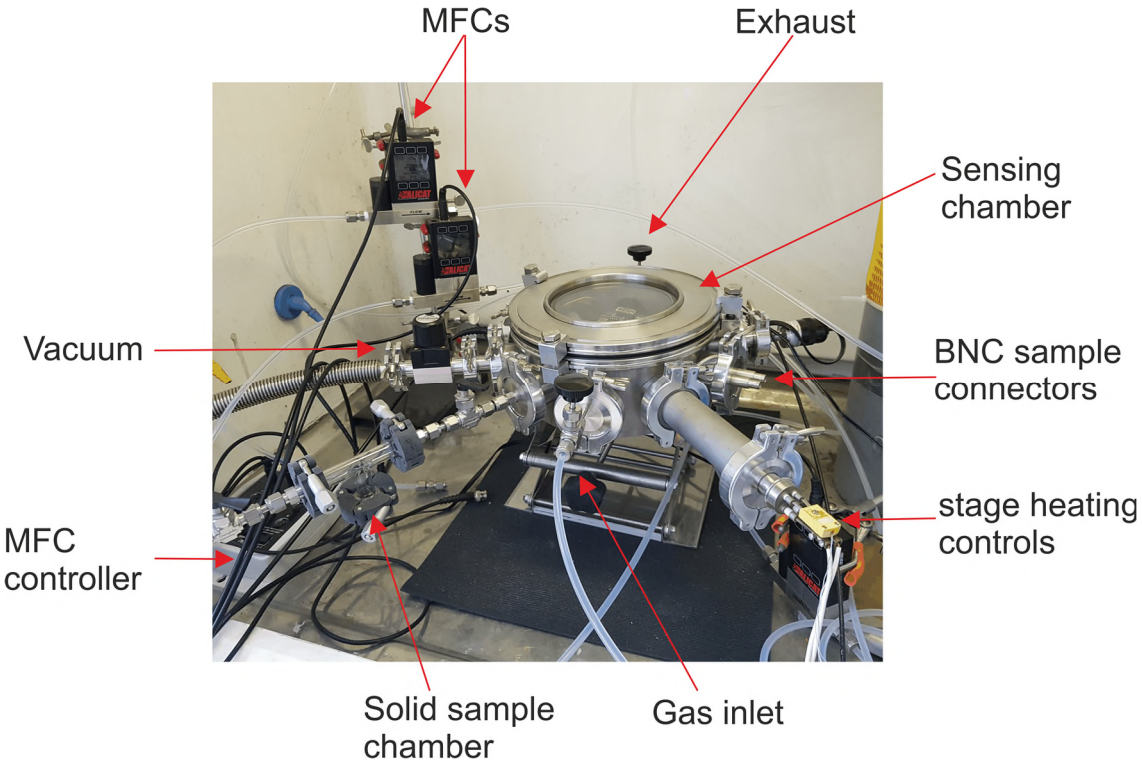


***Figure 2.4**. Image of the custom built sensing chamber, labelled with the functions of some of the feedthroughs.*

Before analyte exposure, each sample was left under carrier gas flow (either N_2 or dry air) for 45 - 60 minutes to purge the chamber and remove any impurities. Then, a stable voltage of between 0.5 – 1.5 V was applied across the electrodes, and current was measured. Once a stable baseline was reached, different concentrations of analyte gas were introduced and changes in current were recorded. This process was repeated for differing concentrations of analyte as required.

2.5 Ultra-high vacuum gold nanoparticle deposition

A large proportion of the experimental work described in chapter 6 is focussed on percolation behaviour enhanced in the presence of gold nanocrystals. In order to deposit these nanoparticle scaffolds via physical vapour deposition (PVD), an ultra-high vacuum (UHV) environment is required, since it provides a high level of cleanliness, and limits

potential contamination and defect formation during deposition. The equipment required to carry out this process is described here.

Wetting and dewetting are terms used in fluid mechanics to describe whether a fluid will spread evenly over a surface (wetting) or retract to form droplets or islands (dewetting). Whether one material wets another materials depends on the relative surface energies of the materials. The energies that must be taken into account are the surface energies of the metal, the substrate and that of the interface between the metal and the substrate.[15] A stable wetted film is generally preferred when the surface energy of the substrate is greater than the combined energy of the metal and interface. In all other cases, dewetting is preferred. In most cases when a thin film is deposited on a substrate it is in a metastable state. When such a film is heated, it will either form a more consistent wetting layer or it will dewet and form islands. Dewetting can take place at temperatures well below the melting point of the metal. In this work, typical surface energies are 1.33 J/m^2 for gold and 58.95 mJ/m^2 for glass. Because the surface energy of the gold is so much greater than that of the glass, dewetting to form islands is promoted at relatively low anneal temperatures.

To form supported metal nanoparticles through thin film dewetting, first a metal thin film is deposited. The metal thin film can be deposited using a thermal evaporation method, for example using an e-beam or as in this work, a K-cell. Next, the sample is heated *in-situ* to encourage dewetting, Thin film dewetting is a convenient method for the formation of supported metal nanoparticles because it, by definition, results in a (sub-)monolayer of particles. Furthermore, this method allows for control over the size and spacing of the metal. Once a film has dewetted the individual particles can continue to change through Ostwald ripening. In Ostwald ripening larger particles continue to become larger and smaller particles become smaller or disappear. It is energetically more favourable to have one larger particle than it is to have many smaller particles because this causes a decrease in the total surface area of the nanoparticles.[14]

The UHV system used to deposit gold consists of two interconnected vacuum chambers, one of which is used for sample loading and transfer, and the other for gold PVD (JEOL, Japan). The system can achieve vacuum pressures as low as 10^{-8} Pa. The PVD chamber is serviced by a Knudsen cell (K-cell) for indirect thermal evaporation (CreaTec Fischer). Gold is placed in a pyrolytic boron nitride (PBN) crucible within the K-cell, which is then heated by a tantalum wire via radiative heating to between 1200 – 1500 °C. Temperature control is achieved by controlling the power applied to the tantalum wire from an external power supply. The K-cell is also equipped with a shutter, operated externally, to cover the evaporation aperture and thus stop deposition quickly if required. These measures allow for fine control of evaporation rates, which typically take place at between 0.02 – 0.03 Å s^{-1}. The thickness of the deposited layer is monitored *in situ* during deposition via a quartz crystal microbalance (QCM) controlled via a PC with an in-house Python script. The system is shown in Figure 2.5.

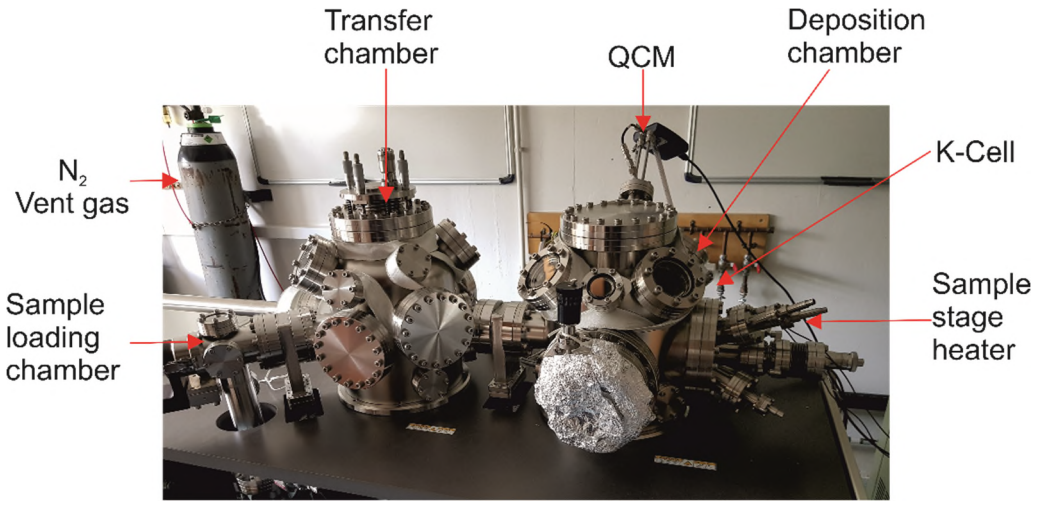


***Figure 2.5**. Image of the UHV deposition chamber setup, used in this work to deposit Au on Pt IDEs.*

The sample, a Pt/glass IDE, prepared as described in chapter 2.2.1, is mounted in a sample holder (JEOL, Japan). All samples studied in chapter 6 have an initial Au NP thickness of 5 nm before annealing and dewetting. Figure 2.6 shows a sample IDE placed in the indirect heating sample holder outside the UHV chamber.

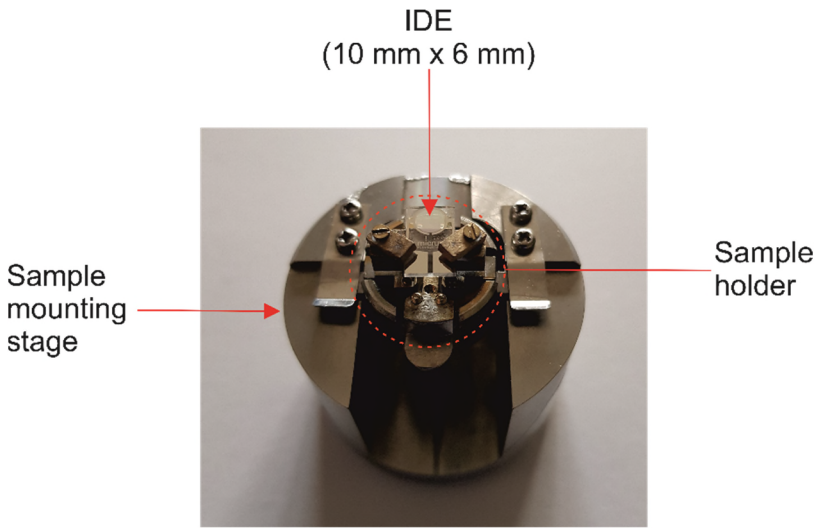


***Figure 2.6**. Image of an IDE mounted on the indirect heating sample holder ready to be placed in the UHV chamber.*

2.6 Sensing demonstrator

After producing a number of different electrodes, it is a valuable resource to be able to deploy them in tandem in order to achieve a finger print response to an analyte of interest, whereby different sensors responding differently to the same analyte can be assessed together in real time, ultimately improving selectivity.

In order to achieve this, the work in this thesis led to a collaboration with a German electronics company, JLM Innovation, who were provided with a list of requirements and produced a sensing demonstrator, shown in Figure 2.7.

This device is relatively small and lightweight. It is powered by an in-built rechargeable battery, charged via micro-USB to any compatible power source. It has four ports for IDE insertion, each of which can have a pre-determined potential applied for sensing. Sensing data is acquired in real time and transmitted via Bluetooth to a custom Android

app, which displays the data as it is gathered and stores it as a .txt file for extraction and analysis at a later point.

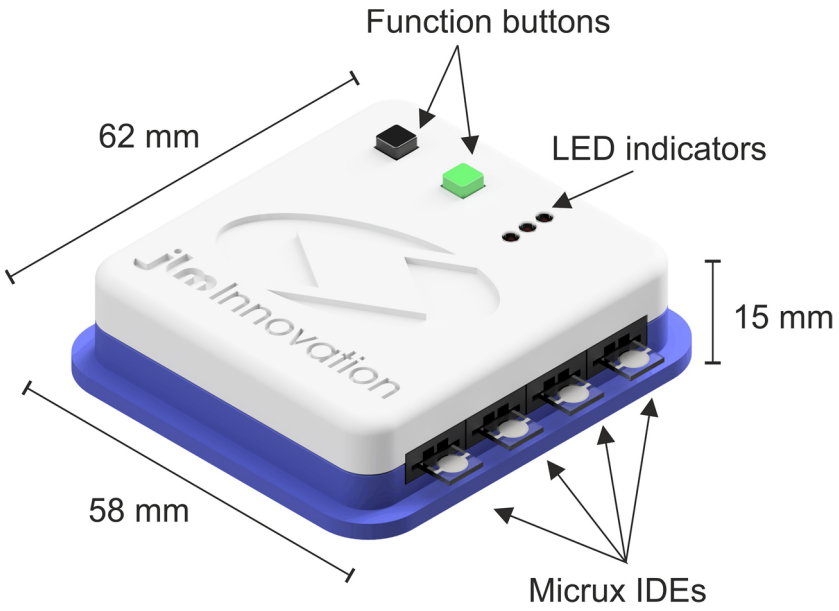


***Figure 2.7**. Image of the sensing demonstrator, containing four IDEs.*

2.7 Summary

This chapter has provided details of the equipment and methods used to produce the work contained in this thesis. The substrates used for sensor construction were described, along with the conductive materials and methods for deposition used to populate the substrates. Sensors were interrogated using a custom built sensing chamber which is detailed. In some cases, UHV techniques were required to deposit gold nanoparticles, and the setup required to achieve this was introduced. Finally, sensors were tested in an array using a demonstrator device, which was built as part of this project. This device is explained.

Chapter 3

Background (I): Vapour detection of clandestine material

Analyte-specific sensors have innumerable potential uses in civilian and security sectors, but this thesis has particular focus on applications for the rapid detection of threat material. Threat material is a broad term typically referring to illegal substances, most commonly drugs and in particular in this case, explosives. Understandably, detection of such materials is of high interest for all law enforcement, military and many humanitarian organisations. Inherently, detection of clandestine material in uncontrolled environments is challenging, not least because in the majority of cases the handler will go to great lengths to conceal and deceive any attempts at detection.

The focus of this chapter, and indeed this thesis, is on vapour detection of clandestine material. Vapour sensors that mimic aspects of mammalian olfactory systems are of great interest to the scientific community, and have received much devotion in terms of research.[16,17] Vapour detection is particularly appealing in this context because it allows stand-off detection, and thus a contactless method with reduced likelihood to detonate or otherwise interfere with the target material. Through continued research into improving existing techniques, along with the development of novel sensing systems, it is likely that technology will replace the requirement for deployment of animals into inhospitable environments, and enable those with no access to trained animals to be able to detect concealed ordnance. This chapter details the current state of the art.

3.1 Explosive materials

Explosives, and particularly chemical explosives, have been utilised for at least a thousand years since crude explosive chemical mixtures were first described in 9th century China.[18] The first known manufactured explosions were created using Black powder. Black Powder consists of a mixture of potassium nitrate, also known as saltpetre, sulphur and carbon, historically in the form of charcoal. Originally, Black Powder was used for signalling, fireworks, mining and construction and was not originally weaponised for use in war. However, the Silk Road enabled Europeans to access Chinese technology and by the 13th century, the predominant western use for black powder was to create ballistic propellants for use in conflict.

Black powder is a messy and crude explosive, with comparatively little explosive power. As a result, by the end of the 18th century, military technology had advanced leading to the development of cleaner, smokeless and higher-powered explosives from which modern explosives are derived. Fast forward to the present day, and the range and capability of explosives has advanced rapidly to incorporate a wide range of materials with an equally diverse range of preparation requirements and explosive capability.

Development of new types of explosive materials coupled with the rise of global access to communication and information have all contributed to significant new challenges for those wishing to develop sensors capable of detecting such material. One of the traits of explosives from the point of view of an aggressor is that the materials can be concealed then left for inordinate amount of time. Inevitably, the result of this is an ever-increasing arsenal of hidden, unexploded ordinance across the globe. Detection of this ordinance then becomes of interest both militarily and from a humanitarian perspective.

Explosive materials, by definition, are any substances that contain a vast amount of stored potential energy. Sudden initiation and release of this stored energy results in a self-propagating decomposition in the form of an explosion, which is accompanied by

the rapid release of heat, pressure, light and sound as the material breaks down into more stable components, many of which are gaseous in nature. It is the build-up of gas pressure that dictates the nature of the explosion. Black powder is classified as a low explosive, the categorisation of which descends from the rate at which the decomposition propagates. Low explosives tend to be combustible solids that deflagrate rather than detonate, and are generally only combustible at the surface. This means that the deflagration follows a distinct path, making low explosives ideal for launching projectiles from a tube or cylinder. Low explosives typically decompose at sub-sonic speeds (less than 0.34 km/s).

High explosives differ because they have a much higher rate of decomposition, and truly detonate upon initiation. They typically expand at supersonic speeds many orders of magnitude higher, generally in the region of multiple km/s.[19] Consequently, high explosives have vastly increased destructive power, but are less suited for use as propellants to launch projectiles.

Commonly, high explosives are manufactured by nitrating organic molecules. Nitration is favoured since it allows incorporation of three essential components, namely nitrogen, oxygen and an oxidisable fuel source (generally carbon and hydrogen). Some familiar examples include nitrating toluene to give trinitrotoluene (TNT) and glycerine to give nitroglycerine. Nitro-compounds tend to be unstable and will readily break down into their stable, gaseous components including CO, CO_2, N_2 and O_2. The liberation of large amounts of heat and gas result in a large pressure differential, and the rate at which the maximum pressure is reached after detonation is known as brisance. Most high explosives are brisant, meaning they detonate with an accompanying shockwave. Figure 3.1 (below) shows the chemical structure of some high explosives.

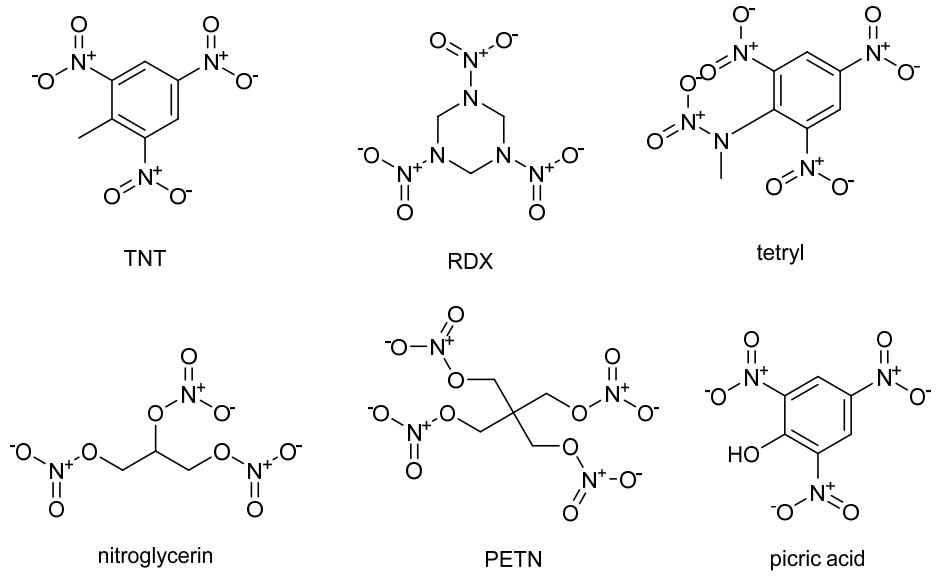


***Figure 3.1**. The chemical structure of some common high explosives.*

Whilst nitrated moieties are a common feature in high explosives, the breadth of materials that have the potential to be highly explosive are not limited to them. Many nitrated organic molecules are actually relatively stable under ambient conditions, and thus are difficult to initiate on their own. For example, TNT has a flash point of 163°C,[20] and thus is difficult to ignite and can even burn in a fire rather than explode. This relative stability makes TNT an excellent choice for bulk explosives since it is relatively safe to transport and handle. However, in order to initiate an explosive event, it must be partnered with a smaller amount of a more sensitive high explosive to instigate the decomposition.

The relative stability of some high explosives leads to a sub-categorisation between so-called primary and secondary high explosives. The nitrated examples detailed earlier, along with most of the structures in Figure 3.1 are secondary explosives. Although difficult to initiate, detonation velocities of secondary explosives are higher than those of primaries, in the region of 5500 – 9000 m/s. Primary explosives display extreme sensitivity to shock and heat, and are thus regularly found in blasting caps and detonators. Primary explosives transit rapidly from combustion to detonation and are

less likely to be nitrated organic molecules, but rather molecules that are under high structural strain. Because less gases are produced upon detonation, explosive velocities for primary explosives are lower, in the region of 3500 – 5500 m/s. Examples include lead azide and lead styphnate.[20]

Modern explosives tend to be a mixture of compounds rather than any one substance in isolation. Considerations such as starting material availability, skill of the handlers and intended purpose for any explosive device must be taken into account by anyone trying to detect them. The breadth of possibilities for explosives manufacturers means that explosives detection is a rapidly expanding field, fraught with complications to consider when fabricating an explosives sensor.

3.2 The gold standard: Animal olfaction

Currently, one of the most effective methods of detecting illicit materials in the field is to employ a hypersensitive mammalian olfactory system in the form of canines. Dogs are in many ways an ideal solution to detection of threat material because they are domesticated, have high odour sensitivity and can be trained to respond very obviously to external stimuli. The most recent estimates state that a canine has between 10^4 and 10^5 times more olfactory sensitivity than a human.[21] The reasons for this are varied, but primarily result from a dog having approximately forty times more chemoreceptors in their nasal cavity, and from fundamental differences in the way a canine olfactory system operates. For example, humans smell and breathe simultaneously. Dogs, on the other hand, have an organ in the nasal cavity which separates olfaction and respiration leading to a dedicated ‘chamber’ for olfactory processing (Figure 3.2).[19]

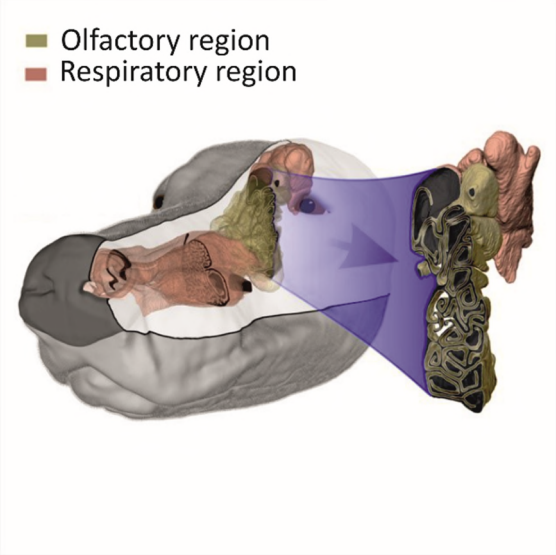


***Figure 3.2**. The separated chambers for olfaction (green) and respiration (pink) in a canine olfactory system. Adapted with permission from ref.[19]*

Whilst using sniffer dogs for the detection of threat materials is an effective and well-utilised technique, it is not without drawbacks. A sniffer dog always requires a handler, both of whom require a significant amount of training and care. Dogs cannot work around the clock and have a relatively short and finite working life. In addition, the training of a sniffer dog is based on response and reward, and dogs can quickly become stressed in inhospitable environments, bored or respond to inadvertent handler cues, which can result in identification of false positives.[22]

These issues have caused some to look to exploit other animals, both mammalian and other classes such as insects, for threat detection with some success.[23] Flying insects such as bees are particularly useful in the field-detection of explosives,[24] as they have no requirement to come into contact with the ground, and so have less chance of triggering a hidden device such as a land mine or improvised explosive device (IED). They have also been shown to have high levels of compound selectivity and sensitivity, the latter being reported as low as the ppt range. However, insects still require a degree of training and specialist handling. In addition, insects have an incredibly short life span in comparison to most mammals. It is clear then that much can be learned from animal

olfaction, but utilising it directly brings many challenges, which could be eliminated if the same level of selectivity and sensitivity could be achieved in a fabricated device.

The fundamental differences between the biological processes involved in olfaction and the physical processes required to illicit a response in a manufactured device derive from chemical interaction. Electrical signals in manufactured devices can be broken down to very good approximations using mathematical functions, whereas the chemical interactions responsible for senses such as taste and smell are both inexorably linked and result from spatial chemical stimuli which are much more difficult to derive mathematically.[25]

Chemical stimuli overall invoke responses which rely on vastly different biological detection systems, resulting in a somewhat less linear and intuitive process and thus much more complicated replication. Chemosensory systems still require a detector, signal recognition, transmission and response but the similarities between the mode of operation of chemical and physical systems end there. In most cases, biochemical sensory stimulation initially involves a stereochemical response, where biological receptors respond to a stimulus based on a ‘lock and key’ mechanism invoked by the precise size and shape of the molecule triggering a specific response in the host detector.[26]

Many biological sensory systems show preference for stereochemical interaction over chemical reaction because a spatially dependent process renders reactionless chemical interaction into a physiological response. In other words, compared to chemical reaction, spatial interaction requires less energy change, lacks potentially harmful by-products and is inherently simpler in terms of reversibility. Reversibility is particularly fundamental for chemosensors, since it is preferable to be able to quickly and efficiently turn over or ‘reset’ the detectors for reuse.

It is clear then, that biochemical receptors are highly developed through millions of years of evolution to detect and respond to chemical compounds. To all intents and purposes, it is a technological impossibility to make an electronic nose with the range and capability of a biologically evolved system. Fortunately, not all aspects of the olfactory system need to be replicated to create an efficient and functional sensor. In the simplest terms, mammalian olfaction relies on absorbance, receptor stimulation then pattern recognition in the brain. Mimicking this process via targeting specific analytes and combining analyte-specific sensors into an array simplifies the requirements of any manufactured device.

3.3 Challenges for explosives detection

In some instances, vapour sensing for the detection of clandestine material is possibly a simpler proposition when screening can take place in a controlled environment. Most airports are equipped with static portals that can carry out non-invasive checks on a high throughput of people relatively easily. Advances in the field of portal detection have led to numerous techniques including X-ray of belongings, vapour and particle detection.[27] Similarly, in some cases material samples or residue found in the field can be transported back to laboratory facilities for further analysis and identification via instruments that are generally large, immobile and operate under non-ambient conditions in terms of temperature and pressure. Another approach has been to swab or wipe potential samples to aid in the detection method.[19]

Whilst these options are valid in a controlled environment, it is not the case in the field. In field detection of explosives, it is safer to be able to detect the presence of a substance with minimum disturbance to the bulk material, and thus stand-off methods such as vapour detection are preferable.[28] Furthermore, any field based sensing device must be portable, easy to operate with minimal training and be relatively cheap to have any true value in real-world situations.

When attempting to design a stand-off detector, by design it is often the vapour given off by any substance that will trigger a response in the sensor. The relative chemical stability of many high explosives not only introduces complications for detonation, but also for detection. Chemical stability often results in very low vapour pressures, and that is certainly the case for many of the most common military-grade high explosives in use today. Other considerations when designing a sensor depend heavily on the type of explosives an operator may wish to target.

The compounds shown in Figure 3.1, particularly TNT, would almost certainly be present in military hardware such as landmines. However, terrorist organisations tend to manufacture less sophisticated devices from readily available materials. Re-purposed plastic explosives such as C-4 (RDX & plasticisers) and Semtex-H (RDX & PETN)[17] are commonly found in improvised explosive devices (IEDs). Homemade explosives (HMEs) are routinely manufactured from ammonium nitrate in the form of fertiliser, mixed with fuel oil (ANFO). More recently, largely due to restrictions on ANFO materials, terrorists have favoured manufacturing explosives based on peroxide derivatives such as triacetone triperoxide (TATP) and hexamethylene triperoxide diamine (HMTD) since these materials can be synthesised from easily obtainable household products.[29] The nature of the explosive plays a huge role in its vapour pressure and thus its ease of detection. *Table 3.1* details some of the explosives discussed here and their equilibrium vapour pressures at 298 K. In this table, and in all future quoted concentrations in this work, ppb units refer to parts per billion by volume (i.e. volume of vapour phase analyte per 10^9 volumes of carrier gas).

Explosive	Vapour Pressure (ppb)
TATP	63,100
Nitroglycerine	645
Ammonium Nitrate	14.7
TNT	9.15
Picric Acid	0.971
Tetryl	0.00741
RDX	0.00485

Table 3.1. *Equilibrium Explosives Vapour Pressures at 298 K.*[211]

As shown in Table 3.1, vapour pressures of many military-grade explosives are incredibly low, and any sensor operating within an electronic nose would ideally be able to identify the presence of more than one compound in the form of an array, and therefore must be capable of covering a wide range of concentration gradients. That said, typically materials used to construct HMEs tend to be less refined and have higher vapour pressures, so detecting some terrorist devices may be less challenging, dependent upon their construction. The issue of low vapour pressures is further compounded by concealment of target devices, where burying explosives or masking them in other ways further reduces the vapour pressures. Ideally, any sensing device should be able to either sample huge volumes, or more preferably from a practical point of view have incredibly low detection limits. Sensors operating in the ppb or ppt range must be achieved to realistically compete with canine capabilities.

Numerous approaches have been attempted to try to combat the issue of low vapour pressure in the detection of explosives in the field. One approach is to attempt to pre-concentrate the sample prior to exposure to the sensor. For instance, Najarro et al described a method of pre-concentration by heating a filter to increase concentration of

analyte in the vapour phase, as one such example.[30] However, any form of pre-concentration is inherently difficult and inevitably adds extra steps and thus complication to any potential device.

Another alternative may be to target taggants associated with the preparation of the explosives that may be more plentiful in terms of vapour than the explosive itself. For example, 2,4-dinitrotoluene (DNT, Figure 3.3) is always a contemporary in the presence of TNT,[31] and has a vapour pressure approximately twenty times higher than its tri-nitrated analogue. Similarly, it is a legal requirement for commercially produced plastic explosives, which do not contain nitroaromatics, to contain the volatile compound 3-dimethyl-2,3-dinitrobutane (DMNB, Figure 3.3).

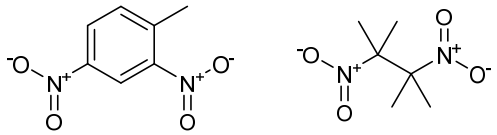


Figure 3.3*. The chemical structure of DNT and DMNB taggants.*

Targeting taggants is certainly a viable option, but can be complicated since explosives preparation may not always be consistent or law abiding. Furthermore, dependent upon the time since manufacture, taggants may change greatly in concentration between samples. However, a combinatory approach that could accurately target both taggants and explosives simultaneously would certainly be of commercial interest and value to the scientific community

3.4 Existing detection techniques

One of the primary issues facing the development of portable vapour sensors comes down to a choice between attempting to miniaturise and reduce the cost of technology that is already available in static devices, or finding new detection methods that satisfy the required criteria by design. Currently, the most sensitive and frequently used

methods for instrument led explosive detection utilise well established analytical techniques which focus on molecular separation[4]

In order to move away from these techniques in favour of investigating different methods to create a portable detector, there are many considerations that must be acknowledged. The size, weight and simplicity of the device are of paramount importance, as are the sensitivity and selectivity. Perhaps more important than any of these factors in the first instance however, is to ascertain the type of detection that is required. Bulk detection and trace detection are different propositions, and thus vastly different techniques can be utilised in each case.

3.4.1 Bulk detection

Bulk detection of explosives appears to be a simpler proposal than trace detection, since intuitively a larger mass of substance should give rise to larger signals. Whilst that is undoubtedly the case, bulk detectors tend to be large, static and complex in design. Most bulk detectors operate by utilising penetrative radiation, either in the form of imaging via X-rays, or via nuclear techniques such as neutron analysis and nuclear quadrupole resonance.[32] Benefits of bulk detection techniques include true stand-off detection capabilities and the ability to see 'through' some attempts at concealment. However, radiative signals follow an inverse square law, and as such suffer from rapidly depleting signal at any kind of distance. Furthermore, most bulk detection techniques rely on high energy ionising radiation that limits application to static, high throughput environments such as airports. These reasons, added to the inherent size of most bulk detectors, means that portable versions are scarce, and beyond the scope of this work.

3.4.2 Trace detection

Trace explosives detection is based upon the collection and analysis of microscopic explosive particulates or vapours left behind during handling and preparation, or emitted after the concealment of explosives. Inherently, it is a more amenable approach for the

field detection of explosives thanks to it being generally more flexible, with a wider variety of techniques and materials potentially capable of trace detection. What follows is a brief summary of some techniques, with particular focus on chemically derived sensors.

3.4.3 Molecular separation

There are three commonly encountered techniques for trace detection based on molecular separation in wide-scale use today. These are gas chromatography, mass spectrometry and ion mobility spectrometry, which can be used individually but tend to perform more efficiently when used in combination. Gas chromatography works by vaporising compounds without degradation and measuring retention times in a stationary phase column to identify them by separation via polar interaction. Detection times can range from minutes to seconds and detection limits have been recorded in the ppm and ppt range.[33] Mass spectrometry (MS) and ion mobility spectrometry (IMS) work slightly differently in that the molecules are fragmented and ionised prior to detection by either mass to charge ratio (MS) or mass, charge and ionic dimension (IMS) in an electric field.[4]

Of these three techniques, the most commonly encountered in detection devices available on the commercial market is IMS.[34] IMS was initially attractive owing to the fact that the ionization technique required for sample analysis could be carried out under atmospheric pressure. Decades of work have followed into fine-tuning the technique to allow potential scope for miniaturisation and simplification. However, progress has been hampered by vapour concentration dependence irregularities and by anomalous results in the presence of humidity. Some, if not all of these issues have been rectified in recent work for stationary detection systems, but incorporating all the necessary components into a hand-held, reliable device has still eluded researchers. Recent independent tests of two commercially sourced IMS-based devices carried out by Tomaszewski et al[35] revealed some reliability issues including repeated false positives in every series of

measurements. Furthermore, in both cases an uncertainty level approaching 15% was observed for the least volatile of the explosives tested (PETN).

Whilst all three of the aforementioned molecular separation techniques can display good sensitivity and/or selectivity, they all have drawbacks. In all cases, miniaturisation is difficult because of the different operations required for each process within the device (e.g. vaporisation, ionisation etc.), and some of the techniques (particularly MS) operate more efficiently under vacuum. IMS is the most commonly used of the techniques because it is possible to bypass some of these complications. However, it is also the technique with the biggest drawbacks in that it is difficult to quantify, meaning that it can efficiently indicate the presence of a species but not quantify the amount, and frequently suffers from masking from environmentally common species.[36] In all cases, these techniques require a minimum of four distinctly separate operations to function efficiently. This is difficult to achieve in a portable device. Furthermore, all three techniques are technologically advanced, and so are both expensive and require extensive training for any users to adequately interpret the data generated by the device.

3.4.4 Trace detection inspired by the natural world

As detailed in section 1, animals, and in particular dogs, are still considered the gold standard in terms of selectivity and sensitivity for trace explosives detection. In addition to dogs, other animals have been successfully employed in trace detection including 'hard-wired' bees[30] (Figure 3.4), moths[37] and rodents.[38] These latter zoological options have in fact started to replace dogs in some places due to simpler training requirements and fewer ethical considerations.[39]



***Figure 3.4**. Hard-wired bees in a sensor array. Reprinted with permission from ref.*[212]

There have also been attempts to exploit the botanical world for explosives trace detection. For example, Strano et al[40] successfully employed spinach plants to detect nitro-aromatics at stand-off distances of up to 0.8 m. However, the method used to create these plant sensors involved grafting carbon nanotubes onto a particular protein in the plant, which was a complex procedure. Furthermore, as with animals, plant-to-plant variation in response was high and the plants take a minimum of three weeks to grow.

Microbes have also been investigated in bio-derived sensors. *E-coli* in particular has displayed some success as a detector for TNT and DNT vapours via bioluminescence.[41] Whilst microbes can display excellent selectivity, unfortunately in most cases microbial sensors have failed to display the sensitivity required to compete with alternative options. That being said, Belkin et al[41] recently reported a method of genetic engineering which saw 3000-fold increase in luminescent intensity in response to DNT for *E-coli.* However, these results were only true in an aqueous solution in direct contact with the ground, and standoff results were less promising. Furthermore, genetic engineering is a complex process, and mass production and distribution of any devices containing potentially harmful bacteria obviously has ethical implications.

Incorporating living things into any detector inherently brings difficulties that could be avoided if the non-living, functional components of them could be reproduced or extracted then employed independently. Generally, the biological transducers that create the responses seen in the cases above are enzymes, and these proteins have been the source of much research in trace detection.[42] One of the major drawbacks of enzyme-based explosives sensors is that the most useful and frequently used enzymes, such as nitroreductase, only operate efficiently in solution.[43] This limits the utility of most enzyme-based systems for vapour trace detection techniques, since vapour detection is often slowed or inhibited completely in solution-based systems due to mass transport and diffusion complications between vapour and liquid phases. However, Schulte-Ladbeck et al were able to detect vapour phase TATP by passing a stream of gas through a solution containing peroxidase enzyme to limits as low as 8×10^{-7} M dm^{-3}.[44]

The difficulties inherent in utilising enzymes directly for vapour detection have led some to attempt to derive new methods based on the way that enzymes work. Enzymes are incredibly complex biological molecules, which are notoriously difficult to synthesise. Synthesising distinct, active component parts of enzymes is less challenging, and has thus received much attention. Attempts have been made to create sensors using aptamers, peptides and oligosaccharides, with varying degrees of success.[42] In fact, rational design and chemical synthesis of small molecules capable of targeting and responding to explosive vapours is perhaps the most promising area of vapour detection research.

3.4.5 Chemical sensors

Chemical sensors, in principle, offer perhaps the simplest and thus most attractive route to creating portable, lightweight and easy to operate explosive detectors. Theoretically, a carefully chosen chemical transducer should react or interact with a vapour analyte of

interest, resulting in an observable response, most commonly in the form of a colour or property change.

One of the most enduring and heavily researched types of chemical sensors make use of metal oxide semiconductors (MOS). MOS sensors are conductivity based, where an interaction with an analyte vapour results in a change in the conductivity of the sensing layer. One of the earliest MOS sensors was a ZnO device developed by Seiyama et al[45] in the early 1960s.

Since then, much work has been done in the field. Recent examples of modified ZnO sensors have shown strong results for vapour detection, recording single figure ppm limits for ammonia, NO_2 and acetone.[46] The concept has been expanded to incorporate a range of other metal oxides, expanding the analytical scope of these kinds of sensors. Recently, Horsfall et al[47] reported the successful use of WO_3 and CTO heterojunction type MOS sensors to successfully detect a range of explosive analytes, all at sub ppm levels. However, in all cases, MOS sensors only operate efficiently when the sensing layer is heated to temperatures in excess of 250 °C, and often as high as 500 °C. This is a difficult feat to achieve in a portable device, and inevitably adds complexity. Furthermore, many of the metal oxides used can be toxic and/or difficult to produce efficiently in large quantity. This has led researchers to look to the domains of analytical and synthetic chemistry for new, more amenable materials to utilise in gas sensing devices.

Explosives, by their very nature, often contain functional groups that cause an electron imbalance within the molecule. TNT, for example, contains strongly electron-withdrawing nitro-groups, which leave the central aromatic ring electron deficient. The molecule is therefore susceptible to the formation of charge-transfer complexes with electron-donating molecules. The formation of such complexes can result in strong colour changes in the presence of basic molecules, for instance.[48]

Whilst no common explosives display fluorescence under normal conditions, there are varieties of ways in which fluorescence can be induced. One way is to induce direct fluorescence using X-rays (XRF) or gamma rays (GRF).[49] In the case of XRF, the high-energy excitation results in the expulsion of an outer-shell electron from a nitrogen atom. The replacement of this electron by one of higher energy from an inner shell results in the emission of excess energy in the form of fluorescence, which can be measured spectroscopically. Blair et al[49] reported a success rate of 100 % utilising this method to detect landmines, and they also found success detecting a range of various nitrated explosives.

GRF utilises even higher energy excitation in the form of gamma rays, and as such results in nuclear resonance fluorescence.[50] In this case, the excitation wavelength results in the in-flight annihilation of fast positrons from ^{14}N. Nuclear fluorescence is observed in areas with above-normal levels of nitrogen concentration, such as near highly nitrated compounds. GRF is also a highly successful and accurate technique for nitrated explosives detection. However, the generation and containment of nuclear processes limits the miniaturisation of GRF instruments. XRF is not as limited by size, and hand-held XRF instruments are commercially available from well-known manufacturers including Bruker and Oxford Instruments, among others. Inevitably, widespread use of such devices is inhibited by the expense of such technology, and the inherent safety concerns when dealing with high-energy excitation sources.

The complications encountered when dealing with direct fluorescence have guided research towards lower energy excitation using either UV or visible light, known as indirect excitation. This is achieved via the employment of secondary chemiluminescent species.[51] The relative ease with which nitrated aromatic compounds form charge-transfer complexes has led many to design and synthesise increasingly sophisticated molecules for use in chemiluminescence based sensors.

In most cases when considering chemiluminescent vapour sensing, the response is a result of an energy exchange between a fluorophore and the non-luminescent explosive compound causing a change in the observed fluorescence. By far the most common and consequently most heavily researched of this type of energy exchange is a redox type reaction resulting in fluorescence quenching. In turn, the most common type of fluorescence quenching arises due to photon-induced electron transfer (PET), although other mechanisms result in the same outcome.[52]

Normally, the UV induced excited state of the fluorophore in isolation would radiatively decay back into the ground state, emitting a photon of visible light as it did so. In PET, the presence of an explosive molecule, particularly nitrated aromatics, leads to the formation of a charge transfer complex, resulting in preferential decay from the excited state into the ground state of the nitroaromatic, an ultimately non-radiative process. This mechanism is detailed in Figure 3.5.

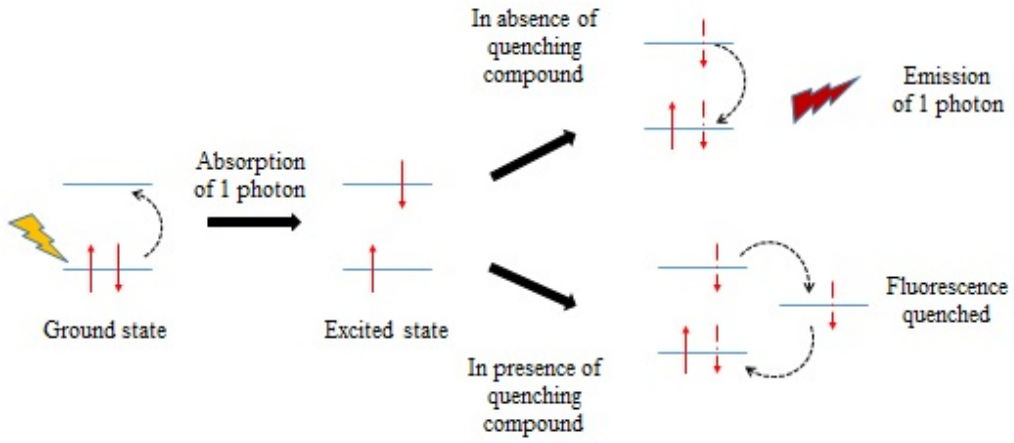


***Figure 3.5**. PET Fluorescence quenching in the presence of a charge transfer complex.*

Quenching with dye-based fluorophores has shown good results for explosives detection. For example, Goodpaster and Mcguffin[53] reported detection limits as low as 44 ng of nitrated explosive material using pyrene as the fluorophore. One major

drawback of this method is that the sensing layer is solution based, which can be problematic in portable devices. As a result, many have looked to create solid-state fluorophores capable of quenching, either via immobilising solution-based systems via incorporating them into stable membranes,[54] or by creating solid state fluorophores by design.[55]

Solid-state fluorophores tend to involve doping small organic molecules into a matrix to form stable, workable materials that can be deposited as thin films. This method has achieved sensing result as low as 1 ppb for nitrated explosives.[55] A major limitation of designing this type of detector is that they are nearly all limited to detection of only nitrated compounds. Furthermore, in many cases, the sensors are susceptible to degradation and sensitivity to environmental factors such as humidity, air and contamination. This has led some to concentrate on supramolecular structures, where the fluorophore is incorporated into a larger structure, adding geometrical order and stability.[56] For example, recent work by Prata et al[57] claimed detection limits in an organic macrocycle of 11.6 ppb for TNT, which is competitive compared to most other chemical sensors.

Incorporation of metals into supramolecular structures is ubiquitous across the field of supramolecular chemistry, and this is certainly the case for vapour detection. The varied oxidation states available to transition metals allows them to form unique binding geometries with organic ligands, and these binding geometries in turn allow access to architectures not possible in organic structures alone. Complex architecture allows for new routes for analyte interaction. These so-called host-guest interactions have seen metallocages[58] and dendrimers[59] successfully utilised for sensing applications. Extending the architectural footprint of chemical sensing materials further allows access to large, connected and conjugated networks, most commonly in the form of polymers and MOFs.

Now, instead of being limited to the formation of charge transfer complexes, stereochemical spatial interaction, electrical behaviour and porosity of sensing layers can expand the scope of potential sensing materials. There are numerous potential benefits to utilising these structures. One is increased opportunity to functionalise the component parts, enabling expanded scope in terms of selectivity when targeting a variety of analytes, potentially within the same macrostructure. Another is that large connected structures give rise to long-range communication mechanisms. This expands the potential scope of these molecules beyond fluorescence, allowing electrical changes to be monitored. Polymers[60] and MOFs[31] have both been successfully investigated for fluorescence-based sensors. However, whilst environmental contaminants and false positives are hurdles that must be overcome for any chemical sensor, perhaps the biggest drawback of any fluorescence-based sensor is that the data output must be analysed spectroscopically. This will always add complexity, component parts and expense to any portable device.

Spectroscopic analysis can be eradicated if the interaction and subsequent output is electrical. Electrochemical sensing materials and the electrical behaviour of these conjugated structures forms the basis of the experimental work in this thesis. The electrical behaviour and sensing capabilities of conducting MOFs and polymers will be detailed further in chapter 4.

3.5 Summary

Accurate and portable detectors capable of mimicking some aspects of mammalian olfactory systems are of great importance, with real value in civilian, humanitarian and military applications. This is particularly true for the detection of explosive materials, since any of these groups can be severely impacted by the effect of concealed explosives. Detection of clandestine material is often particularly challenging, because by design the handler will go to great lengths to make detection as difficult as possible.

There are a large number of explosive materials that are used both in war and by non-military aggressors wishing to cause harm, and some are relatively easy to produce from simple household chemicals. Their properties, and especially in this work their vapour pressure, can vary depending on their chemical make-up and how they were manufactured. Consequently, any detection system will ideally have high levels of selectivity and sensitivity, either for the explosive itself or for taggants and by-products associated with them.

Many techniques currently exist for this purpose, although in all cases there are inhibitory factors that detract from their absolute utility. Bulk detection is often highly accurate and sensitive, but requires a controlled environment and large, static instrumentation. Trace detection is perhaps a more valuable approach in field-based detectors, and currently the sniffer dog is still the gold standard by which any other method must be judged. Moving away from deployment of live animals, enzymes, molecular separation, fluorescence and nanomaterials have all been investigated with varying levels of success.

Chemical sensors are particularly attractive for trace detection, since they meet many of the requirements of a small, cheap and portable device. The trade-off for those properties has historically been a comparative lack of selectivity and sensitivity when compared to other methods. However, recent advances are beginning to address this. Methods of operation in chemical sensors can generally be broken down into two categories. The first is detection based on fluorescence or chemiluminescence in response to the presence of an analyte of interest. Polymers and macrocyclic compounds have been used successfully in this way. The second mode of operation involves long-range communication across a network in the form of conductivity. Whilst the requirement to have connectivity adds a certain level of complication to device production, it also means that new materials can be used that increase ways in which analytes can interact with the sensing layer, ultimately improving selectivity. Conductive

materials allow for the production of chemiresistive sensors whose resistance is altered in the presence of target analytes. Broadly, there are three main classes of conductive materials that have the potential to be used in this way; CPs, MOFs and MOS.

MOS materials have received a great deal of attention for use in threat detection, both academically and commercially. Of these three groups of conductive materials, only MOS sensors are currently deemed to be sensitive, reliable and selective enough to be commercially available. However, in nearly all cases, they operate at elevated temperature which increases device complexity, and have often struggled to display selectivity for analytes of similar size. Advances in the fields of both CPs and conductive MOFs mean that it is only a matter of time before they become competitive in the commercial market. Advantages of them include relatively low power consumption, room temperature operation, relatively simple synthesis and ease of processing. These materials are discussed in more detail in the next chapter.

Chapter 4

Background (II): Electrochemical vapour detection and percolation

This chapter will describe the use of conductive materials for electrochemical vapour sensing, and how percolation theory can be applied in this context to enhance sensing behaviour.

Electrochemical vapour detection offers many attractive benefits in comparison to other vapour detection methods. Sensors produced by electrochemical means can be highly sensitive and relatively easily functionalised to display excellent selectivity.[61] They are cheap, easy to produce and designed so that miniaturisation is inherently simple. In fact, in most cases the production method is flexible enough that it can be easily scaled up or down, in terms of both sensor size and volume of sensors produced. This simplicity extends to their analytical utility, where electrochemical sensors do not necessarily require peripheral equipment such as carrier gas, pre-concentration or spectroscopic instruments often encountered in other methods.[62] Furthermore, response times are generally excellent and, owing to the weak interaction between analyte and sensing layer, reversibility is generally achievable with minimal effort.

Percolation was first described and derived mathematically in the mid-twentieth century[63], and refers to a random process of flow through a medium, driven by the properties of the medium itself and independent of the properties of the fluid. Percolation theory and application will be described thoroughly in section 4.5.

4.1 Electrochemical transduction

One of the main modes of operation for electrochemical sensors is via interaction with a redox-capable analyte species. Generally, observed electrical changes result from an interaction in the flow of electrons or ions at the surface of the sensing layer, which is in turn connected to an electrode. This makes them well suited to detecting electron deficient nitro-aromatic compounds (NACs) found in many explosives, but also extends their capabilities to enable the detection of other types of explosives including those based on peroxides. The type of transduction can vary, but is generally classified into one of three categories; amperometric, potentiometric and conductometric sensors.

Of the three main classes, potentiometric devices have probably been the most commonly used for species-specific detection. They operate by measuring the potential difference between electrodes when no current is flowing, and there are three widespread types of potentiometric sensor; ion-selective electrodes (ISE), coated-wire electrodes (CWE) and ion-selective field effect transistors (ISFETS).[64] ISEs are ubiquitous across the sciences, a form of which is familiar to most as a pH electrode. However, almost all ISEs are solution based and thus of limited utility for portable vapour sensors. CWE's are fabricated by coating an electroactive sensing species onto a conductive wire. In original incarnations, the wires to be coated were metallic in nature,[65] but more recently nanomaterials including carbon nanotubes (CNTs) have been utilised to good effect. ISFETs can be considered as a combination of the other two techniques, and are mostly utilised in solution-based media. Interestingly, some of the best vapour sensing results to date for CWEs have been obtained using a CP sensing layer, with Myung et al reporting NH_3 detection limits as low as 50 ppb when using polyaniline (PANI) as a sensing layer on CNTs.[66] CPs are covered in more detail in section 4.2.

Amperometric sensors measure differences in current flow in an electrochemical cell at a fixed applied potential, and often incorporate voltammetric measurements where

applied potential is scanned across a range and the cell current is recorded as a function of applied potential. Sensors tend to operate by employing a sensing layer as the working electrode in an two-electrode electrochemical cell, immersed in an electrolytic solution.[67] Whilst it is possible to detect gases using an amperometric sensor, this is normally achieved by utilising a gas-selective membrane to introduce the species to the electrolytic solution in which the working electrode is operating. In essence, this means that an amperometric gas sensor must have two components capable of selectively identifying a target analyte. The technique is highly suited to some static applications owing to its low cost and relatively low power consumption, particularly in the biomedical field where in-vivo measurements suit a solution-based device.[67] However, constructing an electrolytic device with two selective components for some of the more exotic explosives vapours is impractical, limiting the utility of this type of device in portable explosives detectors.

Conductometric sensors operate by monitoring the change in conductivity, or inversely resistance. Intrinsically conductivity measurements are non-selective, because the sensors in this instance are passive rather than active like those in the aforementioned techniques. However, the development of modified conductive materials capable of selectivity has seen an explosion in interest in the field of conductometric sensors.[68] The attraction of conductometric devices lies in the fact that they can operate with absolute simplicity, requiring no complimentary components such as reference electrodes or electrolytic solutions. Commercially, this renders them cheaper, simpler to construct and gives more flexibility in terms of scalability than most competitive strategies. From a research perspective, perhaps the most significant advantage is that it allows access to truly solid-state sensors capable of operating under ambient conditions, which vastly improves the pool of potential materials available to use as sensing layers. Finding appropriate materials capable of fulfilling the requirements of a selective and sensitive conductometric device has huge potential. MOS layers have been successfully utilised

in conductometric devices,[69] although most are constrained by the fact that they only become conductive at high temperature. Perhaps the most attractive classes of materials then, are those that are functionalisable and conductive at room temperature. Currently, the two most promising candidates that meet this remit are CPs and conductive MOFs.

4.2 Chemiresistive materials

For any chemiresistive material to have value in a conductometric device, it must have a conductivity above that of an insulator. Electrical conductivity (σ), generally measured in S cm^{-1} is a function of density (n), mobility (μ) of electrons (e) and mobility of holes (h). High conductivity is achieved in the event of high charge density and high charge mobility, and can be expressed as such:

$$\sigma = e(\mu_e n_e + \mu_h n_h)$$

Metals contain a high density of free, loosely bound charge carriers, whereas the charge carriers in semi-conductors tend to be thermally activated.

Band theory can also play a major role in selecting an appropriate material for use in chemiresistive devices. Band theory dictates that materials contain continuous energy levels, known as bands. The Fermi level (E_F) can be defined as the energy level which has a 50% probability of occupation by an electron at any temperature. The valence and conductance bands are the bands closest to E_F. In conductors, the valence and conduction bands overlap, meaning E_F lies within the conduction band, giving rise to a high density of free electron charge carriers and thus high conductivity, in excess of 100 S cm^{-1}.[70] For semiconductors and insulators, the valence band is the highest range of energies in which electrons are normally present at 0 K, whilst the conduction band is the lowest range of vacant energy states at 0 K.

For semiconductors, there exists an activation energy (E_a) above which electrons have sufficient energy to be promoted from the valence band to the conduction band, thus giving rise to conductive behaviour. For intrinsic (undoped) semiconductors, the number of electrons in the conduction band and holes in the valence band are equal, so E_F lies in the middle of the band gap, and thus a smaller band gap is preferable so that thermal activation can occur at ambient temperatures. Extrinsic (doped) semiconductors differ in that the dopant shifts E_F by creating an imbalance of charge carriers, either additional holes in the valence band (p-type) or additional electrons in the conduction band (n-type).[70] For the p-type semiconductors in this work, the charge-carriers are predominantly holes, and dopant-led bipolaron formation (See section 4.3) leads to the creation of new energy states within the band gap. This shifts E_f closer to the valence band, between the new energy state and the valence band, thus reducing E_a. MOFs tend to be intrinsic since doping is rarely required, whereas polymers are generally doped to improve performance and thus become extrinsic semiconductors. In either case, the appeal of both lies in the fact that it is possible to carefully control the constituents that form the macrostructures of both types of material, and thus band gaps and ultimately conductivity can be manipulated.

Polymers and MOFs are highly versatile materials that have each found a plethora of uses in commercial applications. Both are macromolecular structures created by combining smaller component molecules, either chemically or electrochemically, into extended connective networks of identical repeat sub-units. Figure 4.1 shows a simplified schematic for both processes.

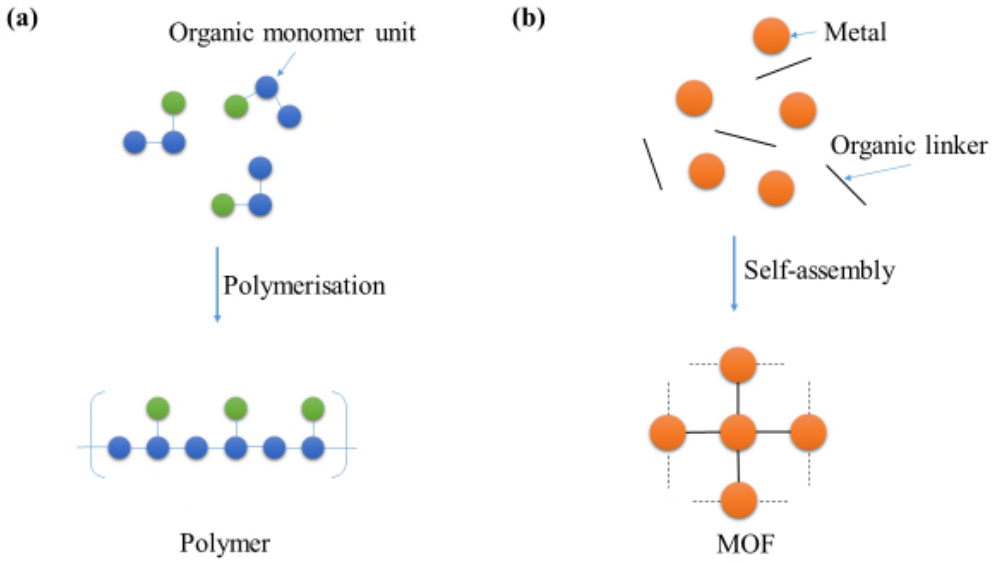


***Figure 4.1**.A Simplified schematic representation of (a) polymerisation and (b) MOF formation.*

Polymers tend to be strictly organic in nature, whereas MOFs, as the name implies, combine metal centres and organic ligands to achieve their structure. In both cases, the vast majority of examples discovered to date are insulating in nature, and thus of little interest as chemiresistive materials. However, in the case of polymers, low resistivities for some examples were noted as early as the 1950's culminating in a Nobel prize in 2000 for Heeger, MacDiarmid and Shirakawa for advancements in the field of conducting polymers (CPs).[71] Conducting MOFs are a more recent discovery, where examples have only become known within the last decade.[72]

4.3 Conductive polymers

The inherent conductivity in CPs occurs due to extended conjugation along the backbone of the polymer chain, where the carbons in the chain are sp^2 hybridised, allowing overlap of p_z orbitals and thus charge mobility through vacant π*-bands. Whilst the number of readily available conducting polymers, especially those which have shown promise in sensors, is finite (Figure 4.2), perhaps the most appealing property for their utilisation lies in the fact that many monomers can be functionalised in an attempt to target specific analytes.[61] Furthermore, most monomers are soluble in a range of solvents, and become insoluble upon polymerisation, which aids in deposition under ambient conditions.

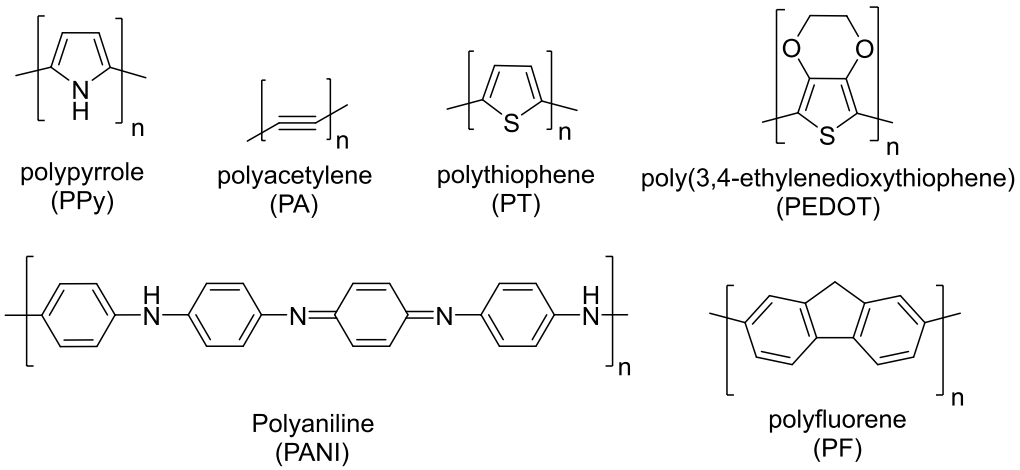


***Figure 4.2**. Common conducting polymers for sensor applications.*

Whilst some CPs can be considered intrinsic semi-conductors, they are more generally classified as extrinsic because in almost all cases doping improves their performance.[73] For example, polyaniline (PANI) and polypyrrole (PPy) are p-type semiconductors, generally lacking stability in their undoped state. Polythiophene (PT) is more stable undoped, but still undergoes enhanced conductive performance when lightly doped.

Dopants tend to be anions, introduced during chemical or electrochemical deposition. The conjugation, and consequent resonance stabilised electron delocalisation in CP structures often leads to a large band gap, and the dopant functions to reduce this band

gap and thus improve conductivity. By removing an electron via the dopant, a localised charge is formed which results in a lattice distortion, ultimately lowering the ionisation energy leading to the polymer being more prone to oxidation. The net result is polaron formation, and increased concentration of dopant results in the loss of another electron, and thus bipolaron formation.[74] Polarons and bipolarons increase the number of available electrical states within the band gap. This process is illustrated in Figure 4.3.

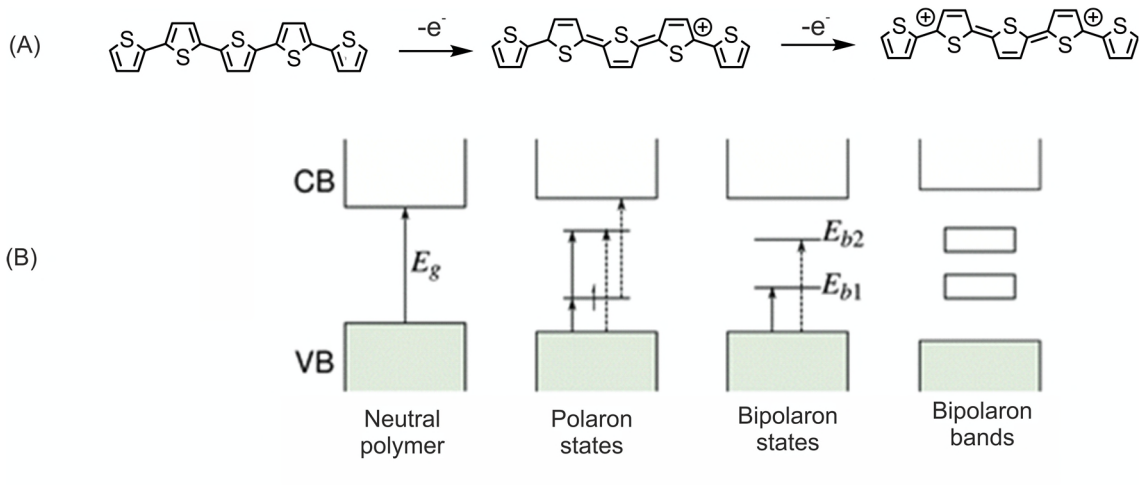


***Figure 4.3**. Removing electrons from the polymer backbone via a dopant (A) results in polaron/bipolaron formation (B), increasing electrical state density and thus CP conductivity. Adapted with permission from ref.*[74]

In gas sensing terms, introducing a gas or vapour to a doped polymer induces 'secondary' doping behaviour, where the electronic behaviour of the doped system is altered further. These changes tend to arise from a gas interacting electronically with a redox active site in the polymer backbone that forms part of the conductive pathway of the polymer,[75] although other types of interaction can and do occur.

4.3.1 Analyte interaction with conductive polymers

As described above, the dopant and doping concentration can play a major role in how analytes interact and are detected. Detailing all possible dopants is beyond the scope of this thesis. However, in nearly all cases, and certainly for p-type polymers, the response depends upon a redox type reaction at the surface of the polymer, where the analyte

gas either acts as a secondary dopant or a de-dopant depending on its electronic nature. Electron acceptors, for example NO_2, remove electrons from the aromatic ring of the CP chain leaving free charge carriers in the form of holes, and thus conductivity increases. The opposite is true for electron donating gases including ammonia. A surplus of electrons in the CP backbone results in fewer holes, and thus a sharp decrease in conductivity.[76] Table 4.1 details the electron abundance in some common explosives and taggants, and thus their expected behaviour upon interaction with frequently utilised p-type CP's:

Compound name		Chemical nature	Expected behaviour
TNT	DMNB	Electron deficient	Conductivity increase
Picric acid	RDX		
Toluene	Benzene	Electron rich	Conductivity decrease
ammonia	Phenol		

Table 4.1 *The electron abundance in some common explosives & taggants, and the expected influence on p-type CPs.*

In some cases, the target analyte may be inert and thus not able to participate in these redox reactions. Whilst this could be expected to have a large impact on the performance of any sensing layer, it has been found that conducting polymers are capable of weak interactions, including charge transfer or hydrogen bonding, that also affect the conductivity of the polymer, further expanding their scope for a variety of target molecules. For example, Dixit et al[77] found that polyaniline showed a resistance decrease in the presence of carbon monoxide, an electronically stable gas, by a partial charge transfer mechanism based on differences in electronegativity between the CP and target gas. There is no reason to doubt that a similar mechanism would not occur

between CPs and explosive analytes that may be inert but will almost certainly have different electronegativity to that found in the polymer. The postulated mechanism is detailed in Figure 4.4.

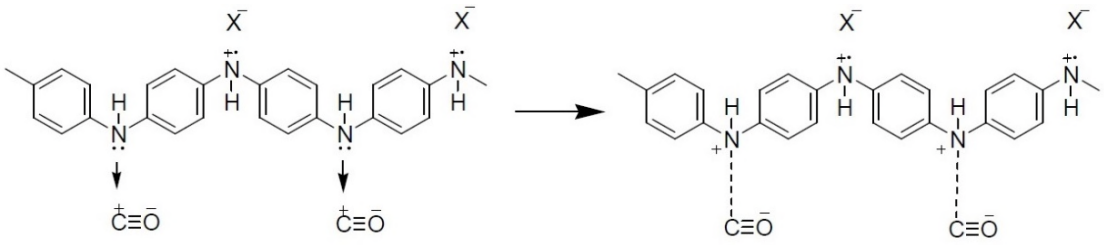


***Figure 4.4**. The charge transfer mechanism between polyaniline and carbon monoxide gas.*[77]

The variety of potential mechanisms available to CPs to detect analytes of interest makes them ideal candidates for use in vapour detectors. Crucially, all the mechanisms detailed above occur at ambient temperature. Furthermore, it is possible to deposit multiple polymers on electrodes within the same device, allowing access to the potential of targeting more than one analyte, or having a 'finger-print' type response for a single analyte based on observed changes for different polymers at the same time. In order to achieve these types of devices, a suitable deposition method must be found that can be used to deposit polymers rapidly and efficiently.

4.3.2 Polymer deposition and electrochemistry

Polymer formation and deposition can be realised in many ways. Arguably, the simplest techniques involve chemically forming the polymer before dip-coating, spin-coating or drop-casting the pre-formed polymer onto a substrate. A well-known derivative of dip coating is the Langmuir-Blodgett (LB) technique, which can be used for both insulating and conductive polymers to achieve thin films. These methods have all been attempted to create vapour sensors.[78,79] The aim of all these techniques is to create a thin film, usually on an insulating substrate, that joins two metallic electrodes. Any analyte

interaction with the sensing layer will then disrupt the behaviour of the system locally. Figure 4.5 details a schematic of such a system.

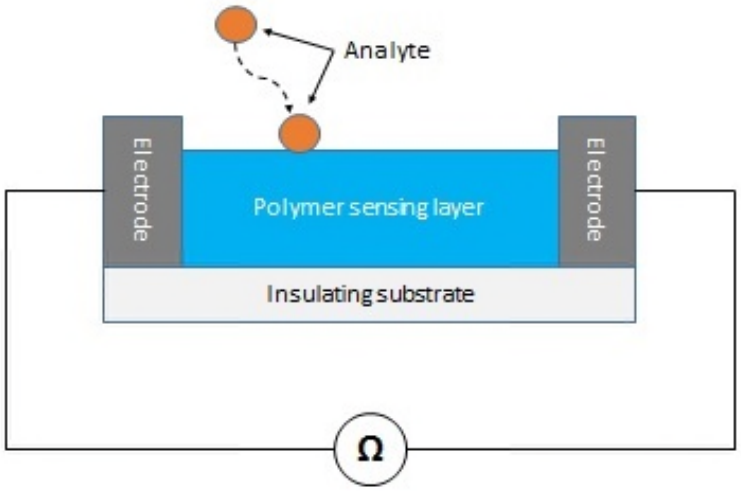


***Figure 4.5**. Schematic representation of a thin-film chemiresistor.*

One major issue with techniques that utilise chemically pre-formed polymer is that the deposition methods generally lack elegance and control. This manifests itself in waste and additional steps but also inhibits depositing polymer with any real long-range structure. Should one require a specific architecture to achieve, for example, a percolation network (see chapter 4.5), then these techniques are of limited use. The technique that allows access to much higher levels of depositional control is dynamic electrochemical deposition. Electrochemical deposition by definition promotes long range structure, since nucleation has to occur at the electrodes where the potential is applied, and any further polymer formation can only occur as long as a conductive pathway is maintained. This reduces contact resistance to negligible levels, which can be a major issue for other deposition types, particularly involving particulate sensing layers.

Dynamic electrochemistry is defined as an electron transfer process accompanied by a change in current flow and hence changes in concentration of an analyte species within the electrolytic solution of an electrochemical cell, containing a minimum of two, but

normally three electrodes. The reference electrode exists to measure any applied potential against, and the counter electrode undergoes an equal and opposite redox reaction to that occurring at the electrode of most interest, the working electrode (WE).[80]

Electrochemical deposition is an amenable approach since it allows accurate regulation of the amount of polymer deposited. Two main dynamic electrochemistry techniques exist; CV and CA. CV is the measurement of current flow as the potential is swept between an upper and lower limit (Figure 4.6(a)). Each sweep, from zero to the maximum, down to the minimum then back to zero again, is known as a scan. At some point towards the upper limit of the scan range, the oxidation potential of the monomer is reached,[81] where a radical reaction occurs and polymer is formed and deposited on the WE. Deposition in CV is limited to whole numbers of scans.

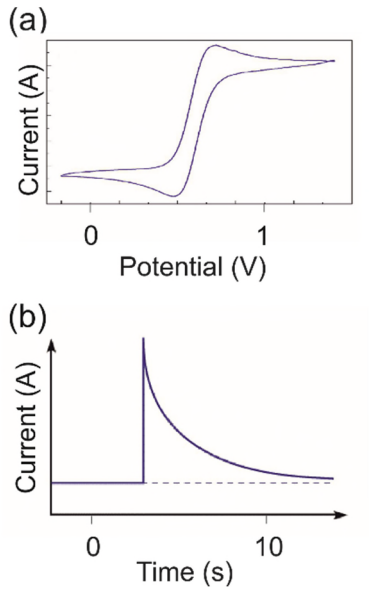


***Figure 4.6**. Typical voltammograms obtained from (a) Cyclic Voltammetry and (b) Chronoamperometry.*

CA differs in that the potential applied is held at a predetermined monomer-specific polymerisation potential, and polymer is deposited for a defined amount of time (Figure 4.6(b)). Of these two deposition methods, it is likely that CA-deposition is preferential for network formation, since deposition is not limited to whole numbers of scans, but

controlled by a highly malleable time parameter. Solvents and salts can impact exactly where the polymerisation potential lies, but because such a large volume of work has been carried out on many of the most commonly used CPs, the range over which the polymerisation potential will occur is often well known. Table 4.2 details a variety of conducting polymers taken from the literature, and the polymerisation potential used for each.

Monomer conc.	Electrolyte solution	Substrate	Potentiostatic Electropolymerisation potential (V)	Ref.
Aniline				
(0.1 M)	H_2SO_4 (0.5 M aq.)	Stainless steel (SS)	0.8 – 1.1	82
(0.05 M)	H_2SO_4 (1 M aq.)	SS	0.75	83
(0.1 – 0.3 M)	HCl (1.5 M aq.)	ITO	0.8 – 1.1	84
(0.12 M)	Oxalic acid (0.5 M aq.)	Al2024 T6 Alloy	1.7 – 1.9	85
EDOT				
(0.01M)	H_2SO_4 (0.1 M aq.)	SS	0.8 – 1.2	86
(0.01M)	H_2SO_4 (0.1 M aq.)	Toray carbon paper foil	0.9	87
(0.02 – 0.2 M)	ACN / TBAP (0.1 M)	Pt disc	1.25 – 1.4	88
(0.01M)	$LiClO_4$ (0.1 M aq.)	Pt disc	0.8 – 1.5	89
Pyrrole				
(0.1 – 0.5 M)	NapTS (0.1 M aq.)	ITO glass	0.8	90
(0.05 M)	KNO3 (0.1 M aq.)	SS	0.9	91
(0.5 M)	$NaNO_3$ (0.01 – 1 M)	Al	0.7 – 1.15	92
(0.5 M)	Sodium tartrate (0.2 M)	Cu/brass	0.8	93
Thiophene				
(0.3 M)	Boron trifluoride diethly etherate	SS	1.3	94
(0.6 mM)	ACN / $TBAPF_6$ (0.1 M)	FTO glass	1.9	95
(0.02 M)	CAN/ $(CH_3)_4NBF_4$ (0.02 M)	FTO glass	3.0	96
(0.02 M)	Boron trifluoride diethly etherate	ITO/Au	1.3	97

Table 4.2. *The salt solution, substrate and electropolymerisation potential of a range of commonly used CPs*

The ability to control both the type of polymers used, and the method with which they are deposited, allows huge scope in terms of potentially sensitive and selective sensing devices. In most cases, and certainly in this work, doping is carried out after polymer deposition and so can still be utilised for both CV and CA. However, functionalisation of monomers often affects the utility of the polymers, both in terms of deposition parameters and sensing capability. Often, adding certain moieties renders the polymer too soluble, or reduces the oxidation potential of the polymer to a point where it is lower than the polymerisation potential of its monomeric parent.[98] In this situation, electrodeposition destroys the polymer as fast as it can be deposited. Whilst polymers undoubtedly show great promise, it would be useful to have an arsenal of materials with differing capabilities to draw upon in order to achieve a flexible and useful device.

4.4 Conductive metal organic frameworks

The attraction of using MOFs for sensing applications lies in the fact that their unique structural arrangement gives rise to an inherent porosity for analyte adsorption. In addition, the metallic component allows further analyte interaction and weak bonding which may not be accessible in a purely organic sensing layer. In theory at least, these factors can all be easily manipulated to allow for targeting specific analytes. Changing the metal and ligands allows relatively simple manipulation of pore size and, owing to the way in which MOFs self-assemble, is not particularly synthetically challenging.

However, since the field of conductive MOFs is in its relative infancy, there are currently surprisingly few real examples of such materials to consider. In fact, for 3D MOFs there does not yet exist an example with a conductivity high enough to rival competitive strategies for chemiresistive sensing. One of the main complications in creation of such 3D materials is that, in most cases, long-range communication is difficult to maintain ‘through-bond’. Competitive ‘through-space’ type conductivity via non-covalent interactions such as π-π stacking tend to dominate in self-assembled structures, and

inevitably through-space interactions are inherently more difficult to control in 3D space. However, progress is being made in the field. Dinca et al communicated the highest conductivity achieved to date, (10^{-4} S cm^{-1}) in an intrinsic 3D MOF in 2012, with a follow up paper showing improvements in 2015.[99,100] The conductivity was tuned by changing the metal centre, where a larger ionic radius allowed for more overlap of p_z orbitals in sulphur atoms of the organic ligand chains, thus increasing conductivity (Figure 4.7).

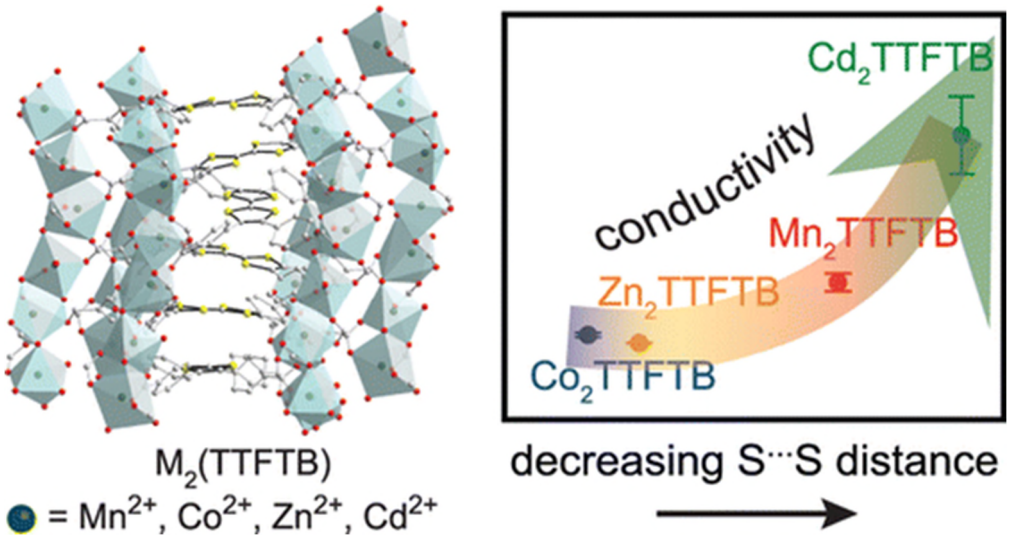


***Figure 4.7**. Work by Dinca et al showing the fine-tuning of MOF conductivity by altering the metal centre. Reprinted with permission from ref.*[100]

Whilst 3D MOFs are not yet advanced enough for applications in sensing devices, this is not the case for 2D MOFs. 2D MOFs appear to be an ideal combination of the porosity and flexibility inherent in their 3D counterparts, but in materials where the 'through-bond' type conductivity associated with CPs dominates. Whilst these materials are quite recently discovered and thus limited in number, there are a few examples that have displayed excellent conductivity and have been utilised in vapour sensing devices.

All materials in this class to date are formed from either benzene- (BHT) or triphenylene (TP) ligands with *ortho*-substituted O, S or N donor atoms. These donors are perfectly positioned to form square-planar binding geometries with suitable late-transition metals, resulting in an extended 2D planar network, [101,102] as detailed in Figure 4.8.

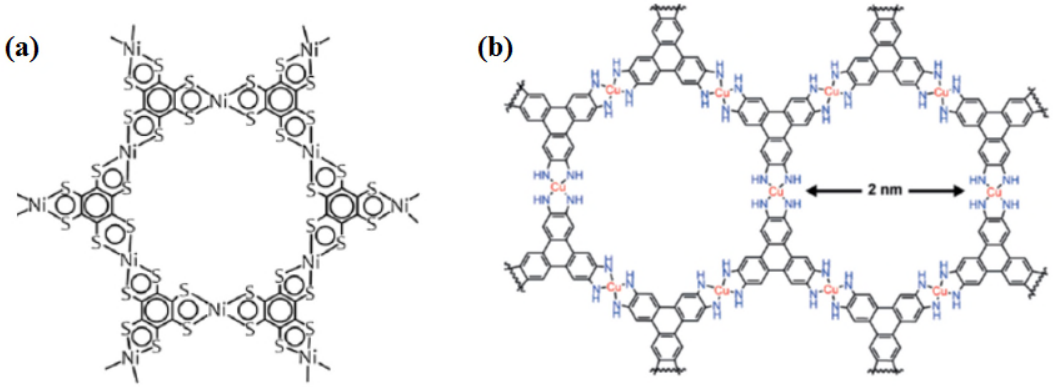


***Figure 4.8**. 2D Macrostructure of (a) BHT[101] and (b) HITP[102] based conductive MOFs. Reprinted with permission from refs.*[101 & 102]

In terms of conductivity, the highest examples have been observed in BHT materials. In 2015, Huang et al[103] reported a $Cu_3(BHT)_2$ MOF with an unsurpassed conductivity of 1580 S cm^{-1} in pellet form. There is no record in the literature to date of BHT MOFs being utilised for sensing applications, although, given their conductivity, it is surely only a matter of time before they are employed as such.

TP-based sensing layers generally have lower conductivities than their BHT counterparts. For example, $Ni_3(HITP)_2$ was observed to have conductivity in the region of 2 S cm^{-1} in pellet form, and 40 S cm^{-1} for thin films, while the copper analogue was slightly lower at 0.2 S cm^{-1} in pellet form.[104] These lower conductivities are not inhibitive in relation to using these materials in sensing devices, and are in fact analogous with many of the CPs detailed in earlier sections. In fact, TP derived layers have been utilised in sensing devices. In 2015, Campbell et al[102] demonstrated that $Cu_3(HITP)_2$ was capable of sensing ammonia at sub-ppm levels in chemiresistive devices. This group

subsequently tested their $Cu_3(HITP)_2$ sensor in conjunction with an Ni analogue against a range of other volatile organic compounds, and found success down to 200 ppm in nearly all cases.[105]

Whilst these levels of sensitivity are respectable, perhaps the most significant advantage of these MOFs over competitive strategies is that their sensing capabilities are almost completely unaffected by atmospheric conditions. Crucially, the devices appear to be able to operate under high levels of humidity, which has a major negative impact on many alternative materials. For instance, the $Cu_3(HITP)_2/NH_3$ detection detailed by Campbell et al[102] maintained performance in air with a relative humidity level of 60 %. This renders these devices extremely attractive for 'in the field' portable sensors, and the sensitivity and selectivity has scope to be improved by optimising deposition and functionalisation in the future.

4.4.1 MOF Deposition

A limited amount of work has been done to date on investigating the effects of MOF deposition methods on sensing performance.[106] The majority of the examples detailed above were formed into thin films using rudimentary techniques including spin casting and drop coating. As already established for CPs, these methods lack the elegance required to form specific architectures, including percolation networks, which may prove to enhance sensory performance.

Electrochemical techniques have been used to deposit MOFs[107], although it is far more complicated proposition for MOFs than CPs. Generally, MOFs require cathodic deposition and pH plays a huge role in the success of the films obtained. Furthermore, owing to the cathodic potentials used and varying pH of the electrolytic solution, some counterions including Cl^- and ClO_4^- have been shown to inhibit MOF growth.[108] It is yet to be seen how electrochemistry can be fully utilised in the deposition of conducting MOFs.

Other methods, which may allow strict control over the layers being deposited, are Langmuir-Blodgett and Langmuir-Schaeffer techniques. These methods involve suspending a monolayer of the desired material on a liquid surface, then immersing the substrate into the liquid to a controlled depth. The monolayer is then adsorbed onto the substrate with each immersion step.[109] Figure 4.9 shows a schematic of both processes. As with electrodeposition, it is too soon to say how effective the Langmuir techniques may be for conducting MOF deposition.

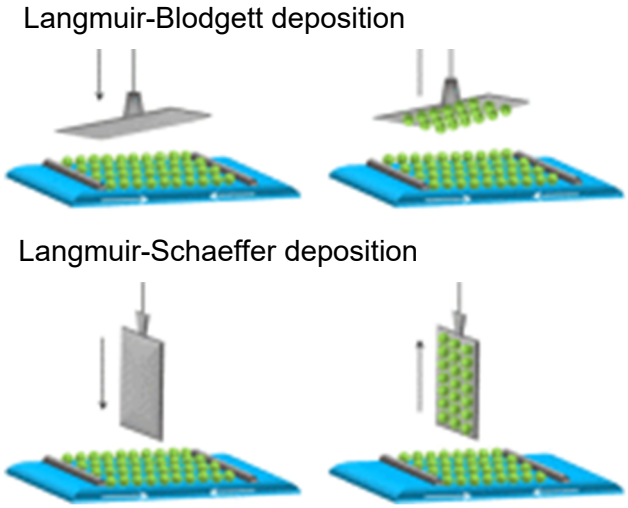


***Figure 4.9**. A schematic of Langmuir-Blodgett and Langmuir-Schaeffer techniques. Taken with permission from ref.*[109]

Inkjet printing is another potential method for MOF deposition, and is appealing because of all the methods discussed, it is perhaps the most adaptable. If a MOF can be dispersed in an 'ink' solution, the potential uses increase substantially. In theory it can be printed onto almost any substrate, particularly flexible ones including plastic, paper and textiles, and over almost any area limited only by the capabilities of the printer. For example, Leonis et al[110] successfully inkjet printed a range of photoluminescent lanthanide-organic frameworks onto transparent, flexible PET substrates for applications in anti-counterfeiting.

MOFs have also been inkjet-printed for gas sensing applications. Zhuang et al[111] deposited patterned layers of $Cu_3(btc)_2$, commonly known as HKUST-1, from a solvent mixture of DMSO (precursor), ethanol and ethylene glycol. These layers then underwent a colour change in response to exposure to different analyte gases, able to distinguish between ammonia, HCl and H_2S vapour.

One common theme consistent across the majority of inkjet-printed MOFs in the literature is the nature of their response. Both photoluminescence and colour change require no long range communication across the printed network. For conductive MOFs however, long range communication is essential, which is probably the reason why examples of inkjet-printed conductive MOFs have, until this work, proven elusive.

Most inks that are designed to be run through a print head will require some form of filtration so that particulates in the suspension do not clog up the system. Typically, this filtration removes any particles greater than 50 μm in diameter. For MOFs in suspension, this is problematic because by decreasing particle size and thus increasing number of particles required to cover an area, it reduces stable intra-particle conductivity and increases the negative impact of inter-particle resistance between MOF particles, especially if they are deposited between two relatively distant electrodes on an insulating substrate. This problem is exacerbated in many commercial-grade inkjet printers, because they work on the basis that printed ink should be clearly legible, and thus tend to deposit multiple droplets either very close or overlaying each other.[112]

One solution to this filtration issue could be to design and use a printer that is custom made for the purpose, with a larger nozzle opening that allows larger particles to pass through. That method was attempted in this work and is detailed in chapter 8. One drawback of this is that a single custom print head will take a long time to cover an area that multiple print heads operating in tandem, as seen in commercial printers, can

complete in seconds. Another approach could be to try and reduce the impact of particle-to-particle resistance within the MOF mixture.

Intrinsically conductive MOFs, as synthesized and undoped, tend to have relatively low conductivity when compared to typical metallic conductors. For example, a MOF used extensively in this work, $Cu_3(HHTP)_2$, also known as Cu-CAT, has a conductivity of 0.2 S cm^{-1}.[113] By comparison, silver has a conductivity of 6.3 x 10^5 S cm^{-1}. Table 4.3 outlines the conductivities of some of the intrinsically conductive MOFs discovered to date.[114]

MOF	Conductivity (S cm^{-1})	Ref.
$Mn_2(DSBDC)(DMF)_2$	2.5 x 10^{-12}	115
$Fe_2(DSBDC)(DMF)_2$	3.9 x 10^{-6}	115
$Cu_3(HHTP)_2$	0.2	113
$Cu_3(HITP)_2$	0.2	105
$Ni_3(HITP)_2$	2	105
$(NBu_4)_2Fe_2(dhbq)_3$	0.16	116

Table 4.3 *The conductivity of a range of intrinsically conductive MOF materials.*

4.4.2 Silver nanowires

Because most MOF conductivities are relatively low, any treatment which serves to reduce conductivity further, including increased inter-particle resistance, quickly renders these species unusable in conductive devices. In fact, in this context it would be beneficial to increase the conductivity of the network overall, but maintain the MOF as an active ingredient and contributory to the conductivity so that it can still function as a sensor. In this work, detailed in chapter 8, this has been attempted by incorporation of silver nanowires (AgNW) into the MOF mixture.

AgNW have been used to tune and improve conductivity previously, and are particularly useful in the context of sensing as they can remain highly conductive even under flexing

and stretching of the substrate.[117,118] This property has led to AgNW being deployed in a number of devices, particularly in conjunction with polymers, for a variety of applications. Liang et al[119] incorporated a percolation network of AgNWs into a polyurethane acrylate elastomeric polymer light-emitting device, and observed significant improvements in light-emitting efficiency, even under high strain. Lee et al[118] Reviewed numerous ways in which nanowires can be used to enhance conductive performance in stretchable electronics. For sensing applications, Park et al[120] developed a wearable sensor by coating a composite of graphene and AgNW with PPy to detect the nerve agent dimethyl methylphosphonate (DMMP) to levels as low as 5 ppm.

Whichever method is utilised, achieving specific architectures is of high importance for any sensing layer, including MOFs. Randomly distributed thin films inevitably inhibit sensory performance for electrochemical vapour detection since all these systems operate based on the efficiency of their ability to communicate long-range. Increasing the order of the deposited films should intuitively improve conductive performance. Furthermore, thin films have a multitude of conductive pathways, which means that a relatively large amount of analyte must interact with the layer before it will register a significant response. By reducing the number of conducting pathways within the device, it should be possible to increase sensitivity regardless of the sensing material used. One of the most promising ways to achieve this is via the fabrication of percolation networks.

4.5 Percolation

Percolation theory is a heavily studied area of statistical physics, and describes a process where systems exhibit a phase transition, based on the probability of a system being connected or not.[121] Generally, it is a useful tool to define behaviour when there is a parameter in the system whose small change results in a disproportionately large change in the behaviour of the system as a whole. Percolation was first introduced by Flory and Stockmayer in the 1940's,[122,123] where their focus was on the description of

macromolecular polymers consisting of multiple branches from smaller molecules eventually resulting in gelation, or the formation of a network of chemical bonds spanning a large system. An example of gelation is the boiling of an egg, where a liquid (the egg white) becomes a 'gel' like substance after the application of heat via cross-linking of denatured proteins.

Flory and Stockmayer's work was built upon and expanded with a more mathematical approach in 1957, by Broadbent and Hammersley.[124] This is often referred to as the start of percolation theory, since it was here that the term was coined and when the theory was approached from a geometric and probabilistic viewpoint. In essence, Broadbent and Hammersley separate diffusion and percolation, where percolation refers to a random process of flow through a medium, driven by the properties of the medium itself and independent of the properties of the fluid. By contrast, diffusion theory is dependent on the properties of the fluid.

4.5.1 Percolation theory

Percolation can be described by considering an interconnected network of channels, which fluctuate between being open or closed.[63] The probability (p) of flow taking place where there are no connections is $p = 0$, and when the network is fully connected, the probability is unity, $p = 1$. Now, starting at $p = 0$ and creating randomly opened connections, eventually enough 'open' channels will connect to form localised connected areas or clusters of neighbouring sites. At some point, connections will form between these localised clusters, merging to form a larger spanning cluster across the medium, allowing flow to proceed. When more connections are added and the maximum number of connections have been made, the entire network is one large cluster and the system is fully open ($p = 1$). The percolation threshold, or critical probability (p_c), represents a phase-change phenomenon, and exists at a medium-dependent point somewhere between $p = 0$ and $p = 1$ (Figure 4.10).

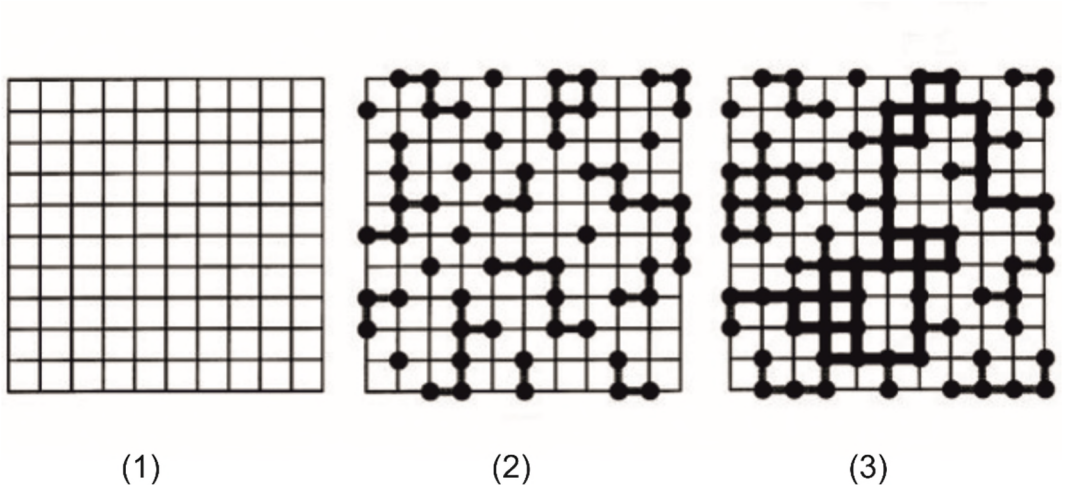


***Figure 4.10**. Schematic representation of percolation, where increasing connected channels from (1) to (3) eventually result in a spanning network.*

The schematic in Figure 4.1 is an example of bond percolation, where bonds can form a spanning network via being open or closed. An alternative type of percolation can also be described, where sites can be either occupied or not leading to a connected spanning cluster across the network. Site and bond percolation can be defined for many lattices, and dependent on the lattice geometry of the substrate can have different p_c, even on the same lattice.[125] For example, in a square lattice p_c (site) = 0.5 and p_c (bond) = 0.593. This is because in this lattice a bond will have more neighbours (6) than a site (4). In a cubic lattice the opposite is true. The percolation threshold and p_c are closely related, where the latter gives a numerical value for the former. Both describe the specific point above which percolation occurs, and below which it does not. In context, p_c is the fraction of neighbouring lattice channels (sites or bonds) that must be connected to form a continuous connection from one side of a network to the other. For some well-studied and commonly used lattices, p_c is known exactly (Table 4.4).[126]

Lattice	Percolation type	p_c
square	bond	0.5
square	site	0.593
triangular	site	0.5
triangular	bond	0.347
honeycomb	bond	0.653

***Table 4.4**. Exact solutions for the critical probability of percolation for some well-known lattices.*

In many cases, including the majority of the work contained here, it is challenging experimentally to target a specific value of p_c for real applications. Instead, it is more beneficial to consider an area or region of a percolation curve, within which p_c is likely to occur (Figure 4.11). In essence, this approach treats each channel as occupying either an area (2D networks) or volume (3D networks) rather than a specific site or bond,[127] and allows a certain margin of error in the exact location of p_c. Furthermore, this method allows a level of independence between the lattice structure and p_c. These are crucial factors when considering conductive materials used in this work.

Owing to deposition methods and topology of deposited layers, they may not be one-dimensional. Furthermore, some moieties associated with each sub-unit within the conductive layers may not contribute to its conductivity. Such moieties could then act as insulating regions between some potentially conductive pathways, resulting in the conductive portion of the network occupying more space than it would intuitively seem. In any case, for many instances and applications, the most interesting facets of percolation behaviour occur across a region rather than a specific point, shown in Figure 4.11, highlighted by the dashed square.

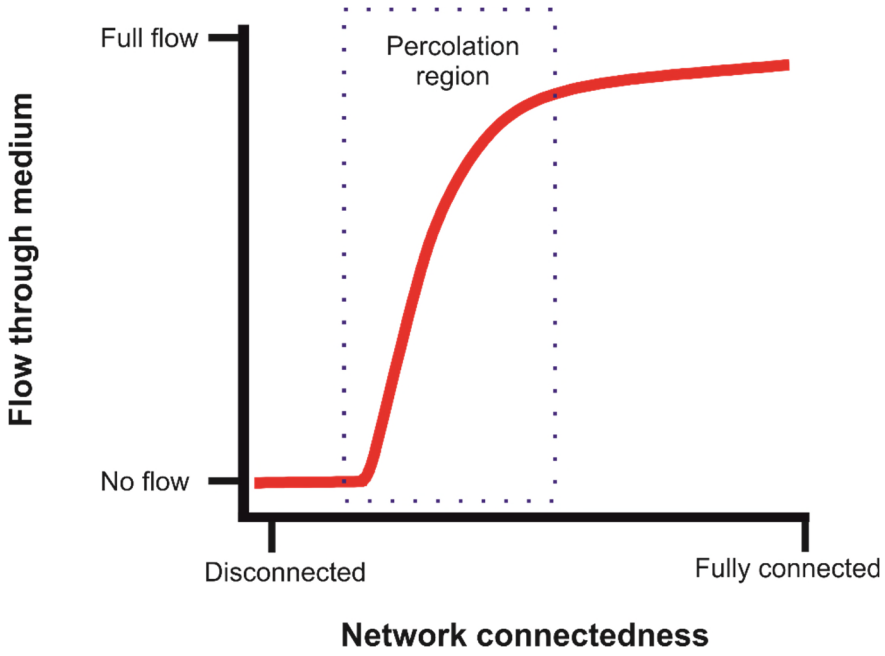


***Figure 4.11**. Schematic graph showing the relationship between the percolation region, network connectedness and flow through a medium.*

Because this percolation region does not represent a step-change but has a gradient, exploiting this behaviour over the range during which the phase change occurs can yield properties not observed at either boundary of the system being either connected or not.

4.5.2 Percolation applications

Percolation has been used to describe a diverse range of processes, from groundwater hydrology to epidemiology in both plants and mammals.[128] One of the most commonly used examples of applied percolation theory is to the spread of fire or disease in a forest or orchard. Upon planning such a venture, percolation theory can be utilised to ensure that during planting, no tree is close enough to another to infect more than two of its neighbours, thus ensuring that $p < p_c$, and so any detrimental event based on proximity can't percolate through the entire population.

Another application of percolation theory is used in the estimation of the distribution and location of fossil fuels in porous rocks.[129] In this case, it is desirable for both fuel location and extraction that the rocks in which they are contained have high porosity, and so for

the network as a whole $p > p_c$. By taking a small sample of rock in the vicinity of a potential new drill site and extrapolating over the projected area that the fossil fuel inhabits, it is possible to use percolation theory to gain a good idea of whether a well will be profitable and productive.

Most pertinent in this work is the application of percolation theory to electrical conductivity or resistance. In this context, in any electrically conductive network consisting of a conductor and insulating matrix, there is a critical point below which resistance is infinite and above which it is finite. This phenomena is well known and has been studied and modelled extensively for a variety of conductive materials in recent decades.[130,131] Understanding percolation behaviour in a conductive system has many potential applications, including for the detection or sensing of electrically active analytes.

4.5.3 Percolation sensing

Percolation networks are of particular interest for use in sensors, since the theory predicts that relatively small amounts of analyte will result in a relatively large response. This is of particular interest when the concentration of any sensing target is low or dilute, and thus may not be easily detectable by other means. One area of sensing where analyte concentrations are nearly always low by design is in the detection of clandestine and often concealed drugs and explosives.

Some of the effects of percolation theory in chemiresistive sensors have been observed and investigated in the literature before, although prior to this work specifically targeting the percolation region as a sensing strategy has not. For example, in metal oxide semiconductor (MOS) sensors, Bruno et al[132] altered film thickness in an SnO_2 layer, which had an influence on sensing performance where thinner layers showed improved performance. More recently Vigna et al[133] constructed a chemiresistor by photopolymerisation of an acrylic resin in the presence of multi-walled carbon nanotubes

(MWCNTs) where sensing performance was enhanced when the MWCNTs were operating in a percolative regime.

Achieving a percolation region sensor using conductive materials can be challenging. Commonly, chemical sensing layers are deposited in films, and in most cases a film of conductive material has already passed the percolation threshold. CPs and MOFs appear to offer a relatively attainable route to a percolation network, since the deposition and thus connection of any network can be strictly controlled via careful choice in the mode of deposition.

4.6 Sensor arrays: An electronic nose

Whilst finding new ways to deposit conductive chemical layers in percolative regimes serves to improve sensitivity, it does not have any impact on selectivity. In fact, given the range of potential analytes, similar electrical behaviour in many of those analytes and background interference in many environments, it is highly unlikely that any one material will have enough selectivity to be used in isolation. Instead, in order to be truly competitive with animal olfaction or molecular separation, any deployable chemiresistive device will be likely to contain a number of sensors operating in tandem in a so called electronic nose (e-nose).

The idea of an e-nose was first suggested by Persaud & Dodd[134] in the early 1980s, building on earlier work by Amoore et al[135] on the stereochemical theory of odour. In many ways, animal olfaction and an e-nose share many similarities in their mode of operation. Both follow a four-step process for analyte detection, consisting of sample acquisition, processing, database comparison and decision. These stages, and the corresponding system responsible for each step in both, are detailed in Figure 4.12.[136]

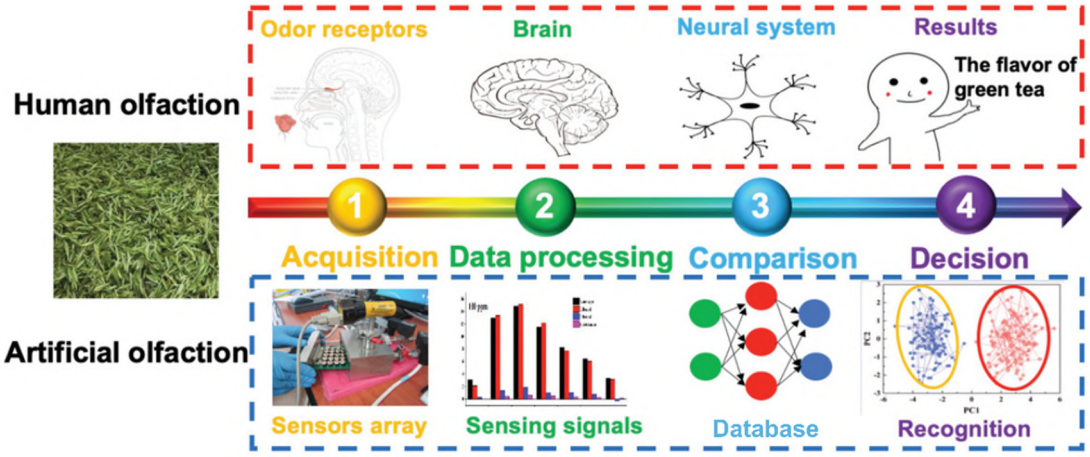


Figure 4.12. Schematic diagram of the comparative working principles between animal olfaction and an artificial e-nose. Taken with permission from ref.[135]

The potential range of applications for an e-nose are huge. They have been shown to be successfully deployed for a variety of purposes, from monitoring of food freshness[137] to clinical diagnosis of disease[138]. In relation to explosives detection, Lichtenstein et al[139] showed high levels of sensitivity for a range of explosives using silicon nanowire FET devices deployed in an array.

Chemiresistors are not the only type of materials that have the potential to be used in e-noses, and materials that have been deployed in this way include field effect transistors (FET), surface acoustic wave (SAW) and QCM sensors.[137] However, the relatively simple production and operation of chemisresistors, along with their potentially small and lightweight design, makes them ideal candidates for use in this way.

4.7 Summary

The aim of the work contained in this thesis is to improve sensitivity and strive for improved selectivity for the detection of analytes associated with clandestine material. This will be achieved by utilising conductive chemical layers operating within the percolation region. This chapter gives an outline of which chemical layers have the

potential to be used in this way, how they can be deposited to achieve percolative behaviour, and exactly what percolative behaviour is in this context.

Electrochemical transduction offers a versatile route to effective sensors, and there are a number of ways in which this property can be utilised. Transduction in this context can be broken down into three classes, potentiometric, amperometric and conductometric. For this work, the main focus is on conductometric devices which operate by employing chemiresistive materials, and measuring responses to analytes in the form of changes in conductivity or resistance.

Chemiresistive materials work by undergoing changes in the amount of charge carriers at the surface, whose efficiency can be affected in the presence of analyte species whose own electronic properties interact in some way with those at the surface of the chemical layer. The most appealing characteristics of many of these materials are that they can be tuneable for selectivity, deposited in ways which improve sensitivity, and can operate under ambient conditions. The most effective materials yet discovered for this purpose are CPs and conductive MOFs.

CPs are well known and well researched. They are generally considered to be extrinsic semiconductors, whose performance as both conductor and sensing materials is improved by doping. Analyte species can then interact by a secondary doping, which results in an anlalyte-dependent change in resistance. Deposition of CPs is typically carried out via either coating preformed polymer onto a substrate, or forming the polymer *in situ* using electrochemical methods. Of the available electrochemical methods, the most advantageous for the work described here is CA, which enables polymer deposition to be controlled as a function of time, giving more control than other strategies.

Conductive MOFs are a more recent discovery, and so research into both the number of materials available and their exact methods of analyte interaction is rarer. However, some 2D conductive MOFs have been discovered which have enough conductivity to be

utilised for vapour sensing, with promising results. Typically, MOF materials are deposited by drop casting or using Langmuir techniques from solution, or by pressing into pellet form. In this work, it is postulated that printing MOFs from an ‘ink’ suspension, augmented by AgNWs to stabilise conductivity, may allow access to a percolation network, and so increased sensitivity.

Regardless of which chemiresistive material is deployed, this work aims to exploit percolation theory to improve sensing performance. Percolation theory describes the connectedness of a system, and the medium-dependent behaviour in terms of probability of flow occurring at the point between the system being open and closed. In relation to electrical conductivity and chemiresistive materials, this translates to a graduated region during deposition when the system migrates from being an insulator to a full conductor. Choosing a mode of deposition for each material that allows the percolation region to be targeted should mean that any analyte interaction has a much larger impact on the conductivity of the system as a whole than that observed for a thin film of the same material, thus improving sensitivity.

Percolation theory can be used to increase sensitivity, but has little impact on selectivity. Owing to the complexity involved in detecting multiple species in a variety of environments, it is unlikely that a ‘silver bullet’ material will be found that has both high sensitivity and selectivity for multiple analytes. Instead, different sensors will be deployed together in an array known as an e-nose. Monitoring and comparative analysis of the output of an e-nose should provide a finger print type response for a given analyte, ultimately providing selectivity. A combination of percolation sensors operating in an e-nose should therefore provide both high sensitivity and selectivity from a single device.

Chapter 5

Chemiresistive sensing data analysis

The aim of this thesis is to demonstrate improvements in the sensing performance of chemiresistive sensors. In order to be able to accurately compare and evaluate sensing performance it is of high importance to be able to analyse sensing output accurately and understand the processes involved in sensor response and recovery as a result of analyte interaction. As will be shown in this chapter, it is not necessarily the case that analyte concentration alone dictates sensor response, and any factor that contributes to the response must be acknowledged and accounted for in the analysis.

This chapter will begin by outlining how external conditions and the type of monitoring required are fundamental to choice of analysis. Then, the current method most commonly used in the literature to assess sensor performance will be described, along with reasons why this method may not always be ideal. Next, a definition of terms will be introduced. Then, two new methods for analysis will be described, the choice of which is dependent on how the sensor is being used and the information intended to be extracted from the analysis.

5.1 Situational analysis

Many different types of materials have and continue to be explored for chemiresistive sensor research, and the output generated must be analysed and ideally compared in order to extract useful information from the raw data. In cases where materials are to be combined into e-nose devices, being able to directly compare cooperative sensors is essential.

Interrogation of sensing data is not a 'one size fits all' process, and the circumstances in which the sensor is operating have a large influence on how analysis should be carried out. For example, a controlled laboratory environment is a completely different proposition to a live minefield, and so it cannot be expected that the same type or breadth of analysis will be equally applicable to both. It is also a necessity to understand the type of monitoring that the sensor is deployed to do.

5.1.1 Monitoring approach

There are broadly three types of monitoring that a chemiresistive sensor could be employed to carry out, single measurement monitoring (SMM), continuous monitoring (CM) and step-change monitoring (SCM).

SMM is typically carried out to obtain a single point measurement, and is slightly beyond the scope of this work. However, it could be applied in future applications of some of the sensors described here, for applications in breath analysis for example. Perhaps the most common type of SMM associated with vapour detection is in roadside breathalyser testing for alcohol impairment whilst driving.[140]

CM generally takes place over a longer period of time, and whilst CM sensors do have an electrical resistance baseline to start with, it may never be recovered after exposure to the analyte of interest and that may not be detrimental to sensing performance. In fact, in some cases baseline drift in CM is the aim of the sensing system. An example of CM

is for monitoring levels of hazardous gases emitted at landfill sites.[141] In this example, changes in analyte concentration exhausted from within landfill sites are monitored over many hours or days to give a good indication of safety for people in close proximity, environmental impact and potential for fires or explosions. In many instances of CM, the analyte of interest is always present at some level, and small fluctuations in that level indicate occurrences worthy of interest.

SCM is particularly relevant for in the field detection of explosives. In this case the electrical resistance baseline is preferably relatively static and stable, and the analyte is often an alien species not usually present in the local environment under normal conditions. In SCM, deviation from the baseline at any level indicates the presence of a target analyte that wasn't present at the start of the SCM process. The magnitude of deviation from the baseline, and the manner in which the baseline is recovered after exposure both contain valuable information about the type and amount of analyte species present and the way in which it has interacted with the sensor. A good example of an environment where SCM is essential is in the detection of concealed mines. Ideally, as a sensor is moved around a minefield, the baseline should be constant unless a mine is present. At that point, a large response should be observed, and upon moving away from that source, the baseline should fully recover ready to illicit the same response for another mine in a different location.

5.1.2 The detection environment: Lab and field

Laboratory testing is by design highly controlled. In the context of sensing, every external aspect can be meticulous, coordinated and reproduceable. This includes temperature, humidity, carrier gas, flow rate and analyte concentration. All of these factors can have an impact on sensing performance. In a 'real' environment, each facet with the exception of analyte concentration can be controlled to some degree, although each may require additional equipment or components, which increases device complexity. Choice of

chemical layers can mitigate against some factors. For example, polymers have been shown to operate efficiently over a range of ambient temperatures around RT, and can in some cases increase in sensitivity with small increases in temperature, making them useful for deployment in warmer climates.[142] MOFs have been shown to operate as chemiresistors with good performance at humidity levels as high as 60%.[102]

Whilst laboratory and 'in the field' sensing are vastly different propositions, both have equal value and the latter cannot exist without the former, irrespective of the sensing system. Similarly, any portable detector will first be tested in a lab environment, but many lab techniques cannot be made portable. This can also apply to analytical methods, where the control afforded by lab conditions means that analysis can be much more expansive and informative in this setting. Conversely, conditions in field detection may preclude some analytical techniques. In fact, in its simplest form a field detector may be highly effective with a simple yes/no binary response for the presence of an analyte of interest.

Although the aim of this project is to create a portable detection system for explosive analytes, the majority of the work was carried out in a lab environment. The result is that the work in this chapter details methods of analysis for both types of circumstance.

5.1.3 Step-change monitoring output

The sensing response curve of a model chemiresistive gas sensor used for step change monitoring (SCM) should perfectly mirror the profile of the analyte entering its vicinity, shown in Figure 5.1 (A) & (B).

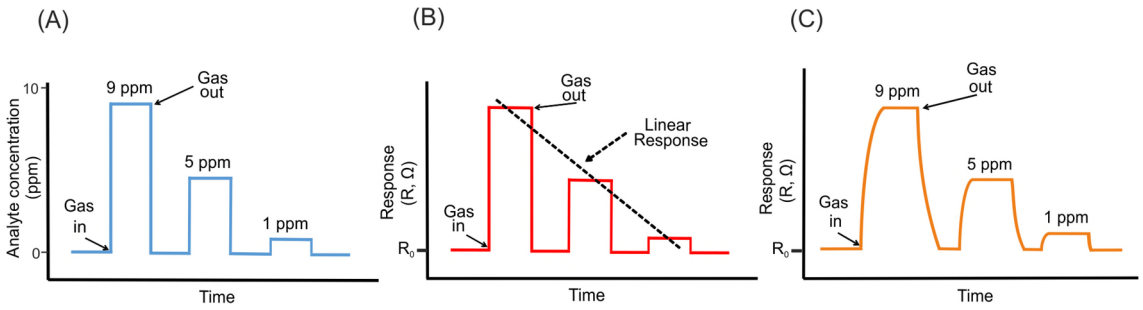


***Figure 5.1**. (A) Profile of analyte concentration in a sensing environment following step changes in ingress and egress of analyte flow. (B) Ideal sensor response to analyte flow in (A). (C) Schematic representation of the closest real-world response to the ideal, seen in some MOS sensors.*

In this scenario, a proportion of the interactive sites on the sensing material are quickly bound with the analyte and the sensor will respond accordingly. Then, upon removal of the analyte of interest, the sensor should rapidly recover to its original state. In reality, this scenario is never observed owing to transport time, diffusion into the sensing layer affecting recovery and transient behaviour in weakly bound analyte interactions at the surface. Instead, the proportion of available sites for analyte interaction, a value that decreases as more interactions occur, governs the sensor response. The amount of free sites available for interaction can be affected by a combination of concentration, flow rate and analyte exposure time. Figure 5.2 shows a schematic representation of analyte behaviour in a dynamic system based on weak interaction between a host sensing material and analyte molecules.

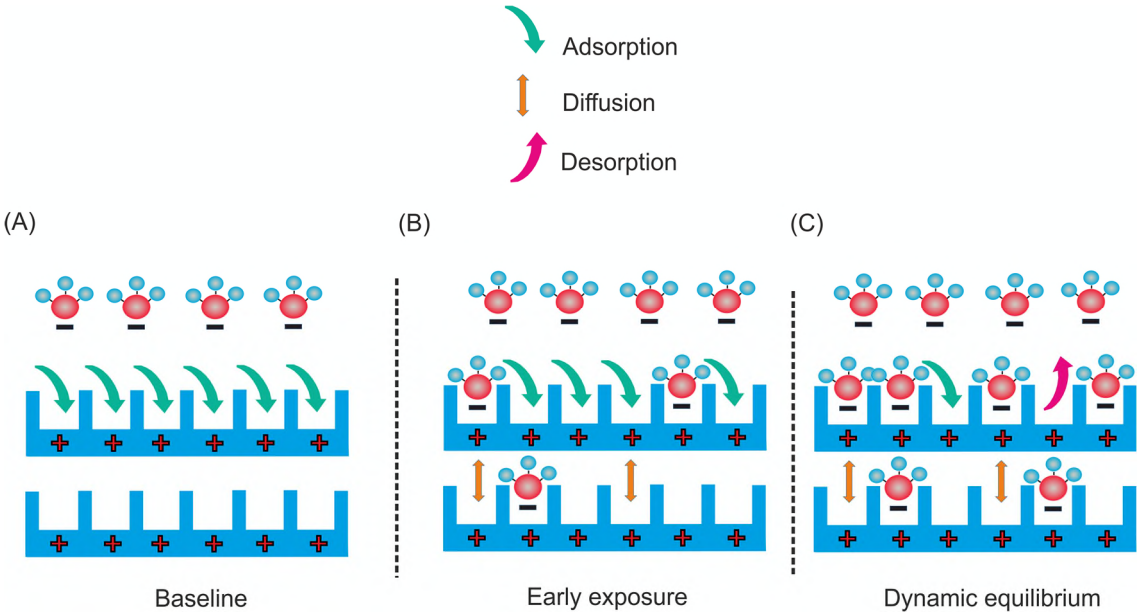


Figure 5.2 *Schematic diagram of sensor/analyte interaction in a dynamic sensing system. (A) Baseline state, where no sensing sites are interacting with analyte. (B) Early exposure, where some sites contain weakly bound analyte and so some response is observed in the system. Diffusion into lower layers of sensing material can slow recovery (C) Dynamic equilibrium, akin to saturation in that adsorption, diffusion and desorption of analyte are in equilibrium and the sensor is performing at its maximum in terms of analyte interaction.*

Ideally, the shape of any response curve should be governed by only one variable, analyte concentration. In the scenarios shown in Figure 5.3 (A) & (B), which are commonly observed in chemiresistive sensing, there are three main variables involved: amount of analyte, governed by both analyte concentration and flow rate, and exposure time. Owing to the nature of testing sensing materials under laboratory conditions, most often exposure time is manually pre-determined by the researcher. This means that it often differs between studies, and is subjective. The result is that peak maxima obtained via this method are also subjective and cannot be confidently used to assess comparative sensing material performance. Changing the exposure time by a relatively small margin in either direction can result in differing figures of merit, which ultimately affect implied sensing performance.

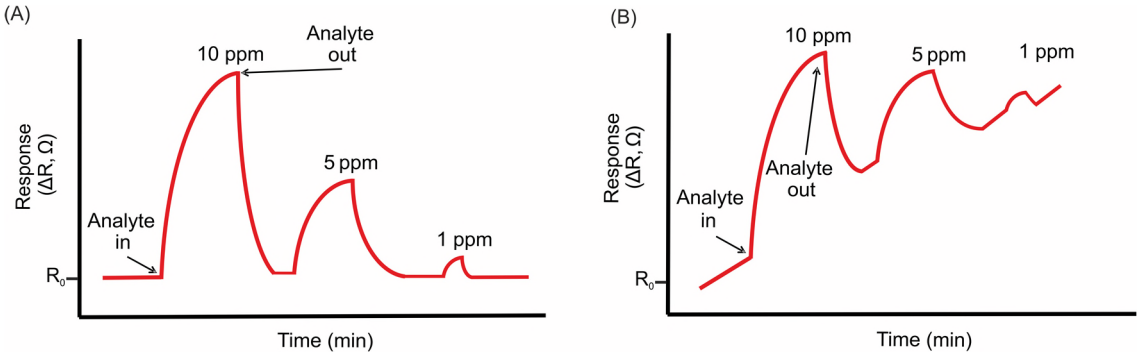


Figure 5.3 *Schematic diagrams of two common chemiresistive response profiles (A) Shark-fin type response. (B) Baseline drift.*

For the majority of chemiresistive sensing materials, the sensing response profiles differ greatly. Generally, transient residence times for analyte molecules result in a continuum of resistance change over the period of analyte ingress. The result is a variety of resistance curve shapes. However, these responses can be grouped into categories based on similarity. Figure 5.1 (C) and Figure 5.3 (A) & (B) show illustrative examples of the most commonly observed response types.

Some MOS sensors have approximations of the ideal behaviour illustrated in Fig 5.1 (B), schematically represented in Fig 5.1 (C),[143] and this perhaps explains why MOS devices have, to date, generally proved to be most easy to interpret and thus the most commonly commercially available type of chemiresistive sensor. This response type is almost exclusively observed in MOS materials because, when operated at elevated temperature, analyte residence equilibrium is achieved quickly, and thus maximum response is achieved relatively quickly, enabling the subsequent total resistance change to remain constant for the remainder of the duration of analyte exposure.[143] Crucially, elevated temperature operation also promotes rapid return to the original baseline, because thermal excitation within the system weakens the bond between analyte and surface, encouraging desorption. In these cases, saturated peak maxima and a consistent baseline make analysis using the $\Delta R/R_0$ model reliable. In fact, in a lab-based

setting with controlled parameters, $\Delta R/R_0$ analysis is a useful tool to obtain figures of merit for a sensing response. However, in some cases, and especially in a real-time environment, it is not necessarily the optimal way to extract useful information from data during acquisition.

5.2 The $\Delta R/R_0$ method of analysis

Currently, the most commonly observed analysis method in the literature for SCM chemiresistive sensing experiments is the $\Delta R/R_0$ method. By definition, chemiresistors operate in a similar way regardless of type of monitoring and material used. Most lab-based SCM chemiresistive experiments in the literature follow a similar format. [144,145] Experimentally, sensors are connected to a power supply and a multimeter and changes in resistivity or conductance are monitored as a function of analyte interaction over time, either at RT or in the case of MOS sensors at localised elevated temperature.

The starting resistance of the material before exposure to analyte of interest is inferred to be the baseline (R_0), and absolute deviation from the baseline over the period during which the analyte is allowed ingress is measured as the response (ΔR). Recovery is the time taken for the resistance to return to the baseline once the analyte has been removed from the system. After each response/recovery cycle, analyte concentration is changed sequentially and ideally, higher concentrations result in larger changes in resistance. Figure 5.4 (A) shows a typical example of a sensing response from the literature.[146]

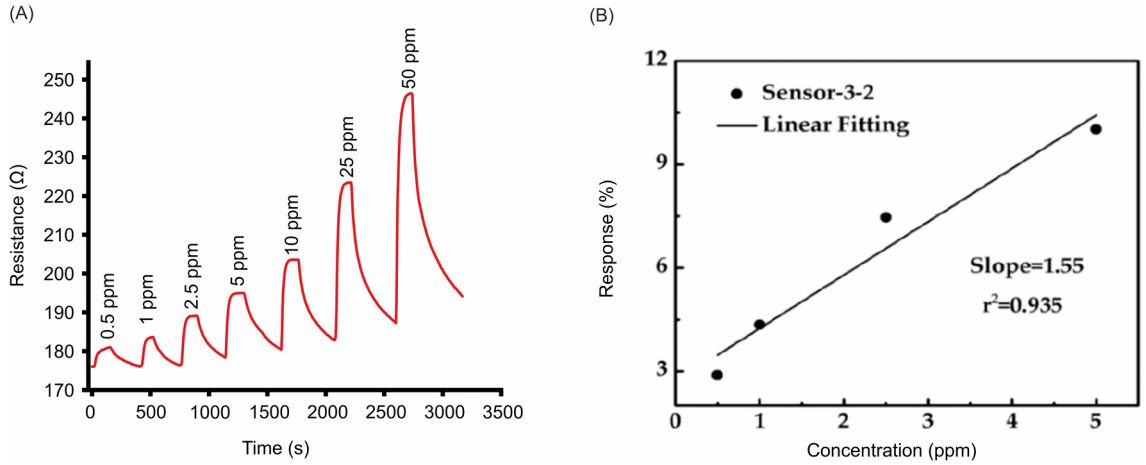


Figure 5.4 *(A) A published example of a typical chemiresistive sensing plot, in this case of a reduced graphene oxide sensor responding to various concentrations of ammonia. (B) The $\Delta R/R_0$ method of analysis as published, performed on the peaks from 0.5 – 5 ppm in (A). Reprinted with permission from ref.*[144]

Once a sensing plot such as the one shown in Figure 5.4 (A) is obtained, then $\Delta R/R_0$ (usually expressed as a percentage) is calculated for each analyte concentration. From this, a calibration curve can be plotted. Figure 5.4 (B) is the published $\Delta R/R_0$ calibration curve of the dynamic range (most linear portion) of the data (0.5 – 5 ppm) in Figure 5.4 (A). Various figures of merit can then be obtained including sensitivity and limit of detection (LOD), although the definitions of some of these terms varies between studies.[79,147,148]

Utilising this method of analysis in a lab setting is relatively simple and can be carried out quickly and easily. Discrepancies arising from baseline drift and exposure time can be accounted for and mitigated against when the analyst has the time and knowledge to do that. However, we have found that using only resistance change to obtain important information pertaining to sensor performance and comparison may be flawed when attempting to export this method into a real-life setting.

If a sensor is based on resistance changes arising as a function of analyte residence time, and a point of absolute saturation is not reached during the exposure time, then

the implied peak maximum is a value based on the duration chosen for exposure. Furthermore, in some cases the baseline is never fully recovered. This is often observed when more than one process is occurring during analyte interaction, where one or more of these interactions may result in an irreversible change in the sensing material.[149] These issues are not easily resolved when the data is being analysed in real time as it is being acquired, especially if the end user is not familiar with the impact that they can have on sensing results.

Almost universally, the method used to extract ΔR is based on peak picking at the point when resistance change has reached its maximum for the chosen analyte concentration after a chosen exposure time. This serves to exclude the majority of the data from evaluation, and so omits valuable information about how the sensor behaves in relation to the analyte of interest. All of these factors have obvious implications on any direct analysis of absolute resistance changes, and may result in large discrepancies in sensing behaviour in real-world applications. In a field-deployed device, starting baselines and peaks can be easily extracted by software, but if the baseline is never recovered, fluctuates over a greater range of resistance than the response, or if exposure time is unknown, then it quickly becomes a complex problem for software to analyse where the baseline is, when recovery occurs, and ultimately what the magnitude of response actually is, and thus what concentration of analyte, if any, has been detected.

For cases where saturation is not achieved within the timeframe chosen for analyte exposure, and especially if the baseline is unstable, it is better in real time to consider the rate of change (RoC) of the sensor during exposure. Maximum rate of change is achieved much more rapidly and consistently than sensor saturation, and is generally an inherent material property that is not greatly affected by baseline fluctuation nor the peak height of a resistance change ultimately achieved as a function of exposure time.

It is anticipated that this will result in a better measure of true sensing ability and will enable different chemiresistive sensors to be reliably compared

5.3 Definition of terms

The development of practical chemical sensors is the driving force behind a rapidly expanding field of research. Obtaining consistent and comparable figures of merit from the raw data of chemiresistive sensing output from sensors produced in different ways by different researchers has historically proven challenging owing to inconsistent analytical methods. However, the following definitions, based on IUPAC and ICH guidelines,[150,151] are the most commonly used in the literature and generally accepted by the sensing community.[152,153]

Sensing Response Curve. Describes how the sensing device responds to exposure to the analyte of interest as a function of time. For chemiresistive devices, the raw sensing trace is usually plotted as resistance or conductance against time.

Calibration Curve. A plot to show the relationship between the response of the sensor and the concentration of analyte. Different conventions exist for plotting this data, but the most common are either a percentage difference relative to the starting baseline (R_0), i.e. $\Delta R/R_0$ as shown in Equation 5.1, or simply the change in response (ΔR) for each analyte concentration in the experimental range.

$$\text{Response (\%)} = \frac{\Delta R}{R_0} \times 100 \qquad (5.1)$$

Dynamic range. The range of analyte concentrations over which a sensor displays a linear relationship between sensor response and analyte concentration, and can thus be calibrated.

Sensitivity. The ability of a method to determine different analyte concentrations. The sensitivity is the gradient of the calibration curve. The error associated with the sensitivity is the goodness-of-fit error (e.g. using the R^2 method) of the gradient of a linear fit to the calibration curve data. In the analysis describing the linear fit it should be specified whether the linear fit has been anchored at the origin, or whether a constant offset has been included to improve the goodness-of-fit error.

Selectivity. The extent to which a method can determine the concentration of particular analytes in a gas without interference from other components in the gas.

Specificity. The use of this term should be avoided within the context of gas sensing. It is sometimes used interchangeably with the term ‘selectivity’. In other fields such as pharmacology the terms ‘specificity’ and ‘selectivity’ have established definitions are not relevant to gas sensing.

Limit of detection (LOD). Defined as the lowest concentration of analyte that can be detected to be present in the gas but not necessarily quantitated as an exact value. To achieve a certainty above 99% that the analyte signal is sufficiently different from R_0, the LOD is calculated as a $3\sigma_{noise}$ deviation from the baseline, where σ_{noise} is the root mean square (RMS) noise level of the baseline. The LOD as an analyte concentration can then be calculated using Equation 5.2.

$$\text{LOD} = 3 \times \frac{\sigma_{noise}}{\text{gradient of the calibration curve}} \qquad (5.2)$$

It should be noted here that for the LOD to be expressed as a concentration (e.g. in ppm), it is necessary for σ_{noise} and the y-axis of the calibration curve to have the same units. This means that if the calibration curve is plotted as $\Delta R/R_0$ against analyte concentration, then σ_{noise} also needs to be expressed in units of $\Delta R/R_0$. Alternatively, if the calibration curve is plotted in units of ΔR then σ_{noise} also needs to be expressed in

units of R. In addition, σ_{noise} can be artificially reduced if smoothing operations are over-used in the data. Whilst smoothing is a valid method of data treatment, it must be ensured that the end result remains representative of the data. The error associated with the LOD is related to the goodness-of-fit error of the calibration curve gradient.

Since a large proportion of chemiresistor sensor research focuses on reducing the LOD, it is important to note that if an LOD is low, high concentrations often result in analyte residence equilibrium and thus non-linear behaviour in the calibration curve. Any non-linear behaviour signifies an analyte concentration outside the dynamic range that should not be used for calibration and/or LOD calculation.

Limit of quantitation (LOQ). The lowest concentration of analyte in a sample that can be determined with acceptable precision. The LOQ is calculated as a $10\sigma_{noise}$ deviation from the baseline, and the analyte concentration can be calculated using Equation 5.3.

$$\text{LOQ} = 10 \times \frac{\sigma_{noise}}{\text{gradient of the calibration curve}} \qquad (5.3)$$

5.4 Rate change analysis for in the field sensing

One issue that arises when attempting to utilise $\Delta R/R_0$ resistance change analysis for many types of chemiresistive sensing materials, particularly those that operate at room temperature, is that response curves tend to fall somewhere between those observed in Fig. 5.3 (A) & (B).[154,155] In this scenario, the shape of the response is determined by a ratio of filled and unfilled adsorption sites as a function of both analyte amount (influenced by both concentration and flow rate) and exposure time. The result is an initial sharp change in resistance on first exposure, followed by a slower change as more active sites become filled. The inverse of this process is observed upon removal of the analyte flow, slowed by surface bound analyte being more reluctant to leave at ambient temperature. Crucially, owing to the transitory nature of the analyte molecule interactions

with the sensor, it is rarely the case that absolute equilibrium, and thus a stable constant maximum resistance, is achieved within a timeframe that would be deemed useable in a real application in the field.

One solution to the issues surrounding response types could be to increase exposure time to a point where it could be inferred that saturation has occurred and thus the maximum resistance change has ensued and stabilised. However, for real applications this would, in most cases, result in impractically long exposure times for any application to be a possibility. Furthermore, this problem is compounded as analyte concentration decreases. One of the primary goals of chemiresistive sensing is to improve the sensitivity and/or reduce the LOD/LOQ to a point where it is competitive with ion separation or animal olfaction. Detection of low analyte concentrations within a reasonable timeframe is the fundamental aim of much sensor research, and if saturation is directly proportional to analyte interaction, at ultra-low concentrations the time to saturation increases dramatically.

Another problem in attempting to analyse sensing data based on absolute resistance changes, highlighted schematically in Fig. 5.3 (B), in the real example in Figure 5.4 (A), and illustrated in many published examples,[148,155] is that of a fluctuating baseline. In some cases, materials undergo fundamental changes upon exposure to analyte gases that result in long-term changes to the baseline. Baseline changes by definition will have further impact on inferred peak maxima, by introducing confusion over where R_0 actually is for each successive analyte exposure.

In the illustrative examples, and in many lab experiments, the baseline is manually enforced between exposures when the resistance value has returned to the value at which it started, at which point the next concentration of analyte is introduced. However, it is often the case that the baseline does not return to its original value. The baseline may stabilise at higher or lower than original values during the course of the assessment

period. This is usually the result of some semi-permanent change in the system because of analyte interaction, external influences including humidity or temperature fluctuation, or because of sensor degradation over time. In any case, a substantial change in baseline will affect the percentage resistance change, sensitivity and LOD/LOQ estimates.

$\Delta R/R_0$ is a valuable lab-based method to quickly extract some useful figures of merit from a sensor. However, the method is really only reliable in the lab where exposure times are known, and even then only truly after data collection is complete when any baseline fluctuations can be accounted for. In real time, and in a real environment, if both the baseline and the peak maxima of absolute resistance changes are unreliable owing to fundamental issues inherent in the method, then a new method is required which addresses both of these issues.

Such a method should be able to assess the performance of a sensing material based on an intrinsic property which is influenced by neither exposure time nor baseline, but which can still be extracted from the raw sensing response curve data, in real time. In cases where saturation does not occur rapidly, the sensing response curve gradient changes proportionally as the availability of vacant adsorption sites reduces. That gradient will have a region where it is steepest, and this corresponds to the point during the exposure where the sensor is responding fastest, and so is most sensitive. Generally, this point occurs relatively soon after exposure because this is the point where the maximum number of vacant adsorption sites are available, and reduces as a function of time (Figure 5.2). Importantly, the steepest point in the gradient is, to a large degree, independent of both baseline and resistance peak maxima.

A graphical representation of this point can be easily extracted from the first derivative of the raw sensing response curve. Schematic examples of how this might look for the responses in Fig. 5.3 (A) & (B) are shown in Fig. 5.5 (A) & (B). Figure 5.3 (A) & (B) are

inset in Figure 5.5 for clarity. Importantly, the derivative plots of each type of sensing response are very similar, regardless of baseline and peak maxima of the sensing response.

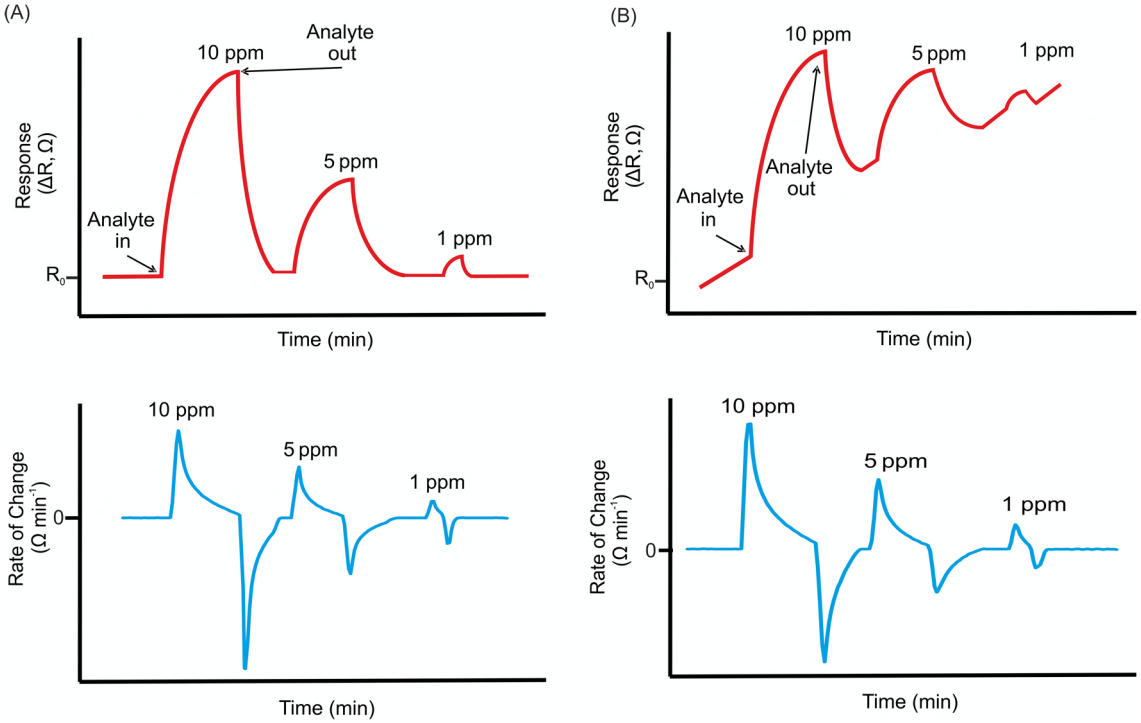


Figure 5.5 *Schematic response profiles from Figure 5.3 (red lines) above rate change plot (blue lines) for two common chemiresistive response profiles (A) Shark-fin type rate change plot (B) Baseline drift rate change plot.*

In this work, derivatives were obtained using the transform of the centred difference formula, where the derivative at point P_i is calculated by taking the average of the slopes between the point and its two nearest neighbours (P_{i-1} and P_{i+1}). This can be written as:

$$f'(x_i) = \frac{1}{2}\left(\frac{y_{i+1} - y_i}{x_{i+1} - x_i} + \frac{y_i - y_{i-1}}{x_i - x_{i-1}}\right)$$

An issue is that differentiation can be detrimental to the signal to noise ratio (SNR), and so some smoothing of the differential plot may be required prior to analysis. One caveat to any smoothing operation is that care must be taken in selecting a smoothing method that does not result in any net loss of information from the original data. It must also be

stated here that, in the strictest terms, differentiation itself results in a net loss of data. This is because constant terms in the original data, in sensing cases this would refer to any flat baseline, cannot be restored if the differentiated data is integrated back to its original form.

However, the new baseline in the differential plot is actually of benefit here, zero-centric and corresponding to areas in the original data where dy/dx is not significantly changing. Furthermore, as reflected in Figure 5.5 (A) & (B), information can be gained about sensor behaviour during both response (positive non-zero values) and recovery (negative non-zero values). This becomes a crucial part of the new analysis, since a relatively static zero-centric baseline allows access to data which is not obtainable when looking at resistance changes alone, and means that calculating a margin of error becomes more accurate.

For the differential plot, the mean value of the range of data for each peak maximum correlates with the stage at which the sensor is responding at its maximum rate. Since the baseline is now centred on zero, the noise level can be determined. Selecting an appropriate range of data prior to analyte exposure, subtracting the background baseline to ensure incomplete/continuing recovery from any previous exposure is not skewing the data, and calculating the root mean square (RMS_{noise}) gives the standard deviation of the rate change plot, or in other words the background noise of the signal. Another benefit of this method is that it utilises a far greater portion of the acquired raw data than the traditional method of peak-picking or using approximations for baseline and single point peak maxima from the raw response plot. This is illustrated in schematic form in Figure 5.6.

Calculating the SNR of the differential plot for each concentration of analyte can now be used to plot a calibration curve against analyte concentration as shown in Figure 5.7.

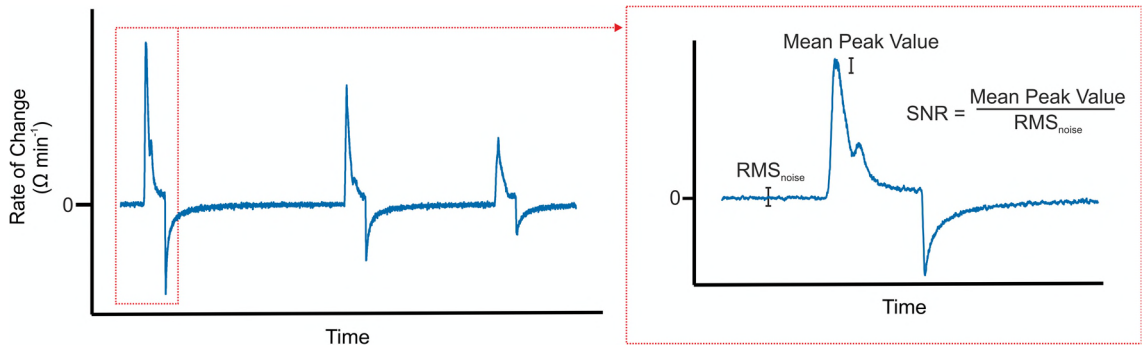


Figure 5.6 *Schematic diagram of the areas of interest of a rate-change plot. On the left, a rate change plot obtained by taking the first derivative of a sensing response curve for decreasing concentrations of analyte. On the right, a close up of the highest peak shows how the calculation of the root mean square noise level (RMS_{noise}) of the baseline prior to analyte ingress and mean of the peak are extracted from the data. From these two values, a signal to noise ratio can be calculated.*

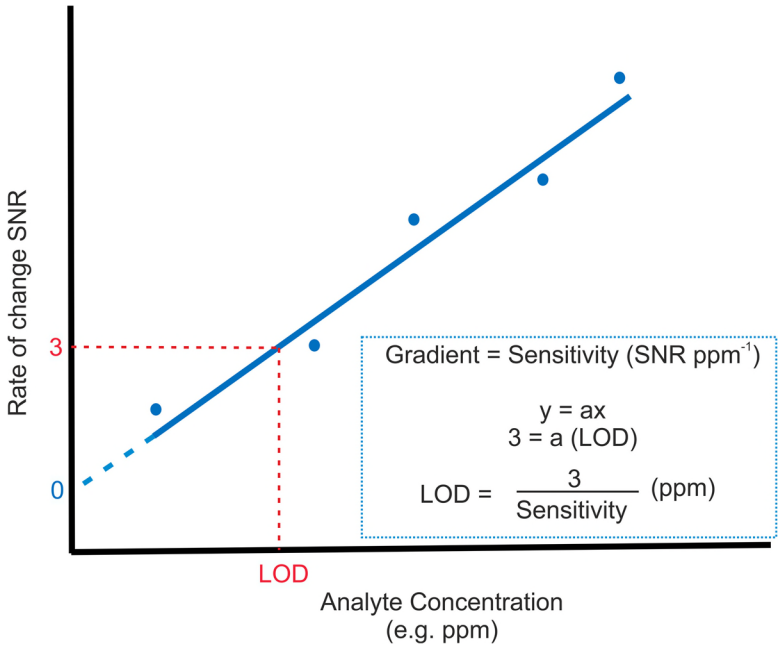


Figure 5.7 *Example of the SNR calibration curve necessary to obtain the sensitivity, the limit of detection (LOD) and the limit of quantitation (LOQ). Highlighted by the red line and the inset calculation, since the SNR of R_0 is unity, the LOD and LOQ are calculated using x – 1, where x is the number of SDs accepted to represent the relevant value.*

The gradient is proportional to the sensitivity, and is a measure of rate of change per unit concentration (e.g. (RoC SNR) ppm^{-1}). Any signal deviating more than 3 standard deviations from the background represents (with a 99% confidence interval) a signal observed in the differentiated data that is significantly different to the background. Since the SNR of the background is on average zero, any signal with an SNR value below three cannot be confidently stated to be significantly different from baseline fluctuation. Therefore, dividing three or ten (inset, Figure 5.7) by the gradient of the calibration curve gives an accurate LOD and LOQ respectively. The error in the fit of the calibration curve, propagates through the calculation, directly corresponding to the error in the quoted LOD/LOQ. Crucially, this method provides a true representation of the sensing response independent of baseline, total resistance change and total exposure time.

In addition to obtaining a sensitivity for response, another benefit of RoC analysis is that you can also obtain information about sensor behaviour during recovery, by repeating the same analytical steps described for the response peaks, but now for negative non-zero peaks in the dataset. Figure 5.8 shows an example of a recovery calibration curve.

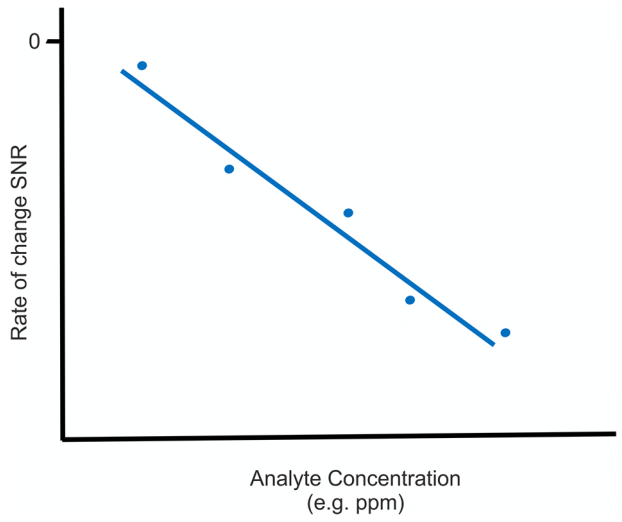


Figure 5.8 *Example of the SNR calibration curve necessary to obtain information relating to sensor recovery, obtained by repeating the same steps used to obtain the response calibration curve in Figure 5.7. The gradient is now negative.*

Comparison of the response and recovery RoC calibration curves begins to provide information relating to analyte/sensor interaction which is not possible to obtain from resistance change data. In all real examples we have applied this analysis to (see future chapters), response calibration curves are linear, indicating that response is a 1st order process, where one interaction dominates response. For chemiresistors this will in most cases be electronic interaction at the sensor surface resulting in charge carrier imbalance and band gap alteration.

Conversely, recovery calibration peaks are often non-linear, which indicates that the process is higher than 1st order, where two or more processes are occuring during recovery at differing rates. This is understandable, since after initial contact, it is reasonable to assume that some analyte will remain bound either electrostatically or through some other process such as H-bonding. Using RoC analysis also provides insight into how long recovery takes, and which process is dominating recovery. This is particularly valuable information for in the field sensing, since a user can start to gain some understanding of turnover time, or how long the sensor will require after a response event to be ready for re-use. Importantly, in RoC terms, this is not the same as the time taken for a sensor to recover to the baseline in the raw resistance plot, where rate change recovery to baseline is always faster. This results in calibration being quicker, and in being able to reassess sensing materials which may have been previously discarded for potential applications because resistance baseline recovery is not fast enough to be useful in a real life environment.

In every real example we have investigated to date, the steepest point in the resistance change occurs within the first minute or less of exposure to the target analyte. This is important when considering use in applied situations, where sub-minute exposures are more realistic for a portable sensing device. Furthermore, experimental examples with a consistently shifting baseline have also been investigated and shown to have consistent responses in terms of rate change, as long as the magnitude of response does not

significantly change proportionally with baseline shift. Below, this method is applied to experimental data acquired from a commercially available chemiresistive sensor, along with a percolation sensor prepared in our lab.

5.5 Experimental case studies

Two sensors were tested and analysed using both methods described. In case 1, the new analytical method was assessed against the $\Delta R/R_0$ method in a highly controlled lab environment. The aim of this was to ascertain the merits of both methods and a direct comparison of both when the conditions allow either to be used accurately. The sensor used was a commercially available MOS sensor. This was chosen as a proof of concept for the method described here, since the sensor has undergone independent testing prior to being made commercially available, and thus is supplied with a verifiable detection range. The sensor is a MICS-4514 Dual Metal oxide sensor for oxidising and reducing gases, with a quoted lower detection limit of 0.05 ppm for NO_2,[156] supplied by SGX Sensortech.[157]

In case 2, a PPy polymer percolation sensor was used (the production of which is fully detailed in chapter 6). In this case, conditions were intentionally imposed where the baseline was unstable, and parameters including exposure time, concentration and recovery time were varied, thus replicating a potential scenario encountered in the field. This experiment was designed to show how in some scenarios, particularly in live environments in real time, the new RoC analysis method has distinct advantages over the standard.

5.5.1 Case 1: Analytical method comparison in a controlled environment

Sensing experiments were carried out in the stainless steel cylindrical custom-built gas-sensing chamber described in Chapter 2.4. The sensors were placed on a SGX Sensortech MICS-EK1 MOS Gas Sensor Evaluation Kit in the chamber with electrical connections running from inside the chamber to a PC outside, equipped with SGX

custom software. The sensing chamber was first purged with dry air for 45 minutes to remove any impurities present in the chamber or in the sensing layer. Once a stable baseline was reached different concentrations of NO_2, diluted in a dry air carrier gas, were allowed into the system. The ppm concentration of NO_2 that was introduced into the sensing chamber was calculated by the relative flowrates of the two mass flow controllers, which were maintained at a combined constant of 500 sccm throughout.

A raw resistance-change sensing profile for a 1-minute exposure of analyte, as measured in our laboratory set-up, is shown in Figure 5.9 (A). The profile is a 'shark-fin' type response, where the analyte exposure time was pre-determined. In this case, the raw data was sufficiently good to require no smoothing, and any attempt to smooth the data resulted in a net loss of information (reduction of peak height), so the data was analysed without smoothing. The next stage in the analysis described in Chapter 5.4 is to calculate and plot the first derivative of the data presented in the raw sensing plot (Figure 5.9 (A)), corresponding to the gradient of the sensing response as a function of time. The resultant plot is shown in Figure 5.9 (B).

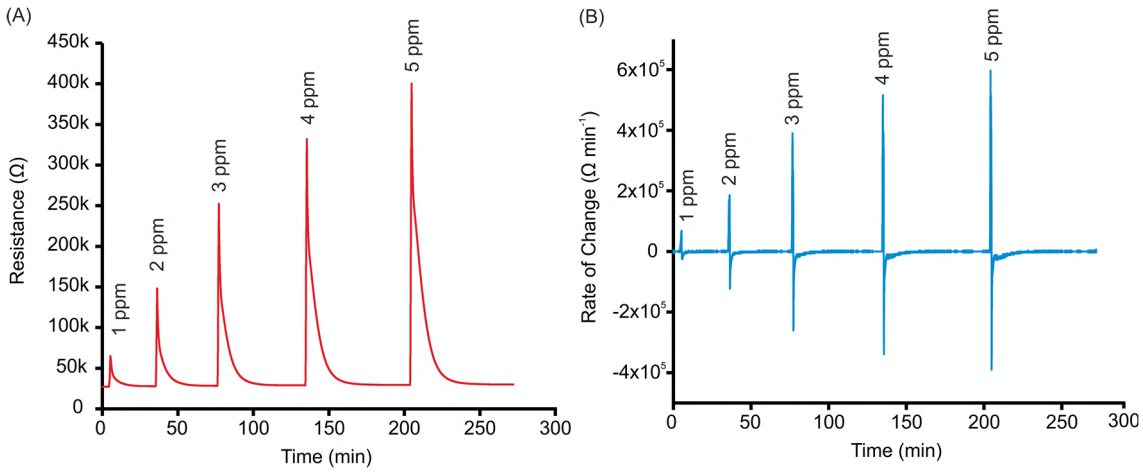


Figure 5.9 *Sensing response curve of the SGX Sensortech MiCS-4514 redox MOS sensor responding to varying concentrations of NO_2 in dry air. (B). Rate of change plot of the sensing profile shown in (A).*

Now, the calculations can be carried out as described. It is important that the data range selected for both the peak range and the baseline are consistent for each exposure within the dataset, and that the time range chosen for the peak maximum is a sensible proportion of the exposure time. In addition, the baseline must representative of the noise of the plot as a whole, and so a longer time-range is advisable. A background subtraction can then be carried out on the selected data in order to remove the influence of any analyte-related behaviour prior to the chosen exposure. To illustrate this, Figure 5.10 shows the resistance change peak at 5 ppm from Figure 5.9 (A), overlaid with the rate of change peak at 5 ppm from Figure 5.9 (B). Because the x-axis remains constant for both, this exercise is useful to see how the rate of change and response plots relate to one another, and how the point of maximum gradient of the response peak is represented by a 'flat-spot' in the rate of change plot (highlighted in green in Figure 5.10).

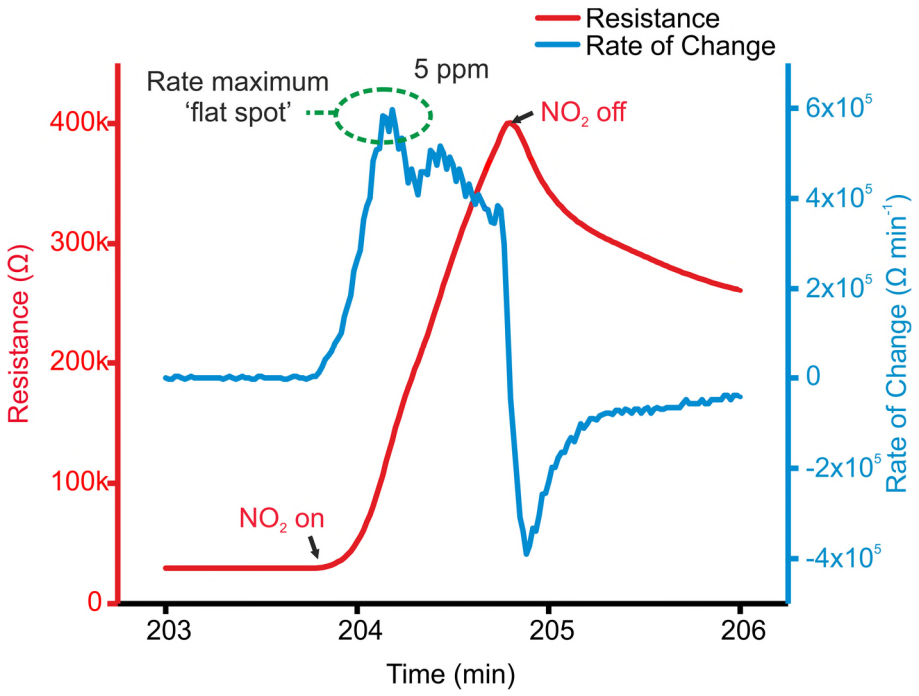


Figure 5.10 *A close up of the peak at 5 ppm from both Figure. 5.9 (A) & (B), overlaid to show how the two are related. The flat spot highlighted in green indicates the area of the sensing response curve where the sensor is responding fastest to analyte exposure.*

In this example, a period of 15 seconds was chosen for the mean peak maxima and 10 minutes for the RMS_{noise} calculation of the baseline. This process was repeated for each analyte concentration, yielding values which were used to construct the calibration curve shown in Figure 5.11. The one minute exposure protocol was repeated in triplicate to attain the error bars shown.

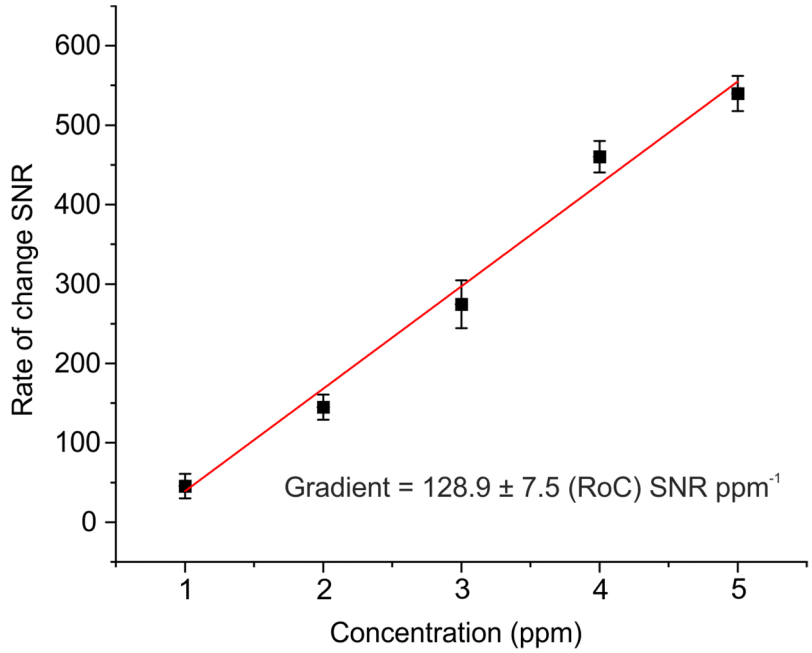


Figure 5.11 *RoC Response calibration curve plotted for the peak maxima detailed in Figure 5.8 (B). The gradient corresponds to sensitivity, which is a measure of rate of change per unit concentration, and is inherent to the sensing material/system utilised.*

The subsequent gradient was calculated using linear regression to give a sensitivity of 128.9 ± 7.5 (RoC SNR) ppm^{-1}. The LOD is therefore:

$$\text{LOD} = \frac{3}{\text{Sensitivity gradient}} = \frac{3}{128.9} = \mathbf{23\ (\pm 2)\ ppb} \qquad (5.4)$$

These values are in good agreement with the manufacturer provided lower limit, where they quote a range of detection of 0.05 - 10 ppm for NO_2. The small discrepancy in the

limit may have occurred owing to the way in which the manufacturer calculated their quoted limit. It is not clear from the manufacturer documentation whether the value they quote is an LOD or an LOQ, nor how they achieved it. In addition, small variation in experimental conditions could also account for the difference. For relative humidity (RH), the manufacturer quoted value was for a level of ≥ 5 %, whereas this experiment was carried out at 0 % RH. Furthermore, the manufacturer-specified guideline temperature was 23 ± 5 °C, whereas the data in this case was acquired at 33 °C.

The process used to obtain the response calibration curve shown in Figure 5.11 was repeated for the negative non-zero peaks in order to construct a recovery calibration curve, shown in Figure 5.12.

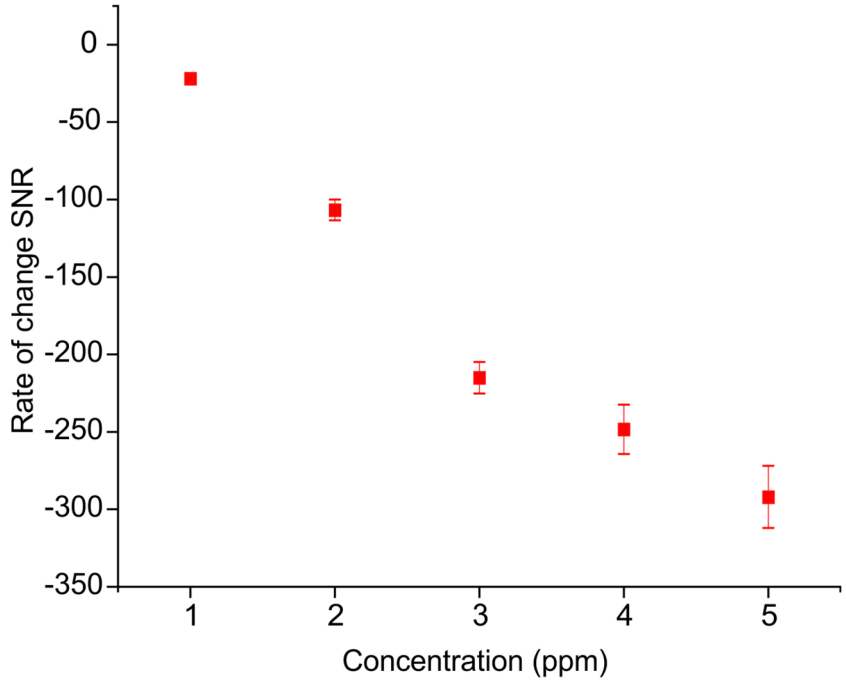


Figure 5.12 *RoC Recovery calibration curve plotted for the peak maxima detailed in Figure 5.9 (B).*

Reflected in Figure 5.12, the recovery calibration curve appears to be non-linear particularly at higher concentrations. In addition, the magnitude of the SNR for each concentration is significantly lower than those observed for the same concentrations in

the response calibration curve. From this, since the noise is the same for both response and recovery in the same sample, it can be determined that the rate of recovery is significantly slower than that of response. This in turn indicates that once bound, a proportion of the analyte remains bound for a significant period of time, even at the elevated temperature at which MOS sensors operate. Furthermore, the non-linearity suggests that the reason for this extended residence time is likely to be due to at least two distinct binding mechanisms, where the one which is stronger and thus causes analyte to be slower to depart is amplified at higher concentration. Another reason for the observed behaviour could be as a result of diffusion of analyte into the MOS layer after initial response. The process of diffusion out of the bulk of the MOS to the surface for desorption would have an associated time constant resulting in slower recovery.

The same data was then analysed via the $\Delta R/R_0$ method to obtain an LOD estimate. The baseline was obtained by selecting the range of data in the sensing response curve from 0 – 5 minutes, before any analyte was allowed entry and the baseline was relatively stable (Figure 5.9 (A)). In order to use the $\Delta R/R_0$ method accurately, it is important in the final calculation of LOD that the units of the calibration gradient and the σ of the baseline match. This is often overlooked in published examples, and represents the first potential issue with utilising this method of analysis. The calibration curve is shown in Fig. 5.13, where the gradient was 334.9 (± 6.4) $\Delta R/R_0$ (%) ppm^{-1}.

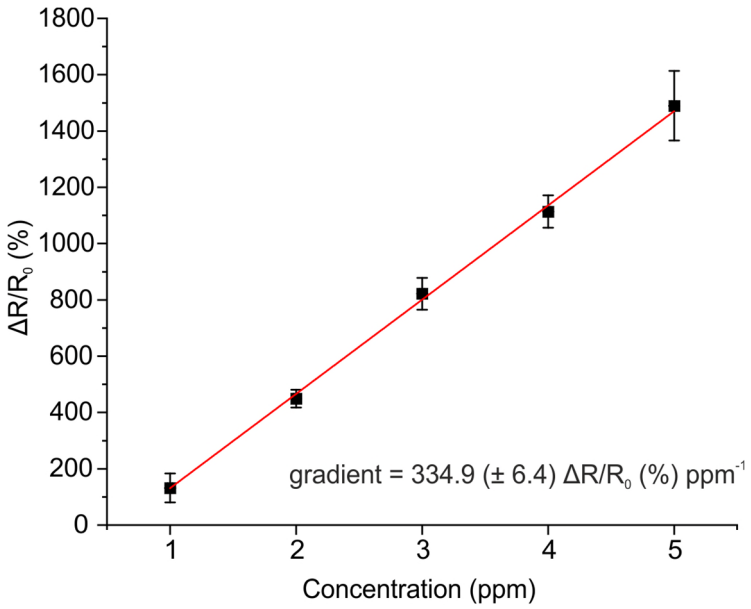


Figure 5.13 *$\Delta R/R_0$ calibration curve plotted for the peak maxima detailed in Figure 5.9 (B). The gradient corresponds to sensitivity, in this case a measure of percentage resistance change per unit concentration.*

In this case, because conditions were highly controlled, the baseline is very stable. In order to calculate σ_{noise} with units of $(\Delta R/R_0)$ %, it is necessary to find the mean of the range of data representative of the baseline, and the SD of that data from the mean. σ_{noise} can then be calculated. Here, from the triplicate sensing results, the average R (R_0) of the blank was 28661 (± 2475) Ω, and the average SD (ΔR) of the data from that blank was 35.7 (± 7.2) Ω. Now, σ_{noise} can be calculated as follows:

$$\sigma_{noise} = \frac{\Delta R}{R_o} = \frac{35.7}{28861} \times 100 = \mathbf{0.12\ (\pm\ 0.02)}\ \%$$

The LOD using this method can then be calculated using Eq. 5.2 as follows:

$$\text{LOD} = 3 \times \frac{0.12}{334.9} = \mathbf{1\ (\pm\ 0.1)\ ppb}$$

As reflected by the LOD obtained using the $\Delta R/R_0$ method, there is significant difference between the obtained LOD and the manufacturer quoted lower detection range. After a 1 minute exposure, the LOD calculated using this method appears to be improbably low, a direct consequence of the baseline being artificially stable under highly controlled laboratory conditions. This has obvious implications for obtaining lab-based LODs using this method, and then expecting those LODs to be applicable in a real environment. In addition, by extending the exposure time in the lab, as long as saturation is not reached it is possible to increase ΔR further, whilst the baseline remains the same. The consequence of doing that is that the LOD reduces further.

The same sensor was exposed to analyte for a range of times, in order to ascertain the efficacy of the RoC method in comparison to the common method of calculating $\Delta R/R_0$. The analyte exposure times selected were one minute, five minutes and ten minutes. Figure 5.14 (A) shows the sensing response curve for each exposure time. The results of calculating the LOD for each exposure time, using each method, are shown in Figure 5.14 (B). In order to visually compare peak heights easily, the x-axis has been normalised in Figure 5.14 (A).

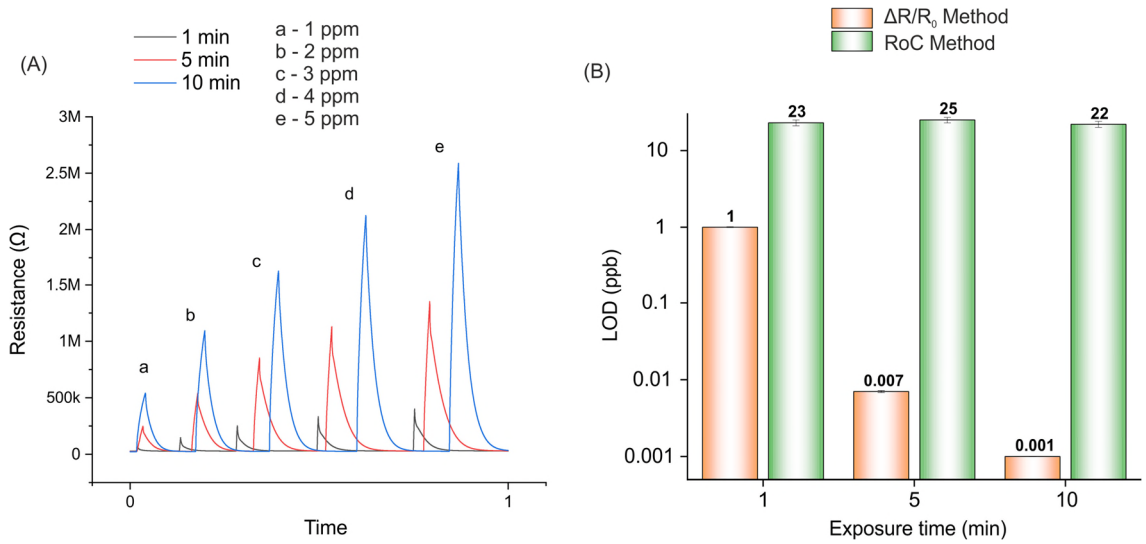


Figure 5.14 *(A) Sensing response curves for 1 min, 5 min and 10 min exposure of an SGX Sensortech MiCS-4514 redox MOS sensor responding to varying concentrations of NO_2 in dry air. (B) Semi-logarithmic bar plot for comparison of the LODs obtained for the $\Delta R/R_0$ analysis method (orange) and the RoC analysis method (green) sensing response curves shown in (A).*

As shown in Figure 5.14, utilising the raw $\Delta R/R_0$ response data to calculate the LOD results in a decreasing limits for increasing analyte exposure times. Because Figure 5.14 (B) is semi-logarithmic, in fact the LOD reduces exponentially with respect to exposure time. After one minute, using the $\Delta R/R_0$ method gives an LOD of 1 ppb, which is already significantly below the manufacturer stated limit of 50 ppb. However, after ten minutes using the same method of analysis results in an LOD of 1 ppt, which is highly inaccurate in comparison to the manufacturer limits provided, and could result in missed detection of material if this limit was expected when transferred to a device operating in the field. Conversely, using the RoC method the LOD remains constant within error, and close to the manufacturer provided lower range, regardless of exposure time.

5.5.2 Analysis of data from conditions simulating field-based acquisition

The work in this section was carried out on a $LiClO_4$-doped PPy percolation sensor on a glass substrate, detailed fully in Chapter 6. Sensing experiments were carried out in the custom built sensing chamber described in Chapter 2. In this case, the analyte of interest was ammonia, and the carrier gas was N_2.

Sensors were mounted in a Micrux IDE holder inside the chamber, and connected to a power supply and multimeter outside the chamber, linked to a PC with Benchvue software. In order to simulate some aspects of real conditions that may affect sensor performance in a real situation, the sensors here were not given a large amount of time to settle before the first exposure of analyte, and consequently the baseline was highly unstable. In addition, the time allowed for sensor exposure to analyte and recovery was varied to simulate a sensor operating in real conditions, where both of these factors are likely to be unknown. Flow rates were also altered for some exposures.

For each series of exposures detailed here, experiments were carried out continuously, allowing the sensor to respond and recover for various times, flow rates and concentrations over the course of the experiment. In the first experiment, the sensor was allowed one hour under 500 sccm of N_2 to eliminate residual air from the system. Then, exposures of 1000 ppb, 800 ppb, 600 ppb, 400 ppb and 200 ppb ammonia were repeated and either the flow rate or the recovery time between exposures was changed. In all cases in the first series of exposures, analyte exposure time was 30 seconds for each response.

The sensing response and parameters for each subset of exposures, divided into colour coded zones in the figure, is shown in Figure 5.15, (A). The corresponding rate if change plot is shown in Figure 5.15 (B). In all cases for the PPy experiments in this chapter, a smoothing protocol of 3-second adjacent averaging was used to clarify peaks. Net peak height before and after this smoothing operation was the same throughout.

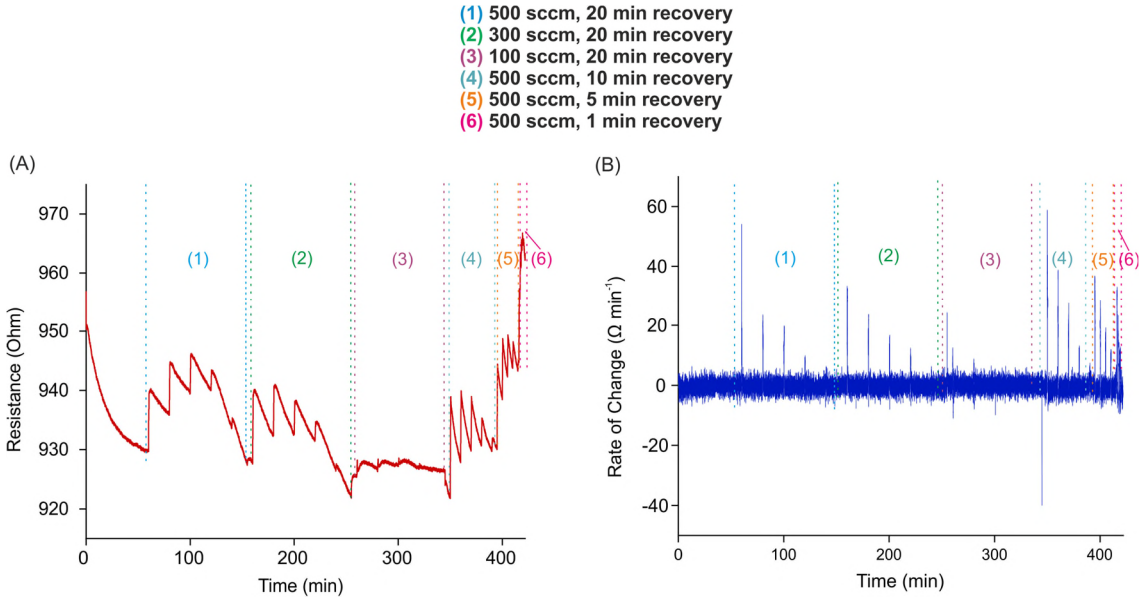


Figure 5.15 *Sensing response curve of a 1kΩ PPy percolation sensor on a glass substrate responding to 30 second exposures to varying concentrations (200 – 1000 ppb) of ammonia in a nitrogen carrier gas. (B). Rate of change plot of the sensing profile shown in (A).*

As reflected in Figure 5.15 (A), in the raw resistance plot the magnitude of the change in baseline prior to any analyte ingress (0 – 60 minutes) is greater than any of the individual response peaks. In addition, the baseline is continuously shifting throughout the experiment dependent on exposure protocol, due to semi-permanent changes as a result of analyte interaction.

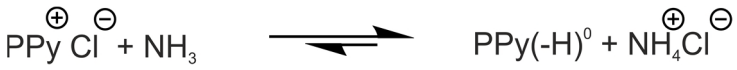
This irreversibility is likely to be a consequence of the manner in which doped PPy sensors interact with ammonia.[158] Doping serves to increase the number of cationic polarons in the PPy, stabilised by anions (Cl^- in this case) associated with the polymer chain which maintain electro-neutrality in the polymer. Holes are therefore the dominant charge carrier in the system making PPy a p-type semiconductor. The electron lone-pair on ammonia can then rapidly interact with these holes via a compensation effect, where ammonia acts as an n-type dopant, decreasing the effect of the initial dopant. Conductivity decreases sharply, giving rise to the fast and reversible initial change

(resistance increase), seen in Figure 5.15 (A). This interaction is highlighted in Equation 5.5.



(5.5)

However, a distinct secondary mechanism of interaction has also been suggested,[159] where a proton transfer occurs between the acidic NH protons in the polymer and ammonia, resulting in a semi-irreversible de-doping of the polymer by stripping out Cl^- ions. Although this process is reversible in the strictest sense, full reversibility relies on the re-doping of the polymer by the product species, which does not occur within the recovery time allowed between exposures in these experiments. This process is shown in Equation 5.6.



(5.6)

The mechanism in 5.6 results in significant baseline shift throughout the experiment. A combination of this and an unsteady baseline to begin with means that the $\Delta R/R_0$ method cannot be used in this instance to assess sensing behaviour and obtain reliable figures of merit.

However, when considering the RoC plot shown in Figure 5.15 (B), it is clear that this method can be used for resolving the analyte interaction, and this data can therefore be reliably used to obtain some figures of merit. Interestingly, for the 30 second exposures here, there are no recovery peaks visible in the RoC data. The only significant recovery peak visible in Figure 5.15 (B) is as a result of a flow rate change from 100 sccm to 500 sccm (at ~ 340 minutes), resulting in a rapid baseline shift.

The mechanism outlined in Equation 5.6 is likely to be responsible for the lack of rapid recovery observed here. This does not necessarily impede the sensor from calibration nor detection, since the RoC peaks are still linear for increasing concentration. However, in a real scenario this behaviour suggest that at an exposure time of 30 seconds, the lifetime over which this sensor can operate accurately is compromised. Whilst ever the sensor does not recover rapidly after exposure, it can be surmised that analyte is not efficiently leaving the sensing surface, or the surface is undergoing permanent changes after being 'overloaded' with analyte. Consequently, the sensor is continuously moving closer to being saturated, and will at some point cease to respond. This is highlighted schematically in Figure 5.16.

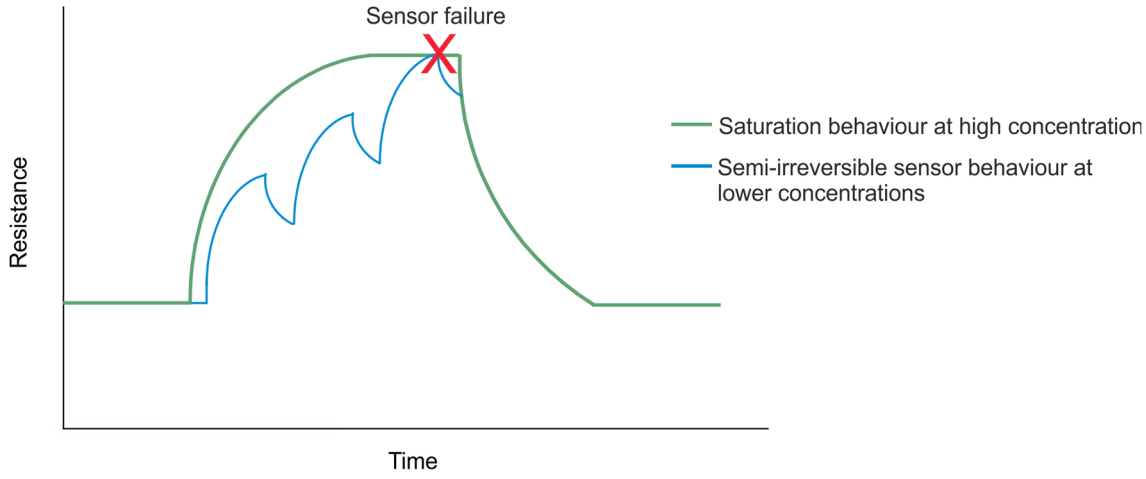


Figure 5.16 *Schematic representation of how a sensor can still respond effectively even if it does not fully recover. However, at some point when saturation is reached, reliable sensing response will diminish rapidly.*

The exact point at which this failure would occur for the sensor in this work is unknown. Attempts to fully saturate this sensor in this set up were unsuccessful, since the highest analyte concentration possible was 10 ppm. In other work involving PPy sensors, saturation has been observed but at concentrations many times higher than used here. For example, Liu et al[160] used a PPy nanofiber sensor and observed saturation behaviour for sensors exposed to ammonia concentrations in excess of 250 ppm.

In this case, because the RoC responses remained linear throughout all exposures, it was still possible to construct calibration curves for all the exposure series' investigated. Figure 5.17 shows the raw resistance responses (red lines) overlaid with the RoC peaks (blue lines) in (A), (C) & (D) and the resultant RoC calibration curves ((B), (D) & (F)) for the exposures of 500 sccm (20 min recovery), 300 sccm (20 min recovery) and 500 sccm (5 min recovery). This corresponds to zones (1), (2) and (5) in Figure 5.15.

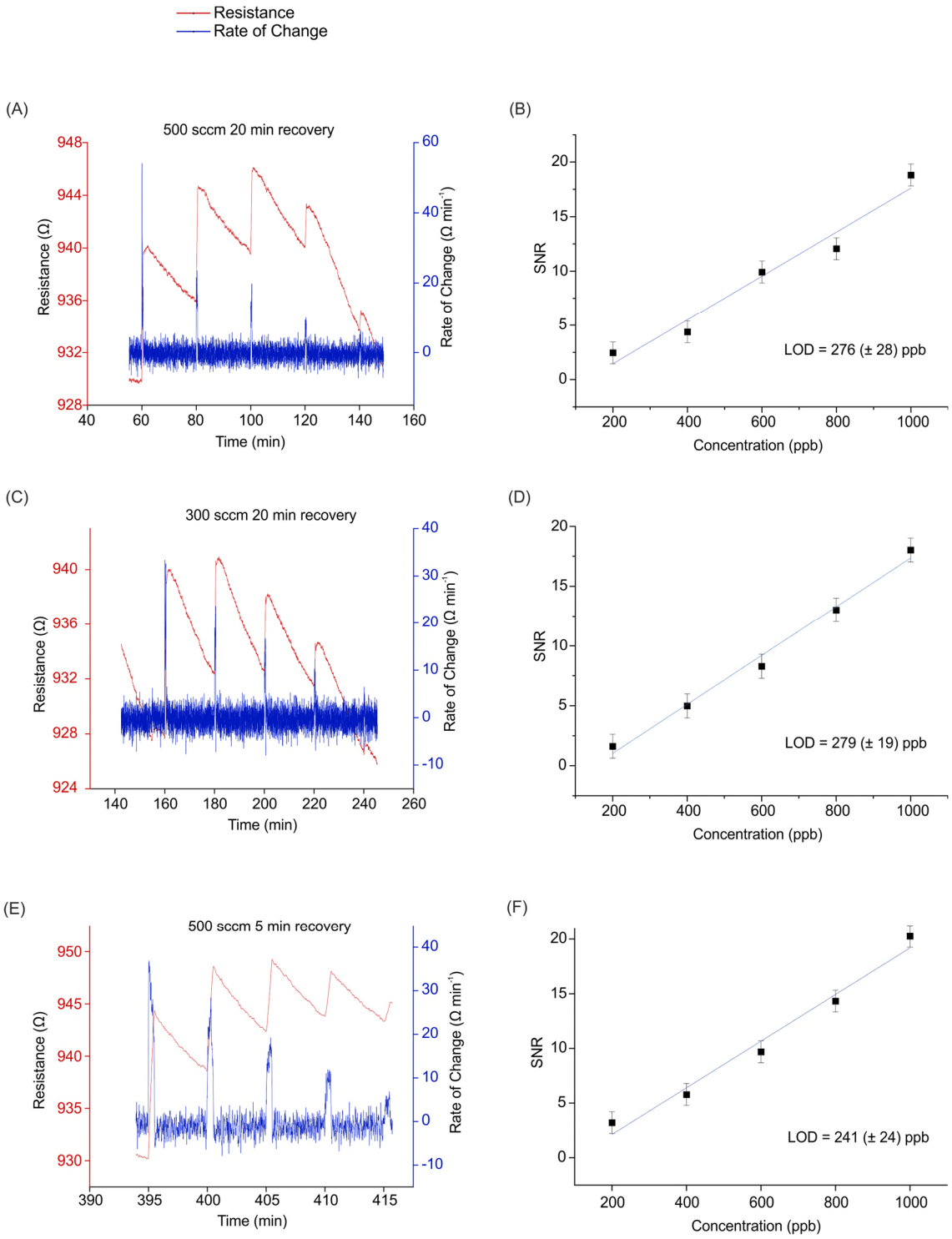


Figure 5.17 *(A), (C) and (E) show the raw resistance response plots (red lines) and RoC plots (blue lines) for a PPy percolation sensor responding to ammonia under a variety of conditions. (B), (D) and (F) show the RoC calibration curves for (A), (C) and (E), and the consequent LODs.*

As reflected in Figure 5.16, using the RoC analysis method results in being able to extract accurate and importantly consistent figures of merit from sensing data which would almost certainly previously have been disregarded as bad data or a bad sensor.

Since the mechanism in Equation 5.5 is rapid, and that in Equation 5.6 appears to occur much more slowly, it was hoped that by reducing exposure time, effects of the secondary mechanism shown in Equation 5.6 could be minimised. This would then allow observation of RoC recovery between exposures and a non-linear recovery calibration curve would help prove that two competing mechanisms were in operation. The exact same parameters were repeated, with the exception that this time exposures were limited to 10 seconds as opposed to the 30 second exposures seen previously (Figure 5.15). The resultant sensing plot and RoC plot are shown in Figure 5.18 (A) and (B) respectively.

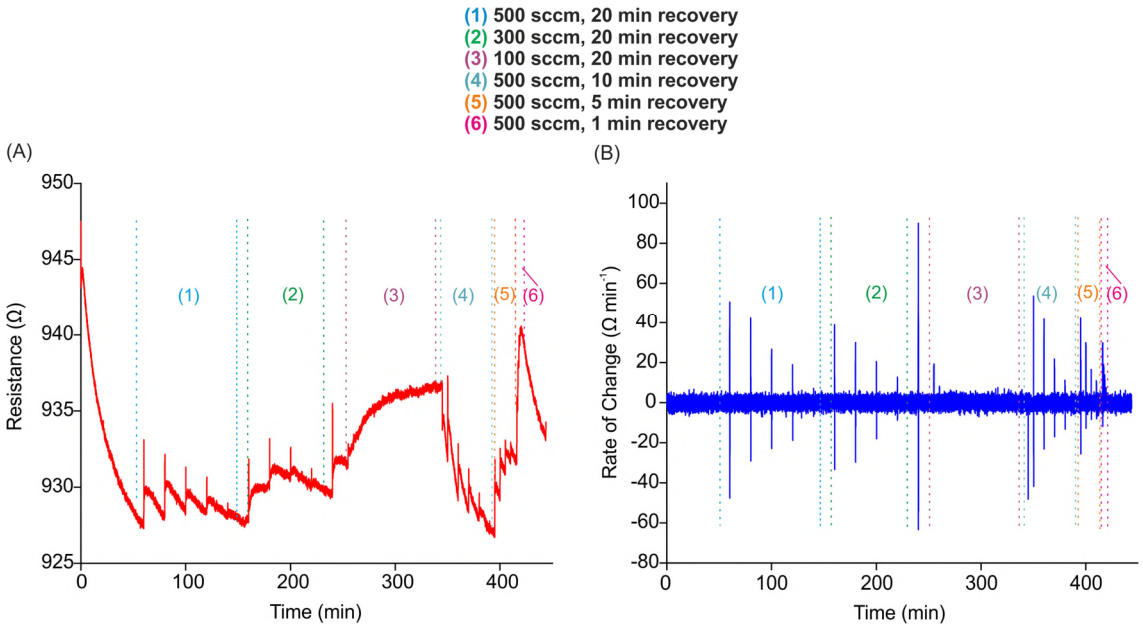


Figure 5.18 *Sensing response curve of a 1kΩ PPy percolation sensor on a glass substrate responding to 10 second exposures to varying concentrations of ammonia in a nitrogen carrier gas. (B). Rate of change plot of the sensing profile shown in (A).*

Now, as reflected in Figure 5.18 (B), with a shorter exposure time of 10 seconds, the sensor does not become overloaded during the exposure, and recovers significantly in all cases with the exception of 100 sccm flow rate, where neither response nor recovery is observed. (zone 3). As a result, calibration curves can now be constructed for both response to obtain figures of merit, and recovery to obtain information about sensor/analyte interaction. RoC calibration curves were constructed for all zones in Figure 5.18. Figure 5.19 (A) shows the RoC response calibration curve, and Figure 5.19 (B) shows the recovery calibration curve, for the 500 sccm 5 minute recovery example in Figure 5.18 (zone 5).

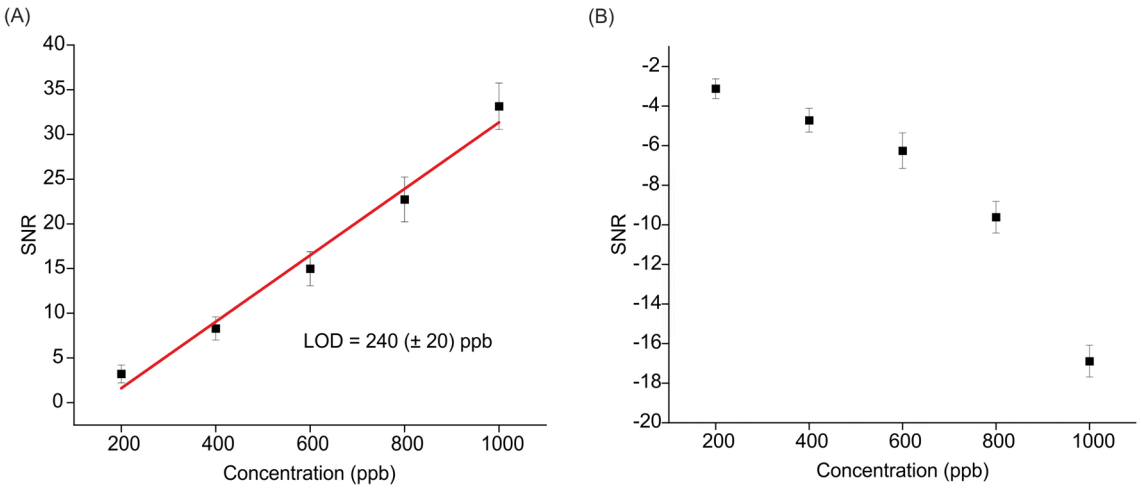


Figure 5.19 *RoC calibration curves for a PPy percolation sensor responding to varying concentrations of ammonia in an N_2 carrier gas. The raw response profile is shown in zone 5 of Figure 5.18. (A) Response calibration curve and subsequent calculated LOD (B) Non-linear recovery calibration curve.*

As shown in Figure 5.19, for the same concentration range but a shorter exposure time (10 seconds), the sensor now both responds and recovers rapidly between exposures. This has dual benefit, since a recovered sensor has both improved LOD and is less likely to stop functioning after numerous repeat exposures. Since a 10 second exposure time is arguably more representative of a real world scenario, this is a promising result for these types of percolation sensors.

Unexpectedly, the SNR is larger (more negative) at higher concentrations, resulting in the arc of the calibration curve being opposite to what may be expected in Figure 5.19 (B). However, in this experiment exposures were carried out starting at 1000 ppb and decreasing to 200 ppb incrementally. It is therefore likely that the mechanism shown in Equation 5.6 that was responsible for no observable recovery after a 30 second exposure is still in effect here, just with much reduced effect because of the reduced exposure time. More experimentation is required, reversing the order of the exposures, to ascertain what effect that may have. What is clear from this data however, is that the recovery in non-linear and thus more than one analyte interaction is occurring at the sensing surface simultaneously.

Because the starting baseline in both Figure 5.15 and Figure 5.19 is higher than any ΔR changes as a result of analyte interaction, and because the change in baseline before analyte ingress is greater than any individual response, utilising the $\Delta R/R_0$ method is highly problematic for this data. However, in the interest of fair comparison this method was attempted. There are two potential methods for obtaining a resistance baseline form this data. The first is to take the baseline from the start of the experiment, and apply it to all subsequent resistance changes, regardless of changes in experimental conditions. Taking the data presented in Figure 5.19, this was attempted. The data was smoothed for 3 seconds as before, and the baseline was taken to be 0 – 10 minutes. σ_{noise} was then calculated:

$$\sigma_{noise} = \frac{\Delta R}{R_o} = \frac{1.9}{941} \times 100 = \mathbf{0.2\ \%}$$

Then, for zone 1 in Figure 5.19 (500 sccm, 20 min recovery between exposures) a $\Delta R/R_0$ calibration curve was plotted for each exposure in zone 1. Because ΔR is lower than the starting baseline, the resulting percentage changes are negative. Nevertheless, the resulting calibration curve has a positive gradient, and so an LOD can still technically be calculated. The calibration curve is shown in Figure 5.20 (A).

The second method for baseline calculation is to take the baseline immediately preceding each set of exposures in each zone. In this example using the data for zone 1, the baseline was taken over three minutes immediately before the 1000 ppb exposure in zone 1 (56 – 59 minutes in Figure 5.19). The resultant calibration curve is shown in Figure 5.20 (B).

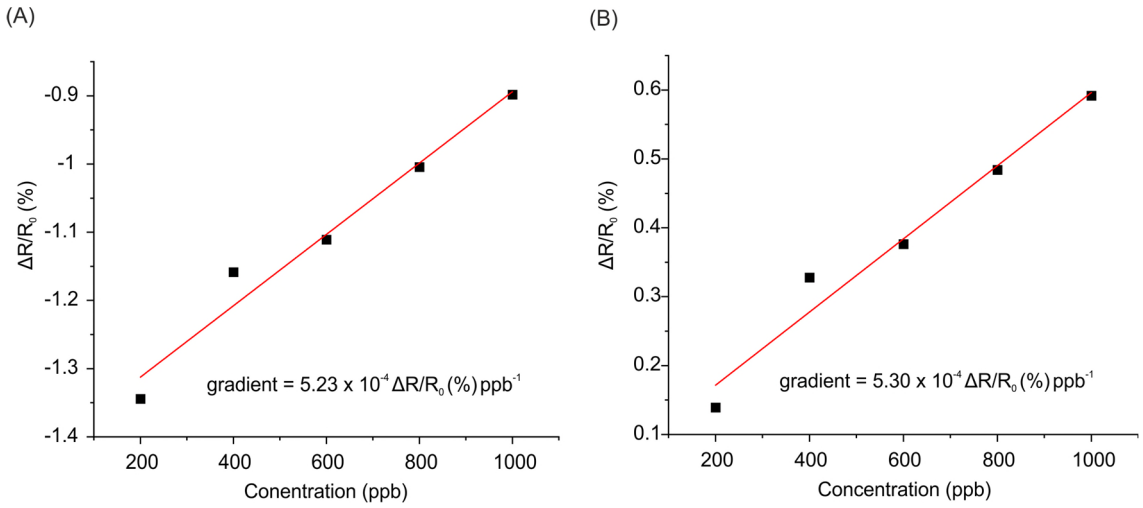


Figure 5.20 *$\Delta R/R_0$ calibration curves for a PPy percolation sensor responding to varying concentrations of ammonia in an N_2 carrier gas. The raw response profile is shown in zone 1 of Figure 5.19. (A) Response calibration curve using the baseline at the start of the experiment (B) Response calibration curve using the baseline at the start of the zone 1 exposure protocol.*

Subsequent LODs using Equation 5.2 and the gradients shown in Figure 5.20 are 1150 ppb for Figure 5.20 (A) and 60 ppb for Figure 5.20 (B), even though the same peaks were used for both, and consequentially the gradients are similar. In the case of Figure 5.20 (A), the LOD calculated is higher than any of the analyte concentrations used during calibration, and in the case of Figure 5.20 (B), the LOD is improbably low when examining the raw data visually. This is because neither of the baselines are satisfactory, and neither are representative of the true behaviour of the sensor. Because of these irregularities, this method was deemed unreliable for this data and not used in the remaining exposures in the experiment.

All of the raw sensing data from both the 30 second exposures (Figure 5.15) and the 10 second exposures (Figure 5.18) was analysed using the RoC method, and the results are summarised in Table 5.1. In all cases, calibration time was calculated as the time difference between the first exposure (1000 ppb) and recovery to the RoC baseline after the final exposure (200 ppb).

Flow Rate (sccm)	Analyte exposure time (s)	Recovery time (min)	LOD (ppb)	Calibration time (min)
500	30	20	280 ± 30	81
300	30	20	280 ± 10	82
500	30	10	260 ± 15	42
500	30	5	260 ± 20	20
500	30	1	320 ± 40	8
500	10	20	200 ± 10	82
300	10	20	200 ± 10	82
500	10	10	250 ± 30	43
500	10	5	240 ± 20	21
500	10	1	260 ± 30	5

Table 5.1 *Comparison of experimental conditions, time allowed for recovery between exposures and figures of merit obtained for a PPy percolation sensor exposed to ammonia gas.*

As shown in Table 5.1, using the RoC method of analysis results in consistent figures of merit being obtained throughout the experiment. Quoted to one significant figure and allowing for error, in nearly all cases the LOD is 300 ppb regardless of operator imposed parameters such as starting baseline, flow rate, exposure time and recovery between exposures. The existence of two distinct mechanisms is further evidenced in this data, since reducing exposure time reduces the time available for the secondary proton exchange mechanism (Equation 5.2) to occur, and LODs improve as a result since the sensor is able to recover more after exposure.

5.6 Summary

The aim of the analysis presented here is to summarise the information contained within a raw resistance change chemiresistive sensing plot into convenient values used to assess sensing performance, namely the sensitivity and detection limits. In addition, translation of any type of analysis method in the wider context of a sensing system that is deployable in the field requires that results obtained in the lab translate directly to results detected in a real environment.

To achieve this, the RoC method accounts for signal values relative not to absolute resistance changes that can be vulnerable to changes owing to external influence, but to the intrinsic behaviour of the sensing material during exposure to and recovery from an analyte of interest. By considering only the rate of change during exposure, baseline fluctuation and inconsistent exposure times are largely eliminated. The sensitivity and LODs obtained are consistent and due to the applicability of this method to many different types of sensing response, can be used to compare any type of chemiresistive sensor, tested under any conditions. It is hoped that in future this analysis can be incorporated into all chemiresistive sensor output evaluation, working in tandem with existing techniques as the sensing community attempts to move towards increasing the breadth of chemiresistive materials available for deployment in real-world sensing applications.

Chapter 6

Conducting polymer percolation sensors

Finding methods to deposit and explore the utility of percolation networks for vapour sensing is the broad aim of the work contained in this thesis. In this, the first fully applied and experimental chapter, that concept is explored on glass substrates.

The chapter begins by introducing the substrate, why it was chosen and how it was altered to facilitate improvements in the percolation networks formed via gold nanoparticle scaffolds. Then, details of the polymer deposition process are provided along with a schematic representation of how percolation networks are formed in this way. Finally, the sensors created will be evaluated in a sensing chamber and a comparison will be made between sensors of the same polymer operating across the percolation region both with and without gold nanoparticle scaffolds. Figure 6.1 shows a schematic representation of the effect of percolation on conductivity in a chemiresistive device.

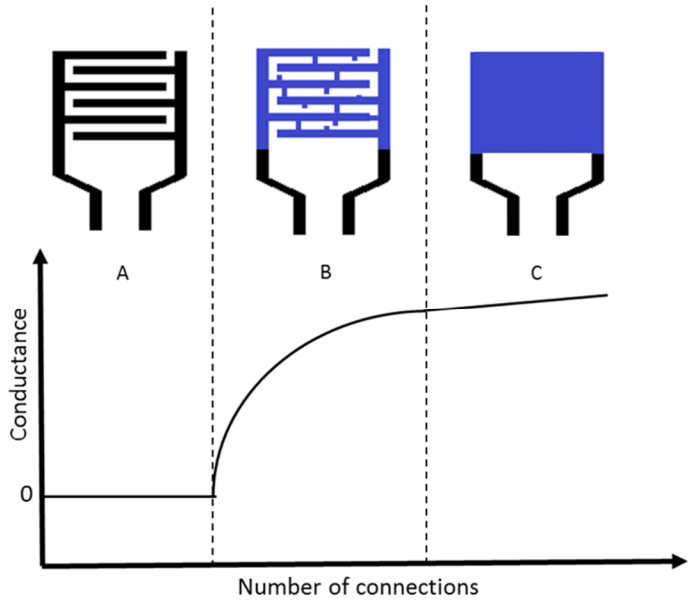


Figure 6.1. *A schematic representation of a conducting polymer network on an IDE and the effect of network formation on the conductance of such a network.*

6.1 Materials and methods

The sensors described in this chapter comprise of the following main components; the substrate and electrodes, the nanoparticle scaffold and the conducting polymer layer. All these components are important for percolation network formation and must be complimentary to each other in order to produce an efficient sensor. This section details each, and why it was chosen.

6.1.1 Platinum IDEs on a glass substrate

As detailed in chapter 4, the most important property of any substrate used for percolation network formation is that it is electrically insulating. In addition, because in this work a gold nanoparticle scaffold was deposited via UHV deposition, the substrate is also required to be able to withstand the high temperature required for that procedure. Finally, the substrate, the gold scaffold and the interface between them must have relative surface energies that result in it being favourable for gold nano-islands to form via dewetting. In this context, dewetting refers to a thin film breaking up during annealing, forming individual gold particles or islands (see section 6.1.2). There are a range of materials that meet these requirements including glass, Al_2O_3, SiO_2 and MgO.[161] Of these possible substrates, the most appropriate for this work was glass. The primary reasons for this are that glass is an insulator, is relatively hardy and IDEs deposited on a glass substrate are readily available with a variety of dimensions from numerous suppliers, at relatively low cost.

The electrode material used in this chapter was platinum. Platinum was chosen because it has a higher melting point than gold, and so was suitable for UHV deposition and annealing of the gold nano-islands without any deformation or degeneration of the electrodes. The gap size between electrodes was 5 μm, and each finger of the IDE was 5 μm in width, with 180 fingers in total. Prior to this work, the Castell research group carried out a great deal of investigation into these IDE parameters, and this was found

to be the best arrangement for percolation network formation.[162] Images of the Micrux IDEs used in this study are shown in Figure 6.2.

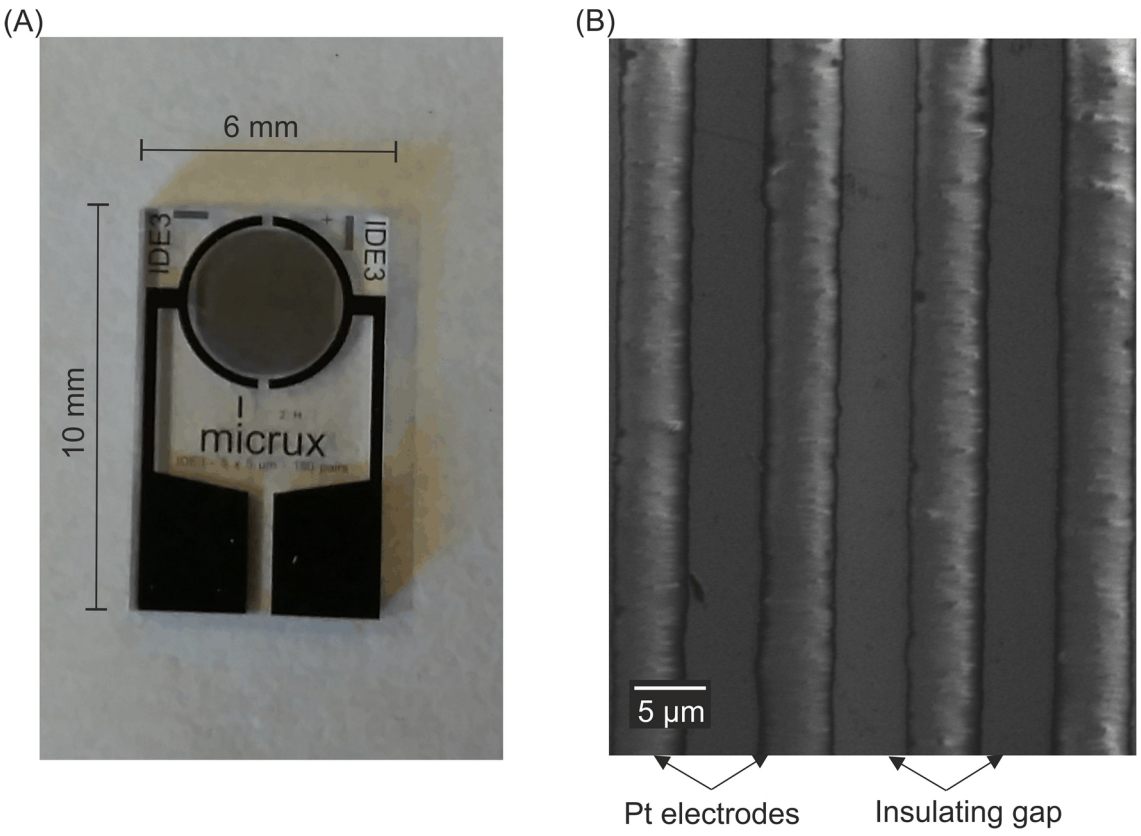


***Figure 6.2**. (A) A photograph of a Micrux IDE with 5 µm Pt electrodes separated by 5 µm gaps. (B) An SEM image of the same type of IDE, showing a close up of the electrodes and gaps.*

6.1.2 Gold nanoparticle scaffold

The 5 µm gap size for Pt IDEs on a glass substrate shown in the previous section is the smallest commercially available IDE configuration. However, in order to promote percolation in a polymer network, it is reasonable to assume that a smaller gap size will be beneficial, since more bridging sites, or nodes, results in more connective pathways whilst still maintaining control over the total number of bridging clusters overall. One way to reduce the gap size is to form a supported network of conductive nanoparticles

between electrodes. These nanoparticles then act as nodes between the electrodes, promoting shorter bridges of polymer to form between them.

For this work, the material chosen for nanoparticle scaffold formation is required to be inert in relation to any sensing analytes targeted by the completed sensor, and must be able to be deposited via UHV and dewet readily on the glass substrate to form the desired nanostructure. Gold fits all of these parameters, and so was chosen here. One of the most effective ways to achieve a scaffold of nanoparticles in this way is via annealing a thermally evaporated thin film of gold *in situ* in a UHV chamber, which results in dewetting to form a sub-monolayer of gold. This method was perfected by the Castell research group.[163] and the same techniques were applied to this work.

First, an IDE was mounted and placed in the UHV chamber operating at 10^{-6} – 10^{-7} Pa before gold was evaporated from a K-Cell (see chapter 2). After deposition, annealing was achieved by ramping the temperature of an indirect heating holder to the desired temperature, then maintaining that temperature for the required amount of time. Generally, thicker films require higher temperature and/or longer anneal times for dewetting to occur.[163] In this work, the thin film depth before annealing was 5 nm, and anneal temperatures were varied for a fixed duration of two hours to assess the effect on particle size and separation. The results are detailed in chapter 6.2

6.1.3 Conductive polymer deposition

The active and final component of the sensors described in this chapter is the polymer PPy. PPy was deposited *in-situ* from a Py monomer electrolyte solution. PPy was selected because it has good conductivity, is well studied and so has a known electropolymerisation potential,[12] and is known to chemically interact with electron rich analytes including ammonia.

All samples in this chapter were deposited using CA electrochemistry, and doped for 60 seconds in a $LiClO_4$ / acetonitrile electrolyte solution as described in chapter 2.

Resistance measurements were obtained after doping. Sensing experiments were all carried out in the sensing chamber detailed in chapter 2.4, with ammonia as the analyte of interest. The results are shown in chapter 6.3.

6.2 Gold nanoparticle size and separation

The ability to control particle size and separation of the gold nanoparticle scaffolds described in this chapter is an important step in sensor manufacture. Individual particles need to be consistent in terms of both size and distance from their nearest neighbour to ensure that the polymer layers deposited to connect them are consistent and predictable for reproducibility. Furthermore, separation must be uniform across the substrate so that prior to polymer deposition, the substrate is still an insulator.

Prior work in the Castell research group focussed on the influence of annealing time and temperature in relation to thin film thickness[163] and ascertained that for sensing applications the optimum gold film thickness prior to annealing was 5 nm. In this work, that study was built upon by investigating the effect of anneal temperature on the nanoparticle scaffold achieved from a 5 nm thin film. To achieve this, 5 nm gold thin films were deposited on IDEs consisting of glass substrates and 5 μm Pt electrodes described previously. Then samples were annealed for 2 hours at a range of temperatures from 100 – 350 °C. The resultant SEM images for anneal temperatures of 100 °C, 200 °C and 350 °C are shown in Figure 6.3 (A) – (C) respectively.

The images were then analysed using ImageJ software by inverting the image and converting to greyscale in order to define each particle boundary. The resultant treated images are shown in Figure 6.3 (D) – (F) Then, using an inbuilt function of the software it was possible to obtain particle size distribution, the histograms for which are shown in Figure 6.3 (G) – (I).

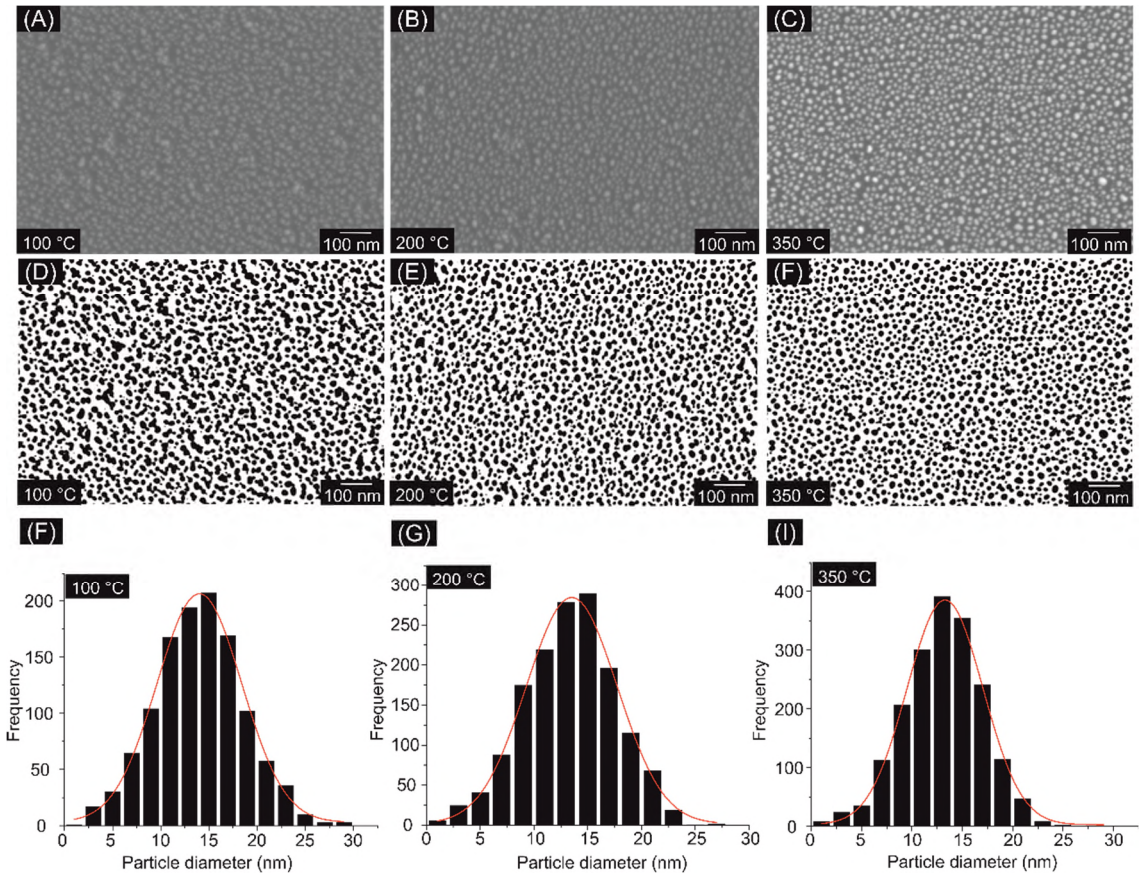


Figure 6.3. The particle size distribution for a 5 nm thin film of gold deposited on a glass substrate and annealed at various temperatures for 2 hours. (A) – (C) SEM images of a 100 °C, 200 °C and 350 °C anneal respectively. (D) – (E) ImageJ treated images, where the corresponding images in (A) – (C) have been inverted and converted to greyscale. (F) – (G) Particle size distribution histograms and Gaussian fits calculated from the images in (D) – (E) for a 100 °C, 200 °C and 350 °C anneal

As reflected in Figure 6.3, as anneal temperatures increase, particle size distribution narrows significantly, number of particles in a given area increase accordingly and uniformity of particles improves. The full width at half maximum (FWHM) for the Gaussian fit of Figure 6.3 (F) is 10.4, whereas at 350 °C it has narrowed by almost 20 % to 8.8 (Figure 6.3 (I)). The smaller FWHM at higher anneal temperatures indicates a narrower spread of particle diameters around the modal value, which is 15 nm particle

diameter at a 100 °C anneal against a modal value of 13 nm for a 350 °C anneal. Furthermore, the density of particles in Figure 6.3 (F) is 110 per μm against 70 per μm in Figure 6.3 (D), an increase of almost 40 % in number of nodes for the same area of substrate.

It is also beneficial, in the context of percolation network formation, to know the inter-particle distance (IPD) between each gold node. Using the image in Figure 6.3 (D - F), it is possible to calculate these values based on analysing the white space between particle boundaries to obtain an average. In this case that IPD was 8 (±2) nm for a 100°C anneal (Figure 6.3 D) against 12 (± 2) nm for a 300 °C anneal (Figure 6.3 (F)).

However, one drawback of utilising this method to create a nanoparticle scaffold is the time required to carry out the procedure. Because the temperature of the anneal is ramped slowly to the required value, any increase in anneal temperature increases the time taken to conduct the procedure significantly. In the UHV chamber used for this work, only one sample can be prepared this way at any one time. This can become problematic if numerous samples are required for sensor preparation. For that reason, a compromise was used in the samples prepared for sensing. In all cases in this chapter, an anneal temperature of 200 °C for 2 hours was used. This provides a good particle distribution (~14 nm) and IPD (~ 9 (± 3) nm), whilst ensuring that the IDE remains insulating after gold deposition and preparation time for each sample remains reasonable.

6.3 Conducting polymer percolation networks

There are numerous techniques for depositing CPs on a substrate, including drop-casting, spin-coating, evaporation and electrochemistry. However, in order to achieve a polymer architecture that displays percolation behaviour, it is most often the case that polymer layers are required that have not yet developed into a thin film. This serves to eliminate the majority of deposition techniques, with the exception of electrochemistry. In this section, percolation in relation to chemiresistors is explained, and details are

provided of how the percolation sensors in this chapter were produced using dynamic electrochemistry.

6.3.1 Percolation theory applied to chemiresistors

CP chemiresistors are usually created as thin film devices,[164–166] but in this work percolation theory has been exploited, specifically targeting a percolation network of polymers to improve the sensitivity. This increased sensitivity is achieved because when an analyte interacts with any part of the polymer chain the conductivity of the whole conducting pathway is disrupted. An electrical percolation network is a lattice of randomly distributed conducting and insulating regions. If there are very few conducting regions then no charge can flow through the network because there will be no spanning cluster, here represented by a continuous conducting pathway, from one side of the network to the other. As the proportion of conducting elements is increased, the probability increases that a conducting pathway is formed until p_c is reached, the point at which the first spanning cluster is formed. Beyond p_c, adding more pathways results in increasing conductivity until parity is reached with thin film levels of conductivity. This behaviour is highlighted in Figure 6.4 (A). A wide variety of experiments have been carried out, and theoretical studies performed, to understand the behaviour of the electrical conductivity of 2D percolation networks.[167,168] What all the models and experiments have in common is that the conductivity of the networks changes most rapidly just beyond the percolation threshold, as shown schematically in Figure 6.4 (B) (the derivative of Figure 6.4 (A)).

The shape of the percolation curve in Figure 6.4 (A) depends on many factors, but the threshold onset in conductivity followed by a rapid increase is common to all these curves. The idea that is central to this chapter is to create a conducting polymer percolation network that takes advantage of this region of high sensitivity. Although Figure 6.4 (B) shows that the sensitivity is greatest at the percolation threshold, it must

be taken into account the degree to which this sensitivity can be exploited within a device setting. For this it is necessary to consider the effect of electrical noise; a device with high sensitivity may be of little use if the signal to noise ratio (SNR) is too low. As an estimate of the noise level we use the RMS of the signal level. The sensitivity (Figure 6.4 (B)) multiplied by the SNR is shown in Figure 6.4 (C) and demonstrates that the most useful region for device applications is slightly beyond the percolation threshold. This is the region of the percolation curve that we intend to exploit for optimal sensor performance.

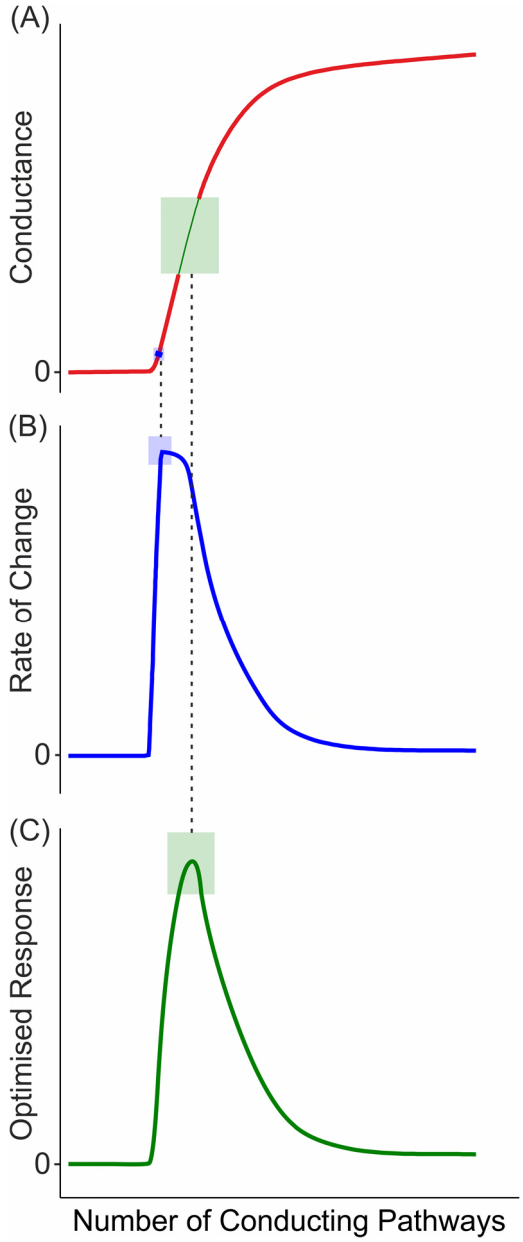


***Figure 6.4**. Conceptual graphs for a percolation network showing the relationship between electrical property and the number of conducting elements. In (A) the conductance of the network is initially zero until the percolation threshold is reached (small purple box), after which the conductance increases rapidly. As many connections are formed the increase is no longer as steep. The graph in (B) is the gradient of the graph in (A) and shows that the rate of change, or equivalently the sensitivity, is greatest at the percolation threshold. The graph in (C) is the graph in (B) multiplied by the root of the conductance, and provides a measure of the optimal sensor response, as indicated by green boxes in (A) and (C).*

6.3.2 Dynamic electrochemical polymer networks

Dynamic electrochemistry is a well-known and well researched method for CP deposition.[169,170] Because this type of deposition results in polymer growth from an electrolyte solution *in-situ,* scalability is amenable, growth is controllable and contact resistance between polymer and electrodes is reduced in comparison to most casting and coating methods. Of the two main potentiostatic techniques discussed in chapter 4.3.2, CA was the favoured method for polymer deposition in this work, primarily because it allows polymer deposition to be controlled as a function of time, where longer CA times result in more polymer growth.[12]

A schematic diagram of the growth process between two IDE fingers is shown in Figure 6.5, where panel 1 is the pristine IDE, panel 2 shows nucleation of the CP beginning from the electrode, and panels 3 & 4 show the advancing front of the polymer film across the insulating substrate. In panel 5 the CP strands meet and this is equivalent to the percolation threshold shown in Figure 6.4. If growth is allowed to proceed then a thin film will result, as shown in panel 6.

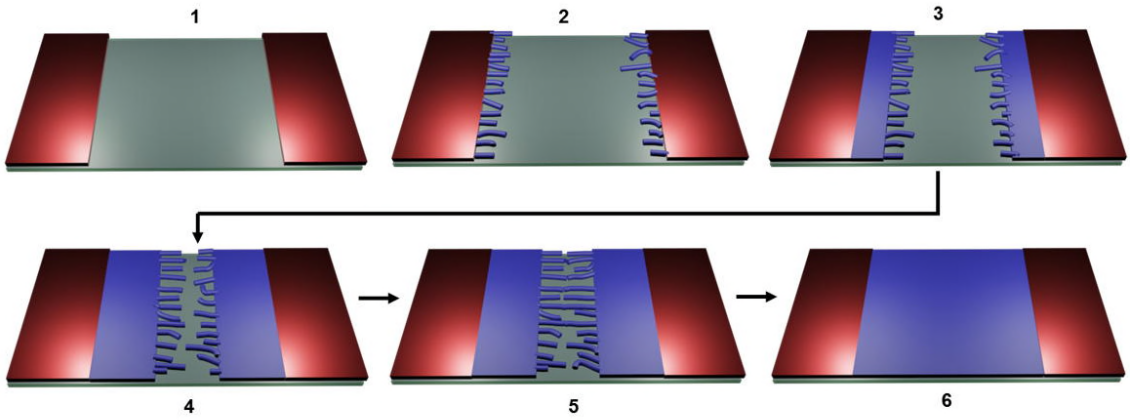


Figure 6.5*. Schematic diagrams of the stages of electrochemical growth of a conducting polymer from the monomer solution. The electrodes are shown in red, and the insulating glass substrate is in grey. The polymer (purple) growth fronts steadily advance towards each other. A few strands meet in panel 5 at the percolation threshold.*

Although a PPy percolation device can be created with the method shown in Figure 6.6, the architecture is not optimal because the growth front of the thin CP film envelops part of the network of the individual polymer strands. To overcome this problem, and create a CP network across the entire IDE gaps we make use of the dispersed Au nanoparticles on the glass substrate detailed in chapter 6.2.

The nanoparticles, which are typically around 13 - 15 nm in diameter act as fresh nucleation centres during the electrochemical polymerisation process, allowing conducting pathways to form more rapidly than without the particles. A schematic illustration of the polymer growth process is shown in Figure 6.6. Panel 1 shows the Au nanoparticles interspersed on the insulating glass substrate between the electrodes. In panel 2 electrochemical growth of the CP nucleates initially on the IDEs, but once an Au nanoparticle has been electrically connected to the electrode it can act as a new nucleation site. In panel 3 an electrical connection has been established between the IDEs, corresponding to the percolation threshold, and in panel 4 the percolation network has expanded. Panel 5 shows the situation where all the Au nanoparticles are connected. If electrochemical growth is continued for an extended period then a thin film will form, burying the nanoparticles (Panel 6).

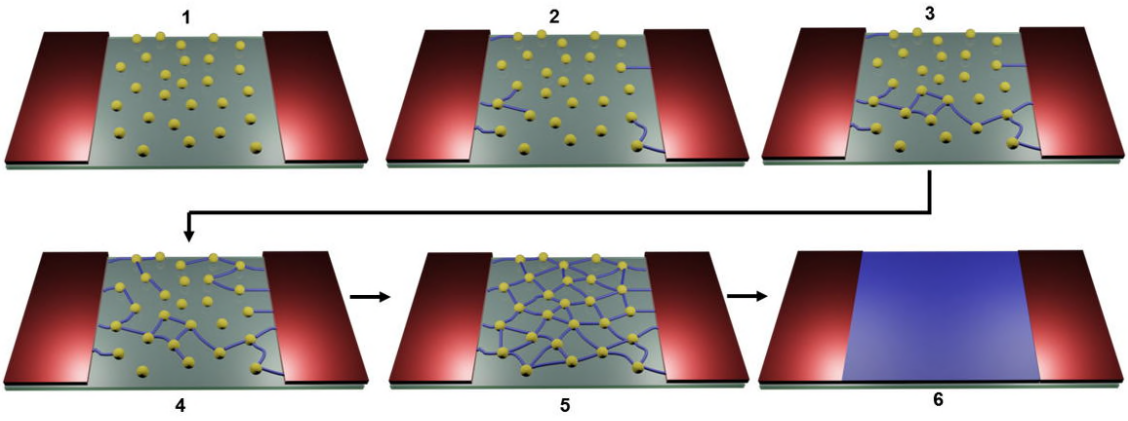


***Figure 6.6**. Schematic diagrams of the electrochemical growth of a conducting polymer from the monomer solution. The electrodes are shown in red, and the insulating glass substrate is in grey. The gold nanoparticles (yellow) act as nucleation centres, and enable a conductive network to be generated more rapidly, and over a larger area than in Figure 6.6. The percolation threshold has been reached in panel 3.*

To create the CP networks illustrated in Figures 6.5 & 6.6, CA polymer growth was carried out for transient times between 5 s and 70 s, followed by p-type doping, for plain electrodes and electrodes decorated with gold nanoparticles. Electrical conductance was determined by applying a DC potential of 1V between the IDEs and measuring the current. The results are shown in Figure 6.7. For the plain electrodes (Figure 6.7, red circles) it can be seen that there is no appreciable increase in conductivity until 40 s, which is equivalent to the beginning of the percolation region in Figure 6.5 (panel 5). As more CP is grown, so the conductivity between the electrodes increases until a continuous thin film is created. Conversely, for the nanoparticle-decorated electrodes (Figure 6.7, blue squares) a jump in conductivity already occurs at 15 s, corresponding to panel 3 in Figure 6.6, and there is a further significant increase at 20 s. Beyond 20 s there is no appreciable increase in conductivity, presumably because once all the nanoparticles have been electrically connected a thick film of CP is required for any further substantial impact.

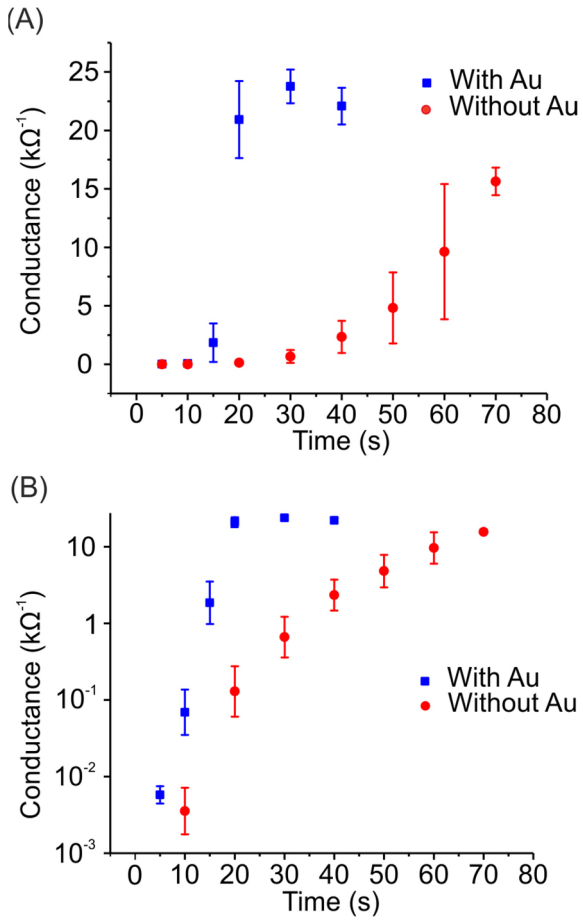


***Figure 6.7**. Conductance as a function of chronoamperometric transient time for plain electrodes (red circles) and electrodes decorated with gold nanoparticles (blue squares). The error bars are obtained from the standard deviation of the conductance values of measurements from three separate samples. The same data is shown in (A) linear and (B) semi-logarithmic plots.*

Acquiring SEM images of the PPy networks after deposition has proven to be extremely difficult. The reason for this is that the accelerating voltage of the SEM, regardless of adjustments, always proved to be destructive towards the polymer layer. However, PEDOT is more stable and so has proven more resistant to these destructive effects, and SEM images of a PEDOT network were successfully obtained. Figure 6.8 shows a comparison between SEM images, taken at the same accelerating voltage (3 keV), for (A) PEDOT and (B) PPy.

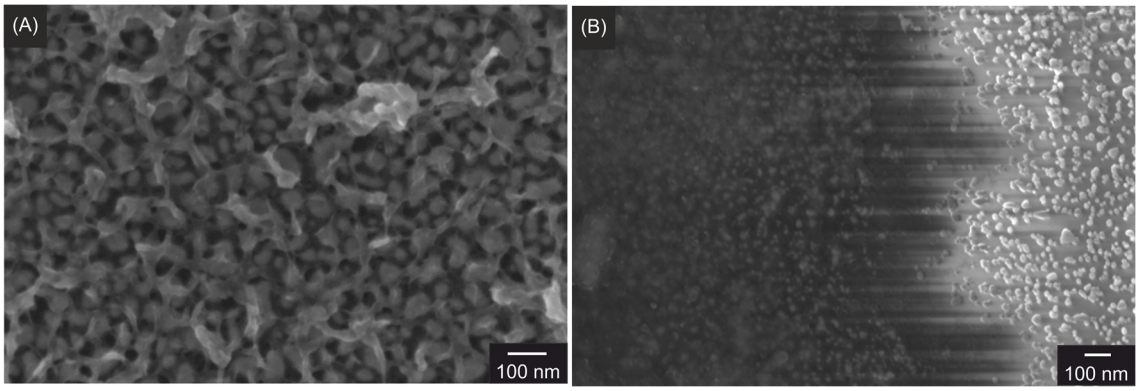


***Figure 6.8**. Scanning electron microscope micrographs of conducting polymers deposited on a gold nanoparticle scaffold arranged between 5 µm Pt IDES on a glass substrate. (A) PEDOT taken at a 3 keV accelerating voltage. (B) PPy taken at a 3 keV accelerating voltage.*

As shown in Figure 6.8, for the PEDOT percolation network in Figure 6.8 (A), connecting bridges are clearly defined between gold nanoparticles. For the PPy percolation network PPy (Figure 6.8 (B)), bridges are not defined and the image quality is lower as the polymer is being destroyed under the accelerating voltage of the microscope as the image is being taken. However, it is possible to take advantage of the charging effect in Figure 6.8 (B) to observe the advancement of the polymer front across the insulating gap between electrodes. The darker area to the left of the image shows a region where conductivity is present, and so polymer has been deposited. On the right, the area is still insulating and so displays charging from the electron beam of the SEM. The frontier between darker and brighter parts of the image corresponds to the polymer front.

6.4 Percolation sensing

Having created the PPy percolation networks with various degrees of connectivity described in the previous section, they were then tested for their performance in a custom-built gas sensing chamber (see chapter 2). Ammonia was the target analyte because it is a strong electron donor in its interaction with p-doped PPy and causes a

dramatic reduction in the polymer conductivity due to the loss of hole charge carriers.[171] Furthermore, ammonia is a target analyte in the presence of many HMEs and IEDs, especially those constructed from ammonium nitrate fertilizers including ANFO.

Typical sensing responses from 700 parts per billion (ppb) to 100 ppb are shown in Figure 6.9 for a 5.5 kΩ network with Au particle-decorated electrodes (Figure 6.9 (A)), and a 20.9 kΩ network with plain electrodes (Figure 6.9 (B)). The effect of 100 ppb ammonia exposure can easily been seen in both the response curves. Numerous sensors were created with a broad range of electrical resistances and these were evaluated using a testing protocol of 5 minutes of ammonia exposure in a dry nitrogen carrier gas, followed by dry nitrogen exposure until the sensor baseline was restored, which was typically in less than 30 minutes, but was shorter for low concentrations of ammonia. Flow rates were fixed at 500 sccm throughout

The sensing response curves in Figure 6.9 (A) & (B) are typical shark fin shaped responses, indicative of the fact that sensor saturation was not achieved in the chosen flow rate and exposure time of 5 minutes. As a result, utilising a $\Delta R/R_0$ type of analysis in this case would be unsatisfactory for evaluating sensing performance. Instead, the sensors were analysed using the RoC analysis detailed in chapter 5. The gradients of the sensing response curves in Figure 6.9 (A) & (B) are shown in (C) & (D) respectively.

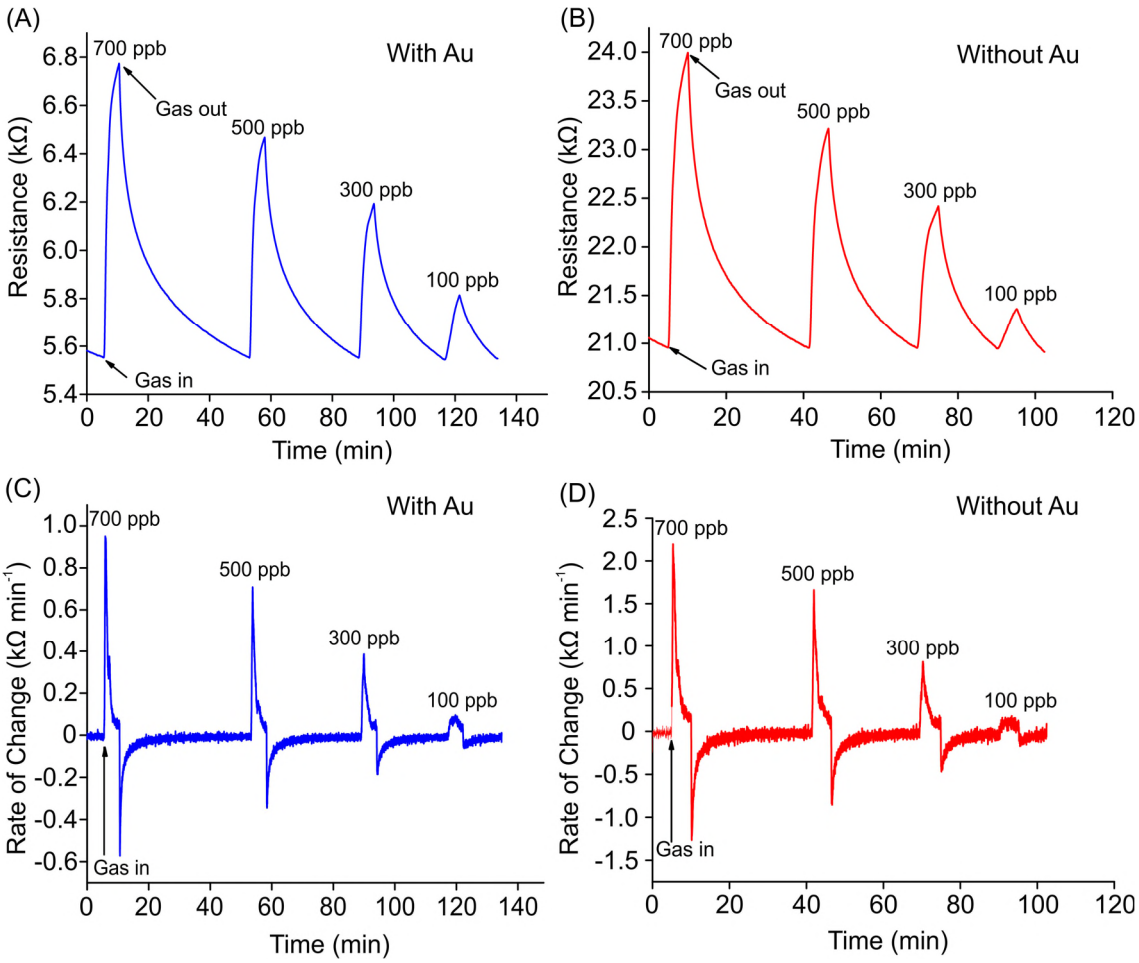


***Figure 6.9**. Chemiresistive responses of doped PPy percolation networks to ammonia in a dry nitrogen carrier gas. In (A) a gold-decorated electrode is used with a starting resistance of 5.5 kΩ, and in (B) a plain electrode is used with a starting resistance of 20.9 kΩ. The gradients of the curves in (A) & (B) are shown in (C) & (D), respectively.*

The peaks of the spikes in Figure 6.9 (C) & (D) correspond to the greatest rates of change (detailed in Chapter 5), and so the point at which the sensor is responding fastest to the analyte. It is these peaks that can be unambiguously associated with sensor performance, as they do not depend on the duration of analyte exposure. Each sensor with a different level of network connectivity will have a different maximum rate of change response, with the networks at the percolation threshold showing the greatest sensitivity (Figure 6.4 (B)). However the percolation threshold networks will also suffer from the greatest noise levels. Ultimately, we are interested in optimising the SNR of the sensor

(Figure 6.4 (C)). So rather than plotting the spike heights in Figure 6.9 (C) & (D), we divide these heights by the root mean square of the noise measured for the individual sensors. These results are shown in Figure 6.10 as a function of analyte concentration.

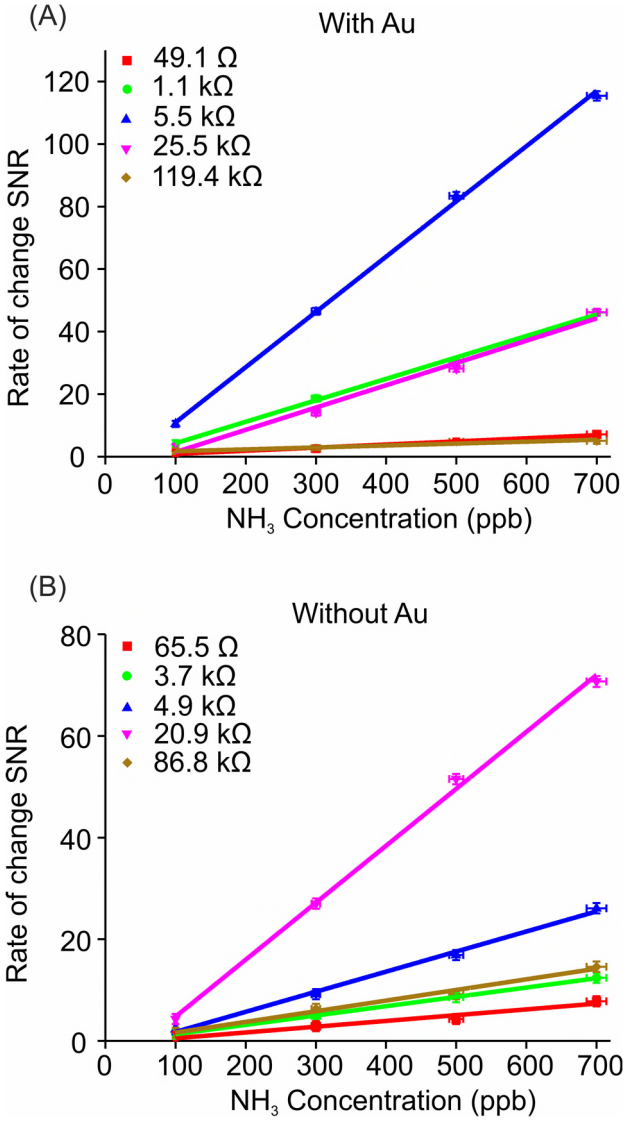


***Figure 6.10**. Rate of change of the signal to noise ratio responses to different concentrations of ammonia of percolation networks with different levels of connectivity for (B) electrodes with gold nanoparticles and (B) for plain electrodes.*

Figure 6.10 (A) shows that the sensor with the steepest gradient, and hence the optimum performance, is the 5.5 kΩ network. For lower network connectivity the 25.5 kΩ and 119.4 kΩ sensors have higher sensitivity, but greater noise levels. Conversely, the

networks with greater connectivity (1.1 kΩ and 49.1 Ω) have lower noise levels, but also lower sensitivities. The 49.1 Ω sensor is in effect operating at maximum connectivity, is not a percolation network, and can be thought of as a thin film device. Data from the chemiresistive percolation sensors with plain electrodes is shown in Figure 6.10 (B), which also shows that the optimum sensor with the highest SNR response lies in a region of the percolation curve that is a little beyond the percolation threshold (green box in Figure 6.4 (A)).

The LODs can be calculated straightforwardly from the linear fits in Figure 6.10 and are defined as the point where the signal is a factor of 3 greater than the noise. The LOD for each sensor is plotted against resistance in Figure 6.11. This figure shows that a more effective percolation device is created when using an Au nanoparticle scaffold (minimum LOD of 18 ± 2 ppb in Figure 6.11, red curve) than without (minimum LOD of 27 ± 5 ppb in Figure 6.11, blue curve).

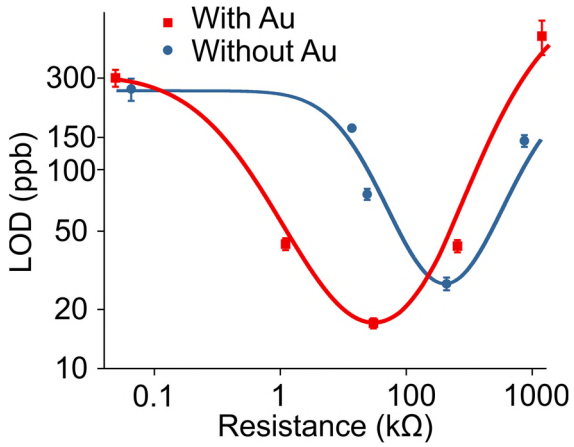


***Figure 6.11**. Limit of detection (LOD) for ammonia gas versus PPy percolation network resistance for nanoparticle-decorated electrodes (red squares) and plain electrodes (blue circles). The red and blue curves are drawn as a guide to the eye in the logarithmic plot. A lower LOD can be achieved by using gold nanoparticle-decorated electrodes.*

6.5 Summary

The results in this chapter demonstrate that doped PPy percolation networks can be electrochemically grown between interdigitated electrodes on glass substrates, and that these networks can be used for high sensitivity ammonia sensing. The strategy of pre-patterning the glass with Au nanoparticles improves the sensitivity and reduces the LOD, presumably because the nanoparticles act as fresh nucleation centres, increasing the ability of the network to spread. The result is that there is more surface area of the active conductive layer available for analyte interaction, whilst maintaining the same overall conductivity and percolative behaviour across the network as a whole. The performance of the sensors in this chapter compares favourably in terms of figures of merit with the majority of PPy sensors produced in the literature (see Chapter 7.4.2, Table 7.1). The ideal level of network connectivity for high sensitivity gas sensing is just beyond the percolation threshold where the SNR is optimised. In this region the LOD of 18 ± 2 ppb is better by a factor of 20 compared with thin film devices made with the same CP.

Sensitivity to ammonia has been demonstrated in the low ppb range, but any electron donating molecule would elicit a similar response. Magnitude of response is likely to differ between analytes, offering some differentiation between them from this single sensor type. However, there is still a need to identify a method to further increase molecular selectivity. The most likely way that this will be achieved is via an e-nose consisting of multiple percolation sensors made from different CPs and other chemiresistive materials that have different functionality that would preferentially bind specific molecular species.[172,173] Such a device with multiple sensors would use pattern recognition to distinguish different analytes. Effects due to changes in ambient temperature and humidity would also need to be taken into account. In a device that utilises CPs this is most likely to be achieved by inclusion of a pre-treatment step that regulates flow rate, humidity and temperature simultaneously.

Percolation is not limited to CPs. If deposition techniques can be refined sufficiently to be able to create a percolation network, this principle could be applied to any chemiresistive material. Apart from investigating a wider range of materials that can be used as chemiresistive percolation networks, exploring a variety of flexible substrate materials will broaden the potential for integration of the sensors into wearable or flexible devices.

Chapter 7

Flexible substrates for increased utility

The glass substrates used in the last chapter were selected primarily because they were amenable to gold nanoparticle scaffold deposition. However, as demonstrated in that chapter it is possible to electrochemically deposit a percolation network without a supported nanoparticle scaffold. One drawback of using rigid substrates such as glass is that they are not ideal for incorporation into wearable technology, where substrate flexibility increases potential use dramatically.

In this chapter, the concept of percolation sensing is expanded onto flexible substrates. The chapter begins by introducing the materials and methods employed to create flexible percolation sensors. Next, the benefits of employing percolation theory to flexible sensors is introduced, and the deposition of polymers operating in the percolation region is described. Finally, sensors are investigated for their gas sensing capability, and a comparison is drawn between flexible percolation sensors and flexible thin film sensors of the same polymer. Figure 7.1 shows a photograph of one of the sensors investigated in this chapter under manual bending stress after polymer deposition.

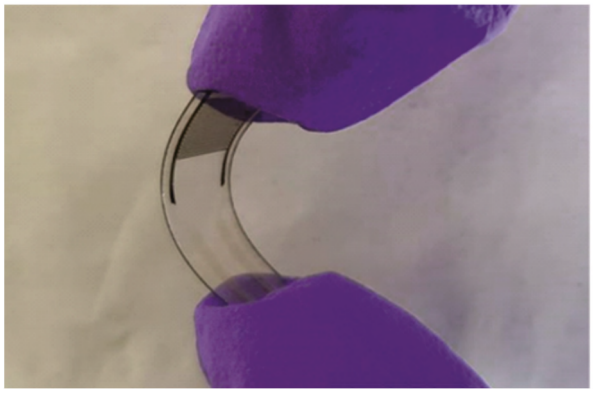


***Figure 7.1**. A flexible IDE under bending stress.*

7.1 Materials and methods

The sensors investigated in this chapter were structurally simpler than those in the previous chapter, consisting of only two main components; the IDE and the CP layer deposited on it. In this case, the IDEs were commercially available from DropSens (Spain), and consisted of an insulating polyethylene tetraphthalate (PET) substrate with gold electrodes, separated by a gap size of 100 µm. Overall, IDE dimensions were 22.8 mm x 7 mm. An image of a pristine IDE as purchased is shown in Figure 7.2.

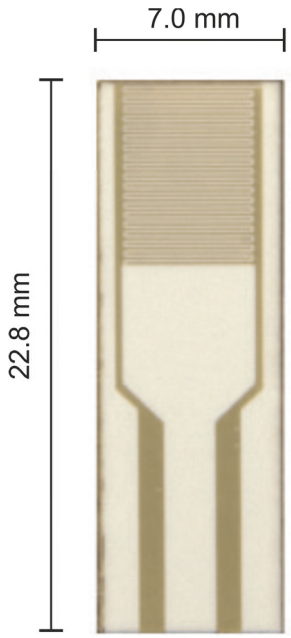


***Figure 7.2**. The dimensions of a pristine IDE, consisting of gold electrodes on a flexible PET insulating substrate sourced from DropSens (Spain).*

The polymer deposition protocol used in this chapter was identical to that used on the rigid substrates of the last chapter (see section 6.1.3). In this case, owing to the vulnerability of PET to degradation in many organic solvents, IDEs were used as purchased with no pre-treatment. The custom built sensing chamber (chapter 2) was used for sensor testing in all cases.

7.2 Conducting polymer percolation networks on flexible substrates

One area of significant potential for chemiresistive sensing devices is incorporation into flexible and wearable technology.[174,175] A structure's resistance to bending scales proportionally with cross-sectional area.[176] A thin film therefore has an inherent level of flexibility, and some reports have emerged of chemiresistive thin films being deposited on flexible substrates.[177,178] However, in many cases repeated flex cycles result in degradation of the sensing layer, since this can cause films to break down and separate from the substrate. Degradation after relatively few flex cycles reduces sensing performance significantly.[179] One approach to avoid this issue is to incorporate additional materials into the sensing layer during manufacture that are can help stabilise the thin film during bending. However, this increases device complexity and can result in reduced sensitivity and selectivity by reducing the proportion of active sensing layer in the device.[30]

A promising approach to reduce the effect of bending on sensor degradation is to deposit polymer electrochemically in a sub-thin film regime, since electrochemistry means that adherence to the substrate is better than comparable deposition methods because the polymer nucleates and grows from the eletrodes outwards in a fully connective network, improving stability. Our previous work on percolation networks of CPs has shown that percolation polymer networks are always sub-thin film architecturally.[180] Furthermore, the advantages of CP room-temperature operation and minimal power requirements lend themselves perfectly towards incorporation into flexible and wearable technology.[181] A series of sensors malleable enough to be both wearable and capable of highly sensitive and selective detection of vapours that constitute a threat to human health would be of great commercial and humanitarian interest.[182]

Several recent studies have successfully incorporated conducting polymers onto flexible substrates for gas sensing. For example, Annapoorni et al.[183] created a flexible room

temperature ammonia gas sensor based on polyaniline on a polyethylene terephthalate (PET) flexible substrate that was able to detect ammonia in the range from 5 to 1000 ppm. Bai et al.[184] created a graphene-polyaniline hybrid sensor on PET substrates and tested concentrations between 10 and 100 ppm of ammonia. Kubersky et al.[185] have shown how a polyaniline sensor on a PET substrate can detect to a limit of 500 ppb for ammonia.

These publications, along with many others, demonstrate the numerous possibilities for utilising CPs as gas sensors on flexible substrates. However, in some cases the techniques used in preparation of the sensing materials prior to deposition are complex. Conversely, subsequent deposition techniques often involve either drop casting or dip coating the final polymer-sensing layer onto the electrode, which can result in a lack of uniformity and refinement.[186,187] The previous chapter showed that CP percolation networks on rigid glass substrates significantly improve the sensitivity compared to thin films. Here, the utility of spanning networks of PPy sensing layers operating within the percolation region on flexible substrates in response to ammonia gas is investigated.

7.2.1 Electrochemical polymer deposition

As observed in chapter 6, several electrochemical strategies exist for polymer deposition from the type of set-up described in chapter 2.3.1, but not all allow access to the control required to achieve a percolation network. Here, first cyclic voltammetry was used to ascertain the polymer deposition potential of the monomer/substrate pairing in question (Figure 7.3 (A)). This figure shows three CV scans. In the first scan, known as the nucleation loop, (red trace), the crossover point (I) is indicative of a homogeneous comproportionation reaction between an oligomer product and the starting monomer.[12] The two follow-on scans (black trace) show the cathodic peak on the reverse scan (II) representative of polymer reduction as a result of process (I), and the polymer oxidation

peak (III) not observed in the nucleation loop because no polymer had formed until after the first scan.

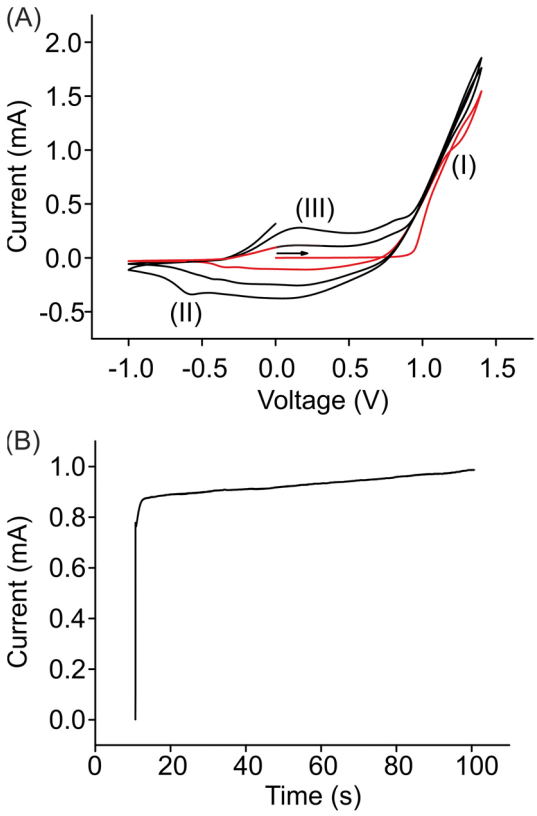


Figure 7.3. *(A) Cyclic voltammetry at a scan rate of 0.1 V/s for the oxidation of 0.1 M Pyrrole on a 100 µm gap Au IDE on a commercial flexible plastic substrate in 0.1M $LiClO_4$/acetonitrile for 3 cycles. The red line is the first scan and the black lines are subsequent scans. The crossover point at (I) represents Pyrrole growth. The peaks at (II) and (III) represent PPy reduction and oxidation respectively. (B) Chronoamperometric transient obtained for the oxidation of Py in 0.1M $LiClO_4$/acetonitrile. The potential was stepped from 0 to 1.3 V and held for 90s*

Based on (I) in Figure 7.3 (A), for the PPy deposition in this chapter an electropolymerisation potential of 1.3 V was chosen. Next, CA was used for the PPy growth. CA involves stepping the potential from a value where no reaction takes place (e.g. 0 V) up to the previously determined electropolymerisation potential (1.3 V), holding it there, and monitoring the change in current as a function of time, as the polymer is deposited (Figure. 7.3 (B)). In all cases, deposited PPy had a deep blue colour. Figure

7.4 (A) & (B) show close-up photographs of an IDE prior to deposition, and an IDE after a 30 s CA deposition time respectively.

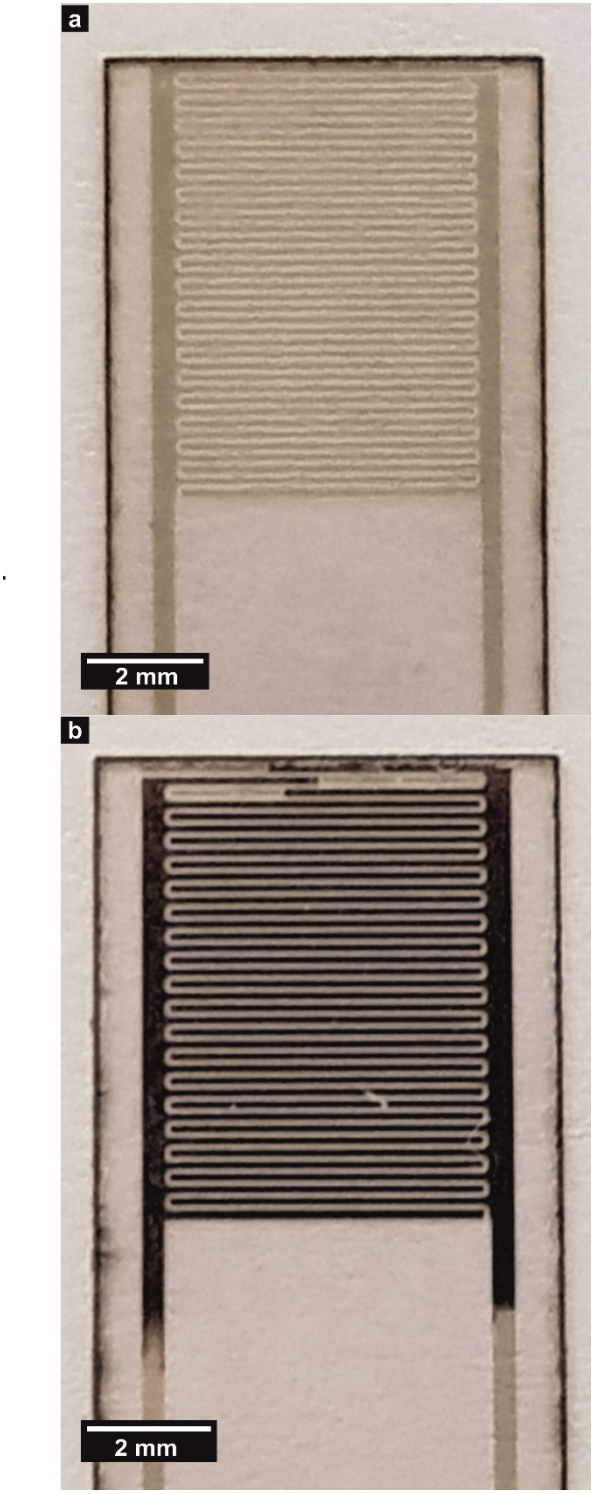


Figure 7.4. Au IDEs with a 100 μm separation on flexible PET substrates. (A) IDE as received and (B) IDE after a 30s PPy deposition.

7.2.2 Percolation networks on flexible substrates

Sensors were created using CA transient times of 10-90 seconds, and the conductance of each sensor was measured (Figure 7.5 (A)). From this, the percolation region could be determined and targeted for this polymer/electrode regime.

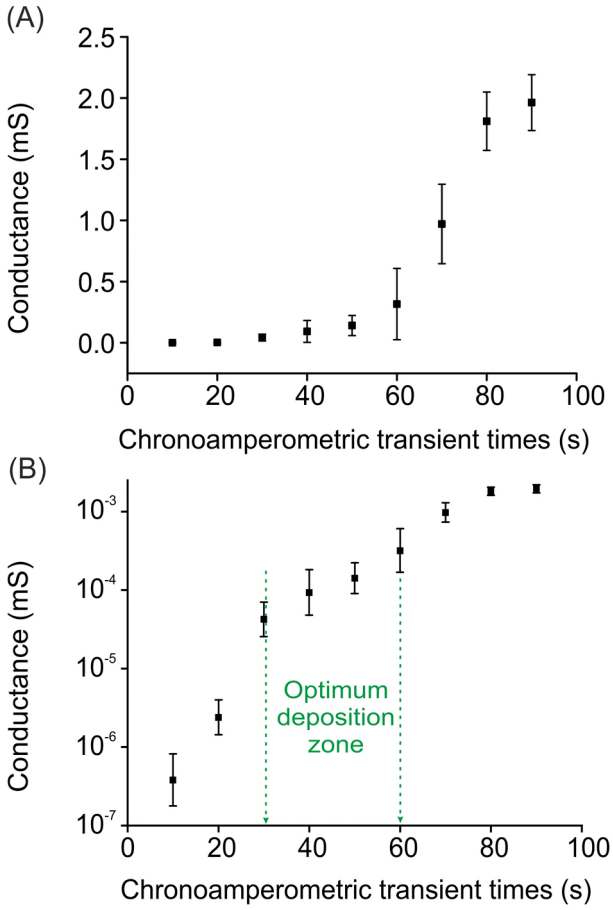


***Figure 7.5**. (A) Conductance vs chronoamperometric transient times for the deposition of polypyrrole on flexible substrate IDEs with 100 µm gaps. Error bars are obtained from the standard deviation of the conductance values of three separate electrode measurements. (B) The semi-logarithmic plot of conductance for the same chronoamperometric transient times. Highlighted in green is the optimum deposition zone, where the lowest LOD values were observed when these networks were used as ammonia sensors*

Initially, the polymer nucleates and grows on the Au electrodes. In this work, this is represented after CA transient times of 10 – 20 seconds, resulting in MΩ resistance

values. Once the metallic electrodes are covered, the polymer continues to grow out into the insulating gaps between the electrodes, steadily forming stable bridges between them. Here, after 30 seconds, a sharp increase in conductance is observed (more easily discernible in the semi-logarithmic plot, Figure 7.5 (B)). This abrupt increase in gradient is representative of the onset of percolation, where stable connections between Au electrodes begin to form. From this point, the increase in conductivity continues as more connections are made, until a plateau is observed beyond a CA time of 80 seconds. This plateau is characteristic of the point during the deposition when the electrodes are fully connected, and the polymer is in the form of a thin film.

The growth front of polymer with increasing deposition times, can be experimentally observed by considering the SEM images of deposition times from 20 – 80 seconds (Figure 7.6). There are no visible connections after 20 - 30 seconds (Figure 7.6 (A) & (B)) of CA deposition, which is consistent with the conductance measurements in Figure 7.5. An interesting point to note in Figure 7.5 (A) and (B), and faintly in (C) is the bright charging effect that is visible between the gaps of the polymer growth fronts. This charging effect is present due to the combination of the insulating nature of the flexible substrates together with the large gap size of 100 μm. This effect is not seen in samples where deposition is carried out beyond 50 seconds, nor was it seen to the same extent in the samples with gold nanoparticle scaffolds in chapter 6. This charging effect, which is usually seen as a negative outcome for imaging, can be used here as an advantage, to visualise conducting bridges forming beyond CA transient times of 40 seconds.

After 40 seconds (Figure 7.6 (C)) the polymer growth fronts have come into contact, and electrical conductivity increases significantly as a result (reflected in Figure 7.5). At 50 s (Figure 7.6 (D)) it can be seen that the insulating gap is coated with CP. However, when considering the conductance values obtained in Figure 7.5, it is clear that conductance commensurate with the thin film region is not reached at 50 seconds. This is likely due to conductive instability because of the porosity of the PPy film at the intersection

between the unsupported growth fronts. For the nanoparticle supported growth fronts of the previous chapter, thin film conductivity was achieved much more quickly, after only 20 seconds (Figure 6.8), as a secondary layer of polymer was not required to achieve stable conductivity in a network with much smaller insulating gaps to bridge.

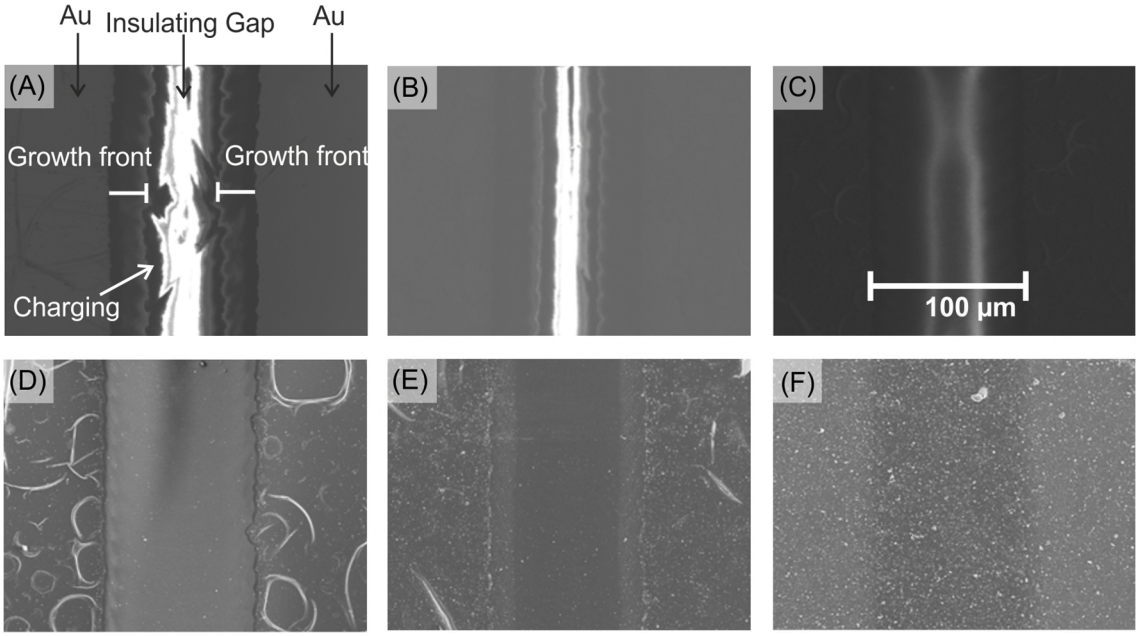


***Figure 7.6**. Scanning electron micrographs of a series of Au IDEs with 100 µm separation on flexible substrates, with increasing chronoamperometric transient times from A) 20s, B) 30s, C) 40s, D) 50s, E) 60s, F) 80s, showing increasing polymer coverage both on top of and between electrodes. Images were taken at 3 keV.*

In this case, after 60 seconds (Figure 7.6 (E)), a secondary layer of CP begins to grow outwards from the electrodes on top of the previously deposited porous film. Then, from a deposition time of 80 seconds (Figure 7.6 (F)), the secondary polymer layer has covered the gap and a stable film of polypyrrole has been deposited. At this point a thin film has been created, consistent with the conductance measurements (Figure 7.5).

7.3 Percolation sensing

After identifying the percolation region as a function of CA deposition time for polymer electrochemically deposited on flexible substrates, a new series of chemiresistors were produced, using the same method, with deposition times and thus conductivities representative of various points along the percolation curve. The resulting sensors had resistances of 4.3 MΩ, 430 kΩ, 63 kΩ, 5.7 kΩ, and 760 Ω after 20, 30, 50, 60 and 80 seconds of CA deposition, respectively. They were then exposed to varying concentrations of ammonia gas, from 100 to 700 ppb.

In all cases here, an increase in resistance was observed when ammonia gas was allowed in to the sensing chamber, in common with the study in the previous chapter. The reverse of this process was observed in all cases upon removal of the analyte, when resistance steadily returned to the baseline as weakly bound analyte departed the adsorption sites. The exposure time for each concentration was predetermined at five minutes, and the flow rate for both response and recovery was again fixed at 500 sccm. The responses decrease linearly with decreasing ammonia concentration for all five chemiresistors investigated.

Each sensor performance could then be analysed to allow a direct comparison of the sensitivity of each sensor, with particular focus on an optimised percolation sensor relative to a thin-film sensor. In this study, the optimum percolation sensor was determined to be the 5.7 kΩ sample, and the thin film was 760 Ω. The response profiles of these two samples can be seen in Figure 7.7 ((A) & (B), red lines).

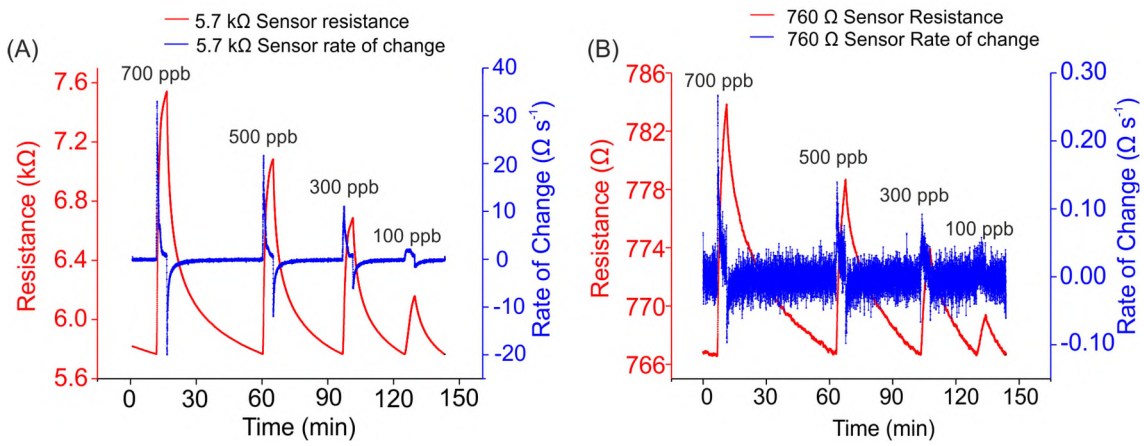


Figure 7.7. *Sensing responses (red lines) and rates of change (blue lines) for PPy chemiresistors on flexible PET substrates in response to 700, 500, 300 and 100 ppb ammonia in a dry N_2 carrier gas for (A) the optimum percolation sensor operating at 5.7 kΩ and (B) the thin film 760 Ω sensor.*

The response profiles observed in Figure 7.7 (red lines) are very similar in shape to those seen in the rigid sensors shown in chapter 6 (Figure 6.10). During the 5 minute analyte exposure in this study, dynamic equilibrium at the sensing surface was not reached, and so neither was maximum resistance change. Consequently, the shark fin responses in this study were not ideal for analysis via the $\Delta R/R_0$ method, for the reasons provided in chapter 5.2. Instead, the RoC method (chapter 5.4) was utilised instead. Figure 7.7 (blue lines) show the gradients of the sensing response curves (red lines) for each sensor, and were used to calculate the RoC sensitivities shown in Figure 7.8.

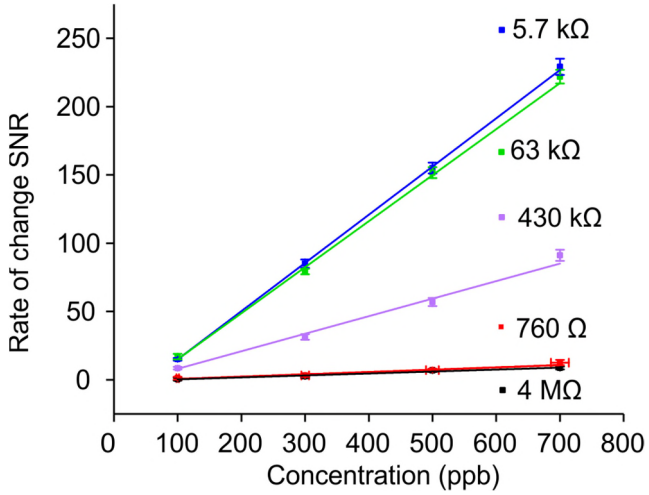


Figure 7.8. Rate of change SNR calibration curves for PPy chemiresistors with different starting resistances on flexible IDEs responding to 100 – 700 ppb of ammonia. The gradient of these curves corresponds to sensitivity, and is intrinsic to each sensor

Another benefit of obtaining the rate change data (Figure 7.7, blue lines) is to aid in the calculation of response times. Response times can be difficult to calculate in instances when the sensing response is changing over time and saturation is not reached. However, since the peak in the rate change data corresponds to the time during which adsorption is occurring at the maximum rate, this can also be used as the optimum response time. In order to calculate response times using this data, values were calculated as the difference between the time of analyte ingress and the time at which the peak maximum occurred for each analyte concentration. The average of these values gives the response time for each sensor over the range of concentrations investigated. Response times in this study ranged from 36 s for the 5.7 kΩ percolation sensor to 78 s for the 760 Ω thin film sensor.

In terms of LOD values, the chemiresistors operating at 4.3 MΩ and 760 Ω returned the highest values in this study, of 385 and 158 ppm respectively (Figure 7.9). It is interesting to note that both these sensors are operating at the opposing extremes of the percolation

profile (Figure 7.5). The best sensors investigated here, namely the 5.7 kΩ and 63 kΩ networks, were produced to operate in the optimum zone of the percolation region, where the SNR is highest, and consequently LOD values are lowest, both achieving an LOD of 9 ppb. These sensors were created ranging between 30s and 60s of CA deposition. This suggests that a comparatively large window exists in terms of deposition time, where sensors with a relatively large difference in resistance (from 5 – 100 kΩ) return similar LOD values. This is highlighted in green in Figure 7.9, where the optimal range of resistances in terms of low LOD correlates with the optimum deposition zone in the percolation region highlighted in Figure 7.5 (B)).

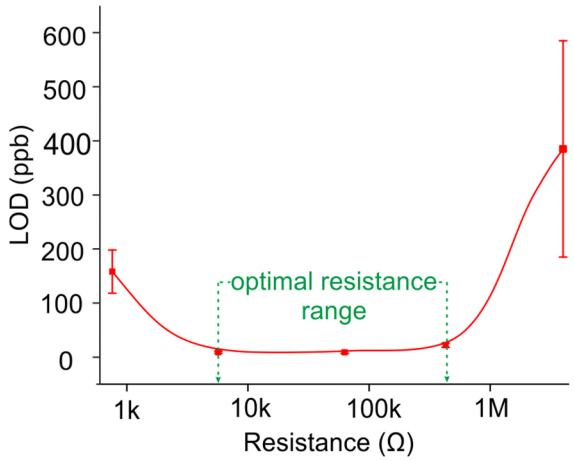


Figure 7.9. *Limits of detection for the five PPy sensors investigated. Highlighted in green, the optimal resistance range represents the resistances with the highest sensitivity and lowest LOD, corresponding to the optimum deposition zone of the percolation region.*

7.4 Sensor comparisons

Historically, directly comparing step-change monitoring vapour sensors produced in different ways has been challenging, not least because analytical methods used to treat sensing data are not always the same (see chapter 5). However, in the interest of attempting to extract some comparable figures of merit, in this section the sensors

created in this thesis will be compared directly, before being more broadly compared to other sensors from the literature.

7.4.1 Comparison of CP percolation sensors

The sensors detailed in this chapter, and those in chapter 6, were created in similar ways and optimised for high sensitivity by targeting the percolation region. They were also all treated in the same way in terms of data analysis. This means that the key figures of merit relating to sensing performance can be directly compared.

The most valuable figures relating to sensing performance in the context of step change monitoring are sensitivity, LOD and response time. All of these can be directly extracted from the RoC analysis carried out in chapters 6 & 7. (Figures 6.10 & 7.7). Those values are presented for an optimum percolation sensor and a thin film sensor for both a glass substrate with gold nanoparticles and a flexible substrate in Figure 7.10.

As reflected in Figure 7.10 (A), (B) & (C), on both flexible and rigid substrates, percolation sensors perform more efficiently than their thin film analogues. Of the four sensors compared in this section the best performing in every category investigated here is the percolation sensor deposited on a flexible substrate. That sensor (Figure 7.10, purple boxes) has the highest sensitivity (0.36 SNR ppb^{-1}) and consequently the lowest LOD (9 ppb), as well as having the fastest average response time (36 s). Because the preparation, deposition and doping level of polymer layers was the same throughout, and the resistances of the two percolation sensors are very similar, the overall number of connections that form the percolation network are comparable.

The reason for the enhanced performance of the flexible percolation sensor must therefore be a function of the insulating substrate itself. The surface energy of glass is considerable higher than that of PET (83.4 mJ m^2 and 37.0 mJ m^2 respectively).[188,189] Where the relatively high surface energy of glass promoted the dewetting necessary for gold nanoparticle scaffold formation detailed in chapter 6, it may also be detrimental

here, providing a less stable base for polymer chain formation. The PET substrate on the other hand, having lower surface energy, provides a stable environment for polymer growth, resulting in more uniform polymer deposition and so a better percolation sensor.

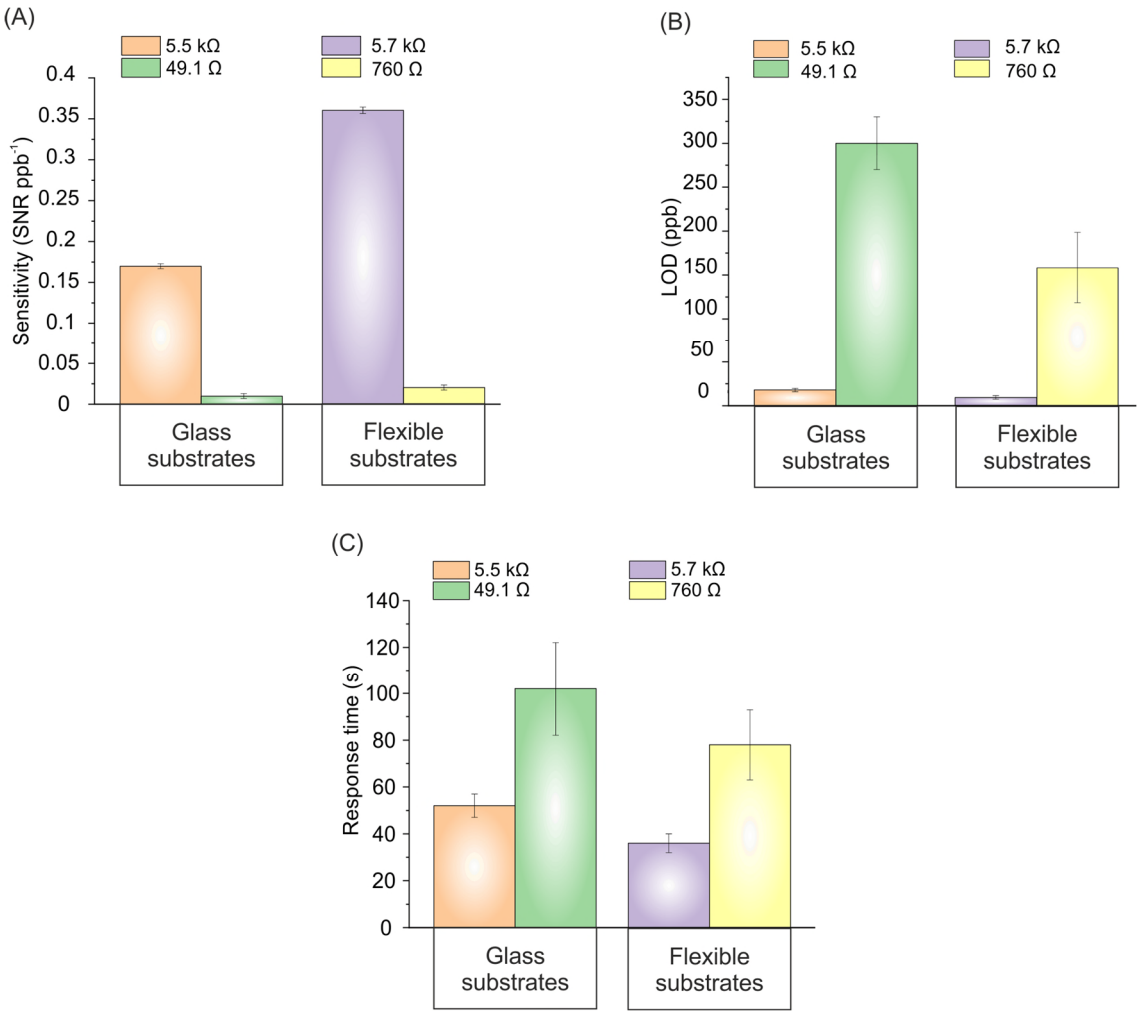


Figure 7.10. *Figures of merit for thin film and percolation PPy sensors deposited on glass substrates decorated with a gold nanoparticle scaffold and flexible PET substrates. (A) Sensitivity, (B) Limit of detection and (C) Response time.*

7.4.2 Comparison to other chemiresistive ammonia sensors

Other PPy-based thin film and fibre chemiresistive sensors tend to have higher LODs than our sensor, and sub-ppm LODs are rarely achieved.[190] Three notable exceptions are reported in the studies. Yan et al[191] reported an LOD of 7 ppb using viral-templated

gold/PPy nanopeapods, although the R_0 baseline was never recovered fully after initial exposure. Chartuprayoon et al[192] achieved a LOD of 500 ppb using PPy nanoribons, and Lee et al[193] who report a minimum detectable level (MDL) of 10 ppb using urchin-like nanoparticles decorated with iron oxide nanoneedles.

The LOD of 9 ppb (response time range of 36 s – 78 s) therefore places the flexible percolation sensor in this chapter amongst those chemiresistors able to detect the lowest concentrations of ammonia. As detailed in chapter 5, comparison between sensors of different types from different researchers, tested under different conditions can be difficult to evaluate directly because methods of calculating LODs and sensitivities can vary. However, in the interest of comparing our sensor to others, we have attempted to obtain LOD and sensitivity values for a range of PPy-based ammonia sensors from the literature, along with our own. The results are shown in Table 7.1. In the interest of reasonable comparison, sensitivities were obtained using the $\Delta R/R_0$ method for the percolation sensors in both this and the previous chapter.

Material & morphology	Sensitivity $\Delta R/R_0$ (%) per ppm NH_3 †	LOD (ppm)	Response time (s)	Flow rate of analyte gas (sccm)	Ref.
Our work: PPy Percolation network on a flexible substrate	39.4	0.01	36 (@ <1 ppm)	500	This thesis
Our work: PPy percolation network on a glass substrate	28.4	0.02	52 (@ <1 ppm)	500	This thesis
Viral templated gold/PPy nanopeapods	0.30[a]	0.007* *R_0 value not reached	900 (@ 5 ppm)	200	[191]
Urchin-like PPy nanoparticles	0.95[b]	0.01	<1 (@ 0.1 ppm)	1 – 5	[193]
Single PPy nanoribbon	9.6[b]	0.5	-	200	[192]
PPy/graphene nanocomposite with titania nanoparticles	1.22[b]	1	36 (@ 50 ppm)	-	[194]
PPy nanowire arrays	1.2[b,c]	1.5	60 (@ 77 ppm)	-	[195]
Graphene oxide/PPy nanocomposite	0.12[b,c]	3	400 (@ 3 ppm)	-	[196]
PPy thin film	0.35[b]	4	20 (@25 ppm)	-	[166]

† [a] – Published sensitivity

[b] – Estimated sensitivity from publication

[c] – Non-linear response, gradient estimated from linear portion of the calibration curve

Table 7.1. Summary of the sensing performance of a variety of PPy-based sensors toward ammonia gas. All sensors were operated at room temperature.

7.5 Summary

This chapter has shown how an electrical percolation network of polypyrrole can be grown between IDEs on a flexible PET substrate. The nature of percolation behaviour in relation to conductivity was supported through SEM imaging of the polymer bridging. Sensors displaying various levels of percolation behaviour were investigated for their sensitivity to interaction with ammonia gas diluted in dry N_2. The highest sensitivities and thus lowest LOD values of 9 ppb were obtained for the chemiresistors operating within the optimum zone of the percolation region. In this work, the window for production of optimal percolation sensors is large, making reproducibility and thus the potential for large-scale production accessible. Furthermore, the opportunity to extend the utility of these types of percolation sensing layers onto flexible printed electronics and large area sensors is promising. The ability to detect concentrations of ammonia below 10 ppb with a response time under 40 s using electropolymerised sensing layers on flexible substrates results in significant improvements in sensitivity when compared with many competitive PPy deposition strategies, and may open up many routes for utilising percolation sensors in wearable devices.

The percolation region achieved on the PET IDEs is unique for this system, and the percolation region behaviour will change according to different CPs and substrates as shown in section 7.4.1. In this chapter, the flexible PET substrate surface provides an environment for stable growth as the conducting polymer develops across the insulating gap, resulting in high sensitivities obtained for the detection of ammonia gas, and thus low LODs. This in turn suggests that these commercially available IDEs on flexible substrates represent an ideal platform for chemiresistors operating within the percolation region.

Chapter 8

Metal Organic Frameworks

In the previous two chapters, it has been shown that percolation sensors display increased sensitivity for vapour detection. However, analyte selectivity for conducting polymers is still relatively low, since any redox-active species will elicit a sensing response for these types of sensing layers. Finding new chemiresistive materials is of high value for use in an e-nose device. MOFs have the potential to show increased selectivity because the additional complexity in their architecture provided by metal centres along with their inherent porosity should enable increased discrimination between analyte species.

This chapter begins by introducing the materials and methods used to create the MOFs investigated here, and the reasons why they were selected. Then, the ways in which the MOFs were prepared and characterised are provided. Next, the way in which MOF percolation networks were achieved is detailed, before the MOF sensors are investigated for sensing performance against different analytes. Figure 8.1 shows a schematic representation of how components combine to provide a MOF structure.

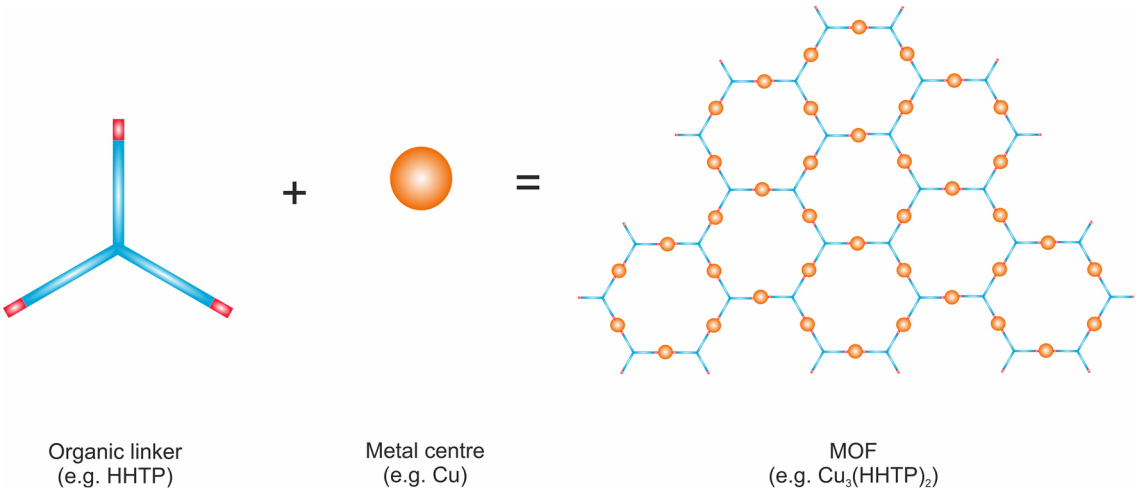


Figure 8.1 *Schematic diagram of a 2D structure where organic linkers connect metal centres to create an ordered honeycomb MOF network.*

8.1 Materials and methods

Contrary to the CP polymers in the previous two chapters, the MOF sensors discussed in this chapter were not grown by electrochemical means, and so new substrates and methods of deposition were required to achieve percolation networks of them. As detailed in chapter 4, the number of conductive MOFs discovered to date which have high enough conductivity to display measurable chemiresistive behaviour is still relatively low. Of those which are available, the most amenable for use in this work were found to be those with triphenylene (TP) derived organic linkers, and metal centres which promote square planar binding geometry and so 2D network formation. TP based MOFs were used because, in the case of HHTP MOFs, they are relatively easy to synthesise from readily available materials. In addition, once prepared they are stable and can be stored for long periods of time with no degradation. Finally, there are a range of metal centres that can be incorporated (e.g. Cu, Co, Ni) to tune their behaviour.

The first stage of creating the MOF sensors in this chapter was to synthesise the MOFs via wet chemistry self-assembly techniques described in chapter 2.3.2. The MOFs were then suspended in solvent mixtures made up of varying amounts of different solvents in order to minimise the coffee ring effect (see section 8.4). In some cases, silver nanowires were incorporated into the mixtures to stabilise and enhance conductivity in the network.

The subsequent mixtures were drop cast onto a substrate. In some cases, these substrates were the glass IDEs introduced in chapter 6, and in other cases standard 80 gsm printer paper was used as the insulating substrate. In these cases, electrodes were drawn on after deposition using a Circuit Scribe conductive ink pen.[197] Gas sensing was carried out in the custom sensing chamber described previously.

8.2 Organic linker synthesis*

MOFs were generally prepared as described in chapter 2.3.2 from commercially available organic linkers (HHTP) and metal salts. However in the case of HITP MOFs, the organic linker 2,3,6,7,10,11-Hexaaminotriphenylene (HATP) is not commercially available, and so was synthesised according to the following method.

8.2.1 2,3,6,7,10,11-Hexabromotriphenylene

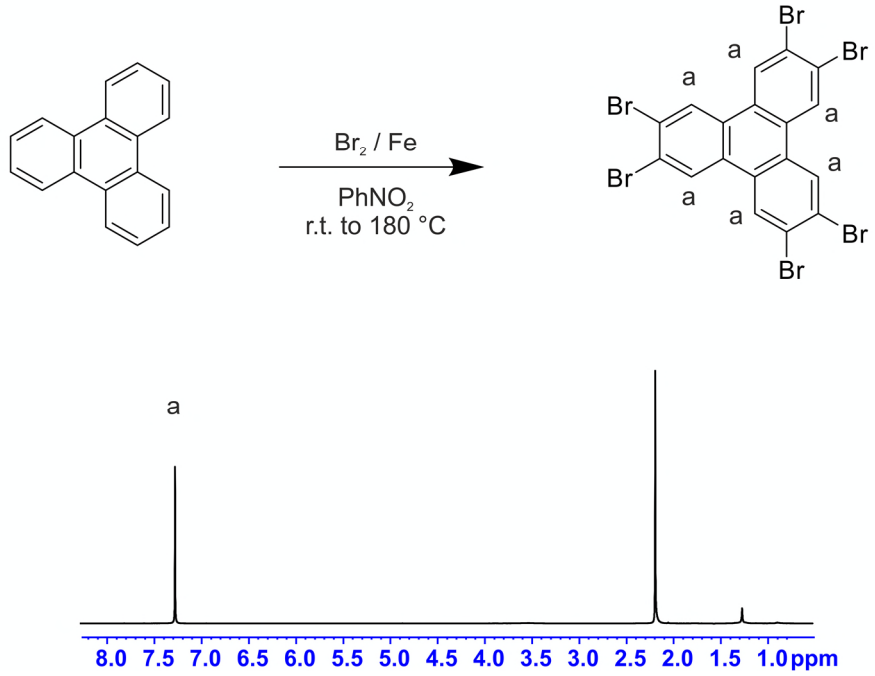


Figure 8.2 *Synthesis and ^{1}H NMR of 2,3,6,7,10,11-Hexabromotriphenylene .*

Triphenylene (2.26 g, 9.91 mmol) was dissolved in nitrobenzene (80 mL) with iron powder (0.18 g, 3.6 mmol). Bromine (8 mL, 160 mmol) was added dropwise over 10 minutes. The solution was allowed to stand for 16 h and heated under reflux at 200 °C

* Owing to difficulties and delays caused by the CV-19 pandemic, the HITP synthesised in this section which was intended for use in the sensors detailed here was instead used to vacuum deposit and STM image HITP MOF as part of a separate project beyond the scope of this thesis.

for 4 hours. The mixture was cooled to room temperature, mixed with diethyl ether (300 mL), and filtered. The crude solid was recrystallized from 1,2-dichlorobenzene to yield 6.2 g (90%) of white needles. ^{1}H NMR ($CDCl_3$) δ(ppm) 7.25 (s, 6H, triphenylene CH).

8.2.2 Triphenylene-2,3,6,7,10,11-hexaylhexakis(1,1-diphenylmethanimine)

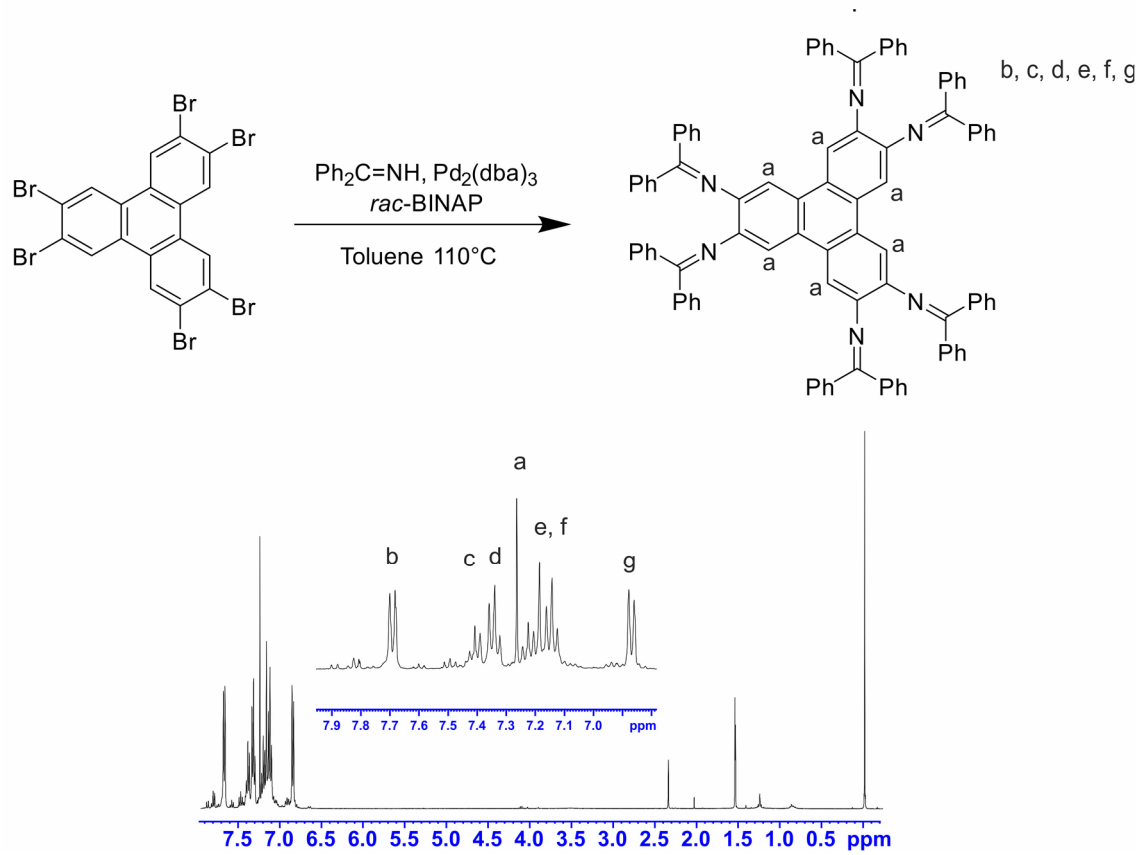


Figure 8.3 *Synthesis and ^{1}H NMR of triphenylene-2,3,6,7,10,11-hexaylhexakis(1,1-diphenylmethanimine).*

Tris(dibenzylideneacetone)dipalladium(0) (0.448 g, 0.49 mmol) and *rac*-BINAP (0.607 g, 0.98 mmol) was degassed by purging under N_2 stirring for 30 minutes, before being heated to 110 °C under N_2 for a further 30 minutes. After cooling to r.t., benzophenone imine (2.65 mL, 15.77 mmol), 2,3,6,7,10,11-Hexabromotriphenylene (1.419 g, 2.02 mmol) and sodium *tert*-butoxide (1.516 g, 15.77 mmol) was added and the mixture was stirred at 105 °C for 12 hours. The mixture was cooled to r.t., diluted with

dichloromethane and filtered through a Celite pad before being dried under evaporation. The residue was purified via column chromatography on silica gel with AcOEt/Hexane (1:4) as eluent. The last fraction was collected and dried under evaporation to yield the product as a yellow solid (1.5 g, 57 % yield). ^{1}H NMR ($CDCl_3$) δ(ppm) 7.62 – 7.64 (m, 12H, *o*-Ph), 7.34 – 7.64 (m, 6H, *o*-Ph), 7.27 – 7.31 (m, 12H, *m*-Ph), 7.19 – 7.22 (m, 6H, *o*-Ph), 7.12 – 7.14 (m, 12H, *m*-Ph), 7.04 (s, 6H, triphenylene CH), 6.92 – 6.94 (m, 12H, *p*-Ph).

At this point in the synthesis impurities became apparent which co-eluted with the product after repeated attempts at purification via column chromatography (see NMR spectrum, Figure 8.3 inset). It is likely that these impurities arose as a function of incomplete Br substitution in one of the six possible positions on the TP ring structure, possibly as a result of steric hindrance owing to the size of the benzophenone imine substituent.

8.2.3 2,3,6,7,10,11-Hexaminotriphenylene

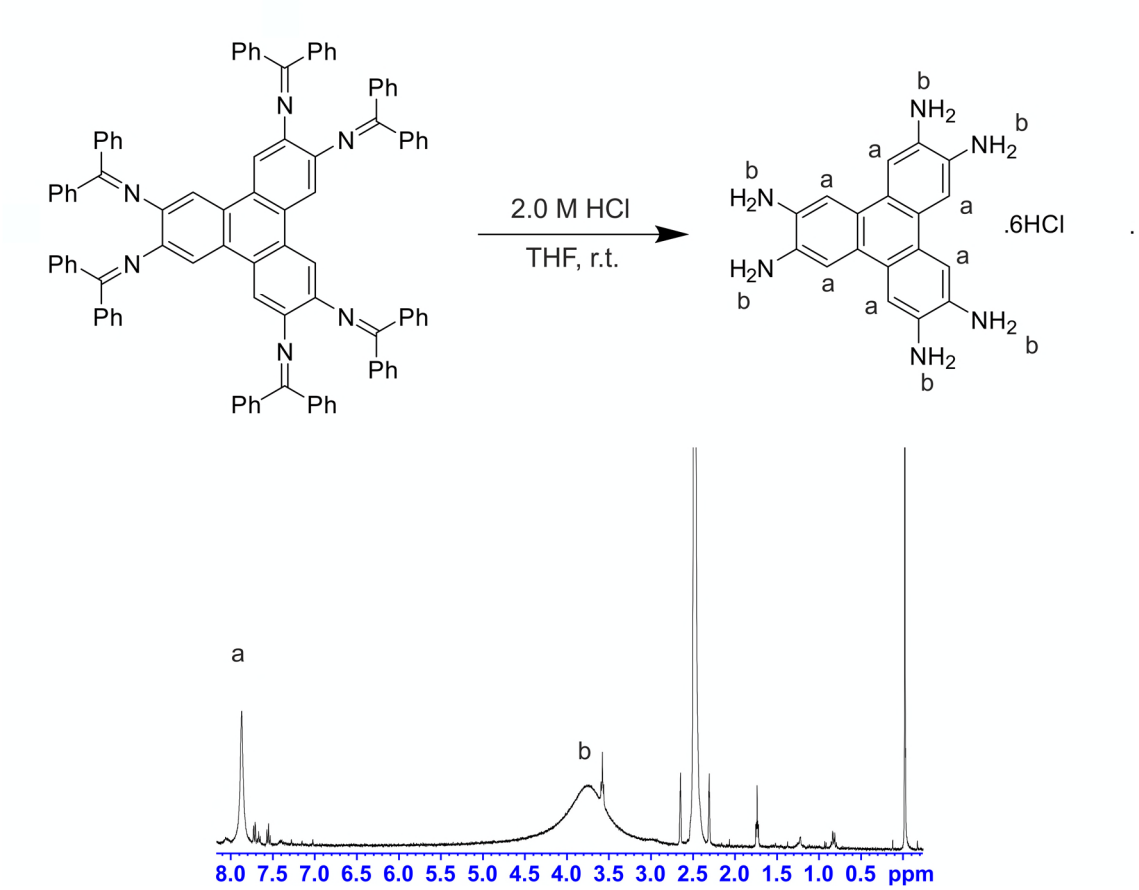


Figure 8.4 *Synthesis and ^{1}H NMR of 2,3,6,7,10,11-Hexaminotriphenylene*

triphenylene-2,3,6,7,10,11-hexaylhexakis(1,1-diphenylmethanimine) (0.219 g, 0.17 mmol) was dissolved in THF (10 mL) before being added to a 2.0 M aqueous HCl solution (0.5 mL, 1.0 mmol) and stirred at r.t. for 30 minutes. The precipitate was isolated by filtration and washed with hexane (5 mL x 3) and dried under vacuum to yield the final product as an off-white solid (0.05 g, 55 % yield). The ^{1}H NMR (DMSO-d6) of the final product is shown in Figure 8.4.

As shown in Figure 8.4, the impurities identified in the previous step (Figure 8.3) were carried through and are also present in the final product. However, since these were likely to be products which were not fully substituted in all 6 relevant positions, it is unblikely that they would interfere with MOF self-assembly, because they would be

incapable of network formation. It was decided to use the product as prepared with no further purification.

It should be noted at this stage that due to delays caused by CV-19, this product was not used in this project and was instead used for a separate MOF project which was incomplete at the time of this publication. As a result, all further work in this chapter uses the commercially available HHTP organic molecule, and it is hoped that in the future the synthesised HITP will be incorporated into this project.

8.3 MOF characterisation

The Cu-CAT MOFs which feature predominantly in this chapter were characterised by p-XRD, NMR and SEM. Many other types of analysis are excluded for use in MOF characterisation because the insoluble nature of MOFs and their extended connectivity render them difficult to analyse in solution, where dissolving them tends to result in destruction of the network.

P-XRD was carried out as described in chapter 2. Figure 8.5 (A) shows the p-XRD carried out on the MOFs as synthesized in this work, and Figure 8.5 (B) (orange line) shows a comparative p-XRD plot from previously published work on the same type of MOF.[198] As reflected in the figure, the two plots are in good agreement, indicating that the MOF was successfully synthesized here.

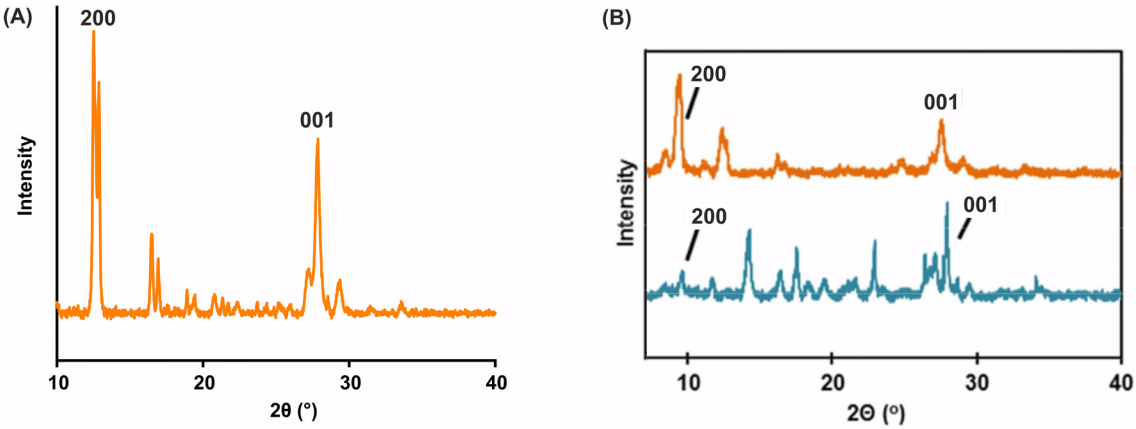


Figure 8.5 *Powder X-ray diffraction plots of $Cu_3(HHTP)_2$. (A) p-XRD plot of the MOFs synthesized in this work. (B) P-XRD of the same MOF (orange line) synthesized by another research group. Reprinted with permission from ref.*[198]

As shown in Figure 8.5, the prominent peak at 2θ = 11.5° corresponding to the 200 reflections indicate long range order within the *ab* plane, which is in good agreement with prior work on TP-derived MOFs, where it has been shown that this type of MOF favours slipped-parallel (AB) orientations.[104] It is interesting to note that this peak in this work is approximately 2° shifted from the 2θ = 9.5° literature example. The most likely cause of this is due to dopant ions distorting the lattice structure, which were likely incorporated during synthesis. The broader, weaker peak at 2θ = 28° corresponding to the 001 reflections is indicative of poorer long-range order along the *c* direction, as expected for covalently linked layered materials.

Cu-CAT was also characterised by SEM. The two starting materials in the MOF synthesis are in powder form, where the HHTP is a black powder and the Cu salt is a light blue powder. The MOF appears visually to be dark blue crystalline flakes, and under SEM in all published examples[104,198,199] Cu-CAT appears as prismatic crystalline rods of varying size. The SEM of the Cu-CAT prepared in this work, deposited on a glass substrate, is shown in Figure 8.6.

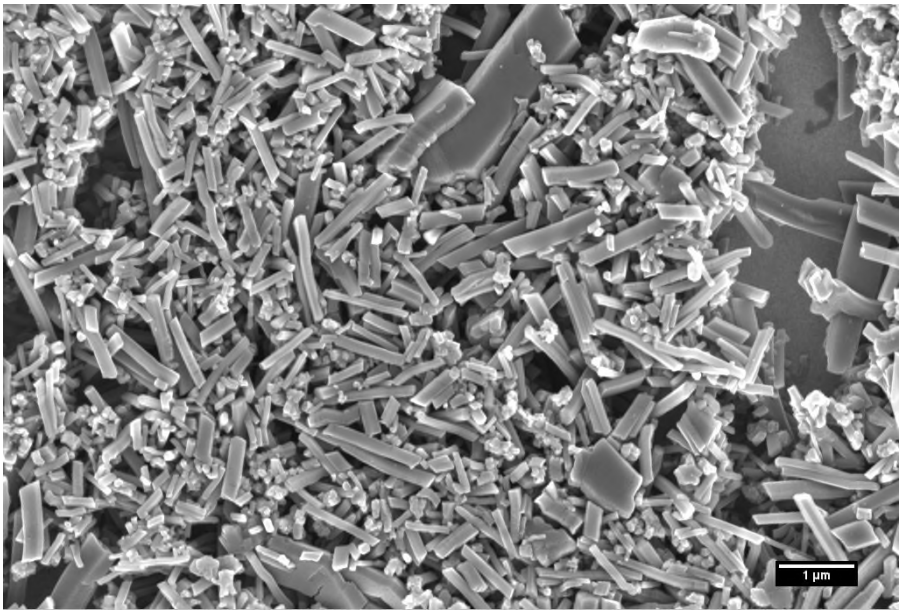


Figure 8.6. *Scanning electron micrograph of $Cu_3(HHTP)_2$ deposited on a glass substrate.*

8.4 Sensor preparation

The MOFs in this work were deposited from solution by drop-casting. Drop-casting from a solvent mixture was chosen because the work contained in this chapter is intended to form the foundation for developing 'ink' type suspensions suitable for inkjet printing of MOF sensors. Inkjet printing is an attractive deposition method for chemiresistive sensors because it allows sensor creation on a variety of flexible and wearable substrate materials including textiles, plastics and paper.

8.4.1 Solvent selection

One common issue when attempting to deposit layers from a solid dispersed in a liquid is the irregular patterns left after drying, commonly known as the 'coffee-ring' effect (CRE). The impact of CRE when attempting to achieve uniform deposition is well known in optical and electronic thin films and coatings.[200–202] This effect was first described by Deegan et al[203] and occurs because the contact line between a droplet and the surface is pinned in place by surface tension, forcing the drop to flatten rather than shrink.

Solvent from the interior of the droplet replenishes that lost at the edges, and this capillary flow draws solvent and solute from the interior towards the edges as drying occurs. Once dry, the result is a ring of particles concentrated around the perimeter of the now absent droplet. This process is illustrated in Figure 8.7.

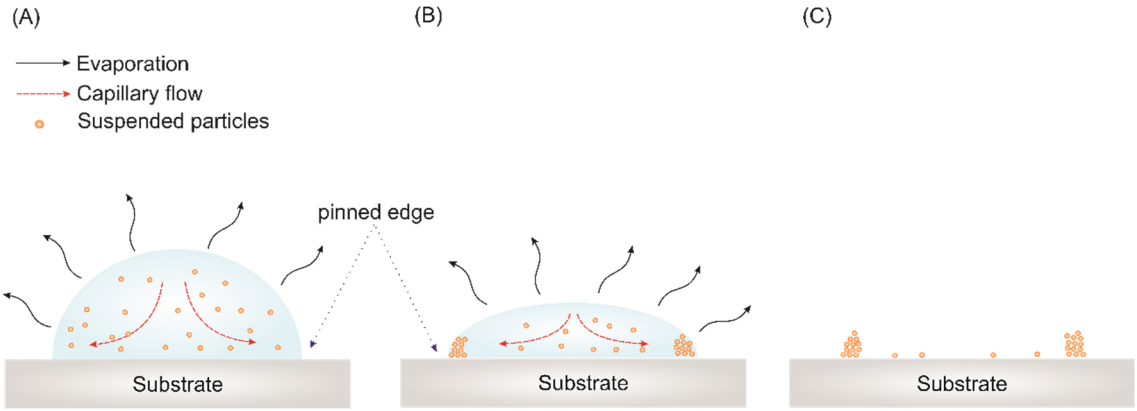


***Figure 8.7**. Schematic representation of the coffee-ring effect in a drying droplet. (A) Evaporation from the fresh droplet begins immediately. Initially particles are homogeneously dispersed. (B) As evaporation removes solvent, the droplet reduces in volume but surface area remains constant because the edge is pinned in place by surface tension. Capillary flow moves solvent and solute towards the edges. (C) The solvent has now evaporated, leaving a ring of particles concentrated around the perimeter of the droplet.*

There are numerous ways in which to reduce the impact of CRE. These can include introducing additional polymers and surfactants to the mixture, or utilising co-solvents with different evaporation rates and surface tensions.[204] In this work, introducing additives to the mixture is undesirable as they could interfere with or inhibit the MOF from sensing accurately. As a result, utilising co-solvents was chosen to mitigate against CRE. Mixing miscible solvents with differing vapour pressure (P_v) and surface tension (γ) introduces a gradient during drying, where faster evaporating solvents enrich the concentration of less volatile solvents at the droplet/substrate contact line. Consequently, Marangoni flow is induced and cycles suspended particles back towards the interior as the less volatile solvent circulates. Particles remain more disperse in the

mixture during drying, and so are more evenly deposited afterwards. In addition, for inkjet printing viscosity (η) and density (ρ) are also key values. They allow the calculation of inverse Ohnesorge numbers (Z), according to the following equation, where (a) is the print head nozzle diameter:

$$Z = \sqrt{\frac{\gamma \rho a}{\eta}}$$

Generally for inkjet printing, a Z number of 1 – 14 provides the most stable droplets and reduces satellite droplet formation (>14) or elongation (<1) during printing.[204] Table 8.1 provides the critical values for the four solvents investigated in this chapter; ethanol, IPA, ethylene glycol and 1,3-propanediol.

In this work, drop-casting was carried out using a pipette tip with a nozzle size of approximately 1mm. In comparison, most inkjet printers have a nozzle size of < 0.3 mm. This will have an impact on performance and Z numbers when transferring the solvent system here to an inkjet printer, since a (above) is dependent on nozzle diameter.

Solvent	P_v (kPa)	γ (m Nm^{-1})	η (mPa s)	ρ (g cm^{-3})	Ref.
Ethanol	5.8	22.4	1.2	0.8	204
IPA	4.4	21.3	3.8	0.8	204
Ethylene glycol	0.01	47.3	16.1	1.1	205
1,3-propanediol	0.005	41.1	52	1.1	205

Table 8.1. *Relevant critical parameters for inkjet printing of the solvents considered in the MOF mixtures detailed in this chapter. All values provided at RT.*

In the initial work in this chapter, solvent mixtures were selected consisting of a 1:1:1 mixture of ethanol, ethylene glycol and 1,3-propanediol. These solvents were chosen because they form a good viscosity gradient during drying to maximise Marangoni flow, are miscible with each other and yielded the best results in terms of even deposition. Figure 8.8 (A), (B) & (C) show Cu-CAT MOF (5 mg ml^{-1}) drop cast onto a glass slide in only ethanol, ethylene glycol and 1,3-propanediol respectively, then dried for 5 minutes at 60 °C. In each case, the CRE is apparent. Figure 8.8 (D) shows a drop cast sample prepared in the same way, now from 1:1:1 mixture of all three solvents. In this case, MOF dispersion after drying is improved and the pinned edge is clearer and more stable.

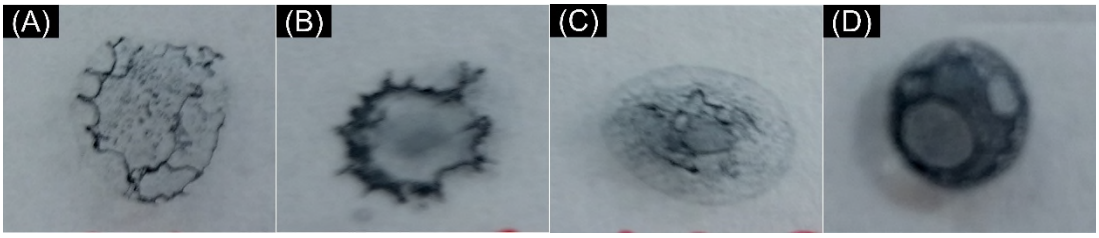


Figure 8.8. *Cu-CAT MOF (5 mg ml^{-1}) drop cast onto a glass slide from (A) ethanol, (B) ethylene glycol, (C) 1,3-propanediol and (D) a 1:1:1 mixture of all three solvents.*

Having obtained an optimised tertiary solvent mixture suitable for even MOF deposition, the process was repeated for CuCAT (10 mg ml^{-1}) in ethanol and in the tertiary ink mixture on 5 µm Micrux Pt IDEs (see chapter 6), which enabled comparison under SEM. The resultant micrographs are shown in Figure 8.9.

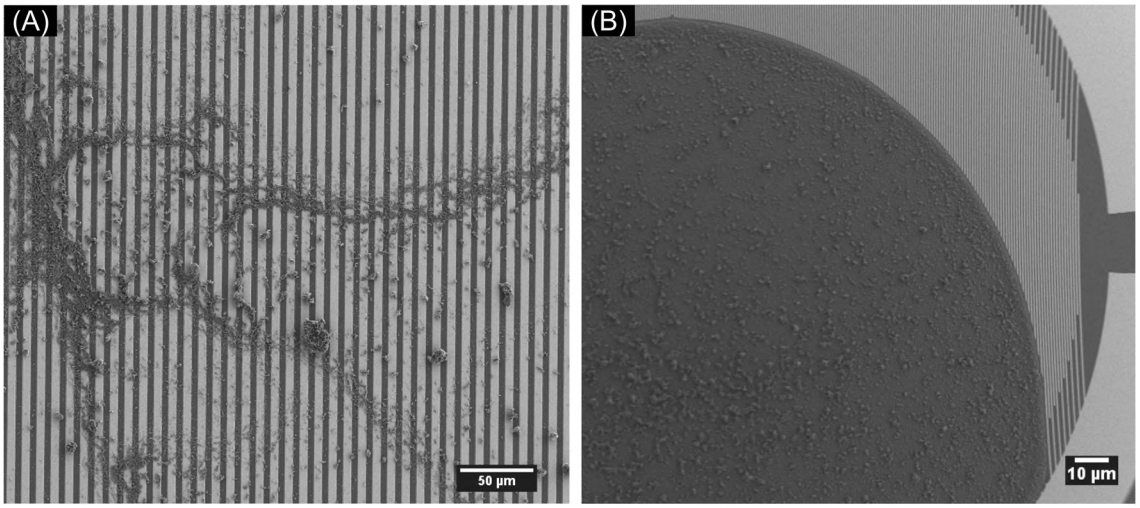


Figure 8.9. *Cu-CAT MOF (10 mg ml^{-1}) drop cast onto a 5 µm Pt/glass IDE from (A) ethanol and (B) a 1:1:1 tertiary mixture of ethanol, ethylene glycol and 1,3-propanediol.*

A 10 mg ml^{-1} mixture was chosen for the SEM samples to ensure good conductivity between electrodes for imaging. As reflected in figure 8.9, the difference in CRE is marked between the ethanol in (A) and the tertiary mixture in (B). In terms of using this tertiary mixture as an ink in printing applications, similar ratios of solvent mixtures of these components for other applications have been found to have Z numbers of 6 – 8,[206] which puts them in an ideal range for inkjet applications.

IPA was incorporated into the mixtures containing AgNW in later work because the AgNWs were purchased suspended in a solution of IPA, necessitating its inclusion. In these instances, IPA replaced ethanol in the mixtures. That work will be detailed in chapter 8.6.

8.4.2 MOF sensor preparation on glass electrodes

The next stage in developing Cu-CAT sensors was to attempt to deposit the MOF in a controlled way in order to achieve percolation, and thus an increase in sensitivity as observed for CP in chapters 6 & 7. Owing to the crude nature of drop casting as a deposition method, this was more challenging for the MOF sensors described here.

The tertiary solvent mixture described in the previous section gave even and consistent deposition across the substrate. Therefore the most obvious way to achieve a percolative regime was to adjust the amount of MOF dispersed in the solvent mixture, in order to tailor the amount of connectedness across the system for equal amounts of solvent deposited.

The mixtures contained 1 – 10 mg mL^{-1} of Cu-CAT, in ~ 2 mg increments. The solvents were mixed, then Cu-CAT MOF was dispersed in them and sonicated for 10 minutes in each case. After sonication, 5 µL of each mixture was drop cast onto Micrux 5 µm Pt IDEs on a glass substrate, detailed in chapter 6.1. Then, each sensor was heated to 80 °C for 5 minutes to remove solvent. The resultant sensors are shown in Figure 8.10.



Figure 8.10. *Increasing concentrations of Cu-CAT MOF (1 - 10 mg mL^{-1}) drop cast onto Micrux 5 µm Pt/glass IDEs*

The conductivity of each sensor was measured after drying using a 2 point probe hand held multimeter. In some prior work on CAT MOF sensing,[102,106] MOFs were activated by soaking the prepared sensor in acetone prior to deployment in order to remove any residual solvent and clear the pores within the MOF to improve sensing performance. That process was repeated for the sensors prepared here, where they were soaked in

acetone for 24 hours, whereupon conductivity was measured again. The resultant conductivities (pre- and post-activation), are shown in Figure 8.11.

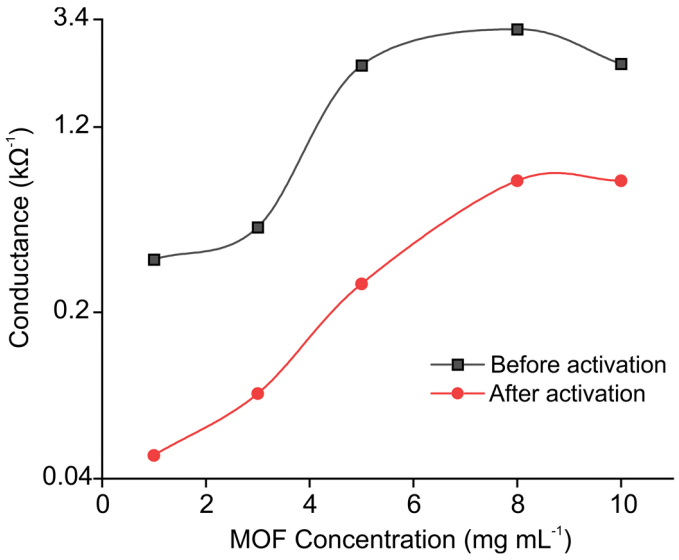


Figure 8.11. *Semi-logarithmic plot of conductance against Cu-CAT MOF concentration for pre-activated (black line) and activated (red line) sensors, prepared by drop casting then drying MOF dispersed in tertiary solvent mixtures on to Pt/glass IDEs.*

As reflected in Figure 8.11, in all cases conductivity decreased after activation. This is likely to be a result of the activation process removing residual solvent from the porous MOF structure, which could have contributed to increased conductivity in the pre-activated samples. Because the conductivity of the MOF particulates in this work was heavily impacted by increased resistance as a result of inter-particle boundaries, it is likely that residual solvent served to bridge between particles, providing a conductive joint and improving conductivity. Removal of this solvent by activation decreased conductivity by removing these solvent bridges between particles. After activation, the shape of the curve (Figure 8.11, red line) is similar to the percolation curves observed in previous chapters, and represents an approximation of percolation-type behaviour in the activated samples, dependent upon MOF concentration. More experimentation is required to ascertain if this is true percolation behaviour, since the curve lacks some

features common in most percolation curves, including a flat baseline and a sharp take-off point. However, having obtained a conductivity curve for Cu-CAT sensors, the next stage was to assess sensing performance of MOF percolation sensors. Details of this are provided in chapter 8.5.

8.4.3 MOF sensor preparation on paper substrates

Whilst drop casting proved more challenging for percolation network formation when compared to electrochemical polymer deposition, one advantage of the method is that it is easier to apply to different substrates. The reason for this is because this method does not necessitate metallic electrodes for nucleation and growth. Consequently, the MOF mixtures in this chapter can be deposited on almost any substrate, either via casting or printing. Electrodes can then be added post-deposition.

In this study, numerous substrates were tried with Cu-CAT dispersed in the tertiary ink described in the last section, and standard 80 gsm office printer paper was found to be a suitable candidate. Printer paper is cheap and malleable in terms of scalability, either pre- or post-sensing layer deposition. Furthermore, it is an easy process to add electrodes to deposited MOF layers on paper using a readily available CircuitScribe conductive ink pen, and the absorbent nature of the paper results in reasonably even MOF deposition because the majority of the solvent soaks through the paper on contact. However, this absorbance did provide some drawbacks, because absorbance in combination with the rough surface of the paper resulted in increased resistance at the junction between MOF particles, and thus conductivity only being achievable with the highest Cu-CAT concentration in this study, 10 mg mL^{-1}.

Because percolation networks were not achievable by increasing MOF concentration, in the case of paper substrates it was hoped that behaviour analogous to percolation could be achieved by increasing the number of 5 µL drops of ink in the same place, drying at

70 °C for 1 minute between each deposition. By definition, this is not a true percolation network because the resultant thick film contains a large amount of material that is capable of analyte interaction without response, since it is present but not connected to the spanning network, resulting in reduced sensitivity. However, this problem could be mitigated to some degree by pressing the sample, and thus forcing more connectivity between MOF particles. That will form the basis of future work in this research.

For the purposes of the work in this chapter, sensors were prepared as described. A photograph of a range of sensors with different amounts of MOF deposition is shown in Figure 8.12 (A), then with electrodes added in Figure 8.12 (B). Finally, Figure 8.12 (C) shows a sensor having been prepared and cut to size placed in the sensing chamber.

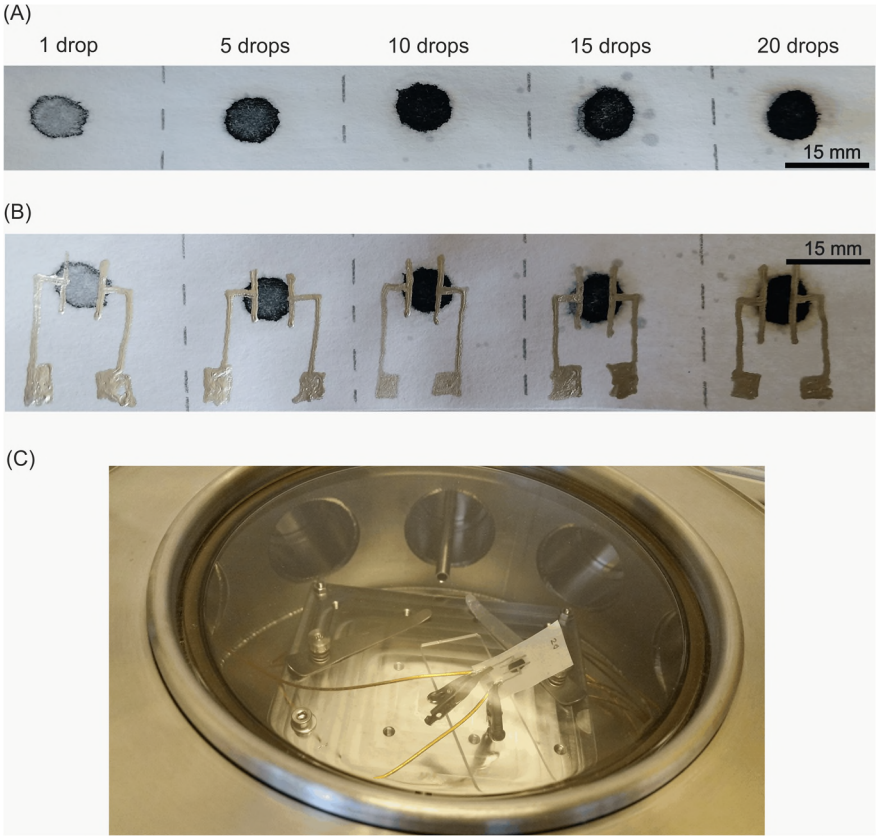


Figure 8.12. *(A) A range of sensors prepared by repeated 5 µL drop casting of Cu-CAT ink from 1 – 20 drops. (B) The same sensors with electrodes drawn on using a conductive ink pen. (C) The 20 drop sample in the sensing chamber.*

Unfortunately, even using this approach, the only conductive sample obtained was the 20 drop sample, and in this case conductivity was relatively low, at 10 MΩ. This is highly likely to be a result of the increased inter-particle resistance discussed previously. However, some sensing results were obtained for this sample (see chapter 8.5.2), indicating that the method is valid, but necessitates some improvement. By stabilising the conductivity through incorporation of silver nanowires into the mixture, it was hoped that more consistent and productive sensors could be produced. and preliminary AgNW experiments are shown in chapter 8.6.

8.5 MOF sensing

Having prepared a series of Cu-CAT sensors on Micrux glass/Pt electrodes along with a paper-based MOF sensor, sensing experiments were carried out in the sensing chamber described in previous chapters. In the experiments in this chapter, sensing was carried out using dry air as the carrier gas, and with an applied voltage of 0.75 V in all cases.

8.5.1 Glass substrate MOF sensing

Sensors were prepared as described in chapter 8.4.2, and chosen to represent various points along the curve shown in Figure 8.11. The sensor representing 1 mg mL^{-1} was found to have MΩ resistance, and owing to a large amount of noise in the signal, it was discounted from further study. The sensors representing 3, 5, 8 and 10 mg mL^{-1} did stabilise enough for analyte exposure, and after stabilisation in a dry air carrier gas for 1 hour had resistance values of 130 kΩ, 40 kΩ, 23 kΩ and 8.4 kΩ respectively. After 1 hour, they were exposed to repeated cycles of 1 and 2 ppm of ammonia for 1 minute in each case.

Baseline stability was consistently problematic for the sensors in this chapter, where resistance was increasing or decreasing steadily throughout the experiment, despite multiple efforts to stabilise it. This type of fluctuation is not uncommon in TP derived

sensing layers.[198,207] In this case, the magnitude of these changes is reasonable for normal baseline drift in a dynamic system, being only 1 or 2 kΩ over the course of the experiment. However, because the magnitude of response in all cases was lower than the overall baseline drift, utilising $\Delta R/R_0$ is not a suitable method for analysis of sensors of this type. Nonetheless, the response is still apparent and measurable using the RoC analysis outlined in chapter 5.4, which can largely eradicate the issue of unstable baseline. Figure 8.13 shows the raw response profile for each sensor.

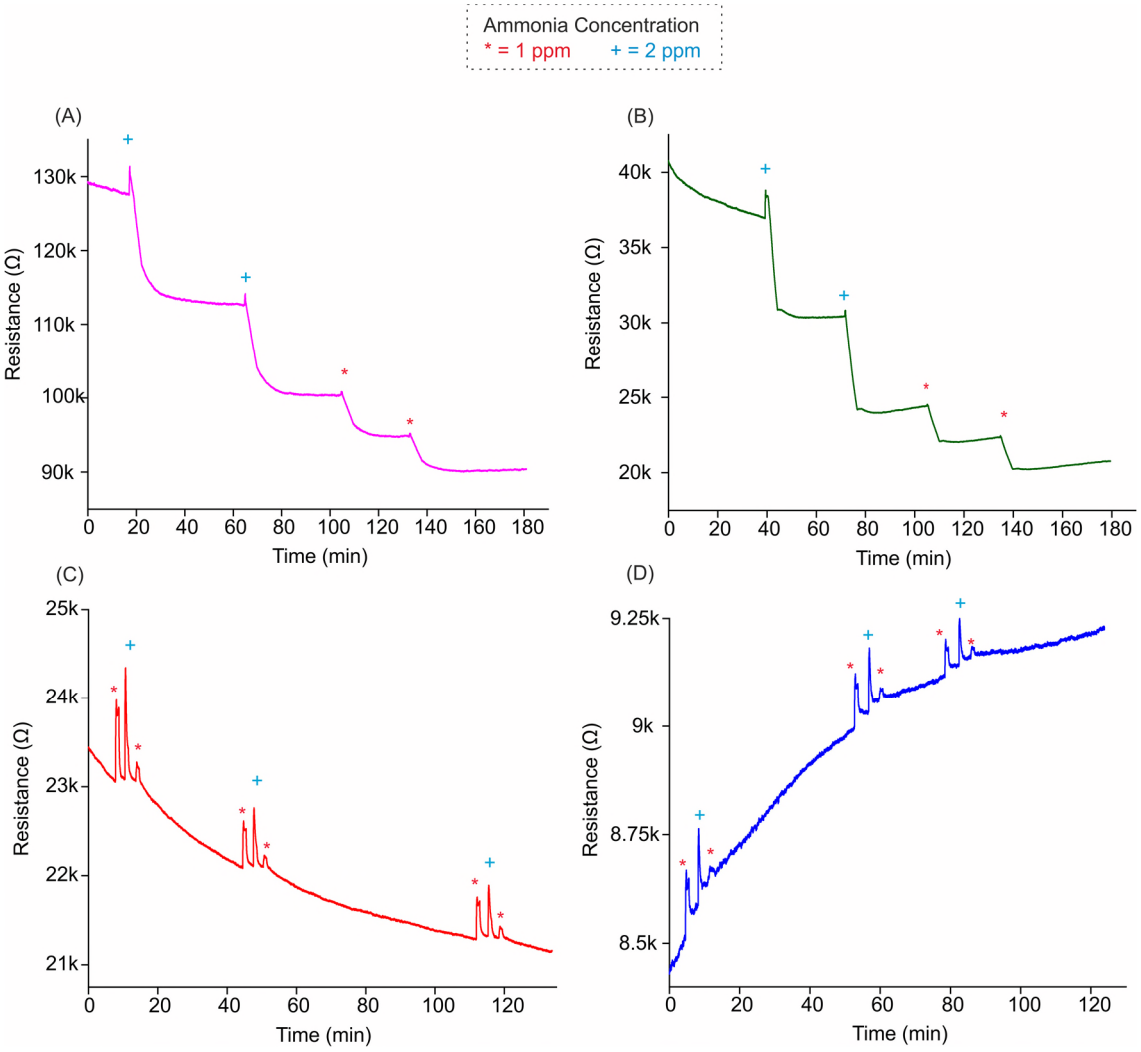


***Figure 8.13**. Chemiresistive responses of activated Cu-CAT MOF sensors to ammonia in a dry air carrier gas. (A) 3 mg mL^{-1} with a starting resistance of 130 kΩ, (B) 5 mg mL-1 with a starting resistance of 40 kΩ. (C) 8 mg mL^{-1} with a starting resistance of 23.5 kΩ and (D) 10 mg mL^{-1} with a starting resistance of 8.5 kΩ.*

As reflected in Figure 8.13 (A) & (B), at lower MOF concentration, and thus higher starting resistance, ammonia interaction results in an initial reversible increase in resistance, as expected for a strong electron donor. However, this increase is quickly followed by an irreversible and much larger decrease in resistance. For lower starting resistances and higher MOF Concentration (Figure 8.13 (C) & (D)), the analyte appears to only cause the expected reversible increase in resistance, although the magnitude of response appears to diminish between closely spaced exposures. For example, in Figure 8.13 (C), the first and third exposure in each subset of exposure cycles are both 1 ppm, but the response is markedly different in peak height. However, the first exposure of each separate subset are also each 1 ppm, and all comparatively equal in response. This indicates that the sensor requires a longer recovery between exposures than is obviously apparent from the response peak height alone.

The reason for the discrepancy in both starting conductivity-dependent reversibility of response and recovery are likely to be a function of how the electronic behaviour of the analyte affects the different constituent parts of the MOF. The exact mechanism of both the electronic structure of TP-based MOFs and how various analytes affect that is still an area of intense study that is not yet fully understood.[105] However, work to date has found that the metal centre, and in particular its d-electron count, dominates interaction.[208] In the case of the Cu metal centres in this work, the relatively high d-electron count (d^9) results in behaviour more analogous to a metal than a semiconductor. The strongly reducing ammonia results in a disruption to the charge-carrying holes in the metal centres, resulting in a rapid and reversible increase in resistance observed in all cases for the sensors in this study.

In addition to the metal centre, electronic behaviour of Cu-CAT is also affected by analyte interaction with the heteroatom of the organic ligand (O for HHTP), this time through H-bonding and charge transfer. It has been speculated previously,[105] and is further evidenced here, that for analytes including ammonia which are both strongly reducing

and strongly H-bonding, this interaction is opposing and competitive with the interaction at the metal centre, decreasing resistance. One consequence of that is that the response is lower than would be expected for relatively large concentrations of analyte of this type. Another consequence suggested by the results obtained here is that as the amount of MOF, and thus the amount of available conductive pathways is reduced, the dominant interaction switches from being that of the metal centre to that of the ligand. As more analyte irreversibly H-bonds to the ligand, and less sites are available for the impact of that to be absorbed via charge transfer by excess material in the sensing layer, its effects become more pronounced.

More work is required in this area to ascertain the point at which each sensing mechanism dominates in relation to amount of material and thus conductivity, and is currently underway in the research group. In this work, the optimum sensing layer in terms of both magnitude of response and reversibility was found to be the 8 mg mL^{-1} sensor, and it was therefore this sample that was selected for further for investigation.

The sensor was exposed to increasing concentrations of ammonia, from 100 – 1000 ppb, again for 1 minute in each case. The aim of this experiment was to attempt to ascertain both a sensitivity and an LOD for this type of sensor, and to establish if recovery was faster at lower concentrations where the effect of ligand H-bonding would be less pronounced. This experiment was carried out after 60 minutes of settling time in dry air, and the starting resistance of the sensor in this case was 21 kΩ. The raw response is shown in Figure 8.14 (A), and the rate of change plot is shown in Figure 8.14 (B). The response for 200 ppb of analyte was uncharacteristically high in comparison to the other concentrations in the range. The reason for this is likely to be an operator error during exposure, where the concentration was miscalculated at the MFC. Because this is an obvious outlier, it has been omitted from analysis.

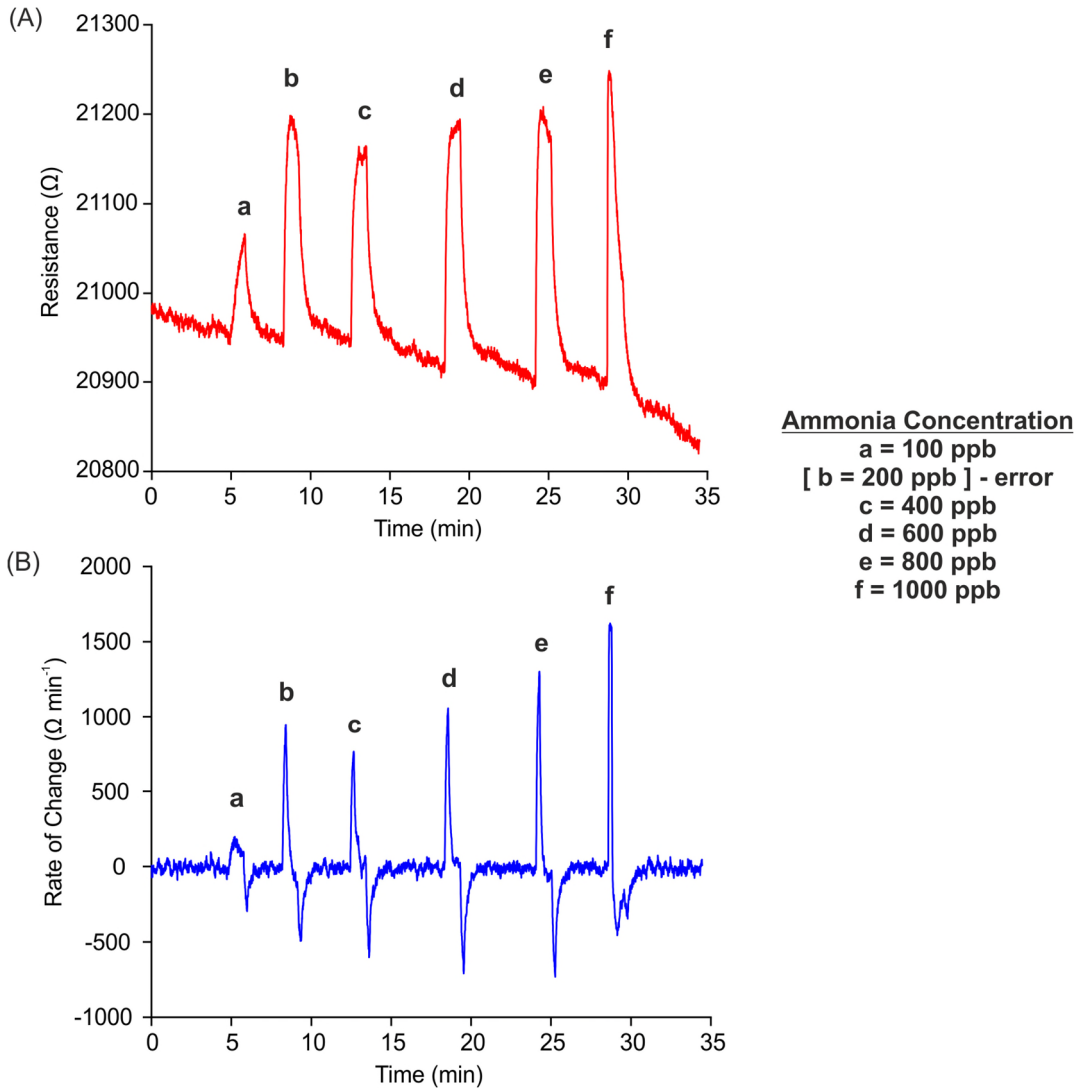


***Figure 8.14**. (A) Chemiresistive responses of an 8 mg mL^{-1} activated Cu-CAT sensor to ammonia in a dry air carrier gas with a starting resistance of 21 kΩ. The gradient of the curve in (A) is shown in (B).*

As can be seen in Figure 8.14 (B), plotting the gradient of the sensing response curve gives access to a zero centric baseline, and eliminates the vast majority of baseline drift. By visual inspection, it can also be seen that the RoC response is more linear than suggested by the raw response peaks, and thus a more reliable way to calculate figures of merit. The analysis outlined in chapter 5.4 was applied here, resulting in the response and recovery calibration curves shown in Figure 8.15.

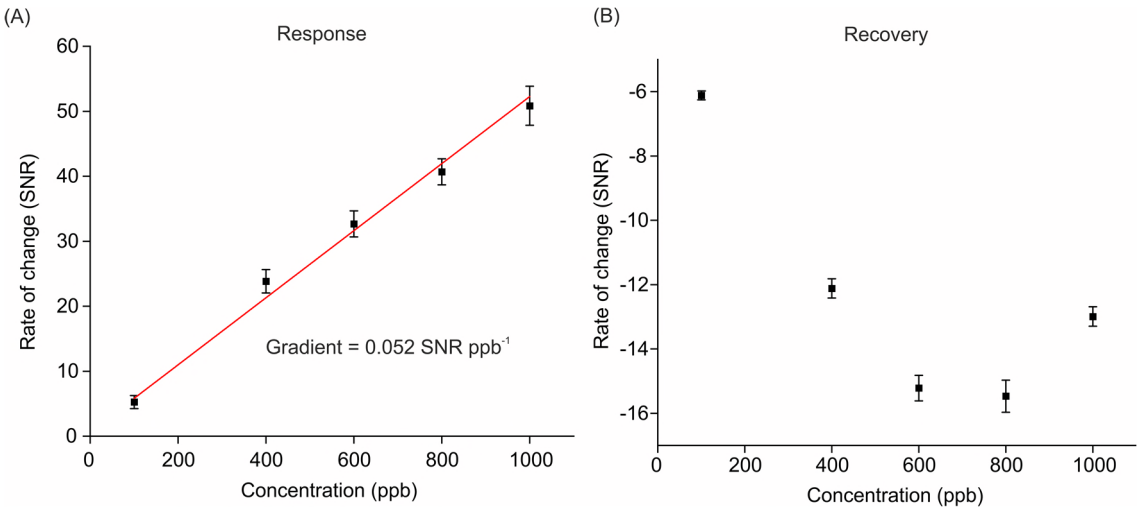


***Figure 8.15**. (A) Rate of change SNR calibration curve for an 8 mg mL^{-1} Cu-CAT MOF chemiresistor with a 21 kΩ starting resistance responding to 100 – 1000 ppb of ammonia. The gradient of this curve corresponds to sensitivity, and is intrinsic to the sensor. (B) The rate of change SNR calibration curve of the same sensor recovering after each exposure to ammonia. Error bars were estimated by propagating the RMS_{base} error through the SNR calculation.*

As reflected in Figure 8.15 (A), the linearity of the SNR signals over this dynamic range is good, with an R^2 value of 0.99. The gradient of the calibration curve, or the sensitivity of this sensor, is 0.052 SNR ppb^{-1}, resulting in an LOD of 60 (± 3) ppb. This LOD compares favourably when assessed against other published examples of Cu-CAT ammonia sensors prepared in different ways, where LOD values are typically in the range of ppm,[207,209] and to our knowledge, the absolute lowest reported Cu-CAT LOD to date, (attained using the $\Delta R/R_0$ analysis method) is 500 ppb, reported by Yao et al.[210] One reason for the higher reported LODs in prior work is likely to be that these sensors were tested at higher concentrations, and thus the impact of the secondary and competitive ligand/analyte binding was enhanced. In the case of Yao et al, testing was carried out over a range of 1 – 100 ppm, and the characteristic baseline drift of observed in this work was also observed in their work.

The linearity of the calibration curve in Figure 8.15 (A) suggests that absorption and thus analyte interaction affecting conductivity at low concentration is a first order process, which is highly likely to be a result of reversible analyte interaction at the metal centre of the MOF. However, the non-linearity of the recovery calibration curve in Figure 8.15 (B), particularly at the higher analyte concentrations in the range, suggest that desorption and thus recovery are not first order, and therefore that more than one process is responsible for the observed behaviour. This adds evidence to the proposed mechanism introduced previously, where at higher analyte concentrations irreversible analyte H-bonding to the organic linker within the MOF inhibits desorption rate and thus extends recovery time, as well as changing the baseline conductivity of the sensing layer.

It is reasonable to assume that at higher concentrations above 1 ppm, the rate of recovery slows further and tends more towards zero, in which case recovery becomes increasingly indistinguishable from baseline in RoC terms, and this explains the reduced response observed in Figure 8.13 (C) for repeated concentrations of the same amount of analyte within a short time frame. For thicker MOF layers, the onset of this behaviour is delayed because more MOF is available to absorb analyte. However, in terms of sensitivity and LOD for real time sensing of ultra-low concentrations of analyte, utilising percolation theory and RoC analysis could prove invaluable in providing MOF sensors capable of ppb detection.

8.5.2 Paper substrate MOF sensing

The sensor in this section was prepared as detailed in chapter 8.4, yielding a Cu-CAT MOF sensor deposited on paper using 20 x 5 µL drops of 10 mg mL^{-1} Cu-CAT dispersed in the tertiary ink described previously. After drawing on electrodes, the sensor was placed in the sensing chamber, as shown in Figure 8.12 (C). The sensor was stabilised for 1 hour under dry air (500 sccm), before being exposed to ammonia in a dry air carrier

gas for 2 minutes for each exposure. The resultant raw sensing plot (red line) and the subsequent RoC plot (blue line) are shown in Figure 8.16.

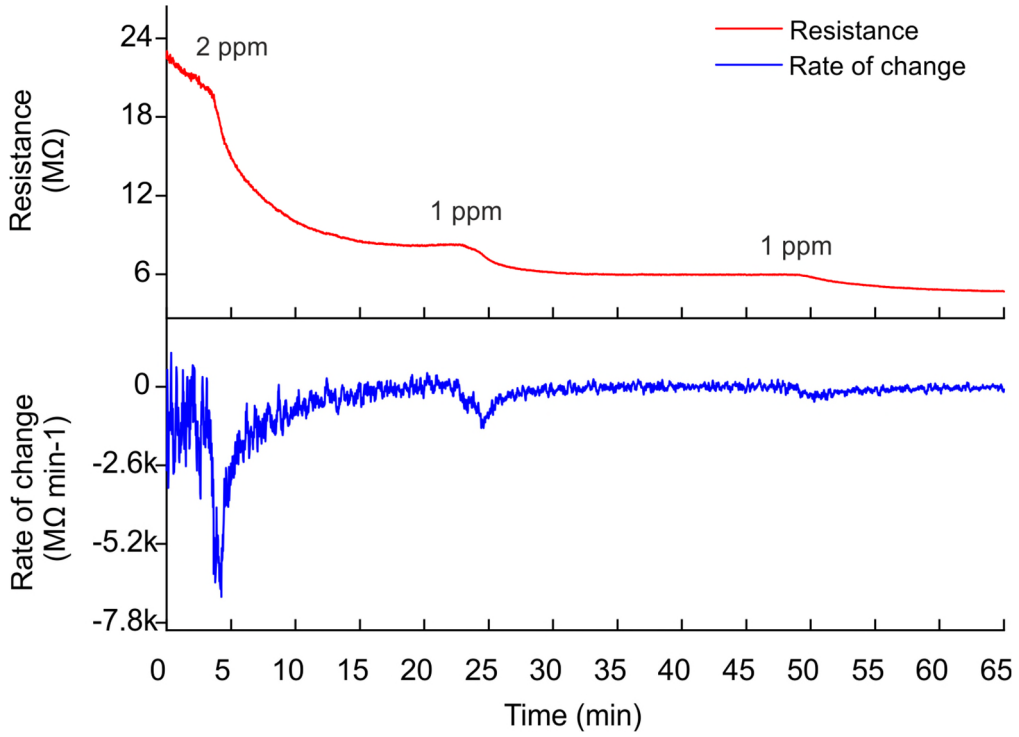


***Figure 8.16**. Chemiresistive response (red line) of a 10 mg mL^{-1} activated Cu-CAT sensor deposited on a paper substrate to ammonia in a dry air carrier gas with a starting resistance of 22 MΩ. The gradient of the curve is shown by the blue line.*

As shown in Figure 8.16, the behaviour of the sensor in this section is very similar to the high resistance glass substrate sensors of the previous section. In this case, the high starting resistance of 22 MΩ results in the dominant analyte/MOF interaction being an irreversible reduction in resistance as a result of H-bonding to the heteroatomic O of the organic linker.

Reflected in the blue line of Figure 8.16, in RoC sensing terms this results in negative non-zero rate change peaks, but a complete absence of positive non-zero peaks. Whilst this type of response has some potential utility in continuous monitoring applications, using this type of sensor for in the field step change monitoring is undesirable because

both a response and recovery peak are required to enable multiple reliable detection events to occur in the same deployment.

In many ways, paper substrates and drawn-on electrodes are an ideal candidate for chemiresistors to be used in the field. They are cheap to produce, and in an ideal scenario, an inkjet printer could print the MOF ink in any pattern, over almost any area, limited only by the size of the printer. Another potential application could be to provide a kit to any end user including a pen containing M-CAT ink (where M is any applicable metal centre) and a CircuitScribe pen. The user could then draw a sensor as and when required on any piece of paper which, after a relatively simple activation process, could be ready for deployment.

However, as shown in this section, paper substrates also have drawbacks. The primary drawback is that owing to the rough and porous nature of the paper surface, resistance at the junction between MOF particles is increased. The reason for this is likely to be because as the ink soaks into the paper, the MOF particles settle in a range of orientations relative to each other. By contrast, on a more solid and smooth surface such as glass, solvent departure can be controlled during drying, and particle orientation in likely to be more uniform, increasing contact area between MOF particles.

Increasing MOF concentration in the ink, or increasing the number of ‘passes’ required to achieve high conductivity on paper has proven unsatisfactory and impractical for solutions containing only MOF particles. One way to try and circumnavigate this issue is to reduce reliability on the MOF as the conductor in the system. It is hoped that using highly conductive AgNWs as the conductor, and regulating that conductivity by incorporating MOF particles into the mixture in a ‘top-down’ approach, may provide a solution.

8.6 Silver nanowire incorporation†

The MOF mixtures in this section were prepared using a paper substrate in the same way described in the previous section, along with a similar tertiary solvent system. However, in this work the AgNWs are supplied in a IPA solution and so IPA was used instead of ethanol, maintaining the same overall 1:1:1 ratio with ethylene glycol and 1,3-propanediol. In all samples, MOF concentration was kept constant at 0.5 mg mL^{-1}.

This concentration was chosen because it represents a point on the percolation curve shown in Figure 8.11 where the MOF is not yet displaying significant conductivity, but is on the verge of becoming conductive. It was hoped that incorporation of AgNWs at this point would increase the conductivity through stabilising the conductive network, but whilst also maintaining enough MOF in the system to ensure that it still contributes to the conductivity and thus maintains analyte sensitivity. Balancing the amount of each component is crucial, since conductivity as a result of AgNWs alone would obviously be unaffected by analyte interaction, and result in no sensing response.

8.6.1 AgNW concentration

The first stage of this process was to ascertain a percolation region for AgNWs deposited on a paper substrate with no other components present. The aim was to determine the point at which the nanowires were just below the onset of percolation behaviour. This was done to minimise the risk that the AgNW would be the only significant conductor in the system, and to therefore ensure that the MOF would play an active role in pushing the conductivity into a percolation regime. If that could be achieved, then any analyte interaction with the MOF would illicit a sensing response, since there would be no conductive pathway that enabled electron flow to bypass the MOF in the network. Figure 8.17 shows the AgNW percolation curve.

† The work in this section was heavily impacted by the Covid-19 pandemic, and thus is partially incomplete in terms of repeats and conclusive results.

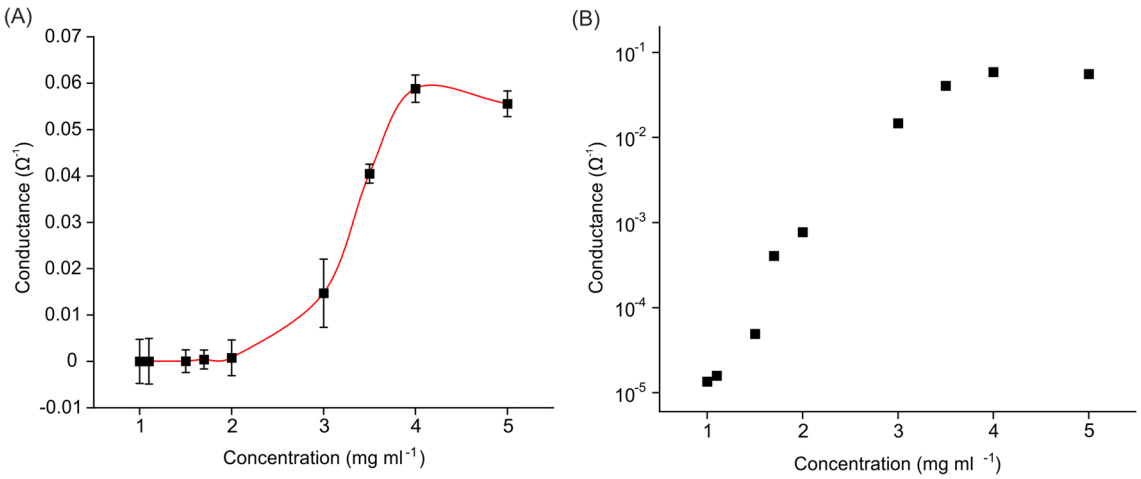


***Figure 8.17**. (A) Plot of conductance against AgNW concentration for AgNWs in IPA as received from the supplier, deposited on a paper substrate. (B) Semi-logarithmic plot of the same data (error bars omitted for clarity).*

Considering Figure 8.17 (A), it appears that the percolation region for this system lies somewhere between 2 – 4 mg mL^{-1} where the gradient of the red line is steepest. However, owing to the magnitude of change between 1 & 5 mg mL^{-1} of AgNW concentration, that is not accurate. The actual percolation region for this system, highlighted more accurately in the semi-logarithmic plot in Figure 8.17 (B) (error bars omitted for clarity), is between 1 & 3 mg mL^{-1}. Since the aim is to produce an AgNW concentration below this point, for AgNW/MOF mixtures, all concentrations of AgNW would need to be below 1 mg mL^{-1}.

Owing to the random nature of percolation, achieving consistent conductivity values for AgNW-only solutions below this concentration proved challenging, so instead a range of MOF/AgNW mixtures were prepared containing a range of AgNW concentrations below 1 mg mL^{-1} whilst keeping the MOF concentration of 5 mg mL^{-1} constant, and after drop casting a single drop of the mixture, conductivity was measured for each mixture to observe the impact of introducing Cu-CAT into the system. The resultant plot is shown in Figure 8.18.

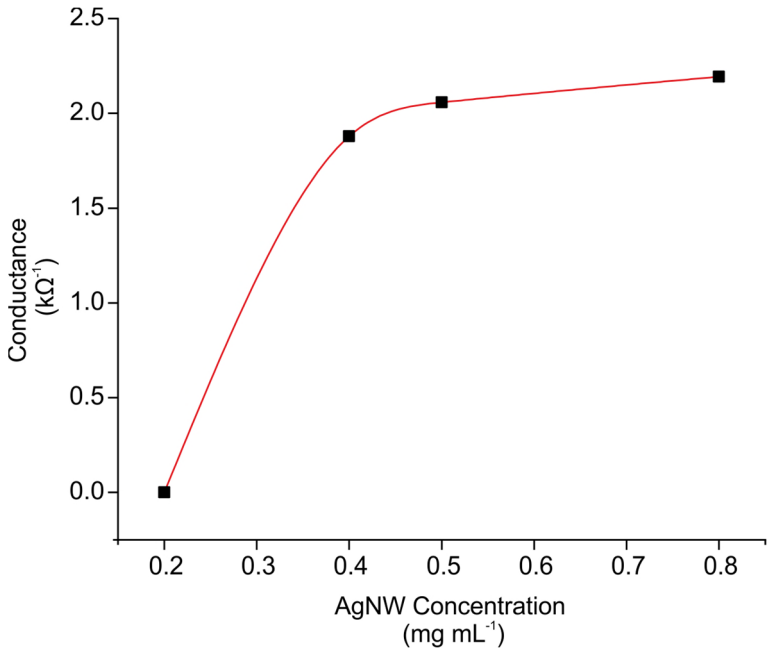


***Figure 8.18**. Plot of conductance against AgNW concentration for sensors prepared using a tertiary ink solution containing 5 mg mL^{-1} of Cu-CAT MOF, prepared by drop casting then drying one drop of the mixtures on to paper substrates.*

As shown in Figure 8.18, MOF incorporation served to increase conductivity in the system significantly. Where previously using only AgNW, 1 mg mL^{-1} had a resistance of 74 kΩ, with MOF incorporation the resistance of a 0.8 mg mL^{-1} AgNW mixture was now 0.5 kΩ. The new percolation region for these modified MOF/AgNW mixtures occurred when the AgNW concentration was below 0.4 mg mL^{-1}.

The MOF/AgNW mixtures were imaged using SEM. However, the relatively low concentrations of AgNW that provided the most promising sensors for analyte testing were not optimal for imaging, because the nanowires were difficult to see in context at lower concentrations. Figure 8.19 shows an SEM micrograph of a mixture with a slightly higher AgNW concentration (1.5 mg mL^{-1}) for better visualisation of each component.

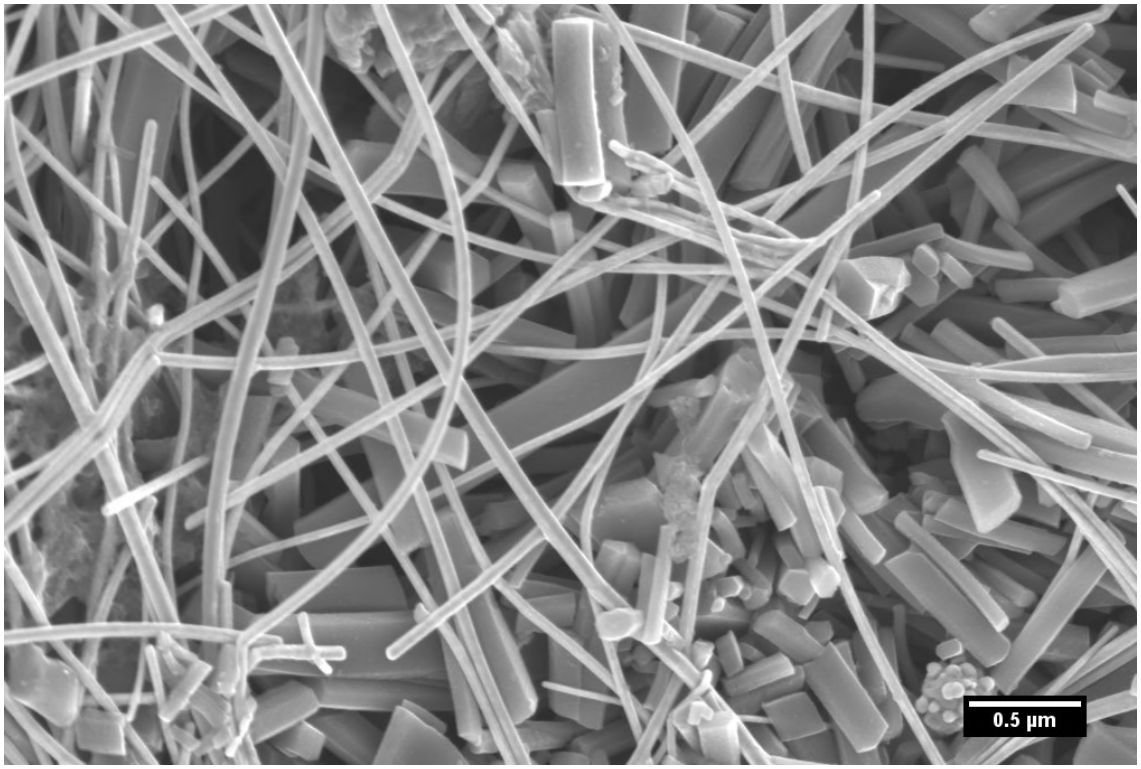


***Figure 8.19**. Scanning electron microscope micrograph of a mixture of 5 mg mL^{-1} of Cu-CAT MOF (thicker crystalline rods) and 1.5 mg mL^{-1} of AgNW (thinner cylindrical rods), drop cast onto a paper substrate from a tertiary ink solvent system.*

As reflected in Figure 8.19, rather than being a homogenous mixture of MOF and AgNW, the two components appear to have separated into two distinct layers. Since the mixtures were well mixed immediately before deposition, it is likely that this separation occurred during drying *in situ* on the substrate after deposition. This may be a result of the nanowires being more mobile in one of the phases of the tertiary mixture, resulting in them being slower to settle as the solvent evaporated. Consequently, the conductivity measurements in Figure 8.18 are likely to only have arisen as a function of AgNW concentration, since it is unlikely that the MOF is playing a significant role when the relative conductivity of the two materials is considered if they are deposited in two distinct layers. Nevertheless, sensing was attempted on the mixtures to ascertain whether the MOF was an active or passive component in these mixtures.

8.6.2 AgNW/MOF sensing

Sensors consisting of AgNW/MOF on paper substrates were prepared as described, and tested in the custom sensing chamber against both ammonia and NO_2, over an analyte concentration range of 1 – 5 ppm. In all cases using ammonia, background noise was relatively high, and no response was observed. This is likely to be a result of any response being concealed due to high noise levels. Similarly, for NO_2 all but one of the sensors showed no significant change after exposure to the analyte.

However, in the case of the 0.4: 0.5 mg mL^{-1} AgNW/Cu-CAT sensor a significant response was observed for 5 ppm of NO_2. The response is shown in Figure 8.20 (A).

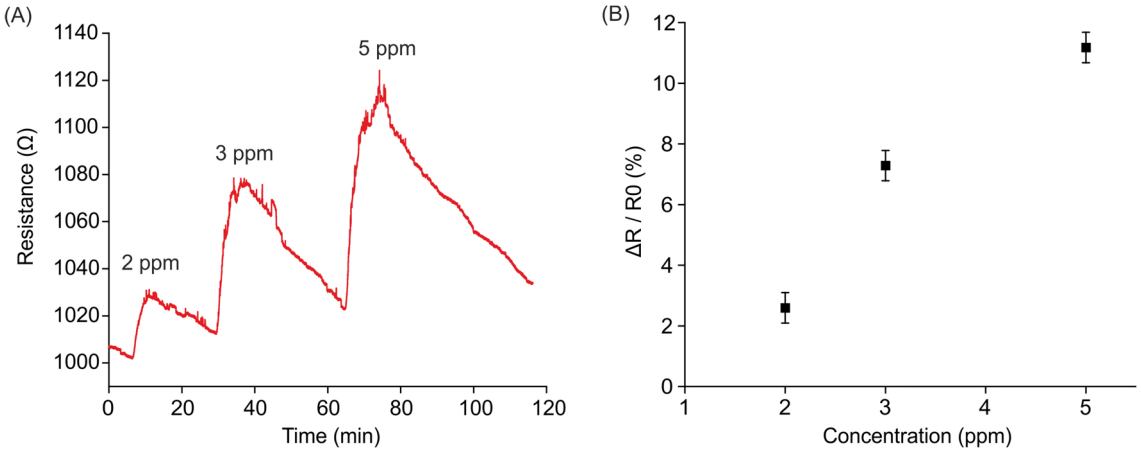


***Figure 8.20**. (A) Chemiresistive response of a sensor comprising of 5 mg mL^{-1} of activated Cu-CAT and 0.4 mg mL^{-1} silver nanowires deposited on a paper substrate responding to NO_2 in a dry air carrier gas (B) Scatter plot of percentage change in resistance of (A) versus analyte concentration, calculated using the $\Delta R/R_0$ analysis method.*

As shown in Figure 8.20 (A), the response appears to be significant visually. However, when attempting to analyse the data using the RoC method, the level of noise and instability in the baseline prior to ingress resulted in these responses being indistinguishable from the baseline. The reason for this is likely to be as a result of the morphology of the AgNW/MOF mixtures shown in Figure 8.19. However, some

information can be drawn from the sensing graph. Prior to this experiment the baseline was decreasing at almost the same rate as the recovery (see Figure 8.20 (A), 0 - ~5 min). Analysis was also attempted using the $\Delta R/R_0$ method instead, and the results of that analysis are shown in Figure 8.20 (B). Using this method, the three data points in the calibration curve are apparently non-linear.

Considering that the data obtained here proved unsatisfactory for both types of analysis, it is reasonable to assume in this case that the responses observed are not chemiresistive in nature. One conclusion drawn from that is that the secondary phase of material in the mixture, the MOF, is not contributing to the resistance changes observed. In that case, the changes observed could be due to another factor, such as swelling in the sensing layer affecting the connectivity of the AgNW, or momentary blips in flow rate continuity as the analyte stream mixes with the carrier gas disturbing the nanowires. It is clear that there are some secondary issues in this method that need further experimentation to resolve.

8.7 Summary

This chapter has revealed that M-CAT MOFs can be synthesised, characterised by p-XRD and SEM, and dispersed in an inkjet-friendly solvent system. These inks can then be deposited on a variety of substrates and used for sensing applications. By controlling the amount of MOF in the system, percolation-like behaviour can be exploited to improve sensing performance. On glass substrates, an optimised Cu-CAT MOF was produced with a detection limit of 60 ppb, which is highly competitive when compared to alternative methods of depositing HHTP MOF in other ways.

Sensing responses were also achieved for MOF inks deposited on paper, both in isolation and when the MOF was supported via the addition of highly conductive silver nanowires. However, drawbacks in using paper as a substrate were also apparent, and more work is required in order to improve the systems investigated in this chapter to

optimise paper-based sensors. One way that this may be achieved is by pressing the mixtures under relatively high force after deposition in order to reduce the amount of boundaries between particles that appears to hinder sensing performance on paper substrates. Work on this is progressing in the research group. Once deposition parameters are optimised to improve stability and sensitivity, using different metal centres and ligands could provide a relatively simple route to increased selectivity

When these issues are addressed, being able to deposit a range of MOF sensors on a wide range of substrates, either by drawing or printing the ink solutions, could offer a highly applicable route to mass producing cheap and effective detectors for many clandestine materials.

Chapter 9

Summary

This thesis describes methods for data analysis and chemiresistive sensor preparation techniques which, when combined, provide a solid platform for creating a deployable, highly mobile and low cost sensing system capable of detecting low concentrations of target analytes in a real world environment. Target analytes in this context refers to clandestine material frequently required to be detected by security and military organisations, particularly explosives and their associated by-products. However, the general ideas put forward here can, theoretically, be applied to any vapour analyte and thus potential applications are numerous and not necessarily limited in scope to clandestine material detection.

This chapter closely follows the layout of the thesis. It begins by explaining the background of and challenges relating to explosives detection, followed by a brief description of some of the most effective and popular current solutions. Next the pros and cons of chemical sensors are discussed, with particular focus on chemiresistive sensing layers and how percolation theory can be applied to chemiresistors to increase sensitivity. Then, the most frequently used analytical techniques to extract figures of merit from chemiresistive sensors is introduced and assessed in terms of transition into an in the field device. An alternative method of analysis that utilises more data, extracts more figures of merit and is more transferrable into a real world device is introduced and compared. Next, a range of percolation and thin film sensors are described, produced from different conductive materials and on a variety of substrates. Finally, sensing performance is analysed using both old and new analytical techniques to assess the merit of each sensing system.

9.1 Explosives detection: Challenges and current solutions

Sensitivity and selectivity are of paramount importantance for explosives detection, since many explosives, especially military grade examples, have very low vapour pressure. Some HME and IDE devices are constructed from less sophisticated explosive components and so have higher vapour pressures, but are inevitably very well concealed when deployed by the originators. These factors all contribute to challenging conditions for detection, necessitating sensitivity to be as high as possible. Selectivity is challenging for different reasons, especially in current and post-conflict zones where various types of explosive materials may be a constant background presence. Many explosives vapours, by-products or taggant vapours associated with explosives are small molecules that are relatively similar in size, chemical composition and interactive behaviour with detectors.

There are three main stages to any sensor strategy for explosives detection. These are (a) sample collection, (b) adsorption and interaction at the sensor resulting in signal transduction and (c) analysis, characterisation and reporting. Working dogs still provide the most efficient and effective method for achieving this strategy. However, there are moral and practical drawbacks to using dogs in conflict zones, and limited access to highly trained dogs and handlers is prohibitive to mass deployment in most other environments.

Man-made alternatives to achieve the same goal include separation techniques such as IMS, mass-spec and gas chromatography. Devices of this type, whilst often displaying excellent sensitivity in particular, are often bulky, complex, time consuming and expensive. Consequently, they are generally only practicably deployable at selected strategic locations such as airports and military bases. One appealing alternative solution that meets many of the base requirements in a highly portable form are chemically derived and produced sensors, and efforts persist to make highly sensitive

explosives detectors from active chemical layers. Of these, perhaps the simplest and most amenable to mass-production at low cost are chemiresistors

9.2 Chemiresistors and percolation

The basic principle of a chemiresistive device is that metallic electrodes are connected by a conductive or semi-conductive chemical layer. This conductivity arises as a function of delocalised electrons propagating along the entirety of the layer, connecting the electrodes and providing a baseline resistance. The balance of charge carriers, both electrons and holes, is disrupted by either direct electronic interaction with an alien species, or by some other host/analyte binding mechanism causing a change in the energy level of the charge carrier band gap. The result of either is a change in the resistance of the system as a whole, and thus a measurable detection event.

Percolation theory describes the connectedness of a system in relation to flow from one side to the other, and how the properties of the medium can dictate connectivity independently of the fluid. In relation to electron flow, the region between a system being an insulator and full conductor is the percolation region, and displays unique properties as a result. Most chemiresistors are made from depositing layers or films of the active chemical(s). At the point of which a conductive chemical layer has formed a thin film, in nearly all cases it has already passed the percolation region, and thus has a practically infinite number of conductive pathways. This means that a relatively large amount of analyte is required to illicit a significant sensing response. By specifically targeting the percolation region for sensing applications, the number of conductive pathways is vastly reduced, and thus sensitivity increases accordingly.

9.3 Chemiresistive sensing data analysis

Chemiresistive sensing data output is generally relatively simple, consisting of a record of absolute resistance changes over time. The sensors are commonly allowed a period of settling time, after which the starting resistance is recorded as the baseline (R_0). Any

deviation from this baseline as a direct result of analyte interaction is desirable and recorded as ΔR. Any other deviation from the baseline as a result of any other influence is undesirable. Calculating the ratio of analyte response peaks in relation to baseline ($\Delta R/R_0$), usually expressed as a percentage change, allows a calibration curve to be constructed. From the calibration curve, the gradient represents sensitivity and can be used to calculate a limit of detection below which a response cannot be distinguished from R_0. In this work, this is known as the $\Delta R/R_0$ method.

The $\Delta R/R_0$ method is valid in a laboratory setting, and provides a relatively straightforward means to extract some useful figures of merit. However, it is not without drawbacks. Since sensitivity is calculated directly from absolute resistance changes, any baseline fluctuation during calibration can cast doubt on figures obtained from the data. Furthermore, in any case where saturation is not reached during exposure, which is very common in chemiresistors operating within reasonable time frames, manually determined exposure time has a huge effect on the sensitivity and detection limits obtained. Finally, recovery time using this method for many sensors, and especially those operating at room temperature, can be impractically long because ideally the sensor must recover to R_0 before it can be exposed to analyte again.

Some of these drawbacks can be mitigated against in a highly controlled environment such as a lab. However, attempting to translate this analytical method into an unpredictable and changeable real world setting becomes increasingly challenging. Factors outside operator control, for example ambient temperature and humidity, will almost certainly have an impact of sensor performance and render limits obtained using the $\Delta R/R_0$ method unreliable at the time when they are needed the most.

In this work we suggest it is more reliable in this context to consider the rate of change of the sensor resistance during response instead. This method, known as the RoC method, eliminates reliance on a static resistance baseline, and largely mitigates against

the effect of exposure time discrepancy. It also vastly reduces the amount of time required between exposures for recovery, because the recovery required for the rate of change to return to being insignificant is less than the time taken for the resistance to return to R_0 in the raw sensing data. These factors mean that the RoC method is much more readily translated into a device used in the field, and because the RoC can be obtained in real time as resistance is changing, detection events can be recorded instantly. Furthermore, the RoC method uses a much larger proportion of the acquired data, and provides extra information pertaining to sensor performance than can be extracted from raw resistance changes alone.

9.4 Novel percolation sensors

The sensors described, produced and investigated in this thesis are all small, lightweight and relatively cheap to produce. They are also scalable and able to be mass produced relatively easily. In all cases, applying percolation theory to the sensing layers has resulted in a marked increase in sensitivity when compared to other sensors made from the same materials in different ways.

The first sensors described in this work are made from a conducting polymer active layer. In many ways, conducting polymers lend themselves perfectly to percolation theory, because electrochemical deposition methods, and particularly chronoamperometry, allow nucleation at the metal electrode and controlled growth which enables selective deposition as a function of time. Applying this here resulted in a large increase in sensitivity. In addition, the particular polymer described here, PPy, proved to be amenable to deposition on both glass and flexible PET electrodes, increasing potential applications for this technology.

On glass electrodes, a gold nanoparticle scaffold was deployed to support polymer percolation network formation. The gold nano-islands serve to reduce the insulating gap between conductive nodes, and thus allow more connections to be made for the same

amount of overall network conductivity. Combining gold nanoparticles and percolation theory resulted in further increases in sensitivity for PPy percolation sensors on glass substrates.

On flexible electrodes, it was not possible to deposit gold nano-islands in the same way owing to the relatively harsh conditions required for nanoparticle deposition under UHV. However, it transpired that the PET substrate, possibly owing to a rougher surface geometry, provided highly sensitive percolation sensors without the requirement for additional architecture. A comparison between glass and flexible substrates revealed that the optimum PPy percolation sensor was produced using a flexible substrate, with the lowest LOD below 10 ppb.

Whilst some conducting polymers are ideal candidates for deposition in a percolation regime, they are not necessarily ideal candidates as chemiresistive sensors deployed in the field. They are often plagued by poor selectivity since in its simplest form, polymer/analyte interaction is a simple redox process, and so any redox active analyte will elicit a response. Humidity and ambient temperature can also affect sensing performance. In fact, it is highly unlikely that any one material will have the selectivity required to detect a single analyte effectively in the field. It is more likely that a sensor array will be required that contains multiple small chemiresistive sensors working together. For that reason, other chemiresistive materials were investigated in this work to ascertain whether percolation theory could be applied to them.

Conductive MOFs have shown increased robustness in relation to the impact of humidity compared to many conducting polymers, and have additional inherent selectivity since, as shown in this work, MOF/analyte interaction is more complicated owing to the more complex architecture of the MOF. Applying percolation theory to MOFs however, is more challenging because they are generally synthesised and then deposited in separate processes, which increases high resistance junctions between MOF particles.

Nevertheless, in this work MOFs were successfully deposited in layers that had not yet reached continuous thin films, and sensitivity was shown to increase significantly as a result. The complications which arise as a function of sensor preparation for MOFs can also be turned into an advantage, since as shown here the method allows deposition in different ways, and on a wider range of substrate materials, ultimately providing numerous applications for MOF percolation sensors.

Whilst work remains to refine some of the processes investigated here, this work has provided a solid basis to build from in order to incorporate multiple chemiresistive sensors, made from a range of different sensing layers, into an electronic nose capable of both high sensitivity and selectivity for sensing clandestine material in the field.

Chapter 10

Future work

Unfortunately, a large proportion of the later stages of this work were heavily disrupted by the Covid-19 global pandemic. My original intention for the project was to combine multiple different types of percolation sensors in a demonstrator model (see chapter 2), and test them against real explosive analytes in DSTL laboratories. My intention was also to take that data and devise an analytical technique to assess each component of the e-nose both in isolation and together, with the aim of being able to identify individual analytes owing to their fingerprint response. None of the work required to achieve that has been possible owing to restricted lab access, both in Oxford and at Porton Down. In terms of future work, achieving a working prototype is essential in order to continue from the foundations provided by this work.

The PPy investigated in this work was ideal for proof of concept, but is likely to be less productive as a sensor in air, and particularly in humidity in a real world environment. Other CPs have been tested during the course of this project, but none have yet been found that are robust enough to withstand the impact of unpredictable humidity as would be found in the field. One idea could be to combine naturally occurring metal-containing macrocycles into the polymer layers to offer both some protection from the effects of humidity and add additional selectivity through new modes of analyte interaction. I began an investigation into incorporating hemin, chlorophyll and vitamin B-12 into the polymer layer, both via doping and via polymer formation in the presence of these molecules. Initial investigations showed some promise in terms of altering polymer behaviour during analyte interaction, and one stream of future work will involve further investigation of this.

In comparison to CPs, the field of conductive MOFs is still in its relative infancy and therefore provides many avenues for further research. Perhaps the most promising of these involve recent developments in being able to deposit some conductive MOFs

electrochemically, or by UHV deposition. Work on both these methods is underway in the research group as a direct consequence of my work on this project, and I am hopeful for and grateful to the researchers undertaking that work. Early results in both research streams have been very promising.

Finally, the commercially sourced metal oxide sensor investigated in Chapter 5 proved to be very stable in air and had good consistent results as a sensor. Its elevated operating temperature reduced the impact of humidity, and the number of metal oxides available to be used in this way is highly promising in terms of selectivity. MOS sensors have been thoroughly researched and still remain the only type of commercially available chemiresistive sensor. Whilst not without drawbacks and complications, my future work is likely to be focussed on attempting to apply percolation theory to MOS sensors. This has not been fully investigated to date, and so provides an avenue of research with lots of potential.

References

1. Liu, X. *et al.* A Survey on Gas Sensing Technology. *Sensors* **12**, 9635–9665 (2012).

2. Gares, K. L., Hufziger, K. T., Bykov, S. V. & Asher, S. A. Review of explosive detection methodologies and the emergence of standoff deep UV resonance Raman. *J. Raman Spectrosc.* **47**, 124–141 (2016).

3. Courbat, J. *et al.* A colorimetric CO sensor for fire detection. *Procedia Eng.* **25**, 1329–1332 (2011).

4. Lefferts, M. J. & Castell, M. R. Vapour sensing of explosive materials. *Anal. Methods* **7**, 9005–9017 (2015).

5. MacLean, E. L. & Hare, B. Enhanced selection of assistance and explosive detection dogs using cognitive measures. *Front. Vet. Sci.* **5**, 236 (2018).

6. Blue, R., Uttamchandani, D., Thomson, N. & Skabara, P. Novel polymer materials for low-cost nitro vapor detection sensors. in *2015 IEEE SENSORS - Proceedings* 12–15 (IEEE, 2015).

7. Singh, S. Sensors—An effective approach for the detection of explosives. *J. Hazard. Mater.* **144**, 15–28 (2007).

8. Kotani, K., Kawayama, I. & Tonouchi, M. Dielectric response of c-oriented SrBi2Ta2O 9 thin films observed with interdigital electrodes. *Jpn. J. Appl. Phys.* **41**, 6790–6792 (2002).

9. Cuchiaro, J. D., Kain, A. & Barnes, F. Voltage Tunable Capacitors Using High Temperature Superconductors and Ferroelectrics. *IEEE Trans.*

Appl. Supercond. **4**, 156–160 (1994).

10. Zou, Z., Kai, J., Rust, M. J., Han, J. & Ahn, C. H. Functionalized nano interdigitated electrodes arrays on polymer with integrated microfluidics for direct bio-affinity sensing using impedimetric measurement. *Sensors Actuators, A Phys.* **136**, 518–526 (2007).

11. Olthuis, W., Streekstra, W. & Bergveld, P. Theoretical and experimental determination of cell constants of planar-interdigitated electrolyte conductivity sensors. *Sensors Actuators B. Chem.* **24**, 252–256 (1995).

12. Murugappan, K. & Castell, M. R. Bridging electrode gaps with conducting polymers around the electrical percolation threshold. *Electrochem. commun.* **87**, 40–43 (2018).

13. Shirakawa, H., Louis, E. J., MacDiarmid, A. G., Chiang, C. K. & Heeger, A. J. Synthesis of electrically conducting organic polymers: Halogen derivatives of polyacetylene, (CH)x. *J. Chem. Soc. Chem. Commun.* 578–580 (1977). doi:10.1039/C39770000578

14. Voorhees, P. W. The Theory of Ostwald Ripening. *J. Stat. Phys.* **38**, 231–252 (1985).

15. Thompson, C. V. Solid-state dewetting of thin films. *Annu. Rev. Mater. Res.* **42**, 399–434 (2012).

16. Zhang, L., Li, C., Liu, A. & Shi, G. Electrosynthesis of graphene oxide/polypyrene composite films and their applications for sensing organic vapors. *J. Mater. Chem.* **22**, 8438 (2012).

17. Gares, K. L., Hufziger, K. T., Bykov, S. V. & Asher, S. A. Review of

explosive detection methodologies and the emergence of standoff deep UV resonance Raman. *J. Raman Spectrosc.* **47**, 124–141 (2016).

18. Meyers, S. & Shanley, E. S. Industrial Explosives - A Brief History of Their Development and Use. *J. Hazard. Mater.* **23**, 183–201 (1990).

19. Song-im, N., Benson, S. & Lennard, C. Evaluation of different sampling media for their potential use as a combined swab for the collection of both organic and inorganic explosive residues. *Forensic Sci. Int.* **222**, 102–110 (2012).

20. Akhavan, J. *Chemistry of Explosives*. (Royal Society of Chemistry, 2004).

21. Craven, B. A., Paterson, E. G. & Settles, G. S. The fluid dynamics of canine olfaction: unique nasal airflow patterns as an explanation of macrosmia. *J. R. Soc. Interface* **7**, 933–43 (2010).

22. Lit, L., Schweitzer, J. B. & Oberbauer, A. M. Handler beliefs affect scent detection dog outcomes. *Anim. Cogn.* **14**, 387–394 (2011).

23. Shaw, J. A. *et al.* Polarization lidar measurements of honey bees in flight for locating land mines. *Opt. Express* **13**, 5853 (2005).

24. Rodacy, P. J., Bender, S., Bromenshenk, J. J., Henderson, C. B. & Bender, G. Training and deployment of honeybees to detect explosives and other agents of harm. in *Detection and Remediation Technologies for Mines and Minelike Targets VII* 474–481 (2002).

25. Turing Tests and the Problem of Artificial Olfaction. *MIT technology Review* (2016). Available at: https://www.technologyreview.com/s/601220/turing-tests-and-the-

problem-of-artificial-olfaction/. (Accessed: 30th October 2016)

26. Breer, H. The Sense of Smell. *Ann. N. Y. Acad. Sci.* **1126**, 7–13 (2008).

27. Hallowell, S. F. Screening people for illicit substances: a survey of current portal technology. *Talanta* **54**, 447–458 (2001).

28. Coffey, V. C. Advances in Standoff Detection Make the World Safer | Features | Apr 2013 | Photonics Spectra. *Photonics Spectra* **47**, 44–47 (2013).

29. Grate, J. W., Ewing, R. G. & Atkinson, D. A. Vapor-generation methods for explosives-detection research. *TrAC - Trends Anal. Chem.* **41**, 1–14 (2012).

30. Brown, K. E., Greenfield, M. T., McGrane, S. D. & Moore, D. S. Advances in explosives analysis - part I: animal, chemical, ion, and mechanical methods. *Anal. Bioanal. Chem.* **408**, 35–47 (2015).

31. Lan, A. *et al.* A luminescent microporous metal-organic framework for the fast and reversible detection of high explosives. *Angew. Chem. Int. Ed. Engl.* **48**, 2334–2338 (2009).

32. Yinon, J. Field detection and monitoring of explosives. *TRAC-Trends Anal. Chem.* **21**, 292–301 (2002).

33. Collin, O. L., Niegel, C., DeRhodes, K. E., McCord, B. R. & Jackson, G. P. Fast gas chromatography of explosive compounds using a pulsed-discharge electron capture detector. *J. Forensic Sci.* **51**, 815–818 (2006).

34. Caygill, J. S., Davis, F. & Higson, S. P. J. Current trends in explosive detection techniques. *Talanta* **88**, 14–29 (2012).

35. Zalewska, A., Pawłowski, W. & Tomaszewski, W. Limits of detection of explosives as determined with IMS and field asymmetric IMS vapour detectors. *Forensic Sci. Int.* **226**, 168–172 (2013).

36. Moore, D. S. Instrumentation for trace detection of high explosives. *Rev. Sci. Instrum.* **75**, 2499–2512 (2004).

37. King, T. L., Horine, F. M., Daly, K. C. & Smith, B. H. Explosives Detection With Hard-Wired Moths. *IEEE Trans. Instrum. Meas.* **53**, 1113–1118 (2004).

38. Mahoney, A. *et al.* Landmine-detection rats: An evaluation of reinforcement procedures under simulated operational conditions. *J. Exp. Anal. Behav.* **101**, 450–456 (2014).

39. Becker, R. A. Meet the Giant Rats that are Sniffing Out Landmines. *National Geographic* (2015). Available at: http://news.nationalgeographic.com/2015/10/151006-giant-rats-landmines-cambodia-science-animals/. (Accessed: 24th July 2017)

40. Strano, M. S. *et al.* Nitroaromatic detection and infrared communication from wild-type plants using plant nanobionics. *Nat. Mater.* **16**, 264–272 (2016).

41. Yagur-Kroll, S., Amiel, E., Rosen, R. & Belkin, S. Detection of 2,4-dinitrotoluene and 2,4,6-trinitrotoluene by an Escherichia coli bioreporter: performance enhancement by directed evolution. *Appl. Microbiol. Biotechnol.* **99**, 7177–7188 (2015).

42. Smith, R. G., D'Souza, N. & Nicklin, S. A review of biosensors and

biologically-inspired systems for explosives detection. *Analyst* **133**, 571–584 (2008).

43. Romolo, F. S. *et al.* Field detection capability of immunochemical assays during criminal investigations involving the use of TNT. *Forensic Sci. Int.* **246**, 25–30 (2015).

44. Schulte-Ladbeck, R. & Karst, U. Determination of triacetonetriperoxide in ambient air. *Anal. Chim. Acta* **482**, 183–188 (2003).

45. Seiyama, T., Kato, A., Fujiishi, K. & Nagatani, M. A New Detector for Gaseous Components Using Semiconductive Thin Films. *Anal. Chem.* **34**, 1502–1503 (1962).

46. Pugh, D. C., Newton, E. J., Naik, A. J. T., Hailes, S. M. V. & Parkin, I. P. The gas sensing properties of zeolite modified zinc oxide. *J. Mater. Chem. A* **2**, 4758 (2014).

47. Horsfall, L. A., Pugh, D. C., Blackman, C. S. & Parkin, I. P. An array of WO 3 and CTO heterojunction semiconducting metal oxide gas sensors used as a tool for explosive detection. *J. Mater. Chem. A* **5**, 2172–2179 (2017).

48. Bernasconi, F. Kinetic and Spectral Study of Some Reactions of 2,4,6-Trinitrotoluene in Basic Solution. *J. Org. Chem.* **36**, 1671–1679 (1970).

49. Blair, H.M, Poteet, W. M. X-ray fluorescence technique for detection and location of buried explosive devices. in *Subsurface Sensing Technologies and Applications II* 494–502 (2000).

50. Guardala, N. A., Farrell, J. P., Dudnikov, V. & Merkel, G. Detection of

Hidden Explosives Using Resonant Gamma Rays From In-Flight Annihilation of Fast Positrons. in *AIP Proc.* **680**, 905–908 (2003).

51. Sun, X., Wang, Y. & Lei, Y. Fluorescence based explosive detection: from mechanisms to sensory materials. *Chem. Soc. Rev.* **44**, 8019–8061 (2015).

52. Lakowicz, J. R. *Principles of Fluorescence Spectroscopy*. (Springer, 2006).

53. Goodpaster, J. V. & McGuffin, V. L. Fluorescence quenching as an indirect detection method for nitrated explosives. *Anal. Chem.* **73**, 2004–2011 (2001).

54. Albert, K. J. *et al.* Field-deployable sniffer for 2,4-dinitrotoluene detection. *Environ. Sci. Technol.* **35**, 3193–3200 (2001).

55. Bakken, G. A., Kauffman, G. W., Jurs, P. C., Albert, K. J. & Stitzel, S. S. Pattern recognition analysis of optical sensor array data to detect nitroaromatic compound vapors. *Sensors And Actuators* **79**, 1–10 (2001).

56. Ding, L. & Fang, Y. Chemically assembled monolayers of fluorophores as chemical sensing materials. *Chem. Soc. Rev.* **39**, 4258–4273 (2010).

57. Barata, P. D. & Prata, J. V. New entities for sensory chemistry based on calix[4]arene-carbazole conjugates: from synthesis to applications. *Supramolecular Chemistry* **25**, 782–797 (2013).

58. Chio, W. I. K. *et al.* Selective Detection of Nitroexplosives Using Molecular Recognition within Self-Assembled Plasmonic Nanojunctions. *J. Phys. Chem. C* **123**, 15769–15776 (2019).

59. Ali, M. A. *et al.* Diffusion of nitroaromatic vapours into fluorescent dendrimer films for explosives detection. *Sensors Actuators, B Chem.* **210**, 550–557 (2015).

60. Deng, C. *et al.* Unusual spectroscopic properties of PPE/TiO2 composite and its sensor response to TNT. *Synth. Met.* **159**, 320–324 (2009).

61. Garnier, F. Functionalized Conducting Polymers - Towards Intelligent Materials. *Adv. Mater.* **1**, 117–121 (1989).

62. Rabenecker, P. & Pinkwart, K. A look behind electrochemical detection of explosives. *Propellants, Explos. Pyrotech.* **34**, 274–279 (2009).

63. Frisch, H. L. & Hammersley, J. M. Percolation Processes and Related Topics. *J. Soc. Indust. Appl. Math* **11**, 894–918 (1963).

64. Stradiotto, N. R., Yamanaka, H. & Zanoni, M. V. B. Review Electrochemical Sensors : A Powerful Tool in Analytical Chemistry. *J.Braz.Chem.Aoc.* **14**, 159–173 (2003).

65. James, H., Carmack, G. & Freiser, H. Coated Wire Ion Selective Electrodes Separation of Fluoride and Chloride by Solvent Extraction Using Triphenylantimony (V) Derivatives. *Anal. Chem.* **44**, 856–857 (1972).

66. Zhang, T., Nix, M. B., Yoo, B. Y., Deshusses, M. A. & Myung, N. V. Electrochemically functionalized single-walled carbon nanotube gas sensor. *Electroanalysis* **18**, 1153–1158 (2006).

67. Stetter, J. R. Amperometric Gas Sensors s A Review. *Chem. Rev.* **108**, 352–366 (2008).

68. Hesse, J. & Zemel, J. N. *Sensors, Chemical and Biochemical Sensors*. (VCH, 2008).

69. Wang, C., Yin, L., Zhang, L., Xiang, D. & Gao, R. Metal oxide gas sensors: Sensitivity and influencing factors. *Sensors* **10**, 2088–2106 (2010).

70. Grosso, G. & Parravicini, G. P. *Solid State Physics*. (Academic Press, 2014).

71. Awuzie, C. I. Conducting Polymers. in *Materials Today: Proceedings* 5721–5726 (Springer, 2017).

72. Hendon, C. H., Tiana, D. & Walsh, A. Conductive metal–organic frameworks and networks: fact or fantasy? *Phys. Chem. Chem. Phys* **14**, 13103–13454 (2012).

73. Nalwa, H. S. *Handbook of Organic Conducting Molecules and Polymers*. (Wiley, 1997).

74. Beverina, L., Pagani, G. a & Sassi, M. Multichromophoric electrochromic polymers: colour tuning of conjugated polymers through the side chain functionalization approach. *Chem. Commun. (Camb).* **50**, 5413–30 (2014).

75. MacDiarmid, A. G. & Epstein, A. J. Secondary doping in polyaniline. *Synth. Met.* **69**, 85–92 (1995).

76. Bhat, N. V, Gadre, A. P. & Bambole, V. A. Structural , Mechanical , and Electrical Properties of Electropolymerized polypyrrole films. *J. Appl. Polym. Sci.* **80**, 2511–2517 (2001).

77. Dixit, V., Misra, S. C. K. & Sharma, B. S. Carbon monoxide sensitivity of vacuum deposited polyaniline semiconducting thin films. *Sensors Actuators, B Chem.* **104**, 90–93 (2005).

78. McGovern, S. T., Spinks, G. M. & Wallace, G. G. Micro-humidity sensors based on a processable polyaniline blend. *Sensors Actuators, B Chem.* **107**, 657–665 (2005).

79. Brady, S., Lau, K. T., Megill, W., Wallace, G. G. & Diamond, D. The development and characterisation of conducting polymeric-based sensing devices. *Synth. Met.* **154**, 25–28 (2005).

80. Compton, R. G. & Banks, C. E. *Understanding Voltammetry*. (Imperial College Press, 2011).

81. Zimmermann, A., Künzelmann, U. & Dunsch, L. Initial states in the electropolymerization of aniline and p-aminodiphenylamine as studied by in situ FT-IR and UV-Vis spectroelectrochemistry. *Synth. Met.* **93**, 17–25 (1998).

82. Sazou, D., Kourouzidou, M. & Pavlidou, E. Potentiodynamic and potentiostatic deposition of polyaniline on stainless steel: Electrochemical and structural studies for a potential application to corrosion control. *Electrochim. Acta* **52**, 4385–4397 (2007).

83. Gupta, V. & Miura, N. Large-area network of polyaniline nanowires prepared by potentiostatic deposition process. *Electrochem. commun.* **7**, 995–999 (2005).

84. Kim, E., Kang, N., Moon, J. J. & Choi, M. A comparative study of

potentiodynamic and potentiostatic modes in the deposition of polyaniline. *Bull. Korean Chem. Soc.* **37**, 1445–1452 (2016).

85. Karpagam, V., Sathiyanarayanan, S. & Venkatachari, G. Studies on corrosion protection of Al2024 T6 alloy by electropolymerized polyaniline coating. *Curr. Appl. Phys.* **8**, 93–98 (2008).

86. Yang, Z., Peng, H., Wang, W. & Liu, T. Crystallization behavior of poly(ε-caprolactone)/layered double hydroxide nanocomposites. *J. Appl. Polym. Sci.* **116**, 2658–2667 (2010).

87. Patra, S. & Munichandraiah, N. Electrooxidation of methanol on pt-modified conductive polymer PEDOT. *Langmuir* **25**, 1732–1738 (2009).

88. Randriamahazaka, H., Noël, V. & Chevrot, C. Nucleation and growth of poly(3,4-ethylenedioxythiophene) in acetonitrile on platinum under potentiostatic conditions. *J. Electroanal. Chem.* **472**, 103–111 (1999).

89. Du, X. & Wang, Z. Effects of polymerization potential on the properties of electrosynthesized PEDOT films. *Electrochim. Acta* **48**, 1713–1717 (2003).

90. Lim, Y. S. *et al.* Polypyrrole/graphene composite films synthesized via potentiostatic deposition. *J. Appl. Polym. Sci.* **128**, 224–229 (2013).

91. Dubal, D. P., Patil, S. V., Kim, W. B. & Lokhande, C. D. Supercapacitors based on electrochemically deposited polypyrrole nanobricks. *Mater. Lett.* **65**, 2628–2631 (2011).

92. Saidman, S. B. The effect of pH on the electrochemical polymerisation of pyrrole on aluminium. *J. Electroanal. Chem.* **534**, 39–45 (2002).

93. Bazzaoui, M., Martins, J. I., Bazzaoui, E. A., Reis, T. C. & Martins, L. Pyrrole electropolymerization on copper and brass in a single-step process from aqueous solution. *J. Appl. Electrochem.* **34**, 815–822 (2004).

94. Dai, Y. *et al.* Electrosynthesis and characterization of polythiophene and corrosion protection for stainless steel. *Int. J. Electrochem. Sci.* **11**, 4084–4091 (2016).

95. del Valle, M. A., Gacitúa, M., Díaz, F. R., Armijo, F. & Río, R. del. Electrosynthesis of polythiophene nanowires via mesoporous silica thin film templates. *Electrochem. commun.* **11**, 2117–2120 (2009).

96. Valaski, R., Canestraro, C. D., Micaroni, L., Mello, R. M. Q. & Roman, L. S. Organic photovoltaic devices based on polythiophene films electrodeposited on FTO substrates. *Sol. Energy Mater. Sol. Cells* **91**, 684–688 (2007).

97. Zhang, J. *et al.* Electrochemical fabrication of polythiophene film coated metallic nanowire arrays. *J. Mater. Sci.* **38**, 2423–2427 (2003).

98. Mccullough, R. D., Lowe, R. D., Jayaraman, M. & Anderson, D. L. Design, Synthesis, and Control. *J. Org. Chem.* **58**, 904–912 (1993).

99. Narayan, T. C., Miyakai, T., Seki, S. & Dincă, M. High charge mobility in a tetrathiafulvalene-based microporous metal-organic framework. *J. Am. Chem. Soc.* **134**, 12932–12935 (2012).

100. Dinca, M. *et al.* Cation-dependent intrinsic electrical conductivity in isostructural tetrathiafulvalene-based microporous metal-organic

frameworks. *J. Am. Chem. Soc.* **137**, 1774–1777 (2015).

101. Kambe, T., Sakamoto, R. & Kusamoto, T. Redox Control and High Conductivity of Nickel Bis (dithiolene) Complex π-Nanosheet. *J. Am. Chem. Soc.* **136**, 14357–14360 (2014).

102. Dinca, M., Campbell, M. G., Sheberla, D., Liu, S. F. & Swager, T. M. Cu3(hexaiminotriphenylene)2: An electrically conductive 2D metal-organic framework for chemiresistive sensing. *Angew. Chemie - Int. Ed.* **54**, 4349–4352 (2015).

103. Huang, X. *et al.* A two-dimensional π-d conjugated coordination polymer with extremely high electrical conductivity and ambipolar transport behaviour. *Nat. Commun.* **6**, 7408 (2015).

104. Sheberla, D. *et al.* High Electrical Conductivity in Ni3(2,3,6,7,10,11-hexaiminotriphenylene)2, a Semiconducting Metal-Organic Graphene Analogue. *J. Am. Chem. Soc.* **136**, 8859–8862 (2014).

105. Dinca, M., Campbell, M. G., Liu, S. F. & Swager, T. M. Chemiresistive Sensor Arrays from Conductive 2D Metal-Organic Frameworks. *J. Am. Chem. Soc.* **137**, 13780–13783 (2015).

106. Campbell, M. G. & Dincă, M. Metal–organic frameworks as active materials in electronic sensor devices. *Sensors* **17**, 1108 (2017).

107. Campagnol, N. *et al.* On the Electrochemical Deposition of Metal-Organic Frameworks. *J. Mater. Chem. A* **4**, 3914–3925 (2016).

108. Li, W. *et al.* Metal-organic frameworks thin films: electrochemical fabrication techniques and corresponding applications &

perspectives. *J. Mater. Chem. A* **4**, 12356–12369 (2013).

109. Labafzadeh, S. R., Vyavaharkar, K., Kavakka, J. S., King, A. W. T. & Kilpeläinen, I. Amination and thiolation of chloroacetyl cellulose through reactive dissolution in N,N-dimethylformamide. *Carbohydr. Polym.* **116**, 60–66 (2015).

110. Da Luz, L. L. *et al.* Inkjet Printing of Lanthanide-Organic Frameworks for Anti-Counterfeiting Applications. *ACS Appl. Mater. Interfaces* **7**, 27115–27123 (2015).

111. Zhuang, J. L., Ar, D., Yu, X. J., Liu, J. X. & Terfort, A. Patterned deposition of metal-organic frameworks onto plastic, paper, and textile substrates by inkjet printing of a precursor solution. *Adv. Mater.* **25**, 4631–4635 (2013).

112. Waasdorp, R., Van Den Heuvel, O., Versluis, F., Hajee, B. & Ghatkesar, M. K. Accessing individual 75-micron diameter nozzles of a desktop inkjet printer to dispense picoliter droplets on demand. *RSC Adv.* **8**, 14765–14774 (2018).

113. Sun, L., Campbell, M. G. & Dincə, M. Electrically Conductive Porous Metal-Organic Frameworks. *Angew. Chemie - Int. Ed.* **55**, 3566–3579 (2016).

114. Bhardwaj, S. K. *et al.* An overview of different strategies to introduce conductivity in metal-organic frameworks and miscellaneous applications thereof. *J. Mater. Chem. A* **6**, 14992–15009 (2018).

115. Sun, L., Hendon, C. H., Minier, M. A., Walsh, A. & Dincə, M. Million-fold

electrical conductivity enhancement in Fe_2(DEBDC) versus Mn_2(DEBDC). *J. Am. Chem. Soc.* **137**, 6164–6167 (2015).

116. Darago, L. E., Aubrey, M. L., Yu, C. J., Gonzalez, M. I. & Long, J. R. Electronic Conductivity, Ferrimagnetic Ordering, and Reductive Insertion Mediated by Organic Mixed-Valence in a Ferric Semiquinoid Metal-Organic Framework. *J. Am. Chem. Soc.* **137**, 15703–15711 (2015).

117. Xu, F. & Zhu, Y. Highly conductive and stretchable silver nanowire conductors. *Adv. Mater.* **24**, 5117–5122 (2012).

118. Lee, H., Kim, I., Kim, M. & Lee, H. Moving beyond flexible to stretchable conductive electrodes using metal nanowires and graphenes. *Nanoscale* **8**, 1789–1822 (2016).

119. Liang, J., Li, L., Niu, X., Yu, Z. & Pei, Q. Elastomeric polymer light-emitting devices and displays. *Nat. Photonics* **7**, 817–824 (2013).

120. Park, J. *et al.* Wearable, wireless gas sensors using highly stretchable and transparent structures of nanowires and graphene. *Nanoscale* **8**, 10591–10597 (2016).

121. Newman, M. E. J. & Ziff, R. M. Fast Monte Carlo algorithm for site or bond percolation. *Phys. Rev. E - Stat. Physics, Plasmas, Fluids Relat. Interdiscip. Top.* **64**, 16 (2001).

122. Flory, B. P. J. & Flory, P. J. Molecular Size Distribution in Three Dimensional Polymers . *J. Am. Chem. Soc.* **63**, 3083–3090 (1941).

123. Stockmayer, W. H. Theory of Molecular Size Distribution and Gel Formation in Branched Polymers II . General Cross Linking. *J. Chem.*

Phys. **12**, 125–131 (1944).

124. Broadbent, S. R. & Hammersley, J. M. Percolation processes. *Proc. Cambridge Philos. Soc.* **53**, 629–641 (1957).

125. Radicchi, F. & Castellano, C. Breaking of the site-bond percolation universality in networks. *Nat. Commun.* **6**, (2015).

126. Stauffer, D. & Aharony, A. *An Introduction to Percolation Theory*. (Taylor & Francis, 1992).

127. Scher, H. & Zallen, R. Critical Density in Percolation Processes. *J. Chem. Phys.* **53**, 3759–3761 (1970).

128. Sahimi, M. *Applications of Percolation Theory*. (Taylor & Francis, 1994).

129. King, P. R. *et al.* Using percolation theory to predict oil field performance. *Phys. A Stat. Mech. its Appl.* **314**, 103–108 (2002).

130. Foygel, M., Morris, R. D., Anez, D., French, S. & Sobolev, V. L. Theoretical and computational studies of carbon nanotube composites and suspensions: Electrical and thermal conductivity. *Phys. Rev. B - Condens. Matter Mater. Phys.* **71**, (2005).

131. Kumar, A., Vidhyadhiraja, N. S. & Kulkarni, G. U. Current distribution in conducting nanowire networks. *J. Appl. Phys.* **122**, (2017).

132. Bruno, L., Pijolat, C. & Lalauze, R. Tin dioxide thin-film gas sensor prepared by chemical vapour deposition. Influence of grain size and thickness on the electrical properties. *Sensors Actuators B. Chem.* **18**, 195–199 (1994).

133. Vigna, L. *et al.* A Flexible, Highly Sensitive, and Selective Chemiresistive Gas Sensor Obtained by In Situ Photopolymerization of an Acrylic Resin in the Presence of MWCNTs. *Macromol. Mater. Eng.* **304**, (2019).

134. Persaud, K. & Dodd, G. Olfactory System Using a Model Nose. *Nature* **299**, 352–355 (1982).

135. Amoore, J. E., Johnston Jr., J. W. & Rubin, M. The stereochemical theory of odour. *Sci. Am.* **210**, 42–49 (1964).

136. Hu, W. *et al.* Electronic Noses: From Advanced Materials to Sensors Aided with Data Processing. *Adv. Mater. Technol.* **4**, (2019).

137. Shi, H., Zhang, M. & Adhikari, B. Advances of electronic nose and its application in fresh foods: A review. *Crit. Rev. Food Sci. Nutr.* **58**, 2700–2710 (2018).

138. Farraia, M. V. *et al.* The electronic nose technology in clinical diagnosis. *Porto Biomed. J.* **4**, 42 (2019).

139. Lichtenstein, A. *et al.* Supersensitive fingerprinting of explosives by chemically modified nanosensors arrays. *Nat. Commun.* **5**, (2014).

140. Alaouie, A. M. & Alawieh, M. B. Critical evaluation of single point measurement-based quantitative analyses in forensic breath alcohol. *Forensic Sci. Int. Reports* **2**, (2020).

141. Penza, M., Rossi, R., Alvisi, M. & Serra, E. Metal-modified and vertically aligned carbon nanotube sensors array for landfill gas monitoring applications. *Nanotechnology* **21**, 105501 (2010).

142. Chiou, J. C., Wu, C. C., Huang, Y. C., Chang, S. C. & Lin, T. M. Effects of

operating temperature on droplet casting of flexible polymer/multi-walled carbon nanotube composite gas sensors. *Sensors* **17**, (2017).

143. Rout, C. S., Hegde, M., Govindaraj, A. & Rao, C. N. R. Ammonia sensors based on metal oxide nanostructures. *Nanotechnology* **18**, (2007).

144. Tang, R., Shi, Y., Hou, Z. & Wei, L. Carbon nanotube-based chemiresistive sensors. *Sensors* **17**, (2017).

145. Fratoddi, I., Venditti, I., Cametti, C. & Vittoria, M. Sensors and Actuators B : Chemical Chemiresistive polyaniline-based gas sensors : A mini review. *Sensors Actuators B. Chem.* **220**, 534–548 (2015).

146. Wang, C. *et al.* A reduced GO-graphene hybrid gas sensor for ultra-low concentration ammonia detection. *Sensors* **18**, 3147–3162 (2018).

147. Šetka, M., Drbohlavová, J. & Hubálek, J. Nanostructured polypyrrole-based ammonia and volatile organic compound sensors. *Sensors (Switzerland)* **17**, 1–28 (2017).

148. Lange, U. & Mirsky, V. M. Integrated electrochemical transistor as a fast recoverable gas sensor. *Anal. Chim. Acta* **687**, 7–11 (2011).

149. Li, J. *et al.* Carbon nanotube sensors for gas and organic vapor detection. *Nano Lett.* **3**, 929–933 (2003).

150. Currie, L. A. INTERNATIONAL UNION OF PURE AND APPLIED CHEMISTRY ANALYTICAL CHEMISTRY DIVISION COMMISSION ON ANALYTICAL NOMENCLATURE*+ NOMENCLATURE IN EVALUATION OF ANALYTICAL METHODS INCLUDING DETECTION AND QUANTIFICATION CAPABILITIES (IUPAC Recommendations 1995).

Pure Appl. Chem **67**, 1699–1723 (1995).

151. Shrivastava, A. & Gupta, V. Methods for the determination of limit of detection and limit of quantitation of the analytical methods. *Chronicles Young Sci.* **2**, 21 (2011).

152. Schroeder, V., Savagatrup, S., He, M., Lin, S. & Swager, T. M. Carbon nanotube chemical sensors. *Chem. Rev.* **119**, 599–663 (2019).

153. Torsi, L., Magliulo, M., Manoli, K. & Palazzo, G. Organic field-effect transistor sensors: A tutorial review. *Chem. Soc. Rev.* **42**, 8612–8628 (2013).

154. Sharma, N. *et al.* Heptazine based organic framework as a chemiresistive sensor for ammonia detection at room temperature. *J. Mater. Chem. A* **6**, 18389–18395 (2018).

155. Wang, C. *et al.* A reduced GO-graphene hybrid gas sensor for ultra-low concentration ammonia detection. *Sensors* **18**, (2018).

156. SGXSensortech. MiCS-4514 Datasheet. MiCS-4514 Datasheet, Available at: https://www.mou

157. SGX Sensortech. Sgxsensortech. (2019). Available at: https://www.sgxsensortech.com/sensor-selector/#prod_1499. (Accessed: 16th August 2019)

158. Gustafsson, G. *et al.* The interaction between ammonia and poly(pyrrole). *Synth. Met.* **31**, 163–179 (1989).

159. Yeole, B., Parshottam Hansora, D., Mishra, S., Sen, T. & Hansora, D. Electrical and Gas Sensing Behaviour of Polypyrrole/silver Sulphide

Nanocomposites. *Am. J. Sens. Technol.* **4**, 10–20 (2017).

160. Liu, P., Wu, S., Zhang, Y., Zhang, H. & Qin, X. A fast response ammonia sensor based on coaxial PPy-PAN nanofiber yarn. *Nanomaterials* **6**, (2016).

161. Campbell, C. T. Metal films and particles on oxide surfaces: Structural, electronic and chemisorptive properties. *J. Chem. Soc. - Faraday Trans.* **92**, 1435–1445 (1996).

162. Lefferts, M. J. Ultra-Sensitive Molecular Detection of Explosives. (University of Oxford, 2017).

163. Lefferts, M. J., Murugappan, K., Wu, C. & Castell, M. R. Electrical percolation through a discontinuous Au nanoparticle film. *Appl. Phys. Lett.* **112**, (2018).

164. Carquigny, S., Sanchez, J. B., Berger, F., Lakard, B. & Lallemand, F. Ammonia gas sensor based on electrosynthesized polypyrrole films. *Talanta* **78**, 199–206 (2009).

165. Chougule, M. A. *et al.* Polypyrrole thin film: Room temperature ammonia gas sensor. *IEEE Sens. J.* **11**, 2137–2141 (2011).

166. Joshi, A., Gangal, S. A. & Gupta, S. K. Ammonia sensing properties of polypyrrole thin films at room temperature. *Sensors Actuators, B Chem.* **156**, 938–942 (2011).

167. Marsden, A. J. *et al.* Electrical percolation in graphene-polymer composites. *2D Mater.* **5**, (2018).

168. Jang, H.-K. *et al.* Electrical percolation thresholds of semiconducting

single-walled carbon nanotube networks in field-effect transistors. *Phys. Chem. Chem. Phys.* **17**, 6874–6880 (2015).

169. Bartlett, P. N., Archer, P. B. M. & Ling-Chung, S. K. Conducting polymer gas sensors part I: Fabrication and characterization. *Sensors And Actuators* **19**, 125–140 (1989).

170. Bartlett, P. N. & Ling-Chung, S. K. Conducting polymer gas sensors part II: Response of polypyrrole to methanol. *Sensors And Actuators* **19**, 141–150 (1989).

171. Bai, H. & Shi, G. Gas Sensors Based on Conducting Polymers. *Sensors* **7**, 267–307 (2007).

172. Wilson, A. D. Review of Electronic-nose Technologies and Algorithms to Detect Hazardous Chemicals in the Environment. *Procedia Technol.* **1**, 453–463 (2012).

173. James, D., Scott, S. M., Ali, Z. & O'Hare, W. T. Chemical sensors for electronic nose systems. *Microchim. Acta* **149**, (2005).

174. Nag, A., Mukhopadhyay, S. C. & Kosel, J. Wearable Flexible Sensors: A Review. *IEEE Sens. J.* **17**, 3949–3960 (2017).

175. Singh, E., Meyyappan, M. & Nalwa, H. S. Flexible Graphene-Based Wearable Gas and Chemical Sensors. *ACS Appl. Mater. Interfaces* **9**, 34544–34586 (2017).

176. Qian, Y. *et al.* Thin-film organic semiconductor devices: from flexibility to ultraflexibility. *Sci. China Mater.* **59**, 589–608 (2016).

177. Zheng, X. Q. & Cheng, H. Y. Flexible and stretchable metal oxide gas

sensors for healthcare. *Sci. China Technol. Sci.* **62**, 209–223 (2019).

178. Wang, L. *et al.* Flexible chemiresistor sensors: Thin film assemblies of nanoparticles on a polyethylene terephthalate substrate. *J. Mater. Chem.* **20**, 907–915 (2010).

179. Wang, T. *et al.* Flexible Transparent Electronic Gas Sensors. *Small* **12**, 3748–3756 (2016).

180. Lange, U., Roznyatovskaya, N. V. & Mirsky, V. M. Conducting polymers in chemical sensors and arrays. *Anal. Chim. Acta* **614**, (2008).

181. Lange, U. & Mirsky, V. M. Chemiresistors based on conducting polymers: A review on measurement techniques. *Anal. Chim. Acta* **687**, 105–113 (2011).

182. An, B. W. *et al.* Smart sensor systems for wearable electronic devices. *Polymers (Basel).* **9**, 303–344 (2017).

183. Kumar, L., Rawal, I., Kaur, A. & Annapoorni, S. Sensors and Actuators B : Chemical Flexible room temperature ammonia sensor based on polyaniline. *Sensors Actuators B. Chem.* **240**, 408–416 (2017).

184. Bai, S. *et al.* Ultrasensitive room temperature NH3 sensor based on a graphene-polyaniline hybrid loaded on PET thin film. *Chem. Commun.* **51**, 7524–7527 (2015).

185. Kuberský, P., Syrový, T., Hamacek, A., Nešpůrek, S. & Stejskal, J. Printed flexible gas sensors based on organic materials. *Procedia Eng.* **120**, 614–617 (2015).

186. Amaya, T., Abe, Y., Inada, Y. & Hirao, T. Synthesis of self-doped

conducting polyaniline bearing phosphonic acid. *Tetrahedron Lett.* **55**, 3976–3978 (2014).

187. Kruefu, V., Wisitsoraat, A., Tuantranont, A. & Phanichphant, S. Gas sensing properties of conducting polymer/Au-loaded ZnO nanoparticle composite materials at room temperature. *Nanoscale Res. Lett.* **9**, 1–12 (2014).

188. Rhee, S. K. Surface energies of silicate glasses calculated from their wettability data. *J. Mater. Sci.* **12**, 823–824 (1977).

189. Yesil, S. & Bayram, G. Poly(ethylene terephthalate)/Carbon Nanotube Composites Prepared With Chemically Treated Carbon Nanotubes. *Polym. Eng. Sci.* **51**, 1286–1300 (2011).

190. Wong, Y. C., Ang, B. C., Haseeb, A. S. M. A., Baharuddin, A. A. & Wong, Y. H. Review—Conducting Polymers as Chemiresistive Gas Sensing Materials: A Review. *J. Electrochem. Soc.* **167**, 037503 (2020).

191. Yan, Y. *et al.* Viral-templated gold/polypyrrole nanopeapods for an ammonia gas sensor. *Nanotechnology* **27**, 325502 (2016).

192. Chartuprayoon, N., Hangarter, C. M., Rheem, Y., Jung, H. & Myung, N. V. Wafer-scale fabrication of single polypyrrole nanoribbon-based ammonia sensor. *J. Phys. Chem. C* **114**, 11103–11108 (2010).

193. Lee, J. S., Jun, J., Shin, D. H. & Jang, J. Urchin-like polypyrrole nanoparticles for highly sensitive and selective chemiresistive sensor application. *Nanoscale* **6**, 4188–4194 (2014).

194. Xiang, C. *et al.* Ammonia sensor based on polypyrrole-graphene

nanocomposite decorated with titania nanoparticles. *Ceram. Int.* **41**, 6432–6438 (2015).

195. Zhang, L. *et al.* A novel ammonia sensor based on high density, small diameter polypyrrole nanowire arrays. *Sensors Actuators, B Chem.* **142**, 204–209 (2009).

196. Tiwari, D. C., Atri, P. & Sharma, R. Sensitive detection of ammonia by reduced graphene oxide/polypyrrole nanocomposites. *Synth. Met.* **203**, 228–234 (2015).

197. Circuit Scribe. (2020). Available at: https://circuitscribe.com/. (Accessed: 14th October 2020)

198. Smith, M. K., Jensen, K. E., Pivak, P. A. & Mirica, K. A. Direct Self-Assembly of Conductive Nanorods of Metal-Organic Frameworks into Chemiresistive Devices on Shrinkable Polymer Films. *Chem. Mater.* **28**, 5264–5268 (2016).

199. Hmadeh, M. *et al.* New porous crystals of extended metal-catecholates. *Chem. Mater.* **24**, 3511–3513 (2012).

200. Kim, S. H., Misner, M. J., Xu, T., Kimura, M. & Russell, T. P. Highly oriented and ordered arrays from block copolymers via solvent evaporation. *Adv. Mater.* **16**, 226–231 (2004).

201. De Gans, B. J. & Schubert, U. S. Inkjet printing of well-defined polymer dots and arrays. *Langmuir* **20**, 7789–7793 (2004).

202. Poulichet, V., Morel, M., Rudiuk, S. & Baigl, D. Liquid-liquid coffee-ring effect. *J. Colloid Interface Sci.* **573**, 370–375 (2020).

203. Deegan, R. D. *et al.* Capillary flow as the cause of ring stains from dried liquid drops. *Nature* **389**, 827–829 (1997).

204. Hu, G. *et al.* A general ink formulation of 2D crystals for wafer-scale inkjet printing. *Sci. Adv.* **6**, 1–7 (2020).

205. *CRC Handbook of Chemistry and Physics*. (CRC Press Inc., 2011).

206. Nayak, L., Mohanty, S., Nayak, S. K. & Ramadoss, A. A review on inkjet printing of nanoparticle inks for flexible electronics. *J. Mater. Chem. C* **7**, 8771–8795 (2019).

207. Ko, M., Aykanat, A., Smith, M. K. & Mirica, K. A. Drawing sensors with ball-milled blends of metal-organic frameworks and graphite. *Sensors* **17**, (2017).

208. Chen, S., Dai, J. & Zeng, X. C. Metal-organic Kagome lattices M3(2,3,6,7,10,11-hexaiminotriphenylene)2 (M = Ni and Cu): From semiconducting to metallic by metal substitution. *Phys. Chem. Chem. Phys.* **17**, 5954–5958 (2015).

209. Koo, W.-T., Jang, J.-S. & Kim, I.-D. Metal-Organic Frameworks for Chemiresistive Sensors. *Chem* **5**, 1938–1963 (2019).

210. Yao, M. S. *et al.* Layer-by-Layer Assembled Conductive Metal–Organic Framework Nanofilms for Room-Temperature Chemiresistive Sensing. *Angew. Chemie - Int. Ed.* **56**, 16510–16514 (2017).

211. Ewing, R. G., Waltman, M. J., Atkinson, D. A., Grate, J. W. & Hotchkiss, P. J. The vapor pressures of explosives. *TrAC - Trends Anal. Chem.* **42**, 35–48 (2013).

212. Zolfagharifard, E. UK Engineers Develop Bee-based Security Device. *The Engineer* (2011). Available at: https://www.theengineer.co.uk/issues/28-march-2011/uk-engineers-develop-bee-based-security-device/. (Accessed: 24th July 2020)